Title
PICOSECOND STUDIES OF VIBRATIONAL LINEWIDTH BROADENING IN LIQUIDS

Author
George, S.M.

Publication Date
1983-03-01

Lawrence Berkeley Laboratory
UNIVERSITY OF CALIFORNIA

Materials & Molecular
Research Division

PICOSECOND STUDIES OF VIBRATIONAL LINEWIDTH BROADENING IN LIQUIDS

Steven McClellan George
(Ph.D. Thesis)

March 1983

Prepared for the U.S. Department of Energy under Contract DE-AC03-76SF00098

DISCLAIMER

LBL-15842

PICOSECOND STUDIES OF VIBRATIONAL LINEWIDTH BROADENING IN LIQUIDS

Steven McClellan George
(Ph.D. Thesis)

Lawrence Berkeley Laboratory
University of California
Berkeley, California 94720

March 1983

PICOSECOND STUDIES OF VIBRATIONAL LINEWIDTH BROADENING IN LIQUIDS

Steven McClellan George

ABSTRACT

The mechanisms of vibrational linewidth broadening in liquids are investigated using picosecond light pulses. Vibrational linewidths in liquids are demonstrated to be both homogeneously and inhomogeneously broadened. The homogeneous broadening is dependent upon rapidly varying processes probably associated with short range, repulsive collisional interactions between the vibration and neighboring molecules. On the other hand, the inhomogeneous broadening is dependent upon slowly varying, long range attractive interactions between the vibration and the surrounding local number density.

Homogeneous and inhomogeneous broadening linewidths are determined for the symmetric CH_3-stretching vibration in a variety of liquids at room temperature and in one liquid at a variety of temperatures. A selective excite-and-probe vibrational dephasing experiment based upon transient stimulated Raman scattering in high laser depletion is used to measure T_2 homogeneous vibrational dephasing times. Homogeneous vibrational linewidths are calculated from these T_2 homogeneous dephasing times. Inhomogeneous vibrational linewidths are calculated by deconvoluting the Lorentzian homogeneous vibrational lineshapes from the

corresponding isotropic spontaneous Raman lineshapes.

Inhomogeneous linewidths are shown to be proportional to the width of the distribution of local number densities in the liquid. This correlation suggests that a distribution of different, slowly varying local number densities in a liquid establishes an inhomogeneously broadened distribution of distinct vibrational frequencies. This inhomogeneous broadening model has recently been placed on firm theoretical foundations by the general vibrational dephasing theory of Schweizer and Chandler.

The relative contributions of homogeneous and inhomogeneous broadening are shown to change significantly with temperature. The temperature-dependent trends are in agreement with the predictions of the Schweizer-Chandler vibrational dephasing theory. New information is provided on the lifetime of the local density sites which cause inhomogeneous broadening.

A general theory for excite-and-probe vibrational dephasing experiments performed using transient stimulated Raman scattering in both low and high laser depletion is presented. The theory reveals that high laser depletion leads to enhanced selectivity in the probing process of the experiment. The differences between recent vibrational dephasing experiments can be explained by the selectivity differences in the high and low laser depletion regimes.

Charles B. Harris.
March 9, 1983

To my Parents

TABLE OF CONTENTS

1. Introduction.....1

2. Theory for Selective Vibrational Dephasing Experiments Using Transient Stimulated Raman Scattering in High Laser Depletion....7

I. Introduction.....7

II. Transient Stimulated Raman Equations including High Laser Depletion.....12

III. Results for a Linewidth with One Vibrational Component.....18

IV. Results for a Linewidth with Three Vibrational Components.....24

V. Probe Signals in the Vibrational Dephasing Experiment...35

VI. Dependence of Selectivity on Various Parameters.....39

VII. Results for a Linewidth with Five Vibrational Components.....52

VIII. Coherent Stokes Signal Decay Curves.....60

IX. Vibrational Dephasing Experiments in the High Laser Depletion Regime.....66

X. Summary and Conclusions.....69

References.....71

3. Inhomogeneous Broadening of Vibrational Linewidths in Polyatomic Liquids.....74

I. Introduction.....74

II. Experimental.....75

III. Results.....77

IV. Homogeneously Broadened Lineshape Analysis.....83

V. Discussion.....84

VI. Stochastic Lineshape Theory for Inhomogeneous Broadening.....92

VII. Summary.....101

References.....102

4. Dependence of Inhomogeneous Vibrational Linewidth Broadening on Attractive Forces from Local Liquid Number Densities.....105

References.....113

5. Temperature Dependence of Homogeneous and Inhomogeneous Inhomogeneous Vibrational Linewidth Broadening in Liquid Acetonitrile.....115

I. Introduction.....115

II. Selectivity in Vibrational Dephasing Experiments.....116

III. Experimental.....118

IV. Temperature-Controlled Cell.....129

V. Results.....134

VI. Temperature Dependent Vibrational Linewidth Broadening.....140

VII. Deviation from Theory at High Temperatures.....150

VIII. Alternative Broadening Mechanisms.....156

IX. Summary.....159

References.....161

6. A Passively Mode-Locked Nd:glass Laser Oscillator Optimized Optimized for TEM_{00} Selectivity and Long Term Stability and Reliability.....166

I. Introduction.....166

II. Design Criteria.....167

III. Laser Cavity.....168

IV. Laser Head.....169

V. Flashlamp Driving Circuit.....175

VI. Mode-Locking Dye Solution and Dye Cell.....176

VII. Oscillator Frame Construction.....178

VIII. Oscillator Frame Connnection to the Optics Table.....178

IX. Micrometers and Mirror Mounts.....183

X. Alignment Procedure and Aperature Placement.....183

XI. Ajustment for Optimum Lasing Action.....188

XII. Dependability.....189

References.....190

8. Picosecond Pulse Characterization.....194

I. Introduction.....194

II. Temporal Width of 1.06 μ Pulse Versus Position in Pulsetrain.....194

III. Spectral Width of 5306 Å Pulse Versus Position in Pulsetrain.....195

IV. Spectra of Individual Shots.....201

V. Evaluation of Laser Variables.....202

References.....214

8. Picosecond Pulse Shortening using Dye #5 or Dye #9860 as a Saturable Absorber.....215

I. Introduction.....215

II. Experimental.....216

III. Results.....217

IV. Discussion.....229

References.....232

9. Summary.....233

ACKNOWLEDGEMENTS.....237

APPENDIX: Computer Programs for Transient Stimulated Raman Scattering in High Laser Depletion.....240

A. STOKES: Program for 5-Component Vibrational Linewidth.....240

B. SPLOT: Program to plot results from TSRMV.....241

C. CURVE: Program to calculate coherent Stokes signal versus delay time.....241

Chapter 1: Introduction

What is the mechanism of vibrational linewidth broadening in liquids? The answers to this question are intimately related to the dynamics and structure of liquids. Despite this close association, however, the distinct effects of liquid dynamics and liquid structure on vibrational linewidths have remained nearly inseparable experimentally. Thus the ability to separate the various mechanisms of vibrational linewidth broadening, if possible, would provide an important means to understand liquids.

Vibrational transitions in liquids can be broadened by frequency perturbations $\Delta\omega$ resulting from both liquid dynamics and liquid structure. Liquid dynamics give rise to perturbations with short lifetimes τ_H which lead to homogeneous broadening. Viewed simplistically in terms of the uncertainty principle, homogeneous broadening processes are those in which $\Delta\omega_H\tau_H<1$. On the other hand, liquid structure generally gives rise to perturbations with long lifetimes τ_{INH} which lead to inhomogeneous broadening. In the simple picture, inhomogeneous broadening processes are those in which $\Delta\omega_{INH}\tau_{INH}>1$.

The majority of vibrational linewidth broadening investigations have utilized isotropic spontaneous Raman studies. By varying various parameters, these investigations have generated a large body of data [1]. Unfortunately, isotropic Raman scattering reveals the convolution in the frequency domain of both homogeneous and inhomogeneous broadening and is powerless to separate their individual contributions.

Because homogeneous and inhomogeneous broadening process occur on different timescales, their contributions to the overall vibrational lineshape can be separated using a time domain experiment. Since homogeneous dephasing caused by liquid dynamics occurs on a picosecond timescale, a time domain investigation must be performed with picosecond light pulses. Even with a picosecond timescale experiment, however, the separation of homogeneous and inhomogeneous broadening is not straightforward.

The basic difficulty can be viewed as follows: Homogeneous and inhomogeneous broadening linewidths have frequency bandwidths and, through the Fourier transform, also have associated decay times known as dephasing times. Likewise, picosecond pulses have frequency bandwidths and associated pulse widths through the Fourier transform. The Fourier transform relationship is an inverse relationship between frequency and time: the shorter the pulse width or decay time, the broader the frequency bandwidth.

In an ideal experiment designed to measure the homogeneous dephasing time (T_2) in the time domain, only a very narrow frequency bandwidth in the total inhomogeneously broadened vibrational lineshape should be coherently excited and probed. In addition, ultrashort excite and probe pulses should be used in order to obtain sufficient time resolution. Thus there is an inherent trade-off between frequency and time resolution in the time-domain experiment.

If the frequency bandwidth required to generate the ultrashort pulse is broader than the homogeneous linewidth in an inhomogeneously broadened lineshape, a vibrational bandwidth larger than the homogeneous linewidth is coherently excited. Through the Fourier transform, this

coherently excited vibrational bandwidth gives rise to a dephasing time faster than the actual T_2 homogeneous dephasing time. Consequently, if the frequency bandwidth of the excitation pulse spans the total vibrational lineshape, many so-called measurements of T_2 have been nothing more than a time domain measurement of the Fourier transform of the total vibrational lineshape.

For many years, the work of Kaiser and coworkers has provided the foundation for picosecond excite-and-probe vibrational dephasing experiments conducted using transient stimulated Raman scattering in low laser depletion [2]. They have attempted to overcome the trade-off between frequency and time resolution using selective, coherent probing techniques. Very recently, however, they have published results which directly contradict their earlier work [3]. As a result, they have altered their theoretical interpretations and have left much of their earlier work unexplained.

Our recent studies of laser depletion in transient stimulated Raman scattering have indicated that most time domain excite-and-probe vibrational dephasing experiments, prior to the recent work by Kaiser and coworkers, have probably been performed using transient stimulated Raman scattering in high depletion of the excitation laser pulse. Unfortunately, there have been no theoretical interpretations for excite-and-probe vibrational dephasing experiments conducted in high laser depletion.

This thesis begins with a general theory for transient stimulated Raman scattering in both low and high laser depletion. This theory and the subsequent interpretation for excite-and-probe vibrational dephasing experiments conducted using transient stimulated Raman scattering in

both low and high laser depletion are presented in Chap. 2. The results of this theory have shown that high laser depletion leads to enhanced selectivity unaccounted for in the low laser depletion analysis of Kaiser and coworkers. This enhanced selectivity allows homogeneous dephasing times to be measured to a high level of accuracy in inhomogeneously broadened linewidths. The contradictions in previous vibrational dephasing work can be explained by selectivity differences in the high and low laser depletion regimes.

Based on the selective vibrational dephasing experiment in high laser depletion and isotropic Raman lineshape investigations, several experiments have been performed in order to explore the relationship between vibrational linewidth broadening and liquid dynamics and structure. These investigations have focused on the symmetric CH_3-stretching vibration in a variety of liquids at room temperature and in one liquid at a variety of temperatures.

The first evidence for inhomogeneous broadening of symmetric CH_3-stretching vibrational linewidths in nonhydrogen-bonded liquids at room temperature is presented in Chap. 3. The inhomogeneous broadening is shown to be correlated with the width of the distribution of local number densities in the liquid. This correlation suggests that a distribution of liquid structures with different, slowly varying local number densities creates a distribution of distinct vibrational frequencies.

This correlation between inhomogeneous broadening and the width of the distribution of local number densities in the liquid has recently been placed on firm theoretical grounds by Schweizer and Chandler [4]. They have shown that attractive forces provide the coupling between the

local number density and the vibration. An analysis of our inhomogeneous broadening data in terms of the Schweizer-Chandler theory is presented in Chap. 4.

The temperature dependence of homogeneous and inhomogeneous vibrational linewidth broadening of the symmetric CH_3-stretching vibration of acetonitrile is presented in Chap. 5. This study has revealed that the relative contributions of homogeneous and inhomogeneous broadening change significantly with temperature. The temperature-dependent trends were in agreement with the predictions of the Schweizer-Chandler theory. In addition, this investigation has provided new information on the temperature dependence of the lifetime of the local density sites which cause inhomogeneous broadening.

These excite-and-probe experiments have relied on our ability to generate single, nearly transform-limited, reproducible picosecond pulses. The passively mode-locked Nd:glass laser used to generate picosecond pulses in these experiments in described in Chap. 6. A characterization of the picosecond pulses from this laser is given in Chap. 7. Lastly, a study of the effects of saturable absorbers on picosecond pulses is presented in Chap. 8.

What is the mechanism of vibrational linewidth broadening in liquids? What is the relationship between vibrational linewidth broadening and the dynamics and structure of liquids? Some answers to these questions provided by this work are summarized in Chap. 9. In addition, an outlook for future vibrational linewidth investigations is also presented.

References

1. D.W. Oxtoby, Adv. Chem. Phys. 40, 1(1979).

2. A. Laubereau and W. Kaiser, Rev. Mod. Phys. 50, 607(1978).

3. W. Zinth, H.J. Polland, A. Laubereau and W. Kaiser, Appl. Phys. B26, 77(1981).

4. K.S. Schweizer and D. Chandler, J. Chem. Phys. 76, 2296(1982).

Chapter 2: Theory for Selective Vibrational Dephasing Experiments Using Transient Stimulated Raman Scattering in High Laser Depletion

I. Introduction

For the last ten years, transient stimulated Raman excitation and coherent Raman probing processes have been used to study ultrashort vibrational dephasing dynamics in liquids [1-6]. During this time, a fairly large experimental base has been developed, upon which a theoretical interpretation has evolved. Recently, Kaiser and coworkers [7] published major revisions of their previous foundational work. Their new study directly contradicts many of their earlier experimental results [1-3,8,9]. In marked contrast to their earlier conclusions [1-3], they judge that their vibrational dephasing experiments are not selective. Consequently, they conclude that the homogeneous dephasing time T_2 can not be measured in a vibrational linewidth that is inhomogeneously broadened.

Vibrational dephasing experiments are performed with excitation pulses and time-delayed probe pulses [1]. The excitation pulse coherently excites vibrations by transient stimulated Raman scattering. The coherent excitation establishes a macroscopic coherent superposition of vibrational states. The time-delayed probe pulse then interacts with the macroscopic coherent vibrational superposition and produces coherent Raman scattering. Selectivity is measured by the ability of the probing process to select out a single, distinct

vibrational subgroup from a vibrational lineshape which is composed of a frequency distribution of vibrational subgroups, i.e., inhomogeneously broadened. The higher the selectivity, the more accurately the decay of the coherent Raman probe scattering is related to the homogeneous dephasing time T_2 of a single vibrational subgroup.

Vibrational dephasing studies have been restricted to various carefully controlled experimental conditions and specific theoretical assumptions. One important experimental restriction in the work by Kaiser and coworkers has been low depletion (<5%) of the excitation laser pulse in the transient stimulated Raman excitation process. This restriction has been indispensable because the theoretical interpretations developed by Kaiser and coworkers have been undertaken exclusively assuming low depletion of the excitation laser pulse.

In order to check the feasibility of this restriction, we recently examined excitation laser pulse depletion in the transient stimulated Raman excitation process [10,11]. We monitered the laser pulse depletion and stimulated Stokes gain in a 10 cm acetonitrile Raman cell using a well characterized experimental set-up [6,11] and a stabilized, passively mode-locked Nd:glass laser system [12]. Figure 1 shows the transmitted laser pulse energy versus the incident laser pulse energy at 5306 Å with and without the 10 cm Raman cell. Figure 1 illustrates that immediately after the stimulated Raman scattering threshold is reached, the laser can be depleted >10% and depletion approaches ≈50% as the incident laser energy increases. In other studies, we measured both transmitted laser and Stokes pulse energies after the Raman cell as a function of incident laser pulse energy [11a]. Coincident sharp thresholds for stimulated Stokes scattering and subsequent laser

FIG. 1. Laser pump depletion examined by monitering the transmitted laser pulse energy versus the incident laser pulse energy with and without a 10 cm acetonitrile Raman cell. The approximate range of incident laser pulse energies used in our vibrational dephasing experiments is also indicated.

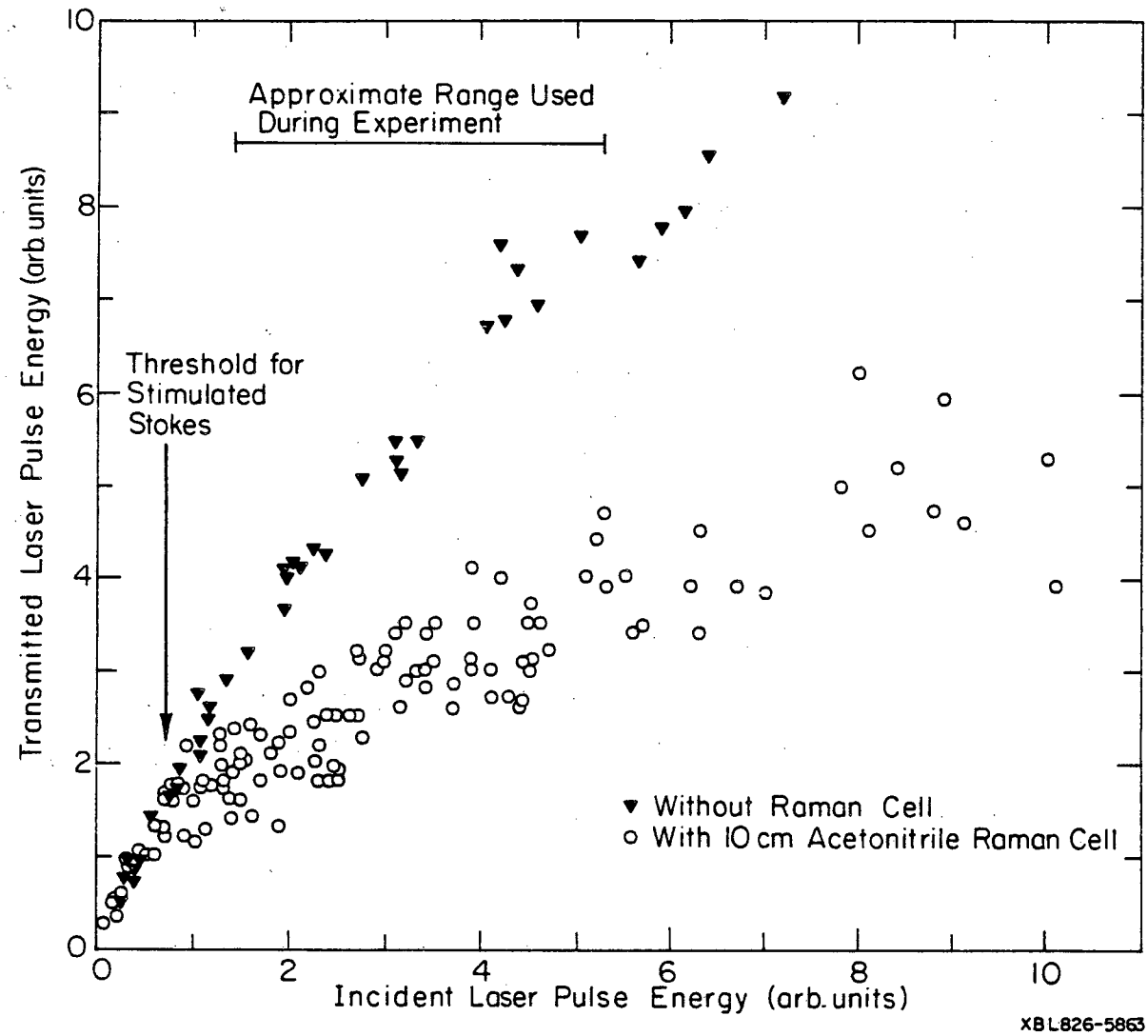
Approximate Range Used
During Experiment
Threshold for
Stimulated
Stokes
Without Raman Cell
With 10 cm Acetonitrile Raman Cell
Transmitted Laser Pulse Energy (arb. units)
Incident Laser Pulse Energy (arb. units)
0
2
4
6
8
10
XBL826-5863

Figure 1

depletion versus incident laser pulse energy were observed. Very few shots could be recorded with Stokes conversions between 1-5%.

Because of these studies, we believe that maintaining stimulated Stokes conversions between 1-5% is nearly impossible given pulse intensity fluctuations from typical pulsed laser systems followed by nearly exponential stimulated Stokes gain in the Raman cell. After the stimulated Raman scattering threshold is reached, the laser pump is rapidly depleted and the Stokes pulse approaches gain saturation [10,11]. This behavior has also been observed by other investigators [13]. Consequently, we believe that most vibrational dephasing experiments [1-6] prior to the recent work by Kaiser and coworkers [7] have been performed with excitation pulses in the high laser depletion regime.

Despite the likelihood of high laser depletion, no theoretical interpretation has been developed for vibrational dephasing experiments performed in the high laser depletion regime. To remedy this situation, we solve the transient stimulated Raman scattering equations including laser depletion for single and multiple component vibrational transitions. This is the first account of the effects of high laser depletion on the vibrational components in an inhomogeneously broadened vibrational linewidth. We then present a general theory for interpreting excite-and-probe vibrational dephasing experiments. The theory reveals that high depletion of the excitation laser pulse leads to greatly enhanced selectivity in the probing process of the vibrational dephasing experiment.

The enhanced selectivity predicted by this theoretical analysis indicates that dephasing times T_2 can be measured under conditions of

high laser depletion using collinear coherent Stokes probe scattering [1,3,6]. Futhermore, recent vibrational dephasing experiments conducted in the high laser depletion region have given results which corroborate these theoretical results [10]. We will give a full account of these experiments in another paper [11]. These theoretical and experimental results suggest that the discrepancies in previous vibrational dephasing studies [1-9] may be explained by the selectivity differences in the high and low laser depletion regimes.

II. Transient Stimulated Raman Equations including Laser Depletion

A. Equations for a 1-Component Vibrational Linewidth

The coupled differential equations for transient stimulated Raman scattering from a homogeneously broadened vibrational linewidth are well known [14-16]. The solution of these equations is dependent upon various simplifying assumptions. In these calculations, the laser and Stokes fields are assumed to be monochromatic. Their spectral bandwidths are accounted for by the Fourier transform of their time dependent envelopes. Coupling to anti-Stokes and higher order Stokes fields is ignored. The population difference between the initial and final vibrational states is set equal to a constant. Dispersion between the laser and Stokes fields is neglected. No attempt is made to account for the laser beam's spatial profile or focusing of the beam.

Using these assumptions, the equations in local time, $\tau=t-zc/n$, and z space can be written as [14,17]:

$$\partial E_L/\partial z = -\kappa_1 \omega_L Q E_S \tag{1}$$

$$\partial E_S/\partial z = \kappa_1 \omega_S Q^* E_L \tag{2}$$

$$(\partial/\partial\tau + 1/T_2)Q = \kappa_2 E_S^* E_L \tag{3}$$

where $\kappa_1 = 2\pi i\lambda/(cn)$ and $\kappa_2 = i\lambda/(2\omega_v)$. The coupling constant $\lambda = N(\partial\alpha/\partial Q)$ where N is the molecular number density and $(\partial\alpha/\partial Q)$ is the change in molecular polarizability α with the vibrational coordinate Q. If the laser pump depletion is ignored, $\partial E_L/\partial z \approx 0$, and the equations reduce to coupled equations in E_S and Q which have been solved by many authors [1,14,18]. If laser pump depletion is not ignored, the coupled equations in E_L, E_S and Q must be solved.

In the following treatment [19], the coupled equations are reexpressed in a form in which the constants κ_1 and κ_2 are related to the steady state stimulated Raman gain constant g, which is a physically measured quantity. In the limit of steady state, $\partial Q/\partial t = 0$ and $Q/T_2 = \kappa_2 E_S^* E_L$. Therefore, if a new vibrational amplitude q is redefined by $Q = T_2 \kappa_2 q$, Eq. (3) becomes:

$$(\partial/\partial\tau + 1/T_2)q = E_S^* E_L/T_2 \tag{4}$$

In the limit of steady state, $dq/d\tau = 0$ and $q = E_S^* E_L$. When $Q = T_2\kappa_2 q$ and the steady state expression $q = E_S^* E_L$ are substituted into Eq. (2):

$$\partial E_S/\partial z = \omega_S \kappa_1 \kappa_2 T_2 E_S E_L^2 \tag{5}$$

This equation for the Stokes field amplitude is similar to the steady state stimulated Raman equation:

$$\partial E_S/\partial z = \tfrac{1}{2}\, g E_S I_L \tag{6}$$

where I_L is the laser intensity $I_L = \tfrac{1}{2}\,\varepsilon_0 c E_L^2$. Using $I_L = \tfrac{1}{2}\,\varepsilon_0 c E_L^2$ and equating Eqs. (5) and (6):

$$\omega_S \kappa_1 \kappa_2 T_2 = \tfrac{1}{4}\, g \varepsilon_0 c \tag{7}$$

Thus the constants κ_1 and κ_2 have been expressed in terms of g, the steady state gain constant.

For further simplification, let $q' = \tfrac{1}{2}\,\varepsilon_0 c q$. In addition, let $e = (\tfrac{1}{2}\,\varepsilon_0 c)^2 E$. These two substitutions and the expression of κ_1 and κ_2 in terms of g transform the three coupled equations into:

$$\partial e_L/\partial z = -\tfrac{1}{2}\, g(\omega_L/\omega_S) q' e_S \tag{8}$$

$$\partial e_S/\partial z = \tfrac{1}{2}\, g q'^{*} e_L \tag{9}$$

$$(\partial/\partial\tau + 1/T_2) q' = e_S^{*} e_L/T_2 \tag{10}$$

In Eqs. (8-10), g has units of (m/W), e has units of $(W/m^2)^{1/2}$ and q' has units of (W/m^2). A typical g is 5 (cm/GW) or 5×10^{-11} (m/W) [1]. Likewise, a typical $I_L = \tfrac{1}{2}\,\varepsilon_0 c E_L^2$ is 1.0 (GW/cm^2) or 10×10^{12} (W/m^2). In units of (m/TW) and (TW/m^2), g= 50 (m/TW) and I_L=10 (TW/m^2). These units are employed in the following calculations.

B. Equations for Multi-Vibrational Component Linewidth

In an inhomogeneously broadened linewidth, each vibrational subgroup q_j has a different, distinct frequency ω_j and a relative number density f_j. In the above equations for a homogeneously broadened linewidth, $\omega_L=\omega_S+\omega_v$ and both sides of each equation have the same frequency. When additional vibrational frequencies are considered, the frequency mismatch $\Delta\omega_j=\omega_L-\omega_S-\omega_v$ must be included. In addition, the relative number density f_j where $\sum_j f_j=1$ and the relative phases Φ_j of the off-resonance vibrational amplitudes where $q_j=|q_j|\exp(i\Phi_j)$ must be considered.

The equations for a multi-vibrational component linewidth are dependent upon the same conditions that were assumed for the 1-component linewidth. In addition, the excitation Stokes field frequency ω_S is determined by $\omega_S=\omega_L-\omega_0$ where ω_0 is the vibrational frequency at the center of the vibrational linewidth [1,2]. After Stokes saturation, no new laser fields at $\omega_L+\Delta\omega_j$ are assumed to be generated. Each vibrational subgroup is assumed to have the same dephasing time T_2. Each vibration is assumed to be spatially independent and uncoupled from the other vibrations.

When these assumptions are made, the equations for transient stimulated Raman scattering from an inhomogeneously broadened linewidth are:

$$\partial e_L/\partial z = -\tfrac{1}{2}\, g(\omega_L/\omega_S)e_S \sum_j f_j \,|q_j|\, \exp(i(\Delta\omega_j\tau+\Phi_j)) \qquad (11)$$

$$\partial e_S/\partial z = \tfrac{1}{2}\, g e_L \sum_j f_j \,|q_j|\, \exp(-i(\Delta\omega_j\tau-\Phi_j)) \qquad (12)$$

$$(\partial/\partial\tau+1/T_2)|q_j|\exp(i\Phi_j) = (e_S^* e_L/T_2)\exp(-i\Delta\omega_j\tau) \quad (13)$$

The real parts of Eqs. (11), (12) and (13) lead to:

$$\partial e_L/\partial z = -\tfrac{1}{2} g(\omega_L/\omega_S) e_S \textstyle\sum_j f_j \, |q_j| \cos(\Delta\omega_j\tau+\Phi_j) \quad (14)$$

$$\partial e_S/\partial z = \tfrac{1}{2} g e_L \textstyle\sum_j f_j \, |q_j| \cos(\Delta\omega_j\tau+\Phi_j) \quad (15)$$

$$(\partial/\partial\tau+1/T_2)|q_j| = (e_S e_L/T_2) \cos(\Delta\omega_j\tau+\Phi_j) \quad (16)$$

The imaginary part of Eq. (13) leads to:

$$\partial\Phi_j/\partial\tau = -[(e_S e_L)/(|q_j|T_2)] \sin(\Delta\omega_j\tau+\Phi_j) \quad (17)$$

These high laser depletion equations in local time are very similar to the low laser depletions equations in real time given by Laubereau and Kaiser [1-3]. Notice that in local time, $\tau = t-zn/c$, however, the spatial k-vector mismatch $\Delta k_j = \Delta\omega_j zn/c$ caused by frequency mismatch is implicitly included in $\Delta\omega_j\tau$. The frequency mismatch $\Delta\omega_j$ and the vibrational phase Φ_j together comprise the total phase of the off-resonant vibrational amplitudes which is defined by $\chi_j=\Delta\omega_j\tau+\Phi_j$. In addition, the resonant vibrational amplitude q_0 has a vibrational phase $\Phi_0=0$. Consequently, Eq. (13) reduces to Eq. (10) for q_0 and q_0 is treated as a real quantity. In constrast, the off-resonant vibrational amplitudes q_j are treated as complex quantities.

C. Numerical Solution

The coupled differential equations given by Eqs. (8-10) or Eqs. (14-17) were solved numerically using a predictor-corrector technique [20,21]. First, $q_j(z,\tau+\Delta\tau)$ and $\Phi_j(z,\tau+\Delta\tau)$ were determined for all z at the new local time using an Euler time step. Then the implicit Crank-Nicolson method [22] was used to form a set of simultaneous equations for $e_S(z,\tau+\Delta\tau)$ and $e_L(z,\tau+\Delta\tau)$ for all z at the new local time. The solution of this set of simultaneous equations yielded solutions for $e_S(z,\tau+\Delta\tau)$ and $e_L(z,\tau+\Delta\tau)$ for all z. These new solutions for e_S and e_L were used to determine the corrector for q_j and Φ_j. Subsequently, corrected e_S and e_L solutions were recalculated. This completed one time step. The process then repeated itself as the corrected e_S and e_L solutions were used to determine $q_j(z,\tau+2\Delta\tau)$ and $\Phi_j(z,\tau+2\Delta\tau)$ at the next new local time for all z using an Euler time step.

The equations were solved in local time $\tau=t-zn/c$ and space z using the following constants and boundary and initial conditions. The incident laser pulse defined the boundary conditions for $e_L(z=0,\tau)$ and $e_S(z=0,\tau)$. Unless otherwise indicated, the calculations were performed with a Gaussian input laser pulse with a full-width at half maximum t_p=7 psec and a peak field amplitude of 6.33 $(TW/m^2)^{1/2}$ corresponding to a peak intensity of 40 (TW/m^2). The incident Stokes field was defined by $e_S(z=0,\tau) = e_L(z=0,\tau)\exp(-13)$. This Stokes field was not statistical noise, but was assumed to be coherent. The initial conditions for q_j and Φ_j were $q_j(z,\tau=0)=0$ and $\Phi_j(z,\tau=0)=0$. In addition, $\omega_L/\omega_S=1.1843$ [23] and g=50 (m/TW). Using the above parameters, Stokes saturation is achieved after propagation distances of approximately

10 cm in the Raman cell.

The calculations were performed for consecutive contiguous sections of the Raman cell. In each section, solutions were calculated using 400 local time points spanning a total time $\tau_T=5t_p$ and 200 space points spanning a total length $z_T=2.5$ cm. As the calculation proceeded through the Raman cell, the solutions for $e_L(z_T,\tau)$ and $e_S(z_T,\tau)$ from a previous section were introduced as the new boundary conditions for the subsequent contiguous section.

More generally, the results of these calculations can be expressed in terms of t_p/T_2 and $t_p\Delta\omega$ or $T_2\Delta\omega$. These quantities are invariant to redefinition of the actual time step used in the calculations. Consequently, the following results are applicable to a wide range of t_p, T_2 and $\Delta\omega$ and are reported using both the specific and general quantities.

III. Results for a Linewidth with One Vibrational Component

The equations for transient stimulated Raman scattering from homogeneously broadened vibrational linewidths have been carefully studied in the low laser depletion limit by Carman et al. [14]. In order to check the consistency of our results with those obtained by Carman et al. [14], we calculated the Stokes pulse width with respect to the laser pulse width and the Stokes pulse peak delay with respect to the laser pulse peak versus the Stokes pulse transient gain coefficient. For the ratio $t_p/T_2=1$ using $t_p=7$ psec and $T_2=7$ psec, our results were in close agreement with Carman et al. [14].

We also calculated the gain of the Stokes pulse amplitude versus the propagation distance shown in Fig. 2. The Stokes gain was measured by the natural logarithm of the ratio of the Stokes peak amplitude at a particular z location versus the Stokes peak amplitude at z=0. Figure 2 illustrates that the Stokes gain is never strictly exponential with z. This behavior occurs because the Stokes pulse peak continually moves away from the laser pulse peak into regions of smaller laser amplitude as a function of Stokes gain. The transient Stokes gain is closely proportional to the square root of the propagation distance z as predicted by Carman et al. [14]. In Stokes gain saturation, the Stokes amplitude gain asymptotically approaches 13 which results from the boundary conditions.

The equations for transient stimulated Raman scattering from a homogeneously broadened vibrational linewidth have been studied in the high laser depletion regime by Kachen and Lowdermilk [17,24,25], Daree [26] and others under different conditions than those considered here [27,28]. Although our numerical solution technique was different than the technique employed by Kachen and Lowdermilk [17], our results were nearly identical. Figures 3(a)-3(e) displays the local time profiles of the field and vibrational amplitudes at various spatial locations a-e, respectively, for progressive degrees of Stokes conversion. These particular locations are labeled in Fig. 2. These results were obtained using a Gaussian laser pulse width (FWHM) t_p=7 psec and a dephasing time T_2=7 psec, or more generally, t_p/T_2=1. Local time is given in units of t_p where τ=0 is the laser pulse peak.

In Fig. 3(a), prior to severe Stokes saturation, the Stokes pulse has grown according to the transient stimulated Raman process. In

FIG. 2. Stokes gain as a function of spatial location for transient stimulated Raman scattering from a homogeneous vibrational linewidth. Spatial locations a-e are referred to in Fig. 3.

FIG. 3. (a)-(e) Local time profiles of the field and vibrational amplitudes at the spatial locations a-e indicated in Fig. 2. Field amplitudes are in units of $(TW/m^2)^{1/2}$. Vibrational amplitudes are in units of (TW/m^2). (f) Local time profiles of the field and vibrational intensities at the spatial location e indicated in Fig. 2.

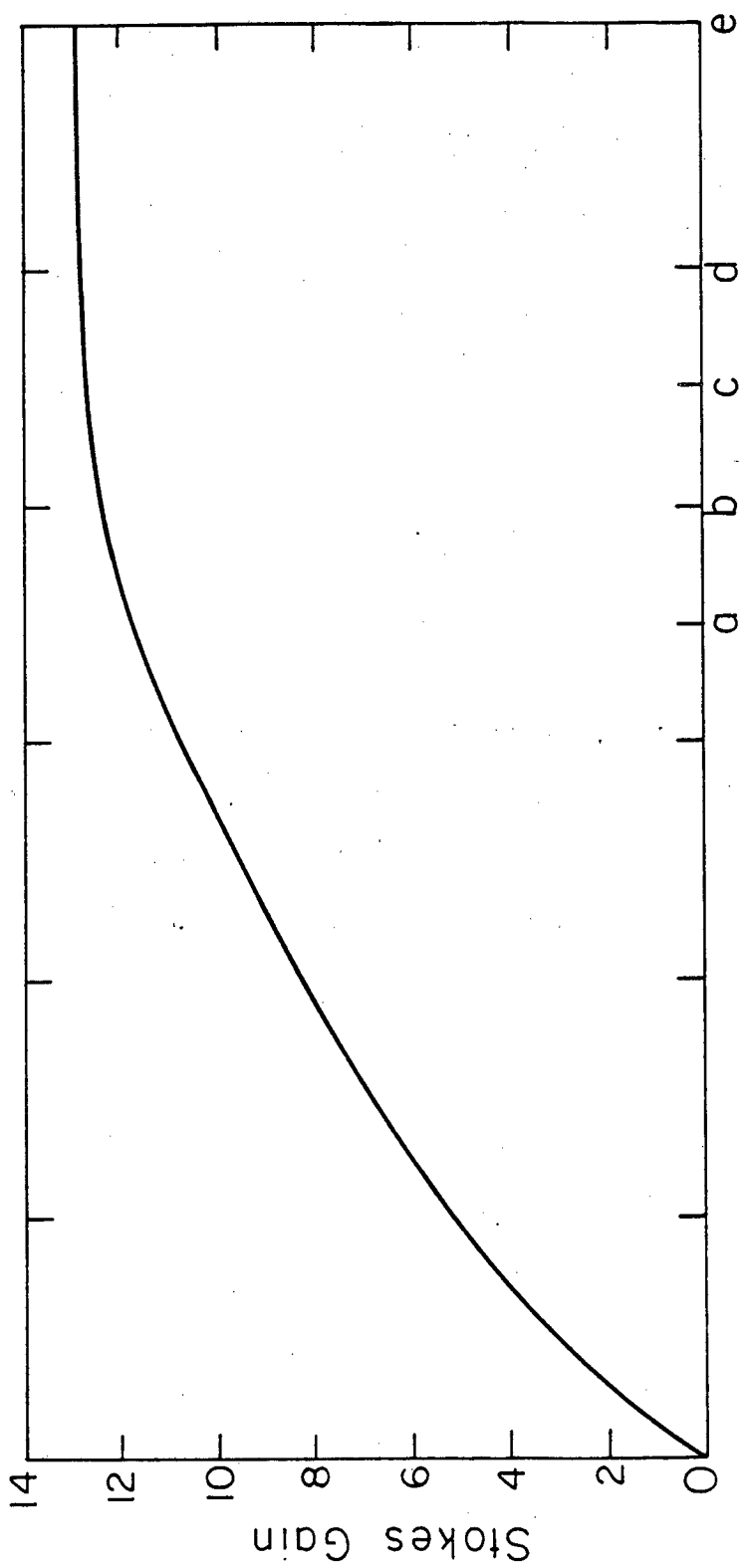

XBL 8211-6902

Figure 2

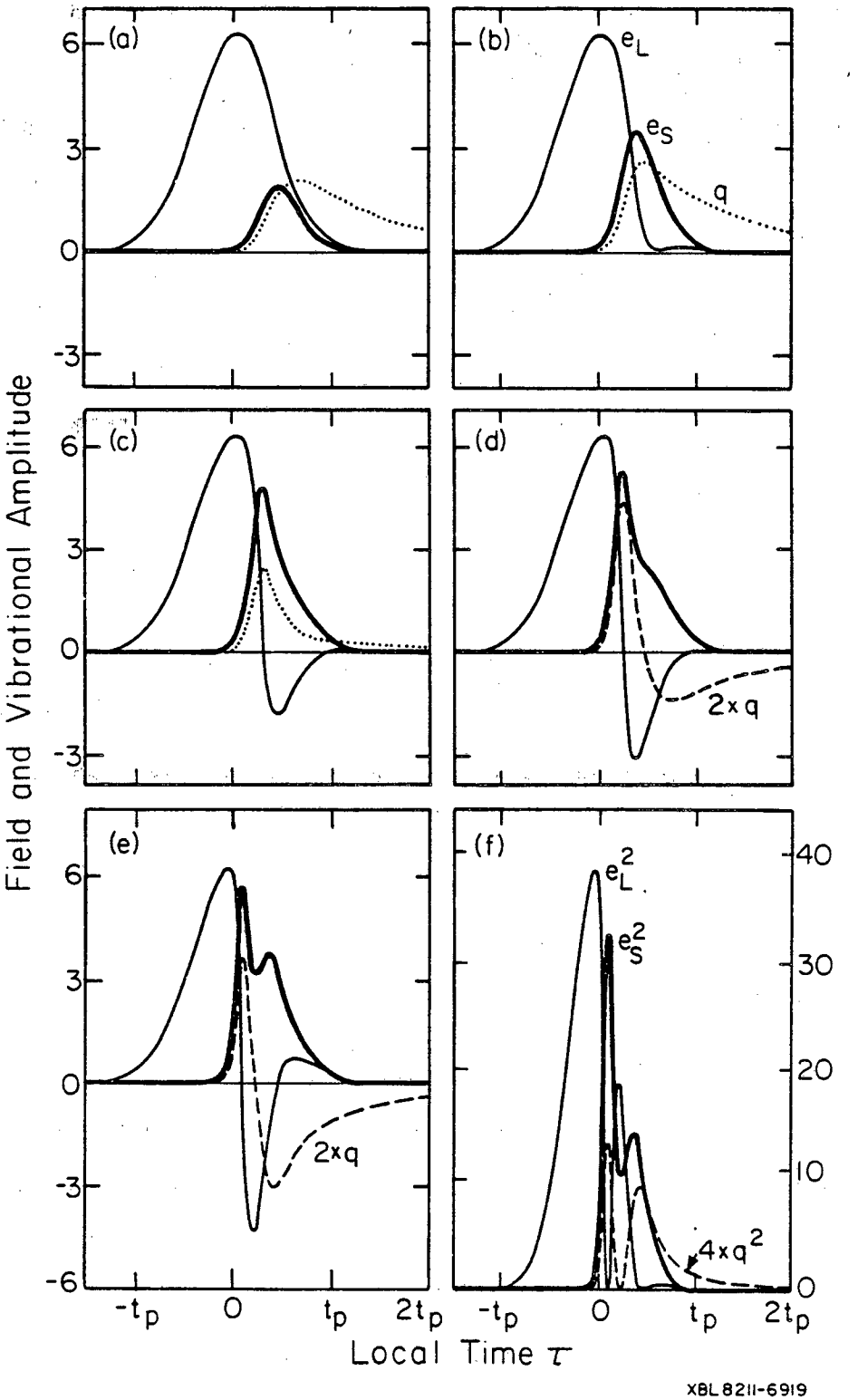
(a)
(b)
(c)
(d)
(e)
(f)
e_L
e_S
q
2xq
e_L^2
e_S^2
$4xq^2$
Field and Vibrational Amplitude
Local Time τ
$-t_p$
0
t_p
$2t_p$
XBL8211-6919

Figure 3

agreement with theoretical [1,14,17,25] and experimental [25] work, the Stokes pulse is shortened and time-delayed relative to the laser pulse. The vibrational amplitude peaks after the Stokes pulse and then decays exponentially.

In Fig. 3(b), the laser pulse is almost completely depleted in the region near the Stokes pulse peak. At this stage of Stokes saturation, the laser pulse's energy has been coherently transferred to the vibrational amplitude and Stokes field. If $T_2 \; t_p$, the coherent polarization stored in the coherent vibrational superposition in the medium does not dephase rapidly. Consequently, the coherent vibrational amplitude, together with the coherent Stokes field, becomes a source polarization for the regeneration of the laser field [24].

Figure 3(c) shows that the regenerated laser field appears with a negative amplitude, i.e., a phase shift of π radians from the initial laser field. In Figs. 3(d) and 3(e), the laser is driven increasingly negative. Notice that in Fig. 3(e), the Stokes field displays a depletion dip where the Stokes field has been depleted by the growth of the regenerated laser field. Figure 3(f) shows the intensity of the field amplitudes shown in Fig. 3(e). Fig. 3(f) reveals that energy oscillates between the laser and Stokes fields. This energy oscillation phenomena has been graphically illustrated by the streak camera traces of the transmitted laser and Stokes pulses following high laser depletion in a Raman cell [17,24].

The 180° phase shift in the regenerated laser field significantly affects the $e_S e_L$ driving force on the vibrational amplitude q. In Figs. 3(a) and 3(b), the $e_S e_L$ driving force remains positive. In Figs. 3(c)-3(e), the laser amplitude is driven negative as the large $e_S q$ product

coherently feeds energy back into the laser field. A negative laser amplitude leads to a negative driving force on the vibrational amplitude. In Figs. 3(d) and 3(e), the vibrational amplitude has responded to the negative driving force and has been driven negative. This 180° phase-shifted vibrational amplitude will be shown to affect the coherent Stokes probing process and significantly enhance the degree of selectivity in the vibrational dephasing experiment.

IV. Results for a Linewidth with Three Vibrational Components

In order to model transient stimulated Raman scattering from an inhomogeneously broadened linewidth in the high laser depletion regime, calculations were performed for a three-component vibrational linewidth with a 0.25:0.50:0.25 number density distribution. In these calculations, a pulsewidth t_p=7 psec and a homogeneous dephasing time T_2=7 psec were used. q_0 is the resonant vibrational amplitude with the central vibrational frequency ω_0. q_1 and q_2 are the off-resonant vibrational amplitudes with $\Delta\omega_1$= -3.0 cm^{-1} and $\Delta\omega_2$= +3.0 cm^{-1}. More generally, this calculation is equivalent to t_p/T_2=1 and $t_p\Delta\omega=T_2\Delta\omega=\pm 3.96$ radians.

The solution in space and local time of Eqs. (14-17) for this three-component vibrational linewidth can be understood by examining the local time profiles at particular spatial locations. Figs. 4(a)-4(f) show the local time profiles of e_L, e_S, q_0 and $|q_j|$ at various progressive stages of Stokes conversion at six different spatial locations a-f, respectively. Because of the symmetry in the equations,

$|q_2|=|q_1|$. Remember that q_0 is a real quantity, whereas $|q_1|$ is the absolute value of the complex quantity q_1. Figure 5 shows local time profiles of $\Phi_1(z,\tau)$ at the same six spatial locations a-f as in Fig. 4. Because of the symmetry in the equations, $\Phi_2=-\Phi_1$. In addition, Figs. 6(a) and 6(b) show the local time profiles of the instantaneous off-resonance frequency $(\Delta\omega_j+\partial\Phi_j/\partial\tau)$ at the same spatial locations as in Figs. 4(b) and 4(d), respectively.

The particular spatial locations in the Raman cell referred to in Figs. 4-6 are labeled in Fig. 7. Notice that the percent laser depletions are shown for reference in Fig. 7(d). The laser pump depletion was determined by the ratio of the integral of the laser intensity time profile at the particular z location versus the integral of the laser intensity time profile at z=0.

A. Results in Low Laser Depletion

For local times $\tau\leq 0$ for both low and high laser depletion, Figs. 5, 6(a) and 6(b) show that the off-resonant vibrational amplitudes q_1 and q_2 behave as forced oscillators. Figure 5 shows that $\partial\Phi_1/\partial\tau=-\Delta\omega_1$ for $\tau\leq 0$. Consequently, Figs. 6(a) and 6(b) illustrate that the instantaneous frequency $\partial\chi/\partial\tau=\partial(\Delta\omega_1\tau+\Phi_1)/\partial\tau=0$ for $\tau\leq 0$.

For local times $\tau>0$, the low and high laser depletion regimes display significant differences in behavior. For times $\tau>0$ in low laser depletion, Fig. 5 shows that $\partial\Phi_1/\partial\tau\to 0$ as the forced oscillators are released at spatial locations a and b. Consequently, Fig. 6(a) shows that the instantaneous frequency $\partial\chi_1/\partial\tau\to\Delta\omega_1$. The forced oscillators are gently released by the forcing field and resume their natural

FIG. 4. (a)-(f) Local time profiles of the field and vibrational amplitudes for the three-component vibrational linewidth at the spatial locations a-f indicated in Fig. 7. Field amplitudes are in units of $(TW/m^2)^{1/2}$. Vibrational amplitudes are in units of (TW/m^2).

FIG. 5. Local time profiles of the vibrational phase for the three-component vibrational linewidth at the spatial locations a-f indicated in Fig. 7. Θ_1 is the resultant vibrational phase in low laser depletion defined by Eq. (18).

FIG. 6. (a) Local time profile of the instantaneous frequencies for the three-component vibrational linewidth at the spatial location b indicated in Fig. 7. (b) Local time profile of the instantaneous frequencies at the spatial location d indicated in Fig. 7.

FIG. 7. (a) Traveling sums of the individual vibrational amplitudes for the three-component vibrational linewidth at $\tau=\tau_D$ versus propagation distance defined by Eq. (21). (b) Vibrational amplitudes at $\tau=\tau_D$ as a function of spatial location. (c) Vibrational phases at $\tau=\tau_D$ as a function of spatial location. Θ_1 is the resultant vibrational phase in low laser depletion defined by Eq. (18). (d) Percent laser pump depletion versus propagation distance. Spatial locations a-f are referred to in Figs. 4-6.

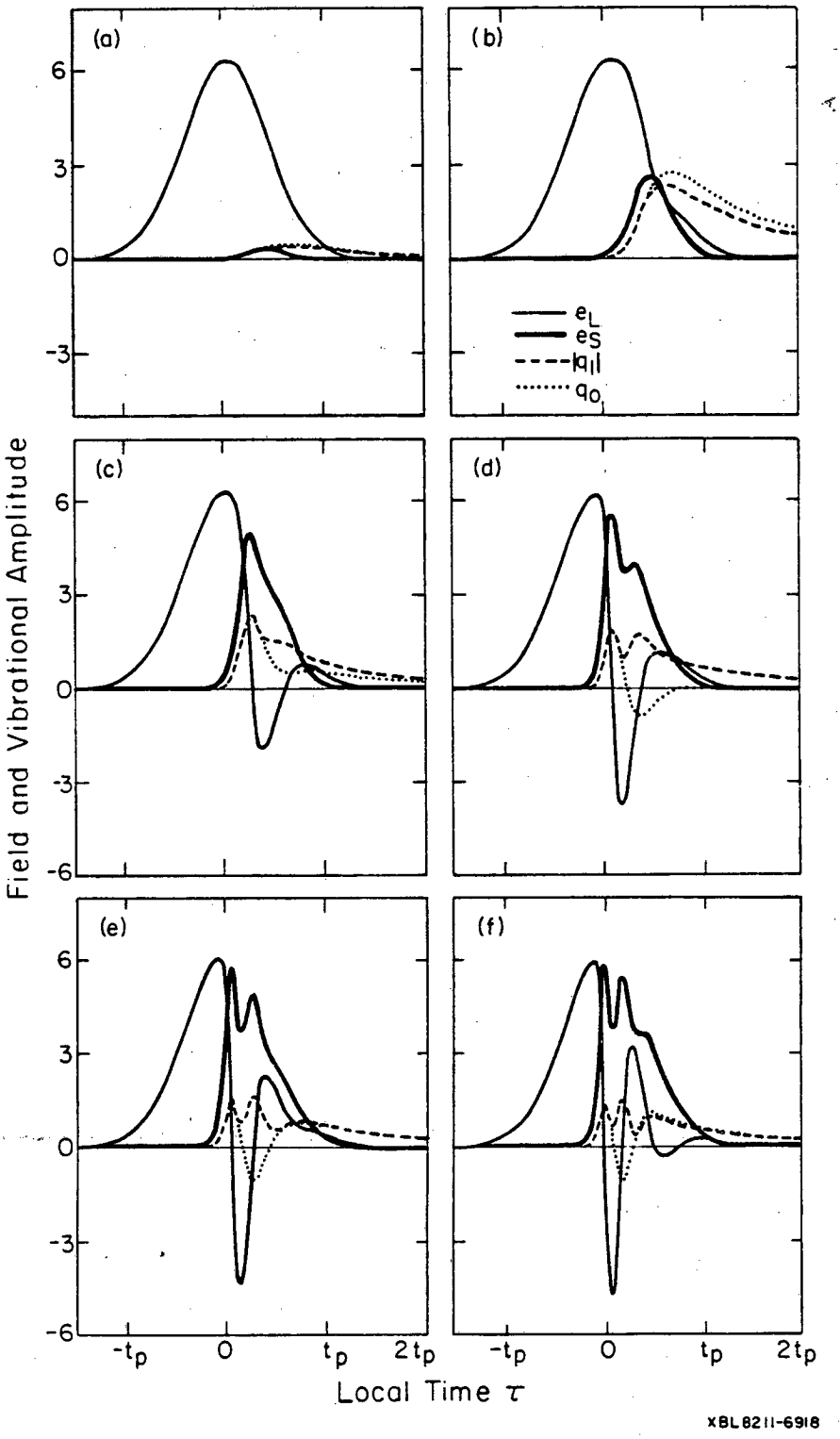
(a)
(b)
(c)
(d)
(e)
(f)
6
3
0
-3
-6
e_L
e_S
$|q_{11}|$
q_{01}
Field and Vibrational Amplitude
$-t_p$
0
t_p
$2t_p$
Local Time τ
XBL8211-6918

Figure 4

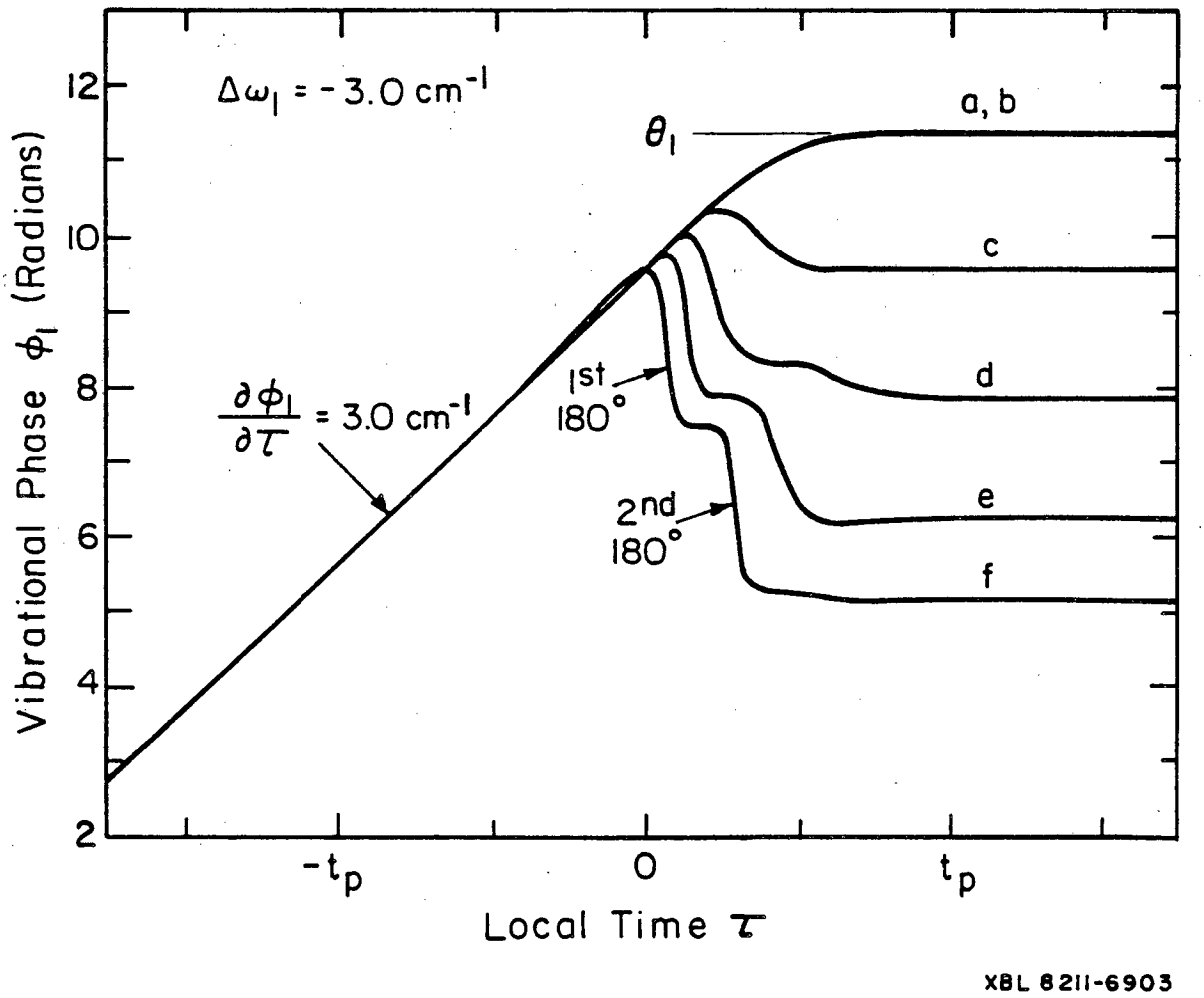
Δω1 = - 3.0 cm-1
θ1
a, b
c
d
e
f
1st 180°
2nd 180°
∂φ1/∂τ = 3.0 cm-1
Vibrational Phase φ1 (Radians)
Local Time τ
-tp
0
tp
2
4
6
8
10
12
XBL 8211-6903

Figure 5

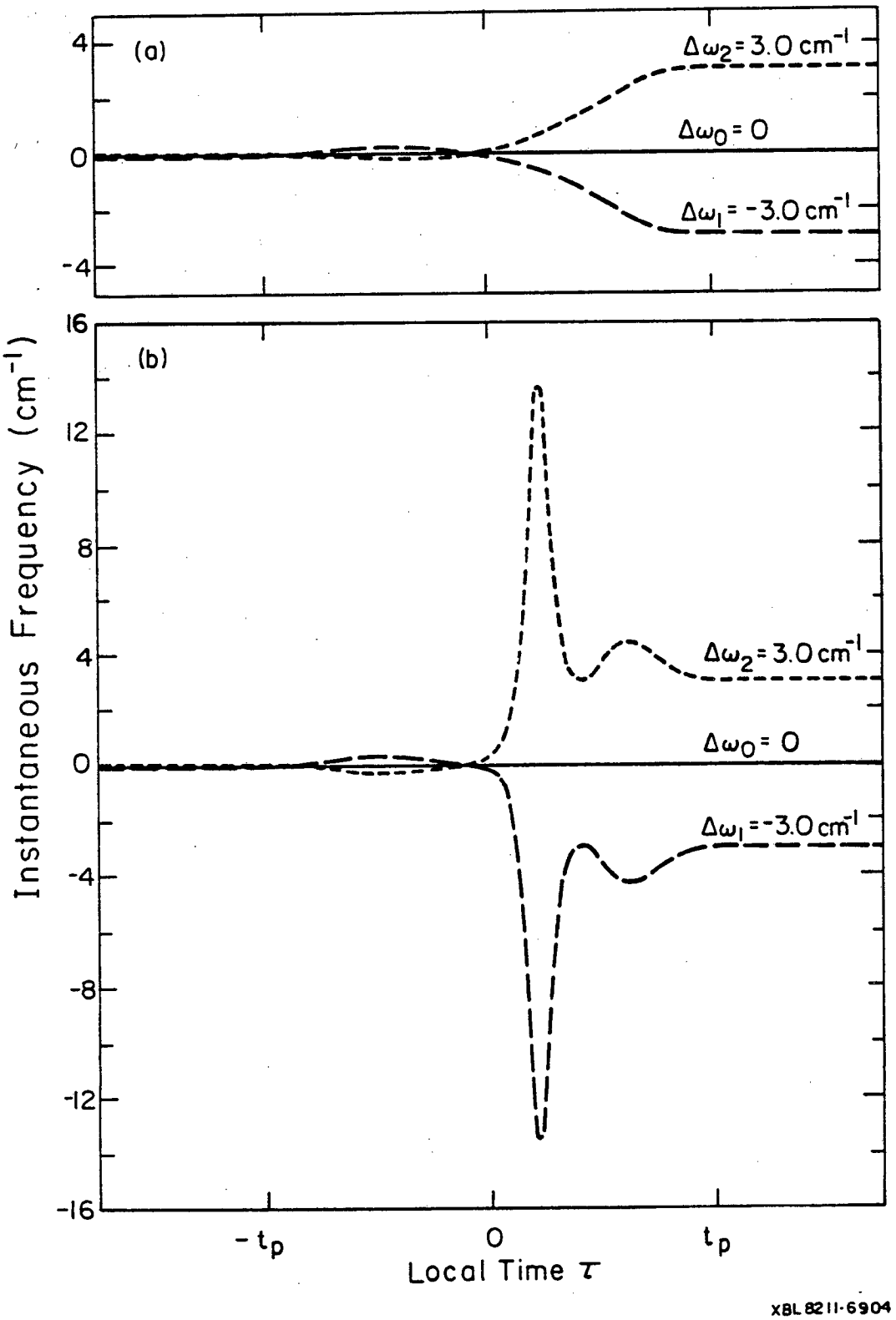
(a)
$\Delta\omega_2 = 3.0\ cm^{-1}$
$\Delta\omega_0 = 0$
$\Delta\omega_1 = -3.0\ cm^{-1}$
4
0
-4
(b)
16
12
8
4
0
-4
-8
-12
-16
Instantaneous Frequency (cm^{-1})
$\Delta\omega_2 = 3.0\ cm^{-1}$
$\Delta\omega_0 = 0$
$\Delta\omega_1 = -3.0\ cm^{-1}$
$-t_p$
0
t_p
Local Time τ
XBL8211-6904

Figure 6

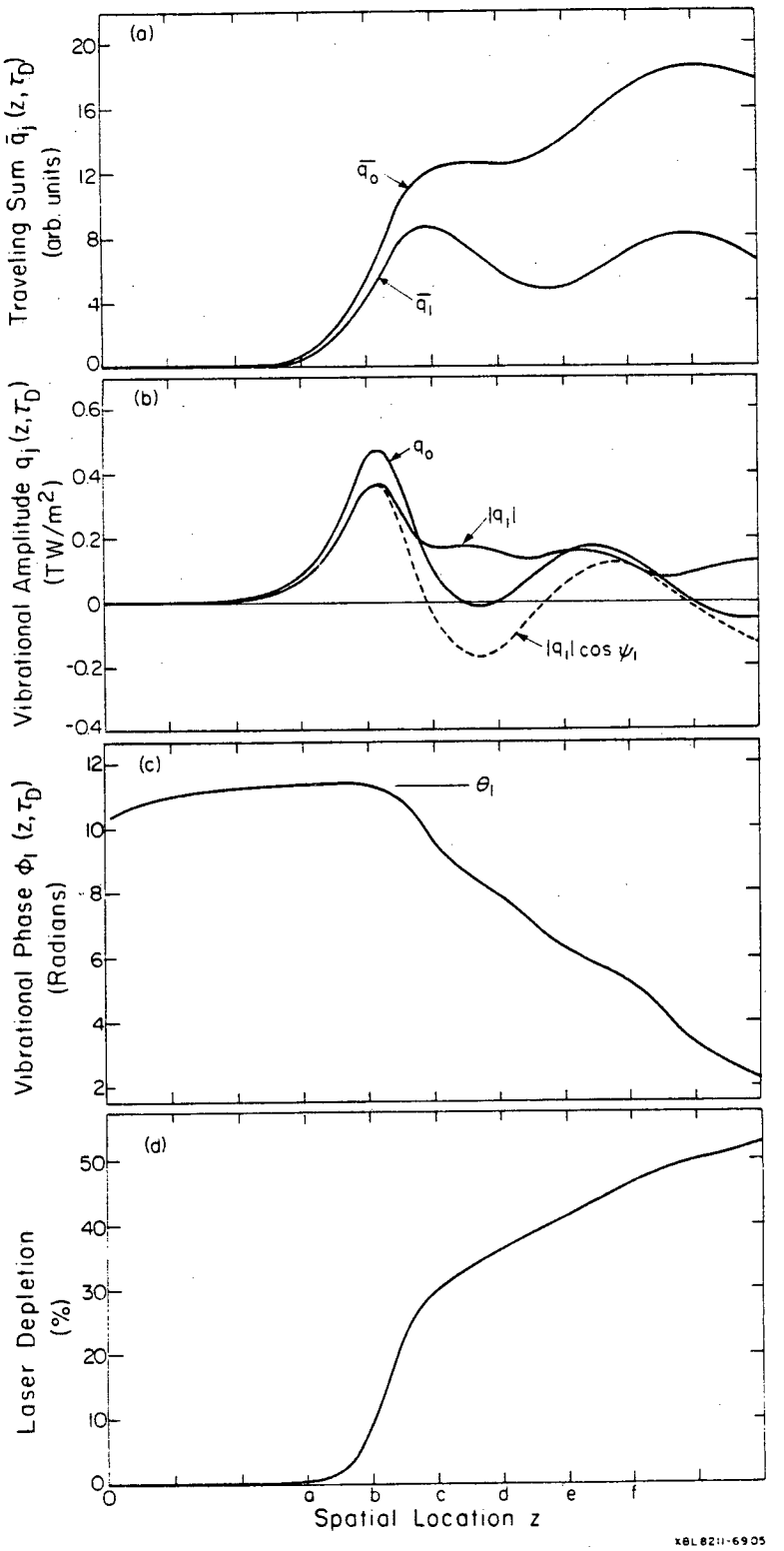
(a)
Traveling Sum $\bar{q}_l(z,\tau_D)$ (arb. units)
$\bar{q}_o$
$\bar{q}_1$
(b)
Vibrational Amplitude $q_l(z,\tau_D)$ (TW/m^2)
q_o
$|q_1|$
$|q_1|\cos\psi_1$
(c)
Vibrational Phase $\Phi_l(z,\tau_D)$ (Radians)
θ_l
(d)
Laser Depletion (%)
a
b
c
d
e
f
Spatial Location z
XBL 8211-6905

Figure 7

frequencies. This low laser depletion behavior has been previously reported by Laubereau and Kaiser [1].

For low laser depletion, Fig. 5 also illustrates that the phase factors for q_1 at spatial locations a and b reach the same constant value Θ_1 for $\tau \gg t_p$. More generally, the calculations reveal a nearly constant vibrational phase for $\tau \gg t_p$ over a wide range of spatial locations prior to high laser depletion. For this three-component calculation, Fig. 7(c) shows the results for $\Phi_1(z,\tau_D)$, the vibrational phase at $\tau_D=2.5t_p$ for various spatial locations. For low laser depletion, Fig. 7(c) illustrates that $\partial\Phi_1(z,\tau_D)/\partial z \simeq 0$. This nearly constant vibrational phase over a wide range of z locations is equivalent to a well-defined spatial k-vector. Because of its later importance in the coherent collinear probing process, this vibrational phase in low laser depletion is specified by Θ_j:

$$\Theta_j = \Phi_j(z,\tau \gg t_p) \tag{18}$$

B. Results in High Laser Depletion

In high laser depletion, a more complicated behavior emerges in the local time profiles shown in Figs. 4(c)-4(f). As discussed in Sec. III, the central characteristic of high laser depletion behavior is the regeneration of a negative, i.e., 180° phase-shifted laser field. The 180° phase-shifted laser amplitude produces a 180° phase shift in the driving force on the vibrational amplitude. This 180° phase shift is the essential feature occuring in high laser depletion which will lead to enhanced selectivity in the probing process of the vibrational

dephasing experiment.

1. Effect on the Vibrational Phase

The off-resonant forced vibrational oscillators respond to the 180° phase shift by rapidly changing their phase in order to eliminate the 180° phase shift. This rapid phase change is illustrated in Fig. 5 for spatial locations c-f which correspond to the field and vibrational amplitudes in Figs. 4(c)-4(f), respectively. As Stokes conversion and percent laser depletion increases, the 180° phase shift in the $e_L e_S$ driving field occurs more rapidly and with greater amplitude. Consequently, the phase of the off-resonant vibrational oscillators changes more rapidly and with greater amplitude. In Fig. 5 for spatial locations e and f, two separate phase shifts are distinctly evident. These phase shifts result from the laser field in Figs. 4(e) and 4(f) which changes sign twice.

Figure 6(b) shows the effect of the rapidly changing phase on the instananeous frequency $\partial\chi_j/\partial\tau=(\Delta\omega_j+\partial\Phi_j/\partial\tau)$. This instantaneous frequency corresponds to the phase evolution in Fig. 5 for the spatial point d and the spatial location and field amplitudes in Fig. 4(d). As the laser field is depleted in Fig. 4(d), the phase change $\partial\Phi_j/\partial\tau$ goes to zero in Fig. 5 and the instantaneous frequency $(\Delta\omega_j+\partial\Phi_j/\partial\tau)$ is rapidly swept toward $\Delta\omega_j$ in Fig. 6(b).

Figure 4(d) reveals that a negative, 180° phase-shifted laser field is quickly regenerated as the instantaneous frequency is undergoing this frequency sweep. As the regenerated 180° phase-shifted laser field grows, the vibrational phase continues to move in response to the 180°

phase shift in the driving field. Consequently, Fig. 6(b) shows that the instantaneous frequency is swept significantly past the natural frequency $\Delta\omega_j$. We believe that this continuous frequency sweep of the off-resonant vibrational frequencies justifies the assumption that no new laser fields at $\omega_L+\Delta\omega_j$ are generated after Stokes saturation.

As a result of these phase changes in high laser depletion, Figs. 5 and 7(c) show that the vibrational phases at different spatial locations no longer evolve to the same nearly constant value Θ_1 for $\tau \gtrsim t_p$. Instead, the phase $\Phi_1(z,\tau \gtrsim t_p)$ reflects the changing time-dependent negative driving force at different spatial locations. Figure 7(c) illustrates that $\partial\Phi_j(z,\tau_D)/\partial z \neq 0$ and the vibrational amplitude no longer has the same well-defined spatial k-vector after the onset of high laser depletion. These changes in the vibrational phase will lead to enhanced selectivity in the probing process of the vibrational dephasing experiment.

2. Effect on the Absolute Value of the Vibrational Amplitude

Figure 4 reveals the important observation that $|q_1|$, the absolute value of the complex off-resonant vibrational amplitude q_1, is never driven to zero by the 180° phase-shifted driving force. This occurs because q_1 is driven off-resonance. Consequently, q_1 can change its phase and move in complex space in response to the 180° phase shift in the driving force. As a result, $|q_1|$ is not driven down significantly by the 180° phase-shifted driving force and q_1 is able to obtain large negative amplitudes soon after the 180° phase shift.

Alternatively, $|q_0|$, the absolute value of the real resonant

vibrational amplitude shown in Fig. 4, is driven to zero before q_0, the real vibrational amplitude, goes negative. This occurs because q_0 is driven at resonance. Consequently, q_0 is confined to a vibrational phase $\Phi_0=0$ and real space. q_0 can undergo a 180° phase shift only when its real amplitude is driven through zero and its absolute value goes to zero. As a result, q_0 obtains much smaller negative vibrational amplitudes than q_1. The larger negative amplitudes for the off-resonant vibrational amplitudes will enhance the degree of selectivity in the collinear coherent Stokes probing process of the vibrational dephasing experiment.

3. Analogous Behavior of a Forced Harmonic Oscillator

It is important to notice that much of the high laser depletion behavior can be understood by recalling the behavior of a forced, damped, harmonic oscillator at steady state which at some time t=0 suddenly experiences a 180° phase shift in its driving field [29]. For example, prior to t=0, the forced harmonic oscillator at steady state has a solution which can be expressed in the usual way as $Z(t)=A\exp(i(\omega_0 t-\delta))$ where ω_0 is the driving field frequency. If the driving field undergoes a sudden 180° phase shift at t=0, the solution for t>0 becomes $Z(t)= A[\ 2\exp(-t/t_d)\exp(i(\omega_j t-\delta)) - \exp(i(\omega_0 t-\delta))\ ]$ where t_d is the damping time and ω_j is the oscillator's natural frequency. Notice that this solution has the proper continuity at t=0.

When the oscillator is driven at resonance, $\omega_j=\omega_0$ and the solution for t>0 can be expressed as $Z(t)=R(t)\exp(i(\omega_0 t-\delta))$ where R(t) is real. The oscillator driven at resonance continues to rotate at frequency ω_0

and the movement of the resonant vector R(t) is confined to the real axis. Consequently, the real amplitude R(t) must go through zero when the oscillator adjusts to the 180° phase shift. This behavior is analogous to the real resonant vibrational amplitude q_0.

When the oscillator is driven off-resonance, $\omega_j \neq \omega_0$ and the solution can again be expressed as $Z(t)=I(t)\exp(i(\omega_0 t-\delta))$. In this solution, however, I(t) is an complex amplitude containing a transient term which oscillates with the frequency $\omega_0-\omega_j=\Delta\omega_j$. Thus the off-resonant vector I(t) can rotate in the complex plane. This rotating term allows the off-resonant oscillator to sweep into proper phase with the phase-shifted driving force without being driven through zero. This behavior is analogous to the complex off-resonant vibrational amplitude q_j.

This analogy between forced harmonic oscillators and the vibrational amplitudes illustrates the generality of these results and provides a simple physical picture for the high laser depletion behavior. Although this analogy will not be elaborated further, the evolution of the larger negative off-resonant vibrational amplitudes and additional results encountered in subsequent sections can be explained qualitatively using this analogy.

V. Probe Signals in the Vibrational Dephasing Experiment

A probe pulse collinear with the excitation pulse produces coherent Stokes Raman scattering [1,3,6] in the vibrational dephasing experiment. In the following analysis, only collinear probe pulses are considered. Collinear probe pulses interact with the macroscopic coherent vibrational superposition over a wide range of spatial

locations. In high laser depletion, this extended interaction length leads to selective coherent Stokes probe scattering.

A. Calculation of Probe Signals

The coherent Stokes probe amplitudes were calculated at local time $\tau_D=2.5t_p$. At this late delay time, far from the excitation laser pulse peak at $\tau=0$, individual probe Stokes fields at frequencies ω_{Sj} were assumed to interact only with the vibrational oscillators at frequencies ω_j according to $\omega_L-\omega_{Sj}=\omega_j$. No depletion of the laser probe pulse at frequency ω_L was assumed. In addition, each individual coherent probe Stokes field e_{Spj} was assumed to develope in phase with the probe laser field e_L and the vibrational amplitude q_j. Thus the total phase of the individual coherent Stokes probe fields e_{Sj} arising from the off-resonant vibrational amplitudes q_j relative to the coherent Stokes probe field arising from the resonant vibrational amplitude q_0 is $\chi_j(z,\tau_D)=\Delta\omega_j\tau_D+\Phi_j(z,\tau_D)$ at $\tau=\tau_D$.

An individual coherent Stokes probe field amplitude grows according to Eq. (9). Because the laser probe amplitude is assumed to be constant, Eq. (9) indicates that the integral of the vibrational amplitude over all z can be used to determine the coherent Stokes probe field amplitude. Because the probing process is coherent, the individual coherent Stokes probe fields are sensitive to the phase of the vibrational amplitudes. In low laser depletion, the individual coherent Stokes probe field amplitudes begin their development in the proper phase relationship to Θ_j. In high laser depletion, the vibrational phases no longer evolve to Θ_j. These phase changes

significantly influence the coherent Stokes probe field amplitudes.

In order to measure the change of the vibrational phases in high laser depletion, a new phase Ψ_j is defined that measures the difference between $\Delta\omega_j\tau+\Phi_j(z,\tau)$, the total phase of the individual vibrational amplitudes and $\Delta\omega_j\tau+\Theta_j$, the total phase of the individual vibrational amplitude prior to high laser depletion:

$$\Psi_j(z,\tau) = \Phi_j(z,\tau)-\Theta_j \tag{19}$$

After this definition is made, the individual real Stokes field amplitudes generated by a collinear laser probe pulse at local time $\tau_D=2.5t_p$ are given by:

$$e_{SPj}(z,\tau_D) \propto f_j\, e_{LP}\, \bar{q}_j(z,\tau_D) \tag{20}$$

where $$\bar{q}_j(z,\tau_D) = \sum_z |q_j(z,\tau_D)| \cos(\Psi_j(z,\tau_D)) \tag{21}$$

Notice that $\bar{q}_j(z,\tau_D)$ is the traveling sum of the vibrational amplitudes at $\tau=\tau_D$ summed over z. Thus Eq. (20) is the discrete numerical equivalent of the integral of Eq. (9). In high laser depletion, the effects of the vibrational phase changes on the Stokes probe field amplitude are accounted for by $\cos(\Psi_j(z,\tau_D))$.

B. Results

The vibrational amplitudes at various spatial locations give rise to the coherent Stokes probe amplitude. Figure 7(b) shows $q_0(z,\tau_D)$,

$|q_1(z,\tau_D)|$ and $|q_1(z,\tau_D)|\cos(\Psi_1(z,\tau_D))$, the vibrational amplitudes at $\tau_D=2.5t_p$ as a function of spatial location for the three-component linewidth discussed in Sec. IV. Figure 7(a) shows the traveling sums of the individual vibrational amplitudes which are related to the individual Stokes probe field amplitudes by Eq. (20).

For low laser depletions, the spatial vibrational amplitudes in Fig. 7(b) increase nearly exponentially and the corresponding traveling sums in Fig. 7(a) grow rapidly with propagation distance z. For laser depletions >15%, the vibrational amplitudes are driven lower and the vibrational phases begin to change. For laser depletions >30%, the vibrational amplitude for $|q_1|\cos\Psi_1$ goes negative. A comparison of $|q_1|$ and $|q_1|\cos\Psi_1$ indicates that the negative amplitude arises from phases changes measured by Ψ_1.

Fig. 7(a) shows that $\bar{q}_1$, the traveling sum for $|q_1(z,\tau_D)|\cos\Psi_1(z,\tau_D)$ is substantially reduced as negative vibrational amplitudes are added to the traveling sum. Thus the phase-shifted vibrational amplitudes in high laser depletion reduce their corresponding coherent probe Stokes fields. This phenomena is equivalent to a coherent Stokes probe field adding in destructively to the existing coherent Stokes probe field.

In high laser depletion, Fig. 7(b) illustrates that the off-resonant vibrational amplitudes $|q_j|\cos(\Psi_j)$ display larger negative amplitudes than the resonant vibrational amplitude q_0. This behavior was previously discussed in Sec. IV.B.2. Consequently, Fig. 7(a) shows that the traveling sum of the resonant vibrational amplitude becomes much larger than the traveling sum of the off-resonant vibrational amplitudes as the traveling sums move through the region of high laser

depletion. As a result, there is enhanced coherent Stokes scattering from the resonant vibrational amplitude in the probing process of the vibrational dephasing experiment. This selective scattering allows the homogeneous dephasing time T_2 to be measured to a high level of accuracy.

VI. Dependence of Selectivity on Various Parameters

In the following discussions, selectivities were measured by $\bar{q}_j(z,\tau_D)/\bar{q}_0(z,\tau_D)$, the ratio of the traveling sums of the vibrational amplitudes. Given this definition, a high ratio corresponds to a low selectivity. Notice that this definition for selectivity does not include the relative number density f_j. The actual experimental selectivities will be enhanced by including the relative number densities f_j. The experimental selectivities will be discussed in Sec. VIII.

The ratios in low laser depletion were determined at spatial locations corresponding to excitation laser pulse depletions $\lesssim$2%. The ratios were nearly constant for laser depletions $\lesssim$2%. The ratios in high laser depletion were determined at spatial locations corresponding to excitation laser pulse depletions $\simeq$38-52%. The range of ratios calculated for high laser depletion gives rise to the error bars on the high laser depletion points.

A. Dependence of Selectivity on $\Delta\omega$

Using a three-component vibrational linewidth with a 0.25:0.50:0.25

number density distribution, calculations were performed to determine the effect of the off-resonance magnitude $\Delta\omega$ on selectivity. In these calculations, the pulsewidth t_p and the dephasing time T_2 were held constant. For t_p=7 psec and T_2=7 psec, the selectivity was determined for three separate three-component vibrational linewidths with $\Delta\omega$= ±1.5, ±3.0. and ±4.5 cm^{-1}. More generally, this is equivalent to t_p/T_2=1 where $t_p\Delta\omega$= $T_2\Delta\omega$= ±1.98, ±3.96 and ±5.94 radians.

The dependence of selectivity on $\Delta\omega$ in both low and high laser depletion is shown in Fig. 8. These results illustrate that selectivity is strongly dependent upon $\Delta\omega$. The low laser depletion selectivities versus $t_p\Delta\omega$ reported here for t_p/T_2=1 are very similar to the low laser depletion selectivities reported by Laubereau and Kaiser [1]. The selectivities are greatly enhanced in the high laser depletion regime.

The vibrational amplitudes of q_0 and $q_1\cos\Psi_1$ at τ_D=2.5t_p are shown in Figs. 9(a)-9(c) for $\Delta\omega$=±1.5, ±3.0 and ±4.5 cm^{-1}, respectively. These vibrational amplitudes give rise to coherent Stokes probe fields as discussed in Sec. V. In order to understand these vibrational amplitudes, their time profiles must be investigated. The local time profiles which give rise to the vibrational amplitudes at the spatial locations a',b' and c' in Figs. 9(a)-9(c) are shown in Figs. 10(a)-10(c), respectively. These spatial locations were selected because they are close to the location of the maximum negative $|q_1|\cos(\Psi_1)$ value. These spatial locations corespond to laser depletions of 32.5, 34.5 and 36.5% for $\Delta\omega$=±1.5, ±3.0 and ±4.5 cm^{-1}, respectively.

Figs. 10(a)-10(c) reveal that the resonant vibrational amplitude q_0 and the forced off-resonant vibrational amplitude q_1 grow until e_L is nearly depleted. As the laser is depleted, q_1 is no longer driven as a

FIG. 8. Dependence of selectivity (not including relative number densities) on the off-resonance magnitude $\Delta\omega$. The off-resonance frequency is measured in units of $t_p\Delta\omega$ where the pulse width t_p is constant.

FIG. 9. Vibrational amplitudes for the three-component vibrational linewidths at $\tau=\tau_D$ as a function of spatial location. (a) $\Delta\omega=\pm 1.5$ cm^{-1}. (b) $\Delta\omega=\pm 3.0$ cm^{-1}. (c) $\Delta\omega=\pm 4.5$ cm^{-1}. Spatial locations a'-c' are referred to in Figs. 10 and 11.

FIG. 10. (a)-(c) Local time profiles of the field and vibrational amplitudes for the three-component vibrational linewidths at the spatial locations a'-c' respectively indicated in Fig. 9 for $\Delta\omega=\pm 1.5$, 3.0 and 4.5 cm^{-1}, respectively.

FIG. 11. Local time profiles of the vibrational phases for the three-component vibrational linewidths at the spatial locations a'-c' indicated in Fig. 9 for $\Delta\omega_1=-1.5$, -3.0 and -4.5 cm^{-1}, respectively.

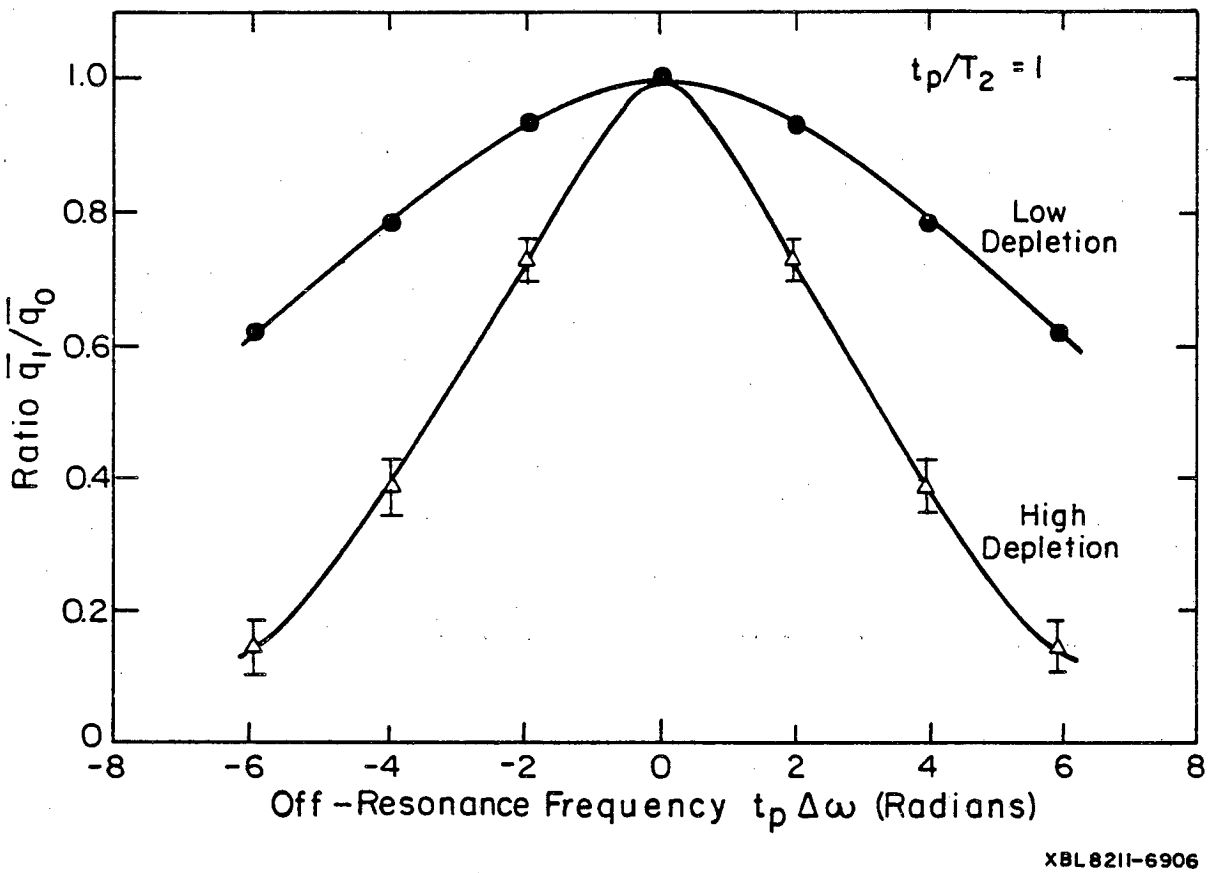
$t_p/T_2 = 1$
Low Depletion
High Depletion
Ratio $\bar{q}_1/\bar{q}_0$
1.0
0.8
0.6
0.4
0.2
0
-8
-6
-4
-2
0
2
4
6
8
Off-Resonance Frequency $t_p \Delta\omega$ (Radians)
XBL8211-6906

Figure 8

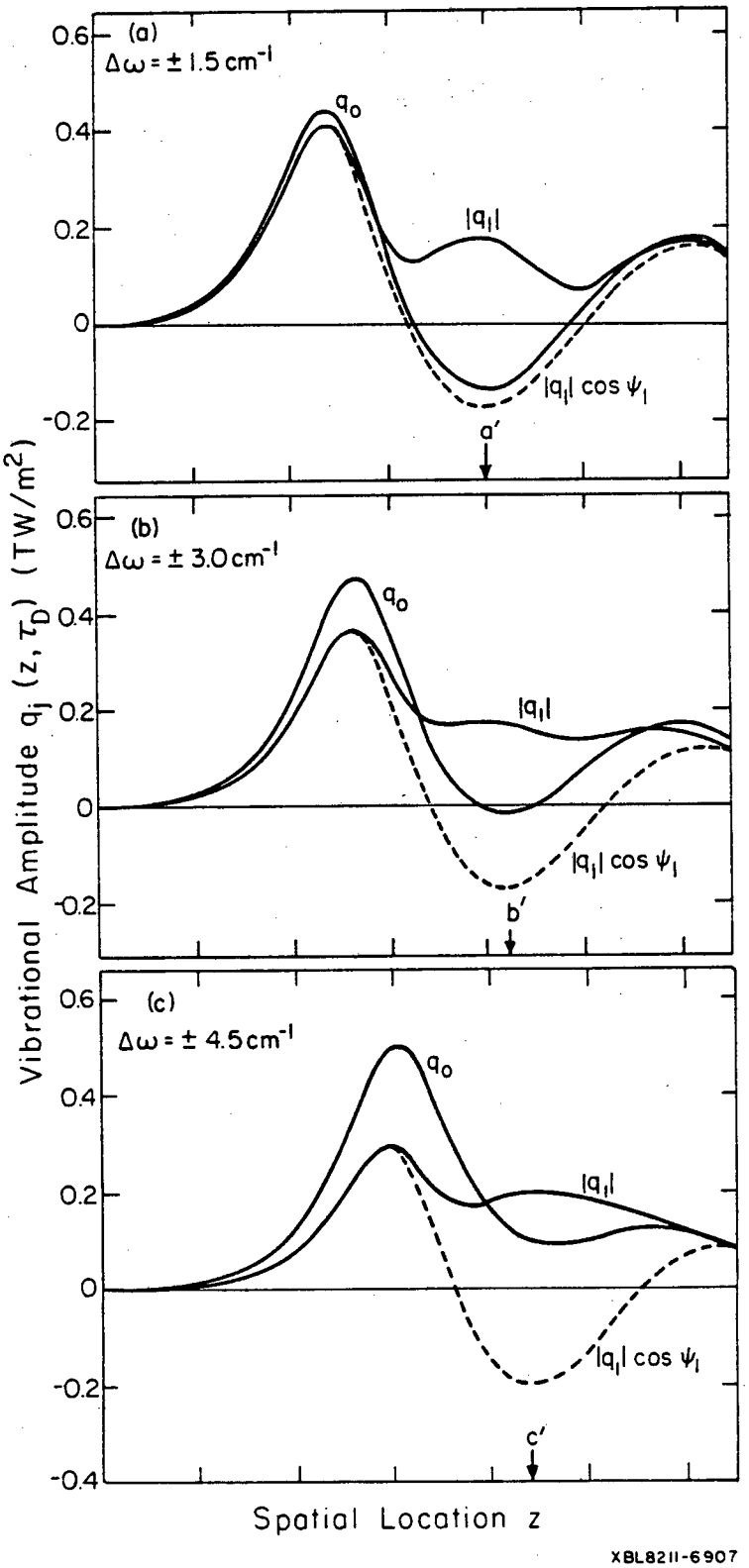
(a)
Δω = ± 1.5 cm⁻¹
(b)
Δω = ± 3.0 cm⁻¹
(c)
Δω = ± 4.5 cm⁻¹
q_o
$|q_1|$
$|q_1| \cos \psi_1$
a′
b′
c′
0.6
0.4
0.2
0
-0.2
-0.4
Vibrational Amplitude $q_j(z, \tau_D)$ (TW/m²)
Spatial Location z
XBL8211-6907

Figure 9

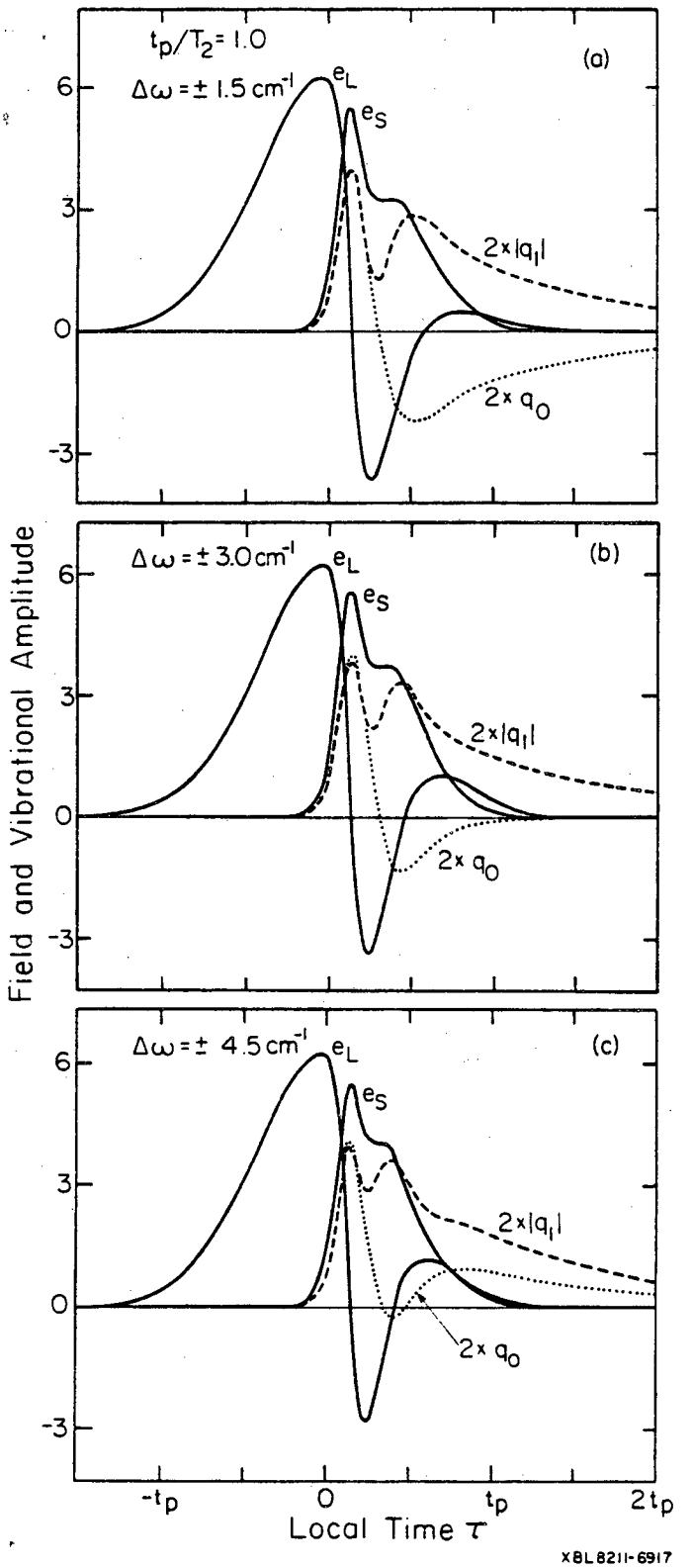
$t_p/T_2 = 1.0$
(a)
$\Delta\omega = \pm 1.5\,cm^{-1}$
e_L
e_S
$2\times|q_1|$
$2\times q_0$
$\Delta\omega = \pm 3.0\,cm^{-1}$
(b)
$\Delta\omega = \pm 4.5\,cm^{-1}$
(c)
6
3
0
-3
Field and Vibrational Amplitude
$-t_p$
0
t_p
$2t_p$
Local Time τ
XBL8211-6917

Figure 10

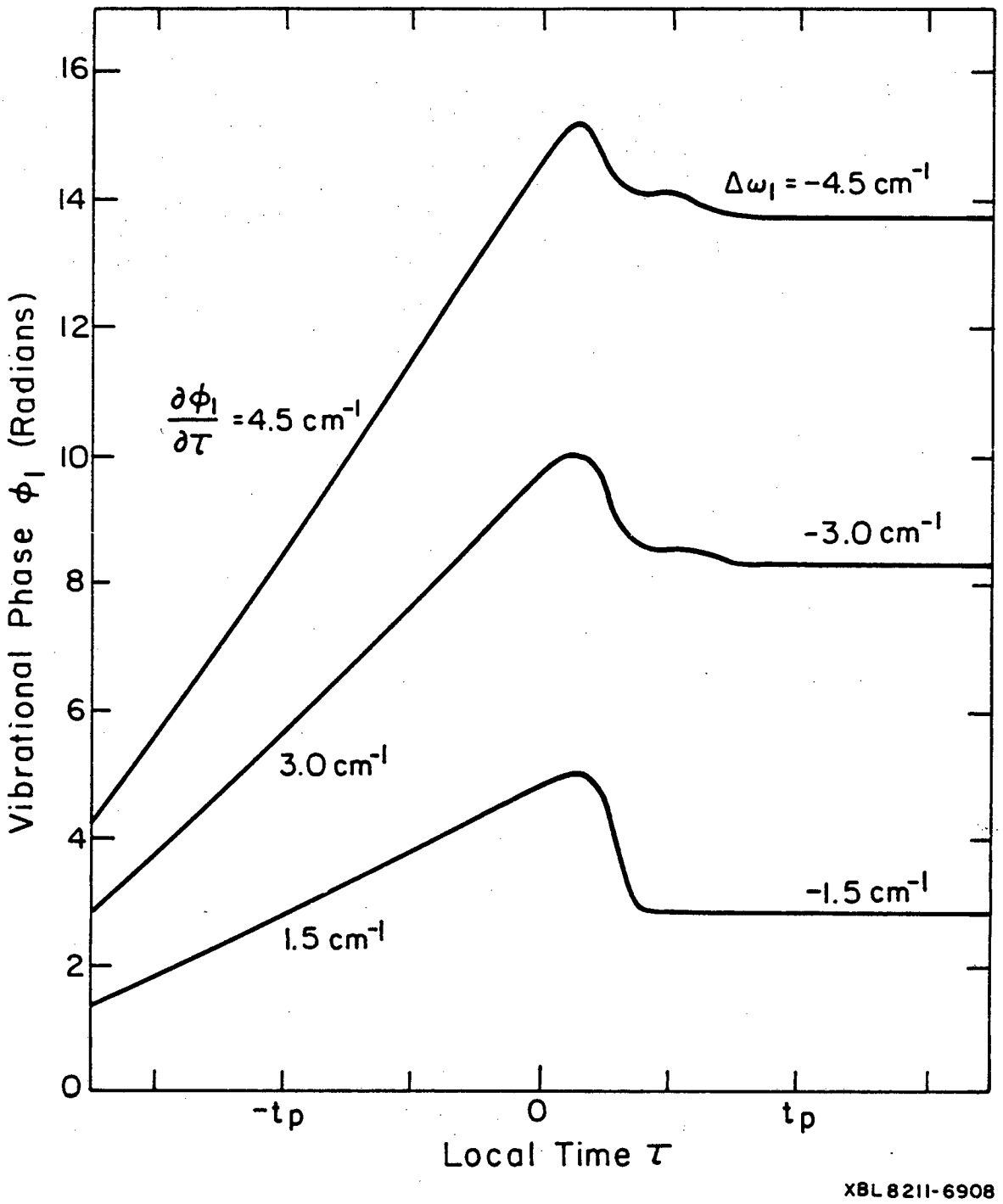
16
14
12
10
8
6
4
2
0
Vibrational Phase ϕ_1 (Radians)
$\Delta\omega_1 = -4.5\ cm^{-1}$
$\frac{\partial\phi_1}{\partial\tau} = 4.5\ cm^{-1}$
$-3.0\ cm^{-1}$
$3.0\ cm^{-1}$
$-1.5\ cm^{-1}$
$1.5\ cm^{-1}$
$-t_p$
0
t_p
Local Time τ
XBL 8211-6908

Figure 11

forced oscillator. Consequently, the instantaneous frequency $(\Delta\omega_1+\partial\Phi_1/\partial\tau)$ is rapidly swept toward $\Delta\omega_1$ and the total phase precesses $\Delta\omega_1\tau+\Phi_1(\tau)$ in the rotating frame at resonance. As a result, q_1 reduces $\langle q_0(\tau)\rangle$, the effective total vibrational amplitude at ω_0 which gives rise to the regeneration of the laser field at ω_L.

Smaller $\Delta\omega_j$ values cause smaller reductions in $\langle q_0(\tau)\rangle$ resulting from $\Delta\omega_j\tau$ precession. Consequently, $\langle q_0(\tau)\rangle$ is larger during the e_L regeneration process for $\Delta\omega= \pm 1.5$ cm^{-1}. This leads to a larger $\langle q_0(\tau)\rangle e_S(\tau)$ product which regenerates a larger negative laser amplitude at the expense of depleting e_S, q_0 and $|q_1|$. For $\Delta\omega= \pm 1.5$ cm^{-1}, the larger negative laser amplitude and larger e_S, q_0 and $|q_1|$ depletions which occur at the peak of the negative regenerated laser amplitudes are clearly apparent in Fig. 10(a).

The magnitude of the negative laser amplitudes affects the subsequent regeneration of the Stokes field and vibrational amplitudes. Fig. 10(a)-10(c) illustrates that the larger negative laser amplitudes regenerate more 180° phase-shifted vibrational amplitude. This leads to the differences between the resonant vibrational amplitudes $q_0(z,\tau_D)$ for $\Delta\omega=\pm 1.5$, ± 3.0 and ± 4.5 cm^{-1} shown in Fig. 9(a)-9(c). These differences give rise to the different selectivities shown in Fig. 8. The dependence of selectivity on $\Delta\omega$ will be discussed in more detail in Sec. VII.

Figure 11 shows the time dependence of the phase $\Phi_1(z,\tau)$ at the spatial locations a',b' and c' in Figs. 9(a)-9(c) for $\Delta\omega_1= -1.5$, -3.0 and -4.5 cm^{-1}, respectively. The time-dependent behavior of the vibrational phase has been previously discussed in Sec. IV.B.1. Notice that the changes of the phase in response to the negative regenerated

laser field are dependent upon the $\Delta\omega_1$ magnitude. This occurs because, over a constant time interval, more of the 180° phase shift of the total phase $\chi_1(z,\tau)=\Delta\omega_1\tau+\Phi_1(z,\tau)$ must be accomplished by Φ_1 if $\Delta\omega_1$ is smaller.

B. Dependence of Selectivity on T_2

Using a three-component vibrational linewidth with a 0.25:0.50:0.25 number density distribution, calculations were performed to determine the effect of T_2 on selectivity. In these calculations, the pulsewidth t_p and the off-resonance magnitude $\Delta\omega$ were held constant. For t_p=7 psec and $\Delta\omega$= $\pm$3.0 cm^{-1}, the selectivity was determined for three separate three-component linewidths with T_2=3.5, 7.0 and 14.0 psec. More generally, this is equivalent to $t_p\Delta\omega$= $\pm$3.96 radians with three separate combinations of t_p/T_2 and $T_2\Delta\omega$: t_p/T_2=2 with $T_2\Delta\omega$= $\pm$1.98 radians; t_p/T_2=1 with $T_2\Delta\omega$= $\pm$3.96 radians; and t_p/T_2=0.5 with $T_2\Delta\omega$= $\pm$7.92 radians.

The dependence of the selectivity on T_2 in both low and high laser depletion is shown in Fig. 12. These results illustrate that, when the pulsewidth is constant, selectivity for a particular $\Delta\omega$ is not noticably dependent upon T_2 in low laser depletion and is only weakly dependent upon T_2 in high laser depletion. The weak dependence of selectivity on T_2 results from two counterbalancing effects. As T_2 increases, the excitation transiency measured by t_p/T_2 decreases which leads to less selectivity [1]. On the other hand, as T_2 increases, the off-resonant oscillators have longer interaction times with the $e_L e_S$ driving field in the falling edge to the laser pulse. After the released off-resonant oscillators have precessed by 180°, they are driven out-of-phase by the

$e_L e_s$ driving field. Consequently, this interaction reduces the off-resonant vibrational amplitudes and leads to higher selectivity. The magnitude of this interaction is measured by $\Delta\omega T_2$.

The $t_p\Delta\omega$ product was constant at $t_p\Delta\omega=\pm 3.96$ radians in these calculations. Likewise, the selectivity was also approximately constant for the various dephasing times T_2. These results indicate that selectivity is approximately determined by $(t_p/T_2)X(T_2\Delta\omega)=t_p\Delta\omega$. This conclusion is important for experimental determinations of T_2.

C. Dependence of Selectivity on t_p

Using the three-component vibrational linewidths with a 0.25:0.50:0.25 number density distribution, the previous calculations were analyzed to determine the effect of pulsewidth t_p on selectivity. In this analysis, the dephasing time T_2 and the off-resonance magnitude were held constant. For T_2=3.5 psec and $\Delta\omega= \pm 3.0$ cm^{-1}, the selectivity was determined for two separate three-component linewidths with t_p= 3.5 and 7 psec. More generally, this is equivalent to $T_2\Delta\omega= \pm 1.98$ radians with two separate combinations of t_p/T_2 and $t_p\Delta\omega$: t_p/T_2= 1.0 with $t_p\Delta\omega=\pm 1.98$ radians and t_p/T_2=2.0 with $t_p\Delta\omega=\pm 3.96$ radians.

The dependence of selectivity on t_p in both the low and high laser depletion limit is shown in Fig. 13. The low laser depletion point at $t_p/T_2=0$ is the theoretical limit when $t_p/T_2 \to 0$ [1]. These results illustrate that selectivity for a particular $\Delta\omega$ is strongly dependent upon the pulsewidth t_p. Longer pulsewidths t_p give rise to greater selectivity. These results agree with the conclusion that selectivity is approximately determined by $t_p\Delta\omega$.

FIG. 12. Dependence of selectivity (not including relative number densities) on the dephasing time T_2. The dephasing time is measured in units of $T_2\Delta\omega$ where the off-resonance magnitude $\Delta\omega$ is constant.

FIG. 13. Dependence of selectivity (not including relative number densities) on the pulse width t_p. The pulsewidth is measured in units of $t_p\Delta\omega$ where the off-resonance magnitude $\Delta\omega$ is constant.

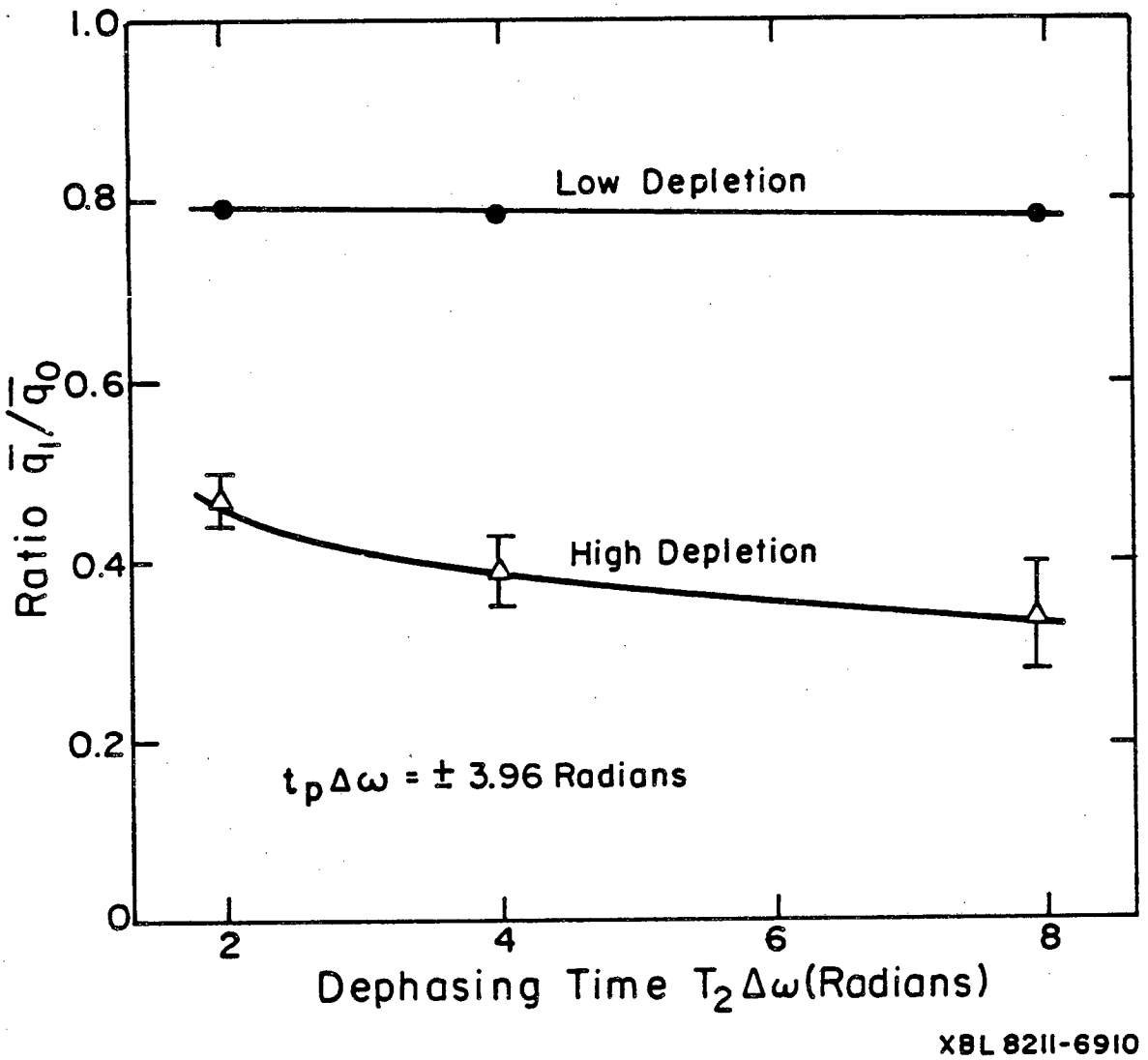
1.0
0.8
0.6
0.4
0.2
0
Ratio $\bar{q}_1/\bar{q}_0$
Low Depletion
High Depletion
$t_p\Delta\omega = \pm 3.96$ Radians
2
4
6
8
Dephasing Time $T_2\Delta\omega$(Radians)
XBL 8211-6910

Figure 12

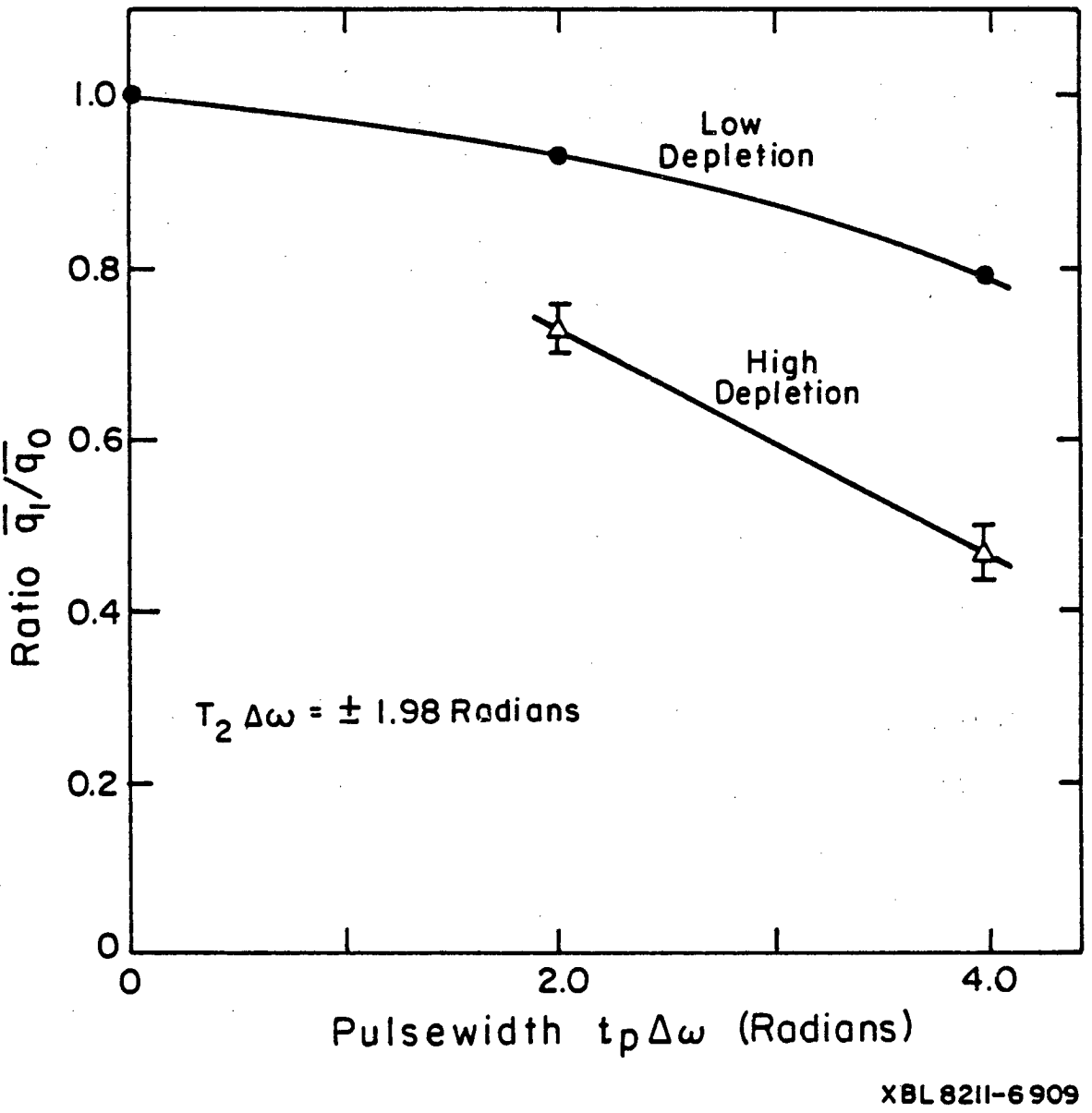
1.0
0.8
0.6
0.4
0.2
0
Ratio $\bar{q}_1/\bar{q}_0$
Low
Depletion
High
Depletion
$T_2 \Delta\omega = \pm 1.98$ Radians
0
2.0
4.0
Pulsewidth $t_p \Delta\omega$ (Radians)
XBL 8211-6909

Figure 13

VII. Results for a Linewidth with Five Vibrational Components

A five-component vibrational linewidth with a 0.1:0.2:0.4:0.2:0.1 number density distribution was used to determine the effect of increasing the number of components in the vibrational linewidth. In this calculation, t_p=7 psec, T_2=7 psec, $\Delta\omega_1$= -1.5 cm^{-1}, $\Delta\omega_2$=+1.5 cm^{-1}, $\Delta\omega_3$=-3.0 cm^{-1}, and $\Delta\omega_4$=+3.0 cm^{-1}. More generally, this is equivalent to t_p/T_2=1 with $t_p\Delta\omega=T_2\Delta\omega=\pm1.98$ and ±3.96 radians.

The vibrational amplitudes of q_0, $|q_1|\cos\Psi_1$ and $|q_3|\cos\Psi_3$ at $\tau_D=2.5t_p$ are shown in Fig. 14. These vibrational amplitudes give rise to coherent Stokes probe fields as discussed in Sec. V. Because of symmetry in the equations, $|q_2|=|q_1|$, $|q_4|=|q_3|$, $\Phi_2=-\Phi_1$ and $\Phi_4=-\Phi_3$. A comparison of Figs. 14, 9(a) and 9(b) shows that the behavior of the $\Delta\omega_1$=-1.5 cm^{-1} and -3.0 cm^{-1} components together in the five-component vibrational linewidth is very similar to their individual behavior in separate three-component vibrational linewidths.

Figure 15 displays the local time profiles of e_L, e_S, q_0, $|q_1|$ and $|q_3|$ at the spatial location a in Fig. 14. The corresponding laser depletion at spatial location a is 34%. A comparison of Figs. 15, 10(a) and 10(b) shows that the time-dependent behavior for the $\Delta\omega_1$=-1.5 cm^{-1} and $\Delta\omega_3$=-3.0 cm^{-1} components together in the five component vibrational linewidth is very similar to the individual behavior for $\Delta\omega_1$=-1.5 cm^{-1} and $\Delta\omega$=-3.0 cm^{-1} in separate three component vibrational linewidths.

Notice the depletion of q_0, $|q_1|$ and $|q_3|$ during the regeneration of the negative, 180° phase-shifted laser amplitude in Fig. 15. There is a larger depletion for $|q_1|$ in comparison to $|q_3|$. Consequently,

Fig. 14 shows that $|q_3|$ is larger than $|q_1|$ at $\tau_D=2.5t_p$. In agreement with the results in Sec. VI.A., these results illustrate that the off-resonant vibrational amplitudes q_j with frequencies ω_j closer to the center of the vibrational linewidth exhibit larger depletions when the excitation laser field is regenerated.

The larger depletions for q_j with smaller $\Delta\omega_j$ lead to smaller negative vibrational amplitudes $|q_j|\cos\Psi_j$ for $\tau \gtrsim t_p$. Consequently, these smaller negative vibrational amplitudes subtract less from their corresponding traveling sum $\bar{q}_j$. As a result, the ratio $\bar{q}_j/\bar{q}_0$ is greater and the selectivity is lower. Thus the depletion of vibrational amplitudes during laser regeneration limits the maximum possible selectivity for vibrational dephasing experiments conducted in high laser depletion.

Figure 16 displays the time dependence of the phase $\Phi_1(\tau)$ and $\Phi_3(\tau)$ at the spatial location a in Fig. 14. A comparison of Figs. 16 and 11 illustrates that the phases for $\Delta\omega_1=-1.5$ cm^{-1} and $\Delta\omega_3=-3.0$ cm^{-1} behave together in the five-component linewidth nearly identically to their individual behavior in separate three-component linewidths. A comparison of Figs. 15 and 16 shows that most of the negative, 180° phase-shifted laser field is regenerated when $\partial\Phi_1(\tau)/\partial\tau\simeq 0$ and $\partial\Phi_3(\tau)/\partial\tau\simeq 0$, i.e., while the instantaneous frequencies of the off-resonant oscillators are swept toward their natural frequencies.

The dependence of the selectivity on $\Delta\omega$ for the five-component linewidth in both low and high laser depletion is shown in Fig. 17. A comparison of Figs. 8 and 17 illustrates that the selectivity for $\Delta\omega=\pm 1.5$ and ± 3.0 cm^{-1} in the five-component vibrational linewidth is almost identical to the selectivity obtained for $\Delta\omega=\pm 1.5$ and ± 3.0 cm^{-1}

FIG. 14. Vibrational amplitudes for the five-component vibrational linewidth at $\tau=\tau_D$ as a function of spatial location. Spatial location a is referred to in Figs. 15 and 16.

FIG. 15. Local time profiles of the field and vibrational amplitudes for the five-component vibrational linewidth at the spatial location a indicated in Fig. 14.

FIG. 16. Local time profiles of the vibrational phases for the five-component vibrational linewidth at spatial location a indicated in Fig. 14 for $\Delta\omega_1=-1.5\ cm^{-1}$ and $\Delta\omega_3=-3.0\ cm^{-1}$.

FIG. 17. Dependence of selectivity (not including relative number densities) on the off-resonance magnitude $\Delta\omega$ for the five-component vibrational linewidth. The off-resonance magnitude is measured in units of $t_p\Delta\omega$ where the pulse width t_p is constant.

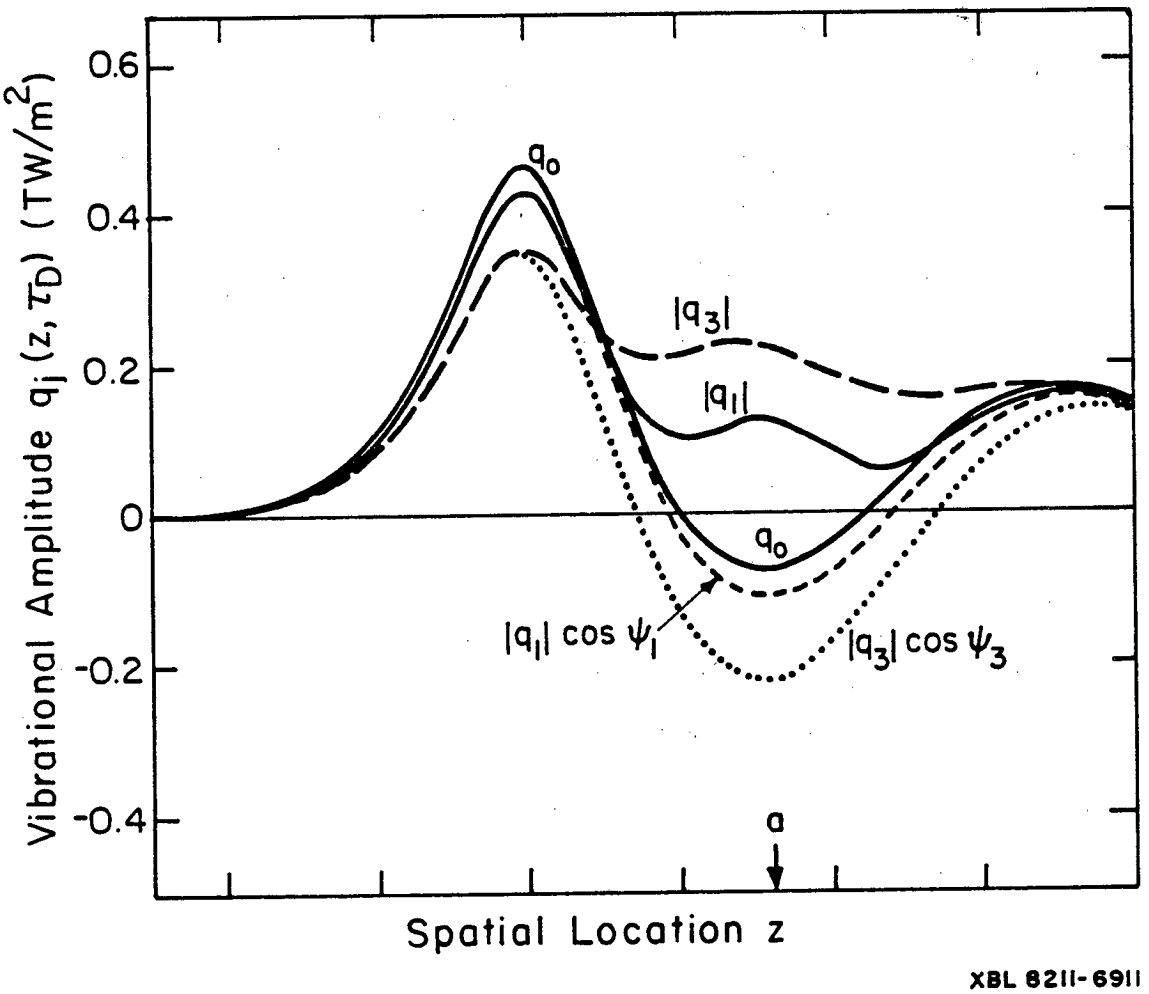
0.6
0.4
0.2
0
-0.2
-0.4
Vibrational Amplitude $q_j(z, \tau_D)$ (TW/m^2)
q_0
$|q_3|$
$|q_1|$
q_0
$|q_1| \cos \psi_1$
$|q_3| \cos \psi_3$
a
Spatial Location z
XBL 8211-6911

Figure 14

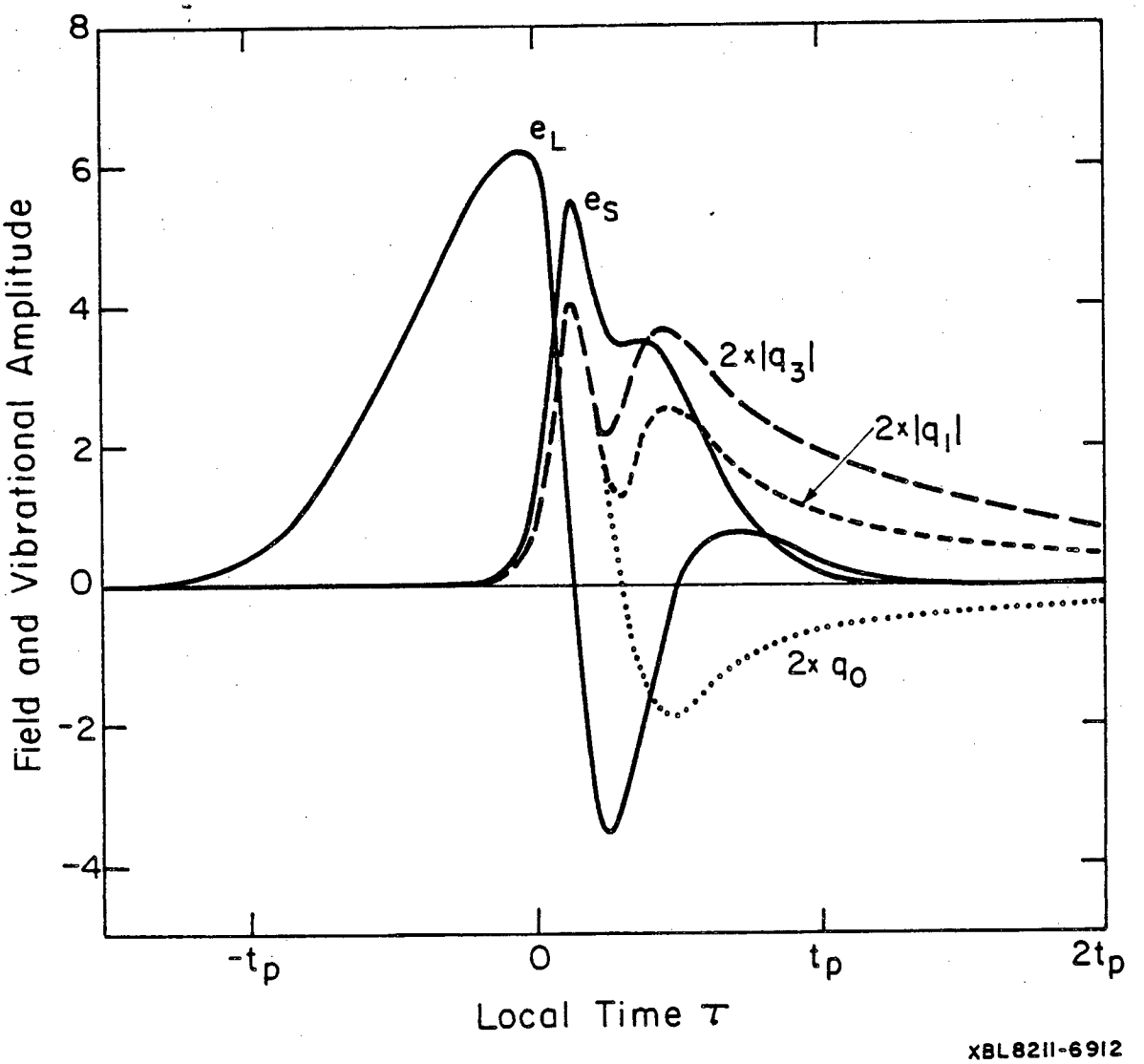
8
6
4
2
0
-2
-4
Field and Vibrational Amplitude
e_L
e_S
$2\times|q_3|$
$2\times|q_1|$
$2\times q_0$
$-t_p$
0
t_p
$2t_p$
Local Time τ
XBL8211-6912

Figure 15

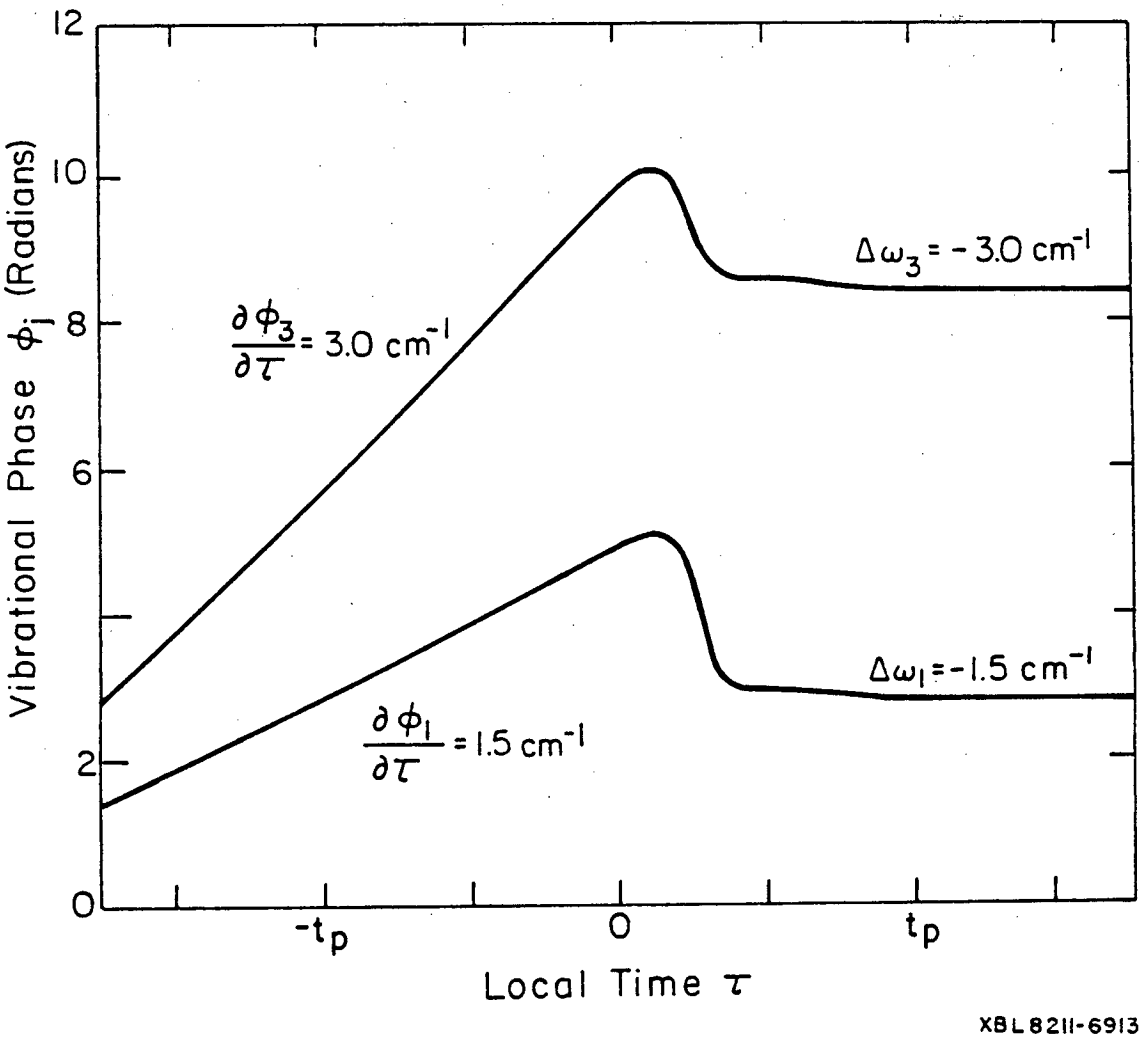
12
10
8
6
2
0
Vibrational Phase ϕ_j (Radians)
$\frac{\partial \phi_3}{\partial \tau} = 3.0\ cm^{-1}$
$\Delta\omega_3 = -3.0\ cm^{-1}$
$\frac{\partial \phi_1}{\partial \tau} = 1.5\ cm^{-1}$
$\Delta\omega_1 = -1.5\ cm^{-1}$
$-t_p$
0
t_p
Local Time τ
XBL8211-6913

Figure 16

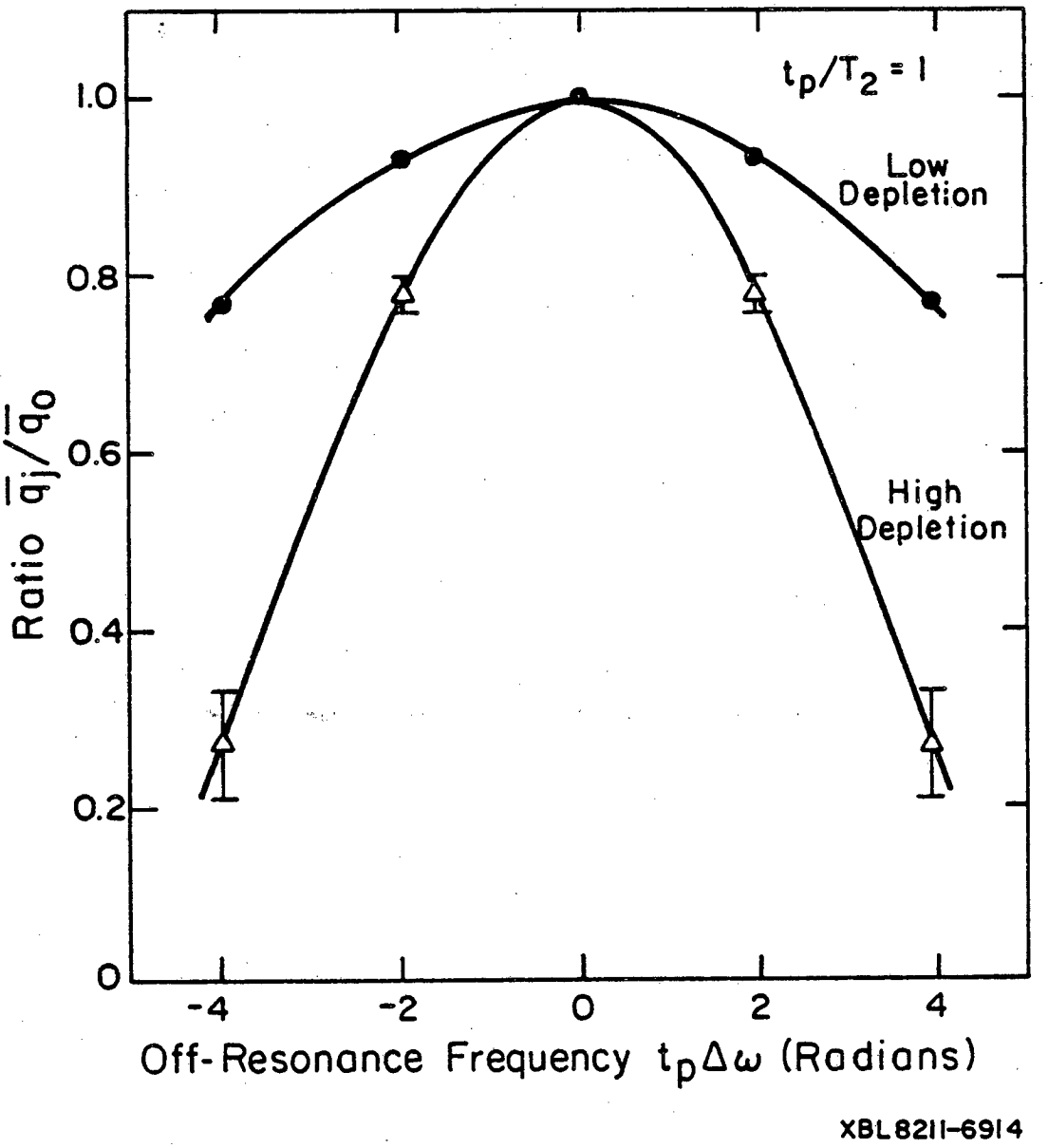
$t_p/T_2 = 1$
Low Depletion
High Depletion
Ratio $\bar{q}_j/\bar{q}_o$
1.0
0.8
0.6
0.4
0.2
0
-4
-2
0
2
4
Off-Resonance Frequency $t_p\Delta\omega$ (Radians)
XBL8211-6914

Figure 17

obtained using separate three-component vibrational linewidths. A close inspection reveals that the selectivity for $\Delta\omega = \pm 1.5$ cm^{-1} is only slightly less and the selectivity of $\Delta\omega = \pm 3.0$ cm^{-1} is slightly more for the five-component compared to the three-component vibrational linewidth. These results demonstrate that the selectivity is not significantly affected by the number of components in the vibrational linewidth.

A. Linewidth with a Continuous Distribution of Vibrational Components

Figures 8 and 17 show that the ratio $\bar{q}_j/\bar{q}_0$ versus $\Delta\omega$ for high laser depletion displays a Gaussian-like distribution. This Gaussian-like distribution, together with the relative number densities, gives rise to an effective lineshape which will be called the effective inhomogeneous lineshape. The effective inhomogeneous linewidth is defined as the frequency width (FWHM) of the population distribution of distinct vibrational oscillators at different frequencies which contribute to the probe Stokes signal. The population distribution is determined by multiplying the ratio $\bar{q}_j/\bar{q}_0$ times the relative number densities. This effective inhomogeneous linewidth is an attempt to generalize to a linewidth with a continuous distribution of vibrational components based on the results for the three and five-component vibrational linewidths.

Using the numerical results for $\bar{q}_j/\bar{q}_0$ versus $\Delta\omega$ and the number density distribution for the five-component vibrational linewidth, an effective inhomogeneous linewidth (FWHM) $\Delta\omega_{INH} \simeq 2.5$ cm^{-1} is determined from the Gaussian-like population distribution. In constrast, if the number densities are equal, an effective inhomogeneous linewidth (FWHM)

$\Delta\omega_{INH}\simeq 4.5\ cm^{-1}$ is determined. The effective inhomogeneous linewidth will contribute to inhomogeneous dephasing and affect the accuracy of the experimental measurement of the homogeneous dephasing time T_2. This will be discussed in Sec. VIII.

VIII. Coherent Stokes Signal Decay Curves

In this section, the total coherent Stokes signals versus delay time are calculated based upon the results of the numerical calculations at $\tau_D=2.5t_p$. The individual coherent Stokes probe amplitudes from each vibrational subgroup at $\tau_D=2.5t_p$ were given by Eq. (20). This expression excludes the relative phase shifts between the different coherent Stokes probe fields. The total coherent Stokes probe amplitude must include the relative phase shifts between the different coherent Stokes probe fields.

The phase shifts between the different coherent Stokes probe fields are determined by $\chi_j(z,\tau)= \Delta\omega_j\tau+\Phi_j(z,\tau)$. For $\tau>t_p$ in low laser depletion, $\Phi_j(\tau)$ reaches the constant value Θ_j as discussed in Sec. IV.A. Thus the total coherent Stokes probe amplitude at $\tau_D=2.5t_p$ measured at z=L is given by:

$$e_{SP}(L,\tau_D) \quad \alpha \quad e_L \sum_j f_j \exp(i(\Delta\omega_j\tau_D+\Theta_j))\ \bar{q}_j(L,\tau_D) \tag{22}$$

Notice that the additional phase shifts which occur in high laser depletion are implicitly included in the traveling sum $\bar{q}_j(L,\tau_D)$.

The total coherent Stokes probe amplitude for delay times $\tau>\tau_D$ must include both the time-dependent phase shifts resulting from $\Delta\omega_j$

frequency mismatch and homogeneous dephasing decay. For $\tau \geq \tau_D$, the total phase for the off-resonant coherent Stokes probe amplitude relative to the resonant coherent Stokes probe amplitude is accounted for by $\chi_j(\tau)=\Delta\omega_j\tau+\Theta_j$. Homogeneous dephasing decay for $\tau>\tau_D$ is accounted for by introducing $\exp(-(\tau-\tau_D)/T_2)$. Thus the real total coherent Stokes probe amplitude versus time delay for $\tau>\tau_D$ measured at z=L assuming a delta function laser probe pulse is given by:

$$e_{SP}(L,\tau) \alpha e_L \exp(-(\tau-\tau_D)/T_2) \times \sum_j f_j \bar{q}_j(L,\tau_D) \cos(\Delta\omega_j\tau+\Theta_j) \quad (23)$$

Experimentally, the coherent Stokes probe intensity, e_S^2, is measured. In addition, actual experimental probe Stokes decay curves are generated by laser probe pulses with a finite pulse width. Thus the coherent Stokes probe intensity versus delay times $\tau' \geq \tau_D$ is given by the convolution:

$$e_{SP}^2(L,\tau') \alpha \int_{\tau_D}^{\tau'} d\tau \left[e_L(\tau-\tau') \exp(-(\tau-\tau_D)/T_2) \times \left(\sum_j f_j \bar{q}_j(L,\tau_D) \cos(\Delta\omega_j\tau_D+\Theta_j)\right) \right]^2 \quad (24)$$

A. Results

Using the discrete numerical equivalent of Eq. (24), coherent Stokes signals versus delay times were calculated based upon the numerical results at $\tau_D=2.5t_p$. Assuming a delta function laser probe pulse, coherent probe Stokes signals in both high and low laser depletion for the three-component vibrational linewidths with T_2=7 psec

and $\Delta\omega$=±1.5, ±3.0 and ±4.5 cm^{-1} are shown in Figs. 18(a)-18(c), respectively. These linewidths were discussed in Sec. VI.A. The differences between high and low laser depletion are dramatically apparent. The straight dashed lines give ideal exponential ($T_2/2$) decay. Notice the slower oscillations for the smaller $\Delta\omega$ values.

Figures 18(a')-18(c') show the coherent Stokes probe signals in high laser depletion generated using a 7 psec (FWHM) Gaussian laser probe pulse for the same three-component linewidths with T_2=7 psec and $\Delta\omega$=±1.5, ±3.0 and ±4.5 cm^{-1}, respectively. The beats observed for $\Delta\omega$=±3.0 and ±4.5 cm^{-1} in high laser depletion in Figs. 18(b) and 18(c) are smeared out in Figs. 18(b') and 18(c'). This occurs because the widths of the beat modulations for $\Delta\omega$=±3.0 and ±4.5 cm^{-1} are less than t_p=7 psec. On the other hand, the beats observed for $\Delta\omega$=1.5 cm^{-1} in Fig. 18(a) are not smeared out in Fig. 18(a') because the width of the beat modulation is longer than t_p=7 psec.

Figure 19 for T_2=7 psec shows the coherent probe Stokes signal for the five-component vibrational linewidth with T_2=7 psec and $\Delta\omega$=±1.5 and ±3.0 cm^{-1} in high laser depletion. This signal was calculated using a 7 psec (FWHM) Gaussian laser probe pulse based on the numerical results at τ_D for the five-component vibrational linewidth discussed in Sec. VII. Recall from Fig. 17 that the ratio $\bar{q}_j/\bar{q}_0$ is quite high for $\Delta\omega_j$=±1.5 cm^{-1}. In addition, the homogeneous dephasing time T_2 is long in comparison to the effective inhomogeneous dephasing time calculated from the effective inhomogeneous linewidth $\Delta\omega_{INH}\simeq$2.5 cm^{-1}. Consequently, the effective inhomogeneous distribution significantly contributes to the probe Stokes signal decay.

Figure 19 also shows the coherent probe Stokes signals calculated

FIG. 18. Coherent Stokes signals versus delay times. (a)-(c) High and low laser depletion signals calculated using a delta function laser probe pulse for the three-component vibrational linewidths with $\Delta\omega=\pm1.5$, ±3.0 and ±4.5 cm^{-1}. Exponential ($T_2/2$) decay is indicated by the straight dashed line. (a')-(c') High laser depletion signals calculated using a 7 psec (FWHM) Gaussian laser probe pulse for the same three-component vibrational linewidths with $\Delta\omega=\pm1.5$, ±3.0 and ±4.5 cm^{-1}.

FIG. 19. Coherent Stokes signals versus delay times for various T_2 dephasing times for the five-component vibrational linewidth in high laser depletion. Exponential decay ($T_2/2$) decay is indicated by the straight dashed line.

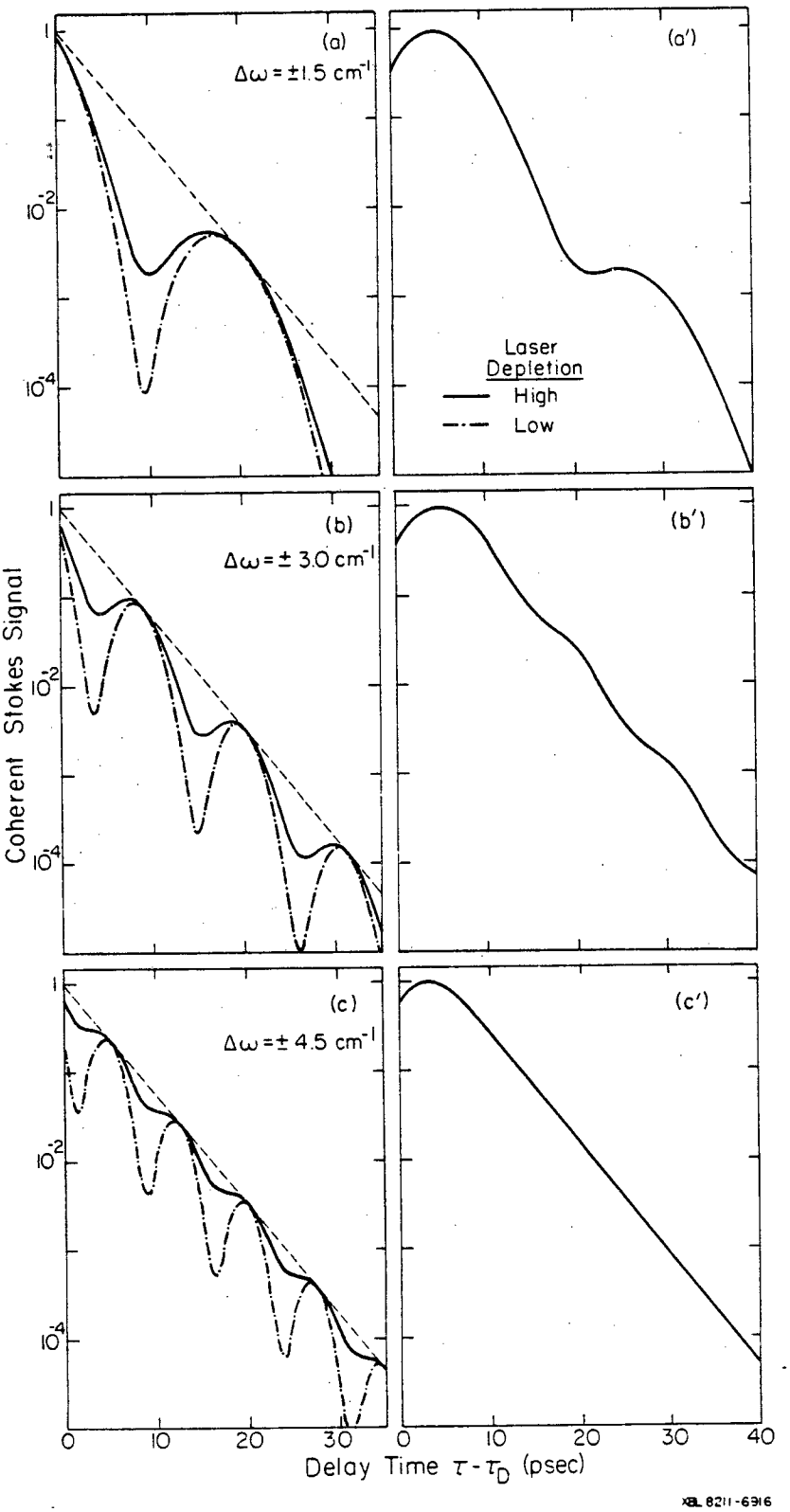
(a)
Δω = ±1.5 cm⁻¹
(a')
Laser
Depletion
High
Low
(b)
Δω = ± 3.0 cm⁻¹
(b')
(c)
Δω = ± 4.5 cm⁻¹
(c')
Coherent Stokes Signal
1
10⁻²
10⁻⁴
0
10
20
30
40
Delay Time τ - τD (psec)
XBL 8211-6916

Figure 18

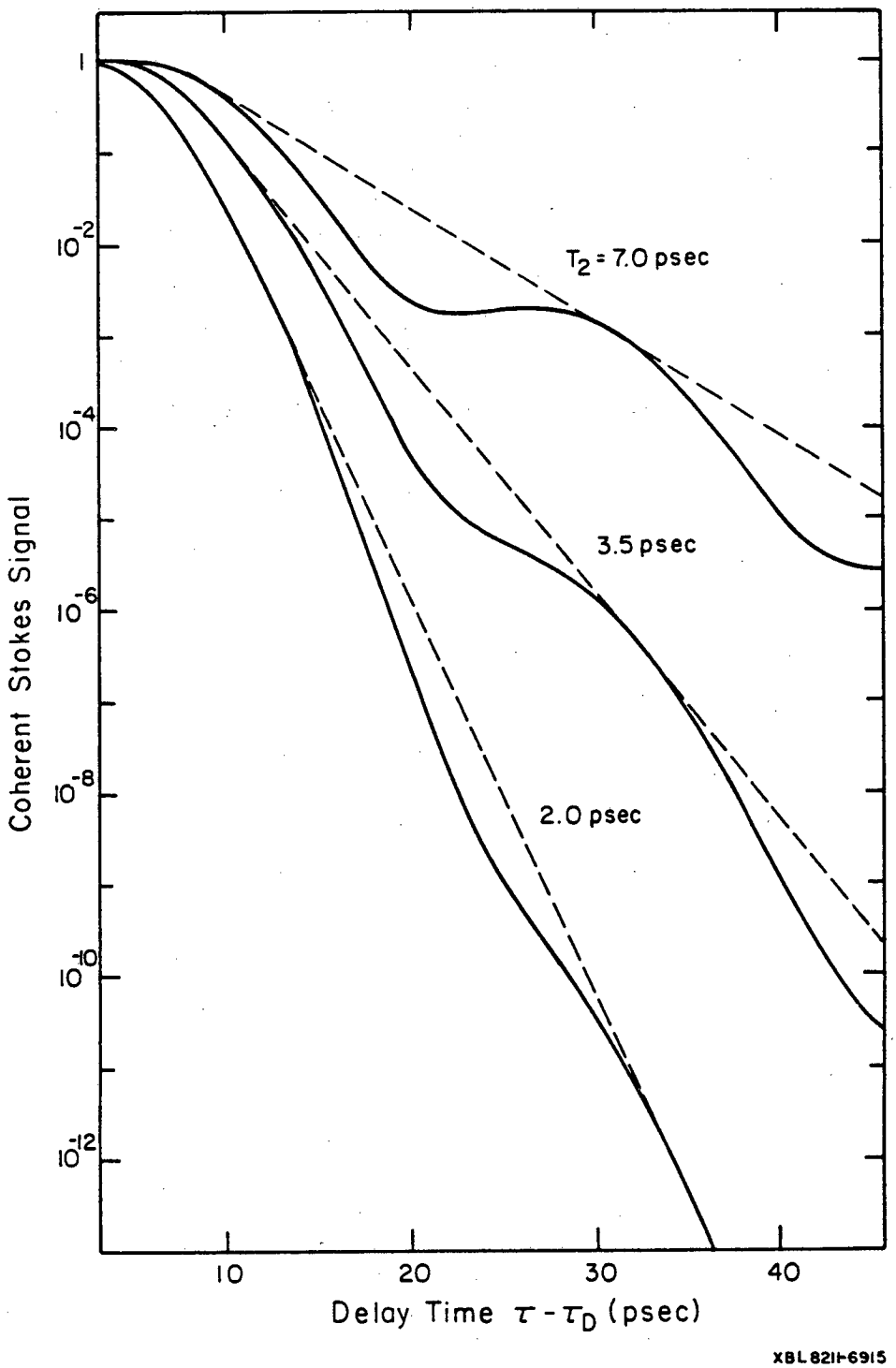
1
10^{-2}
10^{-4}
10^{-6}
10^{-8}
10^{-10}
10^{-12}
Coherent Stokes Signal
T_2 = 7.0 psec
3.5 psec
2.0 psec
10
20
30
40
Delay Time $\tau - \tau_D$ (psec)
XBL821I-6915

Figure 19

for T_2=3.5 psec and T_2=2.0 psec using a 7 psec (FWHM) Gaussian laser probe pulse and the same five-component vibrational linewidth selectivities that were used for T_2=7 psec. These results illustrate that the probe pulse does not obscure the ($T_2/2$) decay of the probe Stokes signal decay curves for ($T_2/2$) decays much faster than the probe pulse width.

For the faster T_2 dephasing times, Fig. 19 demonstrates that the homogeneous decay competes more effectively with the inhomogeneous decay caused by destructive interference. This result illustrates that the off-resonant vibrational components need a certain time period after the excitation process to precess 180° and cause pronounced destructive interference in the probe Stokes signal decay curve. For the faster T_2 dephasing times, the homogeneous dephasing dominates the probe Stokes signal decay curve before the off-resonant vibrational components can influence the decay curve. Likewise, viewed in the frequency domain, the homogeneous linewidth determines the homogeneous decay time and the effective inhomogeneous linewidth determines the effective inhomogeneous decay time. The greater the ratio of the homogeneous linewidth to the effective inhomogeneous linewidth, the more the coherent probe Stokes signal approaches ($T_2/2$) exponential decay.

IX. Vibrational Dephasing Experiments in the High Laser Depletion Regime

The above results demonstrate that selective vibrational dephasing experiments are possible using transient stimulated Raman excitation and coherent Stokes Raman probing. High laser depletion is required in the excitation process. A probe pulse collinear with the excitation pulse

is required in the probing process.

The results from Secs. VI.A-C. indicate that selectivity measured by the ratio $\bar{q}_j/\bar{q}_0$ is determined by $\Delta\omega$ and t_p, but not T_2. The results show that selectivity is approximately determined by $(t_p/T_2)X(\Delta\omega T_2)=t_p\Delta\omega$. On the other hand, the experimental accuracy measured by the coherent probe Stokes signal is also dependent upon the ratio of the homogeneous linewidth versus the effective inhomogeneous linewidth. The larger this ratio, the more closely the probe Stokes signal decay curve approaches $(T_2/2)$ exponential decay.

For t_p=7 psec and high laser depletion, the results for the five-component vibrational linewidth generalized to a continuous distribution yield an effective inhomogeneous linewidth (FWHM) $\Delta\omega_{INH}\simeq 2.5$ cm^{-1}. This effective inhomogeneous linewidth will lead to an inhomogeneous dephasing contribution in the coherent Stokes signal decay curve according to Eq. (24). Consequently, a Stokes signal decay curve faster than the pure homogeneous $(T_2/2)$ decay will be observed.

The experimental accuracy is measured by how well the probe Stokes signal decay curve approaches $(T_2/2)$ exponential decay. Given a Gaussian effective inhomogeneous linewidth (FWHM) $\Delta\omega_{INH}\simeq 2.5$ cm^{-1} and a Lorentzian homogeneous linewidth (FWHM) $\Delta\omega_H(\text{cm}^{-1})=1/c\pi T_2$, we can estimate the accuracy to which the experimentally determined decay τ_{exp} will measure homogeneous dephasing decays $(T_2/2)$ in vibrational linewidths which are inhomogeneously broadened. For homogeneous dephasing times $T_2\leq 4.4$ psec, the estimated accuracy of the experimental measurement is $\tau_{exp}\geq 0.6(T_2/2)$. The experimental accuracy progressively increases as the dephasing time decreases, in agreement with the behavior for the five-component linewidth discussed in Sec. VIII.A. For

homogeneous dephasing times $T_2 \leq 3.2$ psec, the estimated accuracy of the experimental measurement increases to $\tau_{exp} \geq 0.7(T_2/2)$. For homogeneous dephasing times $T_2 \leq 2.3$ psec, the estimated accuracy of the experimental measurement increases further to $\tau_{exp} \geq 0.8(T_2/2)$. For $T_2 \leq 1.4$ psec, the estimated accuracy reaches $\tau_{exp} \geq 0.9(T_2/2)$. These results indicate that dephasing times $T_2 \leq 4.4$ psec can be measured to a high level of accuracy in inhomogeneously broadened vibrational linewidths using collinear coherent Stokes probe scattering.

A typical vibrational dephasing time in a liquid at P=1 Atm. is $T_2 \simeq 3$ psec [1,6]. Assuming this dephasing time in an inhomogeneously broadened vibrational linewidth, the experimentally determined decay τ_{exp} will measure the homogeneous dephasing time to an accuracy $\tau_{exp} \simeq 0.7(T_2/2)$. This level of accuracy is certainly capable of detecting differences between various T_2 dephasing times. This may explain the wide range of dephasing times measured in various liquids [1-6].

A. Experimental Evidence for Selectivity

Recent vibrational dephasing experiments discussed in Chap. 5 have been conducted in high laser depletion with laser pulse widths $t_p \simeq 7$psec. These experiments have provided results which corroborate the results of these calculations [10,11]. Briefly, the vibrational dephasing times $T_2/2$ were measured for the symmetric CH_3-stretching vibration in liquid acetonitrile at various temperatures over acetonitrile's entire liquid range at P=1 Atm. Over the same temperature range at P=1 Atm., the corresponding isotropic Raman

linewidths for the symmetric CH_3-stretching vibration are nearly invariant with temperature [11,30].

The decay times from individual measurements at various temperatures were consistently different and reproducible [10,11]. The error bars on the measurements were well within the differences between various temperatures. If this vibrational dephasing experiment conducted in high laser depletion was not selective, the invariant isotropic Raman linewidth versus temperature should have yielded identical decay curves at various temperatures. This was certainly not the case. Different dephasing times were measured at different temperatures, in agreement with vibrational dephasing models [10,11].

X. Summary and Conclusion

A theory for selective vibrational dephasing experiments using transient stimulated Raman scattering in high laser depletion has been developed. The main features of this interpretation are as follows: The stimulated Stokes field grows until the excitation laser field is substantially reduced. When the excitation laser field is depleted, the Stokes field and the vibrational amplitude regenerate a new 180° phase-shifted laser field. The off-resonant vibrational amplitudes then respond to the 180° phase-shifted driving field by changing their phases. This results in changing vibrational phases at different spatial locations in the Raman cell.

The changing vibrational phases and vibrational amplitudes at different spatial locations lead to a substantial reduction in the collinear coherent probe Stokes fields generated by the off-resonant

vibrational amplitudes. This leads to greatly enhanced selectivity for the resonant vibrational amplitude in high laser depletion. The selectivities for the off-resonant vibrational components close to the center frequency are reduced somewhat because their vibrational amplitudes are reduced by the laser regeneration. This process limits the maximum possible selectivity in high laser depletion.

The theoretical selectivity is greatly dependent upon the laser pulse width t_p and the off-resonance magnitude $\Delta\omega$, but only weakly dependent upon the dephasing time T_2. The accuracy of the experimental measurement of the homogeneous dephasing time T_2 is also dependent upon the competition between the homogeneous and the effective inhomogeneous dephasing times.

Using a laser pulse width t_p=7 psec, the calculations indicate that dephasing times $T_2 \leq 4.4$ psec can be measured to a high level of accuracy in vibrational linewidths which are inhomogeneously broadened. These results demonstrate that transient stimulated Raman scattering techniques can still be used to study vibrational dephasing dynamics in inhomogeneously broadened vibrational linewidths. The contradictions in previous vibrational dephasing studies by Kaiser and coworkers [1-3,7-9] may be explained by the selectivity differences in the high and low laser depletion regimes.

References

1. A. Laubereau and W. Kaiser, Rev. Mod. Phys. 50, 607(1978).

2. A. Laubereau, G. Wochner and W. Kaiser, Phys. Rev. 13A, 2212(1976); Opt. Commun. 17, 91(1976).

3. A. Laubereau, G. Wochner and W. Kaiser, Chem. Phys. 28, 363(1978).

4. C.B. Harris, H. Auweter and S.M. George, Phys. Rev. Lett. 44, 737(1980).

5. C.B. Harris, H. Auweter and S.M. George, in Picosecond Phenomena II, ed. by R.M. Hochstrasser, W.Kaiser and C.V. Shank, Springer Ser. Chem. Phys. 14 (Springer-Verlag, Berlin, Heidelberg, New York, 1980) p.151.

6. S.M. George, H. Auweter and C.B. Harris, J. Chem. Phys. 73, 5573(1980).

7. W. Zinth, H.J. Polland, A. Laubereau and W. Kaiser, Appl. Phys. B26, 77(1981).

8. W. Zinth, A. Laubereau and W. Kaiser, Opt. Commun. 26, 457(1978).

9. D. von der Linde, A. Laubereau and W. Kaiser, Phys. Rev. Lett. 26,954(1971).

10. S.M. George, A.L. Harris, M. Berg and C.B. Harris, in Picosecond Phenomena III, ed. by K.B. Eisenthal, R.M. Hochstrasser, W. Kaiser and A. Laubereau, Springer Ser. Chem. Phys. 23(Springer-Verlag, Berlin, Heidelberg, New York, 1982) p.196.

11. S.M. George, A.L. Harris, M. Berg and C.B. Harris, (submitted to J. Chem. Phys.).

11a. D. Ben-Amotz, S.M. George and C.B. Harris, (submitted to Chem. Phys. Lett.).

12. S.M. George and C.B. Harris, Rev. Sci. Inst. 52,852(1981).

13. M.A. Lewis and J.T. Knudtson, Chem. Phys. 55, 73(1981).

14. R.L. Carman, F. Shimizu, C.S. Wang and N. Bloembergen, Phys. Rev. 2A, 60(1970).

15. M. Maier, W. Kaiser and J.A. Giordmaine, Phys. Rev. 177, 580(1969).

16. S.A. Akhmanov, A.S. Chirkin, K.N. Drabovich, A.I. Kovrigin, R.V. Khokhlov and A.P. Suchorukov, IEEE J. Quantum Electron. QE-4, 598(1968).

17. G.I. Kachen, Ph.D. thesis, UCRL-51753, Lawrence Livermore Laboratory, Univ. of Calif., Livermore, Calif. 94550.

18. S.A. Akhmanov, K.N. Drabovich, A.P. Sukhowukov and A.S. Chirkin, JETP 32, 266(1971).

19. The equation transformations and simplifications were suggested by David Eimerl, Lawrence Livermore Laboratory, Univ. of Calif., Livermore, Calif., 94550.

20. G. Dahlquist and A. Bjorck, Numerical methods(Prentice-Hall, Inc., Englewood Cliffs, New Jersey, 1974).

21. This technique was suggested by John H. Bolstad, Lawrence Berkeley Laboratory, Univ. of Calif., Berkeley, Calif. 94720.

22. G.D. Smith, Numerical Solution of Partial Differential Equations: Finite Difference Methods(Oxford University Press, Oxford, 1978).

23. This Manley-Rowe constant was determined using ω_L=18,846 cm^{-1} and ω_S=15,913 cm^{-1}, the values for transient stimulated Raman scattering from the symmetric CH_3-stretching vibration in acetonitrile using laser excitation at λ_L=5306 Å.

24. G.I. Kachen and W.H. Lowdermilk, Phys. Rev. 14A, 1472(1976).

25. W.H. Lowdermilk and G.I. Kachen, Appl. Phys. Lett. 27, 133(1975).

26. K. Daree, Opt. and Quant. Elect.7, 263(1975).

27. N. Tan-no, T. Shirahata and K. Yokoto, Phys. Rev. 12A, 159(1975).

28. J.N. Elgin and T.B. O'Hare, J. Phys. B: Atom. Molec. Phys. 12, 159(1979).

29. A.P. French, Vibrations and Waves (W.W. Norton and Comp., New York, 1971).

30. J. Yarwood, R. Arndt and G.Doge, Chem. Phys. 25, 387(1977).

Chapter 3: Inhomogeneous Broadening of Vibrational Linewidths in Polyatomic Liquids

I. Introduction

Until recently, there has been no evidence to suggest that non-polar or non-hydrogen-bonded liquids were significantly inhomogeneously broadened and consequently most vibrational dephasing theories and studies have neither made this distinction nor addressed this possiblity. In a recent paper [1], however, we observed that even very simple non-hydrogen-bonded liquids can be significantly inhomogeneously broadened. This immediately poses an important question. Is inhomogenoeus broadening in non-hydrogen-bonded liquids general, and if so, what is the physical origin of the broadening?

In order to study the inhomogeneous broadening of the symmetric CH_3-stretching liquid vibrational linewidths in a variety of liquids, isotropic spontaneous Raman scattering studies and selective excite-and-probe vibrational dephasing experiments [2] were performed. The selective vibrational dephasing experiments allow the homogeneous linewidth of a single, distinct vibrational isochromat to be determined in a vibrational lineshape which may be composed of a continuous frequency distribution of vibrational isochromats established by inhomogeneous broadening processes.

Since spontaneous Raman scattering arises from all the vibrational isochromats in the distribution, isotropic spontaneous Raman scattering yields a lineshape which arises from the convolution of both the

homogeneous and inhomogeneous broadening lineshape functions. Consequently, the inhomogeneous broadening lineshape function can be obtained by deconvoluting the homogeneous lineshape function, determined by the picosecond experiment, from the isotropic spontaneous Raman lineshape function. Thus the inhomogeneous broadening of vibrational lineshapes in liquids can be studied and related to structural and/or dynamic properties of the liquid.

In this chapter the generality of inhomogeneous broadening of symmetric CH_3-stretching vibrational linewidths in non-hydrogen-bonded liquids is established. A simple model is proposed for the broadening's magnitude which is based on the width of the distribution of local number densities in the liquid. In addition, a stochastic lineshape theory is developed which treats homogeneous and inhomogeneous broadening simultaneously in terms of one vibrational correlation function.

II. Experimental

The symmetric CH_3-stretching vibrations studied in this experiment were coherently excited by transient stimulated Raman scattering [3]. Coherent excitation establishes a macroscopic coherent superposition of vibrational states v=0 and v=1 in a group of symmetric CH_3-stretching vibrations, i.e., $\rho_{01}(t)$, an off-diagonal density matrix element in the symmetric CH_3-stretching vibrational oscillator basis set. The coherently excited symmetric CH_3-stretching vibrations were then probed using collinear coherent Stokes Raman scattering [4,5]. The macroscopic coherent superposition of vibrational states v=0 and v=1 oscillates with

a well-defined phase and produces a macroscopic modulation of the optical refractive index at the vibrational frequency through the coupling parameter $\partial\alpha/\partial q$, the change of polarizability, α, with vibrational coordinate, q. The incoming probe pulse scatters off this modulated refractive index producing sidebands, i.e., beat frequencies shifted by the vibrational frequency to higher and lower frequencies. The selectivity of the collinear coherent Stokes scattering is discussed in Chap. 2.

The details of the excite-and-probe vibrational dephasing experiments are discussed in Chap. 5. In constrast to the experiments in Chap. 5, which employ an electronic pulse selector, the following experiments were performed using a spark gap [6] to select single picosecond pulses from the rising edge of pulse trains emitted from a stabilized, passively mode-locked Nd:glass laser. In general, the spark gap was much less reliable and reproducible than the electronic pulse selector. In addition, the pulses were compressed by passage through a 1 cm cell of Eastman Kodak dye #9860 with an O.D.=3.0 at 10,600 Å. The experiments in Chap. 5 were performed using O.D.=1.0. After installing the electronic pulse selector, this change in O.D. was necessary in order to obtain pulses with rapid rising edges equivalent to the pulses used in this chapter.

Isotropic spontaneous Raman lineshapes were obtained using a standard Argon ion laser and a double monochromator scattering unit. The polarized Stokes scattering lineshapes were essentially the same as the isotropic lineshapes because of the very small depolarization factor for the symmetric CH_3-stretching vibrations in the liquids studied.

III. Results

Figure 1 shows the coherently scattered Stokes signal as a function of probe pulse delay for the symmetric CH_3-stretching vibration in methanol and ethanol. The error bars on the data points represent the standard deviation of the individual coherent Stokes signals. On the average, the observed dephasing times were $T_2/2=1.2\pm0.5$ psec for methanol and 1.25 ± 0.5 psec for ethanol. The isotropic Raman lineshapes of the same vibrations are also shown in Fig. 1. From the measured dephasing times, we calculate the corresponding homogeneous Lorentzian lineshapes which are also drawn in Fig. 1. From these superimposed lineshapes the inhomogeneous broadening in these two hydrogen-bonded liquids can easily be visualized.

Figure 2 shows the coherently scattered Stokes signal as a function of probe pulse delay for the symmetric CH_3-stretching vibration in acetone and methyl sulfide. On the average, the observed dephasing times were $T_2/2=1.5\pm0.5$ psec for acetone and 1.9 ± 0.5 psec for methyl sulfide. The isotropic Raman lineshapes and homogeneous Lorentzian lineshapes corresponding to the measured dephasing times are also shown in Fig. 2. The superimposed lineshapes display significant inhomogeneous broadening for both of these non-hydrogen-bonded liquids. Two more examples of non-hydrogen-bonded liquids are given in Fig. 3 for trichloroethane and acetonitrile. There was no observable broadening within the error limits in trichloroethane, which is consistent with the results of Laubereau et al. [7,8].

The average experimental dephasing times, calculated homogeneous linewidths, and isotropic Raman linewidths for all the liquids studied

FIG. 1 Experimental data for the symmetric CH_3-stretching vibration in methanol and ethanol. Coherently scattered Stokes signal as a function of probe pulse delay in (a) methanol and (c) ethanol. Isotropic Raman lineshapes and homogeneous Lorentzian lineshapes calculated from the measured dephasing times in (b) methanol and (d) ethanol.

FIG. 2 Experimental data for the symmetric CH_3-stretching vibration in acetone and methyl sulfide. Coherently scattered Stokes signal as a function of probe pulse delay in (a) acetone and (c) methyl sulfide. Isotropic Raman lineshapes and homogeneous Lorentzian lineshapes calculated from the measured dephasing times in (b) acetone and (d) methyl sulfide.

FIG. 3 Experimental data for the symmetric CH_3-stretching vibration in trichloroethane and acetonitrile. Coherently scattered Stokes signal as a function of probe pulse delay in (a) trichloroethane and (c) acetonitrile. Isotropic Raman lineshapes and homogeneous Lorentzian lineshapes calculated from the measured dephasing times in (b) trichloroethane and (d) acetonitrile.

TABLE 1. Experimental dephasing times, calculated homogeneous linewidths, isotropic Raman linewidths and inhomogeneous broadening linewidths for the symmetric CH_3-stretching vibrations in the various liquids studied.

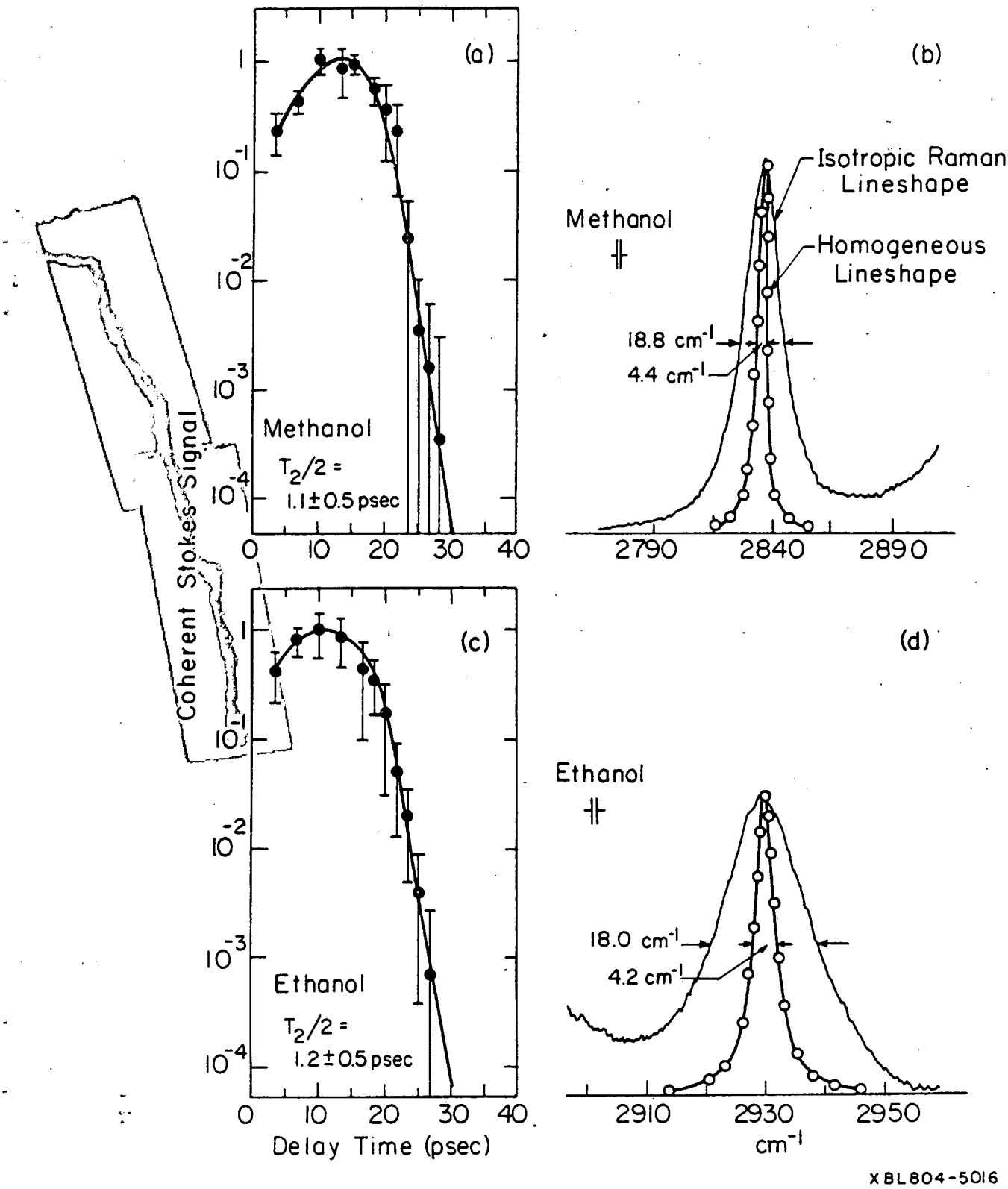
(a)
Methanol
$T_2/2$ =
1.1±0.5 psec
(b)
Isotropic Raman Lineshape
Homogeneous Lineshape
Methanol
18.8 cm^{-1}
4.4 cm^{-1}
2790
2840
2890
(c)
Ethanol
$T_2/2$ =
1.2±0.5 psec
Coherent Stokes Signal
Delay Time (psec)
(d)
Ethanol
18.0 cm^{-1}
4.2 cm^{-1}
2910
2930
2950
cm^{-1}
XBL804-5016

Figure 1

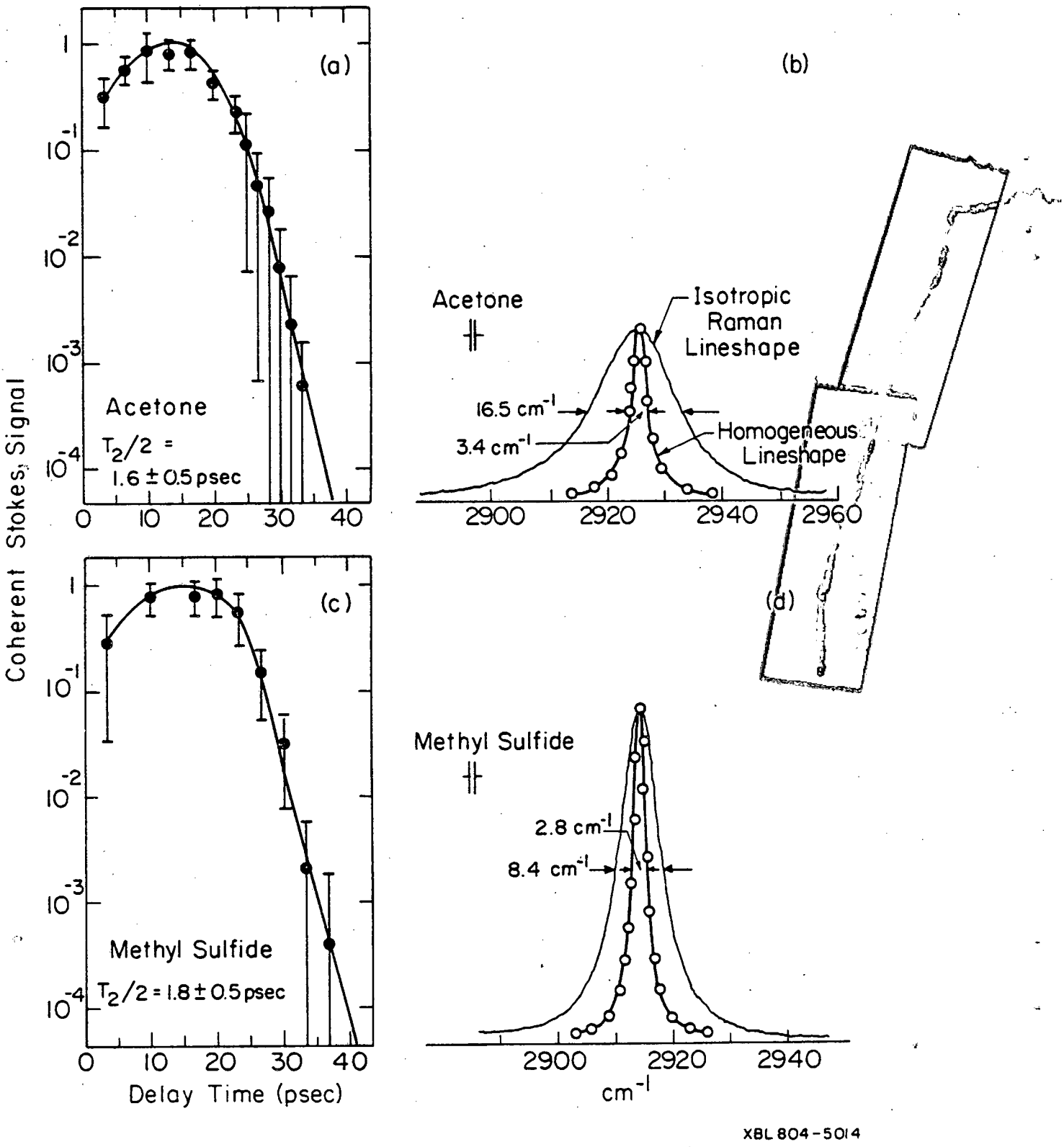
(a)
Acetone
$T_2/2$ =
1.6 ± 0.5 psec
(b)
Acetone
Isotropic
Raman
Lineshape
16.5 cm^{-1}
3.4 cm^{-1}
Homogeneous
Lineshape
2900
2920
2940
2960
(d)
(c)
Methyl Sulfide
$T_2/2$ = 1.8 ± 0.5 psec
Coherent Stokes Signal
Delay Time (psec)
Methyl Sulfide
2.8 cm^{-1}
8.4 cm^{-1}
2900
2920
2940
cm^{-1}
XBL 804-5014

Figure 2

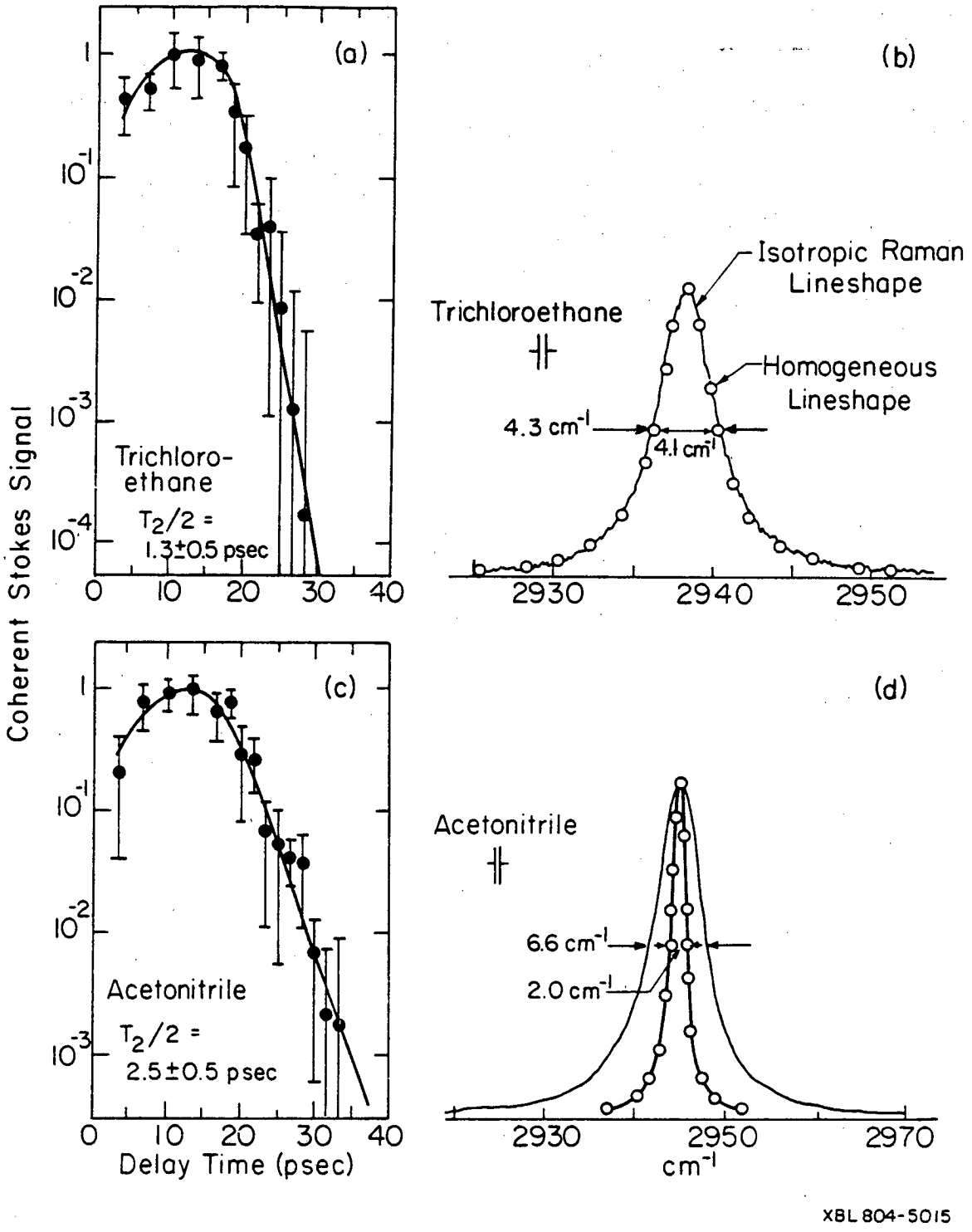
(a)
Trichloro-
ethane
$T_2/2$ =
1.3±0.5 psec
(b)
Trichloroethane
Isotropic Raman
Lineshape
Homogeneous
Lineshape
4.3 cm^{-1}
4.1 cm^{-1}
2930
2940
2950
(c)
Acetonitrile
$T_2/2$ =
2.5±0.5 psec
Coherent Stokes Signal
Delay Time (psec)
(d)
Acetonitrile
6.6 cm^{-1}
2.0 cm^{-1}
2930
2950
2970
cm^{-1}
XBL 804-5015

Figure 3

TABLE 1

Molecule	$\omega(cm^{-1})$	Average Experimental T_2(psec)	Calculated Homogeneous $\Delta\omega(cm^{-1})$	Isotropic Raman $\Delta\omega(cm^{-1})$	Gaussian Inhomogeneous $\Delta\omega(cm^{-1})$
1,1,1-Trichloroethane	2938.5	2.6	4.1	4.3	0.9
Methyl Iodide	2948	2.4	4.4	5.0	1.7
Acetonitrile	2945	5.4	2.0	6.6	5.5
Methyl Sulfide	2913.5	3.8	2.8	8.4	6.8
Dimethyl Sulfoxide	2914.5	1.4	7.6	11.8	6.9
Acetic Anhydride	2942.5	2.2	4.8	16.8	14.1
Acetone	2925	3.0	3.5	16.5	14.6
Methyl Formate	2961	2.2	4.8	17.5	14.8
Pentane	2877	2.7	3.9	$\simeq$17	$\simeq$14.8
Ethanol	2929	2.5	4.2	18.0	15.6
Methanol	2836	2.4	4.4	18.8	16.3

are compiled in Table 1. We found that symmetric CH_3-stretching vibrational linewidths in non-hydrogen-bonded liquids are inhomogeneously broadened to various degrees [9]. Thus the symmetric CH_3-stretching vibrational linewidths of non-hydrogen-bonded liquids are not motionally narrowed, presumably because the liquid site relaxation times are much longer than earlier predictions.

IV. Inhomogeneously Broadened Lineshape Analysis

If the liquid vibrational band is inhomogeneously broadened, the lineshape observed by isotropic spontaneous Raman scattering arises from the convolution of two independent lineshape functions: $L(\omega)$, the homogeneous lineshape function which is Lorentzian; and $G(\omega)$, the inhomogeneous broadening lineshape function. The resultant vibrational lineshape function, $I(\omega)$, can be written as a convolution integral:

$$I(\omega) = \int_{-\infty}^{\infty} L(\omega')G(\omega-\omega')\, d\omega' \qquad (1)$$

Since isotropic spontaneous Raman scattering gives the lineshape for $I(\omega)$ and the picosecond measurement gives the homogeneous Lorentzian lineshape, $L(\omega)$, the inhomogeneous broadening lineshape, $G(\omega)$, can be obtained by deconvoluting the isotropic spontaneous Raman and homogeneous Lorentzian lineshapes. Unfortunately, $I(\omega)$ is not easily represented by a simple functional form. In most cases, however, $I(\omega)$, the isotropic spontaneous Raman scattering lineshape, is somewhere in between a Gaussian and Lorentzian lineshape.

One well-studied lineshape which is intermediate between a Gaussian

and a Lorentzian is a Voigt profile, which is a convolution of independent Gaussian and Lorentzian lineshapes [10,11]. If the isotropic spontaneous Raman lineshape is assumed to be a Voigt profile, which is usually the case, and the inhomogeneous broadening lineshape is assumed to be a Gaussian [12], the problem of deconvolution is greatly simplified. Numerical deconvolution is not necessary because if the linewidths for the Voigt and Lorentzian lineshapes are known, the linewidth for the Gaussian lineshape can be determined from numerical Voigt profile tables [11]. The linewidths for $G(\omega)$, the inhomogeneous broadening lineshape function, were determined after making the above assumptions and are listed in Table 1.

Several general observations can be made about the data in Table 1. First, the homogeneous widths are rather uniform relative to the inhomogeneous widths. Second, even non-polar liquids such as pentane are highly inhomogeneously broadened. Moreover, although the hydrogen-bonded liquids display the greatest inhomogeneous broadening, they do not form a class by themselves. Several non-hydroden-bonded liquids are broadened almost as much as the hydrogen-bonded liquids.

V. Discussion

After determining that the inhomogeneous broadening lineshape linewidths varied from 1 to 15 cm^{-1}, attempts were made to correlate the inhomogeneous broadening linewidths with various liquid parameters. Initally, we assumed that the inhomogeneous broadening was determined by a distribution of environmental sites which establishes a certain continuous frequency distribution of vibrational isochromats. This

assumption is supported by studies on hydrogen-bonded liquids [13,14] which suggest that the attractive portion of the intermolecular potential, viz., the hydrogen bond, causes long range correlations in the intermolecular forces and creates a distribution of environmental sites which establishes a distribution of vibrational frequencies. Furthermore, recent picosecond experiments have demonstrated that hydrogen-bonded liquids are severely inhomogeneous broadened [4], presumably because the attractive portion of the intermolecular potential causes long-range correlations which enable environmental sites to persist for >5 psec.

Because the attractive portion of the intermolecular potential is implicated in the inhomogeneous broadening of hydrogen-bonded liquids, attempts were made to correlate the inhomogeneous broadening in non-hydrogen-bonded liquids with various liquid intermolecular attraction parameters. No correlation was observed, however, with: Trouton's ratio; B.P./M.W. (Boiling Point/Molecular Weight); the molecular dipole moment; the hydrogen bonding parameter; or the polarizability. In addition, no correlation was observed with the Kirkwood dipole correlation factor [15]. On the other hand, the ultrasonic absorption constant displayed a slight correlation with the inhomogeneous broadening [16]. The correlations of these liquid attraction parameters and the inhomogeneous broadening have been discussed in detail [17].

Since the inhomogeneous broadening linewidths did not correlate with liquid attraction parameters, attempts were made to find a correlation with other liquid parameters. The inhomogeneous broadening does tend to scale with the molecule's deviation from spherical symmetry. The simplest, most spherical molecules, trichloroethane and

methyl iodide, are nearly homogeneous, whereas the longest, least spherical molecules, methyl formate and pentane are extremely inhomogeneous. This suggests that the molecules's shape determines how the molecule can pack with other molecules, which may influence the number of environmental sites that are formed in the liquid [18].

A. Correlation with Liquid's Local Number Density Distribution Width

A correlation was observed between the inhomogeneous broadening linewidth and the liquid's free volume [19]. The correlation is shown in Figure 4. This correlation suggests that the liquid's entropy participates in establishing the number of environmental sites in the liquid since the liquid's entropy may cause the liquid's free volume to distribute itself in order to maximize the number to interactions of molecules with other molecules and/or free space. In such a case, the number of different environmental sites in the liquid would be functionally dependent upon the liquid's free volume.

Free volume alone does not elucidate the distribution of values in a liquid parameter which may give rise to a distribution of environmental sites. The liquid's free volume, however, is closely related to the distribution width of the liquid's local number density through the isothermal compressibility. Since a distribution of local number densities could conceivably create a distribution of distinct vibrational frequencies, this parameter will be derived and discussed in detail.

Following the standard treatment [20,21], we treat the liquid as an open, isothermal system of volume V, and apply the method of most

FIG. 4. Graph of the inhomogeneous broadening linewidth versus the free volume percentage in the liquid.

FIG. 5. Graph of the inhomogeneous broadening linewidth versus the width of the distribution of local number densities in the liquid.

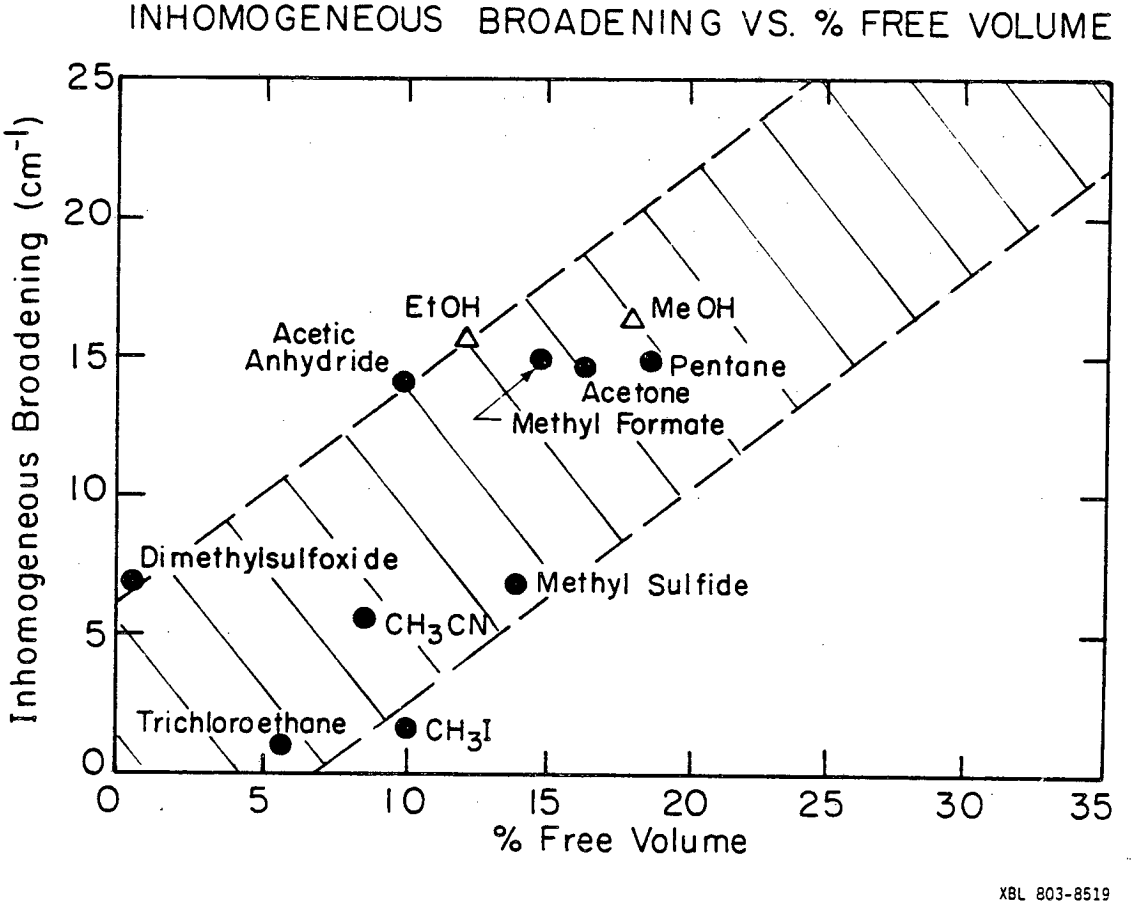
INHOMOGENEOUS BROADENING VS. % FREE VOLUME
Inhomogeneous Broadening (cm^{-1})
% Free Volume
0
5
10
15
20
25
30
35
EtOH
MeOH
Acetic Anhydride
Pentane
Acetone
Methyl Formate
Dimethylsulfoxide
Methyl Sulfide
CH_3CN
Trichloroethane
CH_3I
XBL 803-8519

Figure 4

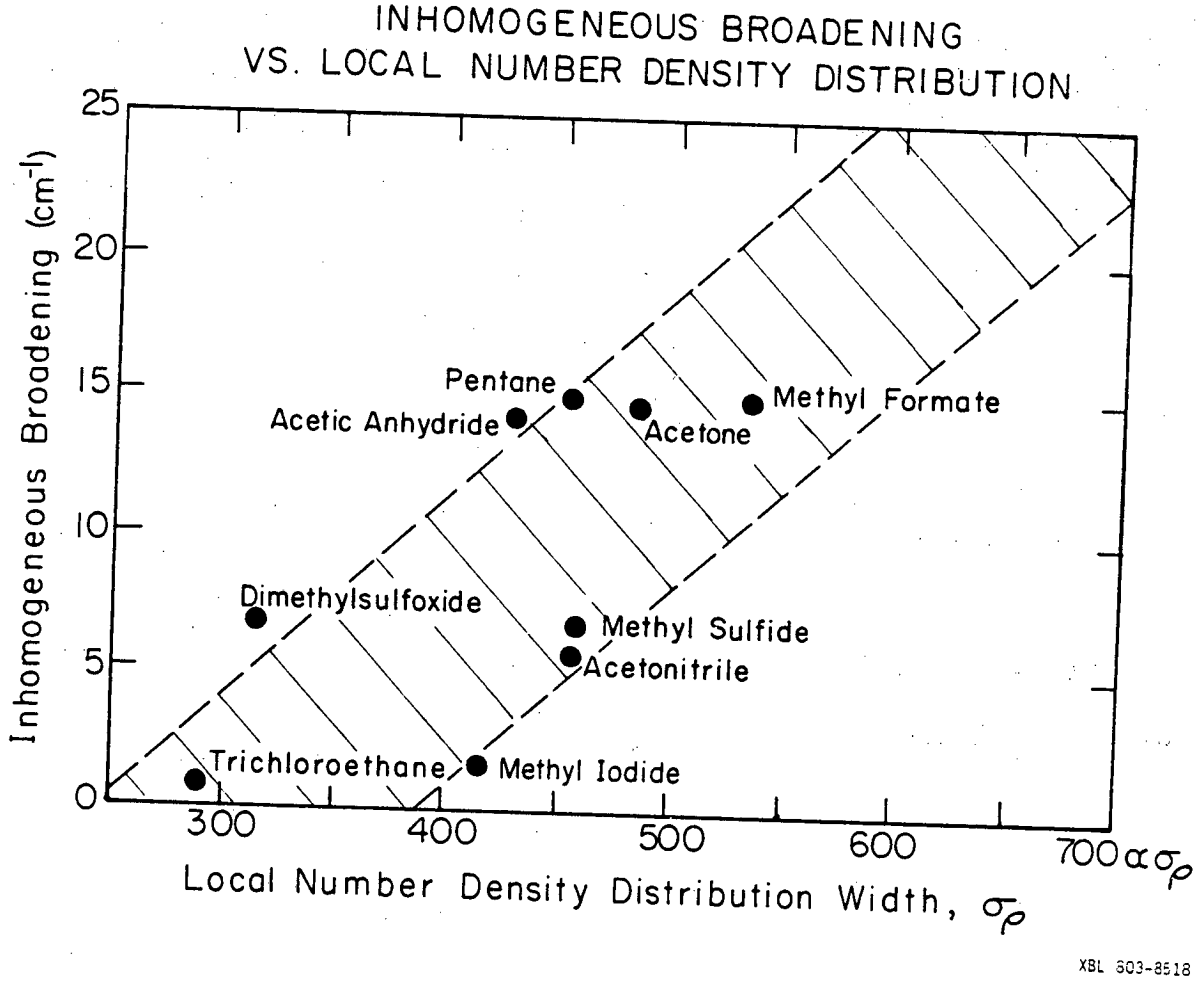
INHOMOGENEOUS BROADENING
VS. LOCAL NUMBER DENSITY DISTRIBUTION
Inhomogeneous Broadening (cm⁻¹)
25
20
15
10
5
0
Pentane
Acetic Anhydride
Acetone
Methyl Formate
Dimethylsulfoxide
Methyl Sulfide
Acetonitrile
Trichloroethane
Methyl Iodide
300
400
500
600
700 α σρ
Local Number Density Distribution Width, σρ
XBL 803-8518

Figure 5

probable distributions to characterize the spread in the distribution of the number of molecules, N :

$$\bar{N}^2-(\bar{N})^2 = \sigma_N^2 = kT(\partial\bar{N}/\partial\zeta)_{V,T} \qquad (2)$$

where ζ is the chemical potential. Introducing the number density, $\rho=N/V$, and using the relation $d\zeta=Vdp$, one can show that:

$$\sigma_N^2 = (\bar{N})^2(kT) \text{ X } (\kappa_T/V) \qquad (3)$$

where κ_T is the isothermal compressibility of the liquid. Since V is constant, Eq. (4) can be rewritten to yield σ_ρ, the fluctuation in the liquid's number density:

$$\sigma_\rho = \rho \text{ X } [(kT\kappa_T)/V]^{1/2} \qquad (4)$$

σ_ρ characterizes the spread in the number density distribution, i.e., the root mean-square deviation from the mean of the number density. We will refer to σ_ρ as the <u>local</u> number density distribution width since the volume, V, can be arbitrarily scaled down to molecular dimensions.

In order to calculate σ_ρ, the local number density distribution width, values for the isothermal compressibility are needed. Unfortunately, very few experimental liquid isothermal compressibility values have been determined. The isothermal compressibility, κ_T, can be calculated, however, using the equation [22]:

$$\kappa_T = [1/K_0 - (2/V)(\Delta H_{vap} - RT)]^{-1} \quad (5)$$

where K_0 is the isothermal compressibility for a fluid of hard spheres:

$$K_0 = (V/NkT) \times [(1-y)^2/(1+2y)]^2 \quad (6)$$

This equation is derived from the free volume theory of liquid and has been shown to give satisfactory agreement with experimental values [22]. In the expression for K_0, the packing fraction of the liquid, y, is defined as:

$$y = (\pi/6)\ \rho_1 \sigma^3 \quad (7)$$

where ρ_1 is the number density of the liquid and σ is the hard sphere diameter. The hard sphere diameter can be approximated using the relationship [23]:

$$\sigma^3 = 1.04/\rho_s \quad (8)$$

where ρ_s is the number density of the solid at the melting point [24]. All parameter values, calculated isothermal compressibilities and local number density distribution widths have been given previously [17].

Figure 5 shows a graph of the inhomogeneous broadened linewidth magnitudes versus $\sigma_\rho \propto \rho(\kappa_T)^{1/2}$. This plot demonstrates that the amount of inhomogeneous broadening in approximately proportional to the liquid's local number density distribution width. This correlation suggests that either the local number density distribution causes the

inhomogeneous broadening or that the local number density distribution scales with some other liquid property that causes the inhomogeneous broadening.

VI. Stochastic Lineshape Theory for Inhomogeneous Broadening

A. Kubo-Anderson Stochastic Theory

In order to develop a model for inhomogeneous broadening of vibrational transitions in a more formal way, the inhomogeneous broadening problem was constructed in the time domain. The Kubo-Anderson stochastic theory of lineshape [25,26] provides a simple theoretical framework from which inhomogeneous broadening can be formalized and visualized. Formally, the Hamiltonian for the vibrational oscillators can be written:

$$H = H_0 + H_p + H_m \tag{9}$$

where $$H_0 = \sum_j \hbar(\omega_0 + \Delta\omega(t))\, a_j^+ a_j \tag{10}$$

$$H_p = \sum_j n_j\, V(a_j, a_j^+, R_j(r), \Theta_j(r)) \tag{11}$$

$$H_m = \sum_{j,k} \hbar g_{jk}\, (a_j a_k^+ + a_k a_j^+) \tag{12}$$

$$g_{jk} = F(R_j(r,t), R_k(r,t), \Theta_j(r,t), \Theta_k(r,t)) \tag{13}$$

The subscript j sums over the various sites and n_j is the

population fraction at each site. H_0 is the unperturbed Hamiltonian containing $\Delta\omega(t)$, which gives rise to the homogeneous lineshape of each vibrational isochromat. H_p is the perturbing Hamiltonian which causes a frequency splitting according to the particular environmental sites which are dependent upon $R_j(r)$, the molecular radial distribution around site j. H_m is the motional Hamiltonian which interconverts environmental sites at a rate g_{jk}, determined by changes in the molecular distribution and orientation.

The commutation relationships are as follows:

$$[H_0,H_m] \simeq 0 \tag{14}$$

$$[H_0,H_p] \neq 0 \tag{15}$$

$$[H_m,H_p] \neq 0 \tag{16}$$

H_0 commutes with H_m in the limit that H_0 and H_m operate on different timescales. Since $\Delta\omega(t)$, viz. the time-dependent processes in H_0 which give rise to the homogeneous linewidth, fluctates on the picosecond or subpicosecond timescale and g_{jk}, the site interconversion rate, occurs on the timescale of diffusion or rotation, this limit is probably obeyed.

H_p does not commute with H_0, therefore H_p can change ω_0, the natural frequency of H_0. H_m does not commute with H_p, therefore H_m causes a time variation of H_p according to:

$$i\hbar\dot{H}_p = [H,H_p] \tag{17}$$

$$= [H_0,H_p] + [H_m,H_p] \simeq [H_m,H_p] \tag{18}$$

$[H_0,H_p] \simeq 0$ since H_p is assumed to have no important matrix elements connecting various unperturbed states of H_0. H_p only changes the frequency without causing transitions.

B. Randomly Modulated Oscillator Model

The precise form of the formal Hamiltonians given above is not known. In the absence of exact Hamiltonians, however, a randomly modulated oscillator model can be used [26]. This approach treats the vibration as as oscillator with a randomly modulated frequency and allows both the homogeneous and inhomogeneous broadening problems to be treated easily.

In this treatment, the vibrational oscillator, with a natural frequency ω_0, is given an equation of motion:

$$\dot{x} = i\omega(t)x \tag{19}$$

where $\omega(t)$ is the frequency with random modulation. The time average of $\omega(t)$ is ω_0 and $\omega(t)$ can be written as:

$$\omega(t) = \omega_0 + \omega_1(t) \tag{20}$$

where $\omega_1(t)$, the stochastic process, represents the fluctuation in frequency.

$\omega_1(t)$ can be described in terms of two characteristic parameters: Δ, the amplitude of the frequency change during the modulation; and τ_c, the correlation time of the modulation. Given a probability distribution $P(\omega_1)$ for the frequency modulation:

$$\Delta^2 = \int \omega_1^2 P(\omega_1) d\omega_1 \tag{21}$$

and $$\tau_c = {}_0\int^{\infty} \Psi(\tau) d\tau \tag{22}$$

where $$\Psi(\tau) = 1/\Delta^2 \langle \omega_1(t)\omega_1(t+\tau)\rangle \tag{23}$$

A relaxation function, $\Phi(t)$, can be defined for the oscillator.

$$\Phi(t) = \langle \exp i \; {}_0\int^t \omega_1(t')dt' \rangle \tag{24}$$

If $\omega_1(t)$, the frequency displacement modulation, is a Gaussian process:

$$\Phi(t) = \exp[-\Delta^2 {}_0\int^t (t-\tau)\Psi(\tau)d\tau \tag{25}$$

If $\Psi(\tau)$, the correlation function for the modulation, is assumed to be exponential, i.e. $\Psi(\tau)=\exp[-t/\tau_c]$, the correlation function of the oscillator can be written [27]:

$$\Phi(t) = \exp(-\Delta^2[\tau_c^2(\exp(-t/\tau_c)-1)+t\tau_c]) \tag{26}$$

Given this formalism, there are two limiting situations which are

distinguished by the relative magnitudes of Δ and τ_c [26]. For $\Delta\tau_c>>1$, i.e. slow modulation related to inhomogeneous broadening, τ_c is large compared to $1/\Delta$ and the frequency intensity distribution mirrors the amplitude distribution of the modulation. Thus a Gaussian distribution of frequency amplitude modulations yields a Gaussian lineshape. For $\Delta\tau_c<<1$, i.e. fast modulation related to homogeneous broadening, τ_c is small compared to $1/\Delta$ and the frequency intensity distribution approaches a Lorentzian in the limit $\Delta\tau_c \to 0$.

C. Vibrational Correlation Functions for Rapid and Slow Modulations

If the liquid has slowly varying intermolecular forces creating local structure, individual vibrational oscillators can vibrate in a distribution of different molecular environments which establishes a frequency distribution of vibrational isochromats. The frequency distribution of vibrational isochromats causes vibrational dephasing because of destructive interference among the individual frequencies in the distribution. The slowly varying intermolecular forces can be characterized by a frequency modulation amplitude, $\Delta_{INH}=\sum_j n_j\Delta_j$, which can be formally derived from H_p, and a modulation correlation time, τ_{INH}, which is related to the time dependence of H_p through $i\hbar\dot{H}_p=[H_m,H_p]$. These characteristics define the vibrational correlation function contributed by the slowly varying intermolecular forces:

$$\Phi(t)_{INH} = \exp(-\Delta_{INH}^2[\tau_{INH}^2(\exp(-t/\tau_{INH})-1)+t\tau_{INH}]) \qquad (27)$$

In addition to the slowly varying intermolecular forces, short

range, rapidly varying, dynamical modulation processes can cause vibrational dephasing of individual vibrational subunits. The short range, rapidly varying modulation processes can be characterized by a frequency modulation Δ_H and a modulation correlation time τ_H. These quantities can be derived from $\Delta\omega(t)$ in H_0. Particular forms for $\Delta\omega(t)$ are given by various vibrational dephasing models [28]. The characteristics of the rapid, short range modulation processes define the vibrational correlation function for an individual vibrational isochromat:

$$\Phi(t)_H = \exp(-\Delta_H{}^2[\tau_H{}^2(\exp(-t/\tau_H)-1)+t\tau_H]) \qquad (28)$$

$[\Delta^2{}_H\tau_H]^{-1}$ in the above expression is equivalent to T_2, the homogeneous vibrational dephasing time, for $t \gg \tau_H$ in the limit of fast modulation [27].

D. Unification of Rapid and Slow Vibrational Correlation Functions

Since the homogeneous vibrational linewidth comprises a substantial fraction of the spontaneous Raman lineshape, the spontaneous Raman lineshape is treated as a convolution of two independent lineshapes. Likewise, the vibrational correlation function corresponding to the inhomogeneously broadened spontaneous Raman lineshape must be expressed as a product of two modulation correlation functions. The product is strictly valid only when $\Phi_H(t)$ and $\Phi_{INH}(t)$ decay on different timescales. This is tantamount to the requirement that H_0 and H_m must operate on different timescales in order for them to commute.

$$\Phi(t) = \Phi(t)_H \Phi(t)_{INH} \tag{29}$$

The vibrational spectrum is related to the vibrational correlation function by:

$$I(\omega) = 1/2\pi \int_{-\infty}^{\infty} \exp[-i\omega t]\Phi(t)dt \tag{30}$$

Because $I(\omega)=\int L(\omega')G(\omega-\omega')d\omega'$ for inhomogeneously broadened spontaneous Raman lineshapes:

$$\int_{-\infty}^{\infty} L(\omega')G(\omega-\omega')d\omega' = 1/2\pi \int_{-\infty}^{\infty} \exp[-i\omega t]\Phi(t)dt \tag{31}$$

$$= 1/2\pi \int_{-\infty}^{\infty} \exp[-i\omega t]\Phi(t)_H \Phi(t)_{INH} dt \tag{32}$$

Since the Fourier transform of a product of two functions is given by the convolution integral over the products of Fourier transforms of the separate factors, $L(\omega)$ can be identified as the Fourier transform of $\Phi(t)_H$ and $G(\omega)$ can be identified as the Fourier transform of $\Phi(t)_{INH}$. Thus the problem of inhomogeneous broadening has been constructed in the time domain. This is useful because the time domain picture easily relates the inhomogeneous and homogeneous broadening to frequency displacement amplitudes and correlation times, and treats the inhomogeneous and homogeneous broadening <u>simultaneously</u> in terms of one vibrational correlation function.

This stochastic lineshape theory unifies the various slow and fast modulation approaches to vibrational dephasing. In the slow modulation limit, a static or quasi-static frequency distribution of vibrational

isochromats causes vibrational dephasing because of destructive interference among the individual frequencies in the distribution. In the fast modulation limit, rapidly varying processes cause vibrational dephasing by randomly modulating the frequency of the individual vibrational isochromats. These slow and fast modulation limits can be unified using the parameters τ_H, τ_{INH}, Δ_H and Δ_{INH} to define the complete vibrational correlation function.

E. Model for Inhomogeneous Broadening

The amount of inhomogeneous broadening was previously demonstrated to be approximately proportional to σ_ρ, the width of the distribution of local number densities in the liquid. Now a model is developed which relates σ_ρ to Δ_{INH} and τ_{INH}. First, we propose that Δ_{INH} is related to the mean intermolecular force that the environment imposes on a molecular vibration. Second, we propose that the intermolecular force has a distribution which is proportional to the width of the local number density distribution. Therefore:

$$\Delta_{INH} \propto \sigma_\rho \tag{33}$$

We note that these ideas have been further developed on theoretical grounds by Schweizer and Chandler as discussed in Chap. 4.

Δ_{INH} can be formally derived from $H_p=\sum_j n_j V(a_j,a_j^+,R_j(r),\Theta_j(r))$ or $\Delta_{INH}= \sum_j n_j \Delta_j$ where individual Δ_j values result from the particular $R_j(r)$ and $\Theta_j(r)$ configurations which give rise to the site. Specific local number densities in the local number density distribution affect Δ_j

through $R_j(r)$ and possibly $\Theta_j(r)$.

Third, we expect that τ_{INH}, the inhomogeneous broadening modulation correlation time, is proportional to the time required for positional or orientational interconversion of molecules, i.e., proportional to diffusion or rotation times. This can be derived from $i\hbar\dot{H}_p=[H_m,H_p]$. Since $H_p=\sum_j n_j V(a_j,a_j^+,R_j(r),\Theta_j(r))$ and $H_m \propto F(R_j(r,t),\Theta_j(r,t))$, the changes in $R_j(r,t)$ and $\Theta_j(r,t)$ give rise to a time variation in H_p.

Formally, H_m is constructed as an exchange Hamiltonian. In time τ_{INH}, therefore, site j is converted into some site k because of positional, $R_j(r,t)$, and orientational, $\Theta_j(r,t)$, movements of molecules. In agreement with these ideas, the temperature dependent inhomogeneous broadening behavior discussed in Chap. 5 is consistent with τ_{INH} proportional to 1/D where D is the translational diffusion constant.

In this experiment, we observed that $\Delta\omega_{INH}$, the linewidth of the inhomogeneous broadening lineshape function is approximately proportional to σ_ρ, the width of the distribution of local number densities in the liquid. In addition, the broadening must be proportional to $f(\tau_{INH})$, a function dependent upon τ_{INH}, the inhomogeneous broadening correlation time. Therefore we propose that the linewidth of the inhomogeneous broadening lineshape function is proportional to the product of σ_ρ or Δ_{INH} and $f(\tau_{INH})$:

$$\Delta\omega_{INH} \propto f(\tau_{INH}) \times \sigma_\rho \tag{34}$$

In the limit $\tau_{INH}\to 0$, i.e. the fast modulation limit $\Delta_{INH}\tau_{INH}\ll 1$,

the lineshape is Lorentzian and $f(\tau_{INH})$ approaches $\Delta_{INH}\tau_{INH}/\pi c$ in order to give the correct linewidth for a Lorentzian lineshape. In this limit, the inhomogeneous broadening processes have become homogeneous processes as will be discussed in Chap. 5. In the limit $\tau_{INH}\to\infty$, i.e. the slow modulation limit, the inhomogeneous broadening lineshape function is Gaussian and $f(\tau_{INH})$ approaches the factor $(2\ \ln 2)^{1/2}/\pi c$ in order to give the correct linewidth for a Gaussian lineshape. The picosecond data in this experiment is in the best agreement with this limit since $\Delta\omega_{INH}$ is approximately proportional to σ_ρ.

VII. Summary

We believe this is the first account of inhomogeneous broadening in non-hydrogen-bonded liquids and the first attempt to relate inhomogeneous broadening to various liquid parameters. We emphasize that symmetric CH_3-stretching vibrational linewidths in non-hydrogen-bonded liquids are inhomogeneously broadened to various degrees. A correlation is established between the inhomogeneous broadening and the width of the distribution of local number densities in the liquid. Based on this correlation, a model for inhomogeneous broadening in liquids is constructed. A stochastic lineshape theory is developed in which homogeneous and inhomogeneous broadening processes are treated simultaneously in terms of one vibrational correlation function. This treatment unifies the fast and slow modulation approaches to vibrational dephasing. This approach demonstrates how isotropic Raman scattering studies and selective vibrational dephasing experiments can be used to study the inhomogeneous broadening of vibrational linewidths.

References

1. C.B. Harris, H. Auweter and S.M. George, Phys. Rev. Lett. 44, 737(1980).

2. S.M. George and C.B. Harris, (submitted to Physical Review A).

3. R.L. Carman, F. Shimizu, C.S. Wong and N. Bloembergen, Phys. Rev. A2, 60(1970).

4. A. Laubereau, G. Wochner and W. Kaiser, Chem. Phys. 28, 363(1978).

5. A. Laubereau and W. Kaiser, Rev. Mod. Phys. 50, 607(1978).

6. D. von der Linde, O. Bernecker and A. Laubereau, Opt. Comm. 2, 215(1970).

7. A. Laubereau, D. von der Linde and W. Kaiser, Phys. Rev. Lett. 28, 1162(1972).

8. S.F. Fischer and A. Laubereau, Chem. Phys. Lett. 55, 189(1978).

9. Our results seriously jeopardize some of the conclusions of isotropic Raman lineshape investigations, which have assumed that vibrational linewidths were homogeneous in order to extract dynamical information. Unless the vibrational linewidth is known to be homogeneous under all experimental conditions, isotropic spontaneous Raman lineshape investigations can say nothing definitive about the homogeneous linewidth.

10. B. DiBartola, Optical Interactions in Solids (John Wiley, New York, 1968) p.357 ff.

11. J.T. Davies and J.M. Vaughan, The Astrophysical Journal 137, 1302(1963).

12. A Gaussian lineshape is consistent with the theory of stochastic processes when the modulation correlation times are long so that $\Delta\tau_c >> 1$, i.e. the slow modulation limit (Ref. 26).

13. G.C. Pimentel and A.L. McClellan, The Hydrogen Bond (Freeman, San Francisco, 1960).

14. M.V. Thiel, E.D. Becker and G.C. Pimentel, J. Chem. Phys. 27, 95(1957).

15. Y. Marcus, Introduction to Liquid State Chemistry (John Wiley, New York, 1977), p.108.

16. K.F. Herzfeld and T.A. Litovitz, Absorption and Dispersion of Ultrasonic Waves (Academic Press, New York, 1959).

17. S.M. George, H. Auweter and C.B. Harris, J. Chem. Phys. 73, 5573(1980).

18. D. Chandler, Accts. Chem. Res. 7, 246(1974).

19. H. Eyring and R.P. Marchi, J. Chem. Educ. 40, 562(1963).

20. D.A. McQuarrie, Statistical Mechanics (Harper and Row, New York, 1976), pp. 61-62.

21. T.L. Hill Introduction to Statistical Mechanics (Addison-Wesley, Reading, Mass., 1960), pp. 36-37.

22. K. Arakawa and K. Kojima, Bull. Chem. Soc. Japan 48, 26(1975).

23. W.G. Hoover and F.H. Ree, J. Chem. Phys. 49, 3609(1968).

24. $\sigma^3 = 1.04/\rho_s$ is determined from Monte Carlo calculations on a system of hard spheres at the point of coexistence for the solid and fluid phases.

25. P.W. Anderson, J. Phys. Soc. Japan 9, 316(1954).

26. R. Kubo in Fluctuations, Relaxation and Resonance in Magnetic Systems, ed by D. ter Haar (Plenum, New York, 1962), p. 23 ff.

27. W.G. Rothschild, J. Chem. Phys. 65, 455(1976);
J. Chem. Phys. 65, 2958(1976).

28. D.W. Oxtoby, Adv. Chem. Phys. 40, 1(1979).

Chapter 4: Dependence of Inhomogeneous Vibrational Linewidth Broadening on Attractive Forces from Local Liquid Number Densities

George, Auweter and Harris(GAH) [1] recently demonstrated that vibrational linewidths in non-hydrogen-bonded liquids were inhomogeneously broadened to various degrees as discussed in Chap. 3. A correlation was observed between the inhomogeneous broadening and σ_ρ, the width of the number density distribution in the liquid. The correlation suggested that a distribution of different, slowly varying, local number densities in a liquid created a distribution of distinct vibrational frequencies. This model led to the proposal that the inhomogeneous broadening linewidth is proportional to σ_ρ:

$$LW \propto \rho\,(k_B T \kappa_T)^{1/2} \tag{1}$$

where ρ is the number density, $k_B T$ is the thermal energy and κ_T is the isothermal compressibility.

As probably suspected from earlier work [1-11], Schweizer and Chandler(SC) [12] subsequently demonstrated that vibrational linewidths in liquids are broadened by two types of forces which are separable in time: rapidly varying repulsive forces which give rise to homogeneous broadening and slowly varying attractive forces which lead to inhomogeneous broadening. When the attractive force correlation time, $T_A=\infty$, their model led to the prediction that the absolute inhomogeneous broadening linewidth is given by:

$$LW = 2(2\ln 2)^{1/2} \langle \Omega_A \rangle / (\bar{N})^{1/2} \; X \; (\rho k_B T \kappa_T)^{1/2} \qquad (2)$$

where $\bar{N}$ is estimated to be the average number of nearest neighbors and $\langle \Omega_A \rangle$ is the attractive force contribution to the vibration's gas-to-liquid frequency shift. $\langle \Omega_A \rangle$ is a measure of the magnitude of the slowly varying attractive forces from the surrounding liquid density and is thought to be associated with multipole interactions [12].

Notice that the SC theory makes a prediction for the absolute magnitude of the inhomogeneous broadening linewidth. However, the density, temperature and isothermal compressibility dependence of the two predictions are almost identical. This indicates that both predictions are proportional to σ_ρ [1]. The substantial difference between the predictions is $\langle \Omega_A \rangle$, which raises important questions concerning the physical mechanism of inhomogeneous broadening. Does $\langle \Omega_A \rangle$, in fact, play a significant role in inhomogeneous broadening? Which factor, $\langle \Omega_A \rangle$ or σ_ρ, is more important for inhomogeneous broadening?

The inhomogeneous broadening predictions of the SC theory were tested and the importance of $\langle \Omega_A \rangle$ on the proportionality was determined by comparing the SC predictions to the measured inhomogeneous broadening linewidths for various symmetric CH_3-stretching vibrations [1]. The measured inhomogeneous linewidths were determined using a combination of picosecond vibrational dephasing experiments and isotropic Raman investigations [1]. This combined approach, unlike isotropic spontaneous Raman studies alone, can separate the contributions of homogeneous and inhomogeneous broadening [1,13]. By contrasting the SC

and GAH correlations, the relative importance of $\langle\Omega_A\rangle$ and σ_ρ in the inhomogeneous broadening correlation plot for the various liquids at room temperature and 1 atmosphere pressure was determined.

According to the SC theory, $\langle\Omega_A\rangle$ is derived from $\langle\Omega\rangle_{exp} = \langle\Omega_A\rangle + \langle\Omega_R\rangle$ where $\langle\Omega\rangle_{exp}$ is the experimental gas-to-liquid vibrational frequency shift. The repulsive force contribution to the gas-to-liquid vibrational frequency shift, $\langle\Omega_R\rangle$, is calculated theoretically by $\langle\Omega_R\rangle = \Delta q \langle F_R\rangle$ where Δq is the length change along the normal mode coordinate for a v=0→1 transition and $\langle F_R\rangle$ is the liquid's repulsive force along the normal mode coordinate. $\langle F_R\rangle$ can be defined in terms of forces along individual bonds. In order to calculate the repulsive force on a particular bond, the "free floating bond" approximation is utilized and the particular bond is replaced by a homonuclear diatomic which defines the bond [12]. $\langle F_R\rangle$ is subsequently determined by the slope of the two-point cavity distribution function for this solute homonuclear diatomic dissolved in a hard sphere solvent [10,11].

We calculated $\langle F_R\rangle$ along an individual C-H bond following the SC treatment of the C-H stretch in chloroform [12]. The cavity distribution function was evaluated using the polynomial expression and numerical tables for the cavity distribution function [10]. We determined the total repulsive force on the symmetric CH_3-stretching vibration by projecting the repulsive forces along the individual C-H bonds onto the methyl group's C_{3v} axis. This procedure converted the methyl group into an equivalent diatomic. Thus, the repulsive force on the equivalent diatomic representing the methyl group, $\langle\overline{F_R}\rangle = 3 \cos\alpha \langle F_R\rangle$, where $\cos\alpha = 1/(3)^{1/2}$.

For consistency, we also calculated the length change along the

symmetric methyl normal mode coordinate after converting the methyl group into an equivalent diatomic. After the masses are projected onto the methyl group's C_{3v} axis, the reduced mass needed to define the effective diatomic bond length change, $\overline{\Delta r}$, is given by $\mu=(3\ m_C m_H\ \cos\alpha)/(m_C+3\ m_H\ \cos\alpha)$. The bond length change, $\overline{\Delta r}$, was defined using expectation values given by Oxtoby [5] and was evaluated using a measured anharmonicity constant [14].

$\langle\Omega_A\rangle$ was evaluated using the calculated $\overline{\Delta r}$, $\langle\overline{F_R}\rangle$ and $\langle\overline{\Omega_R}\rangle$ values and the measured $\langle\Omega\rangle_{exp}$ values listed in Table 1. Using the calculated $\langle\Omega_A\rangle$ values, the SC absolute inhomogeneous broadening linewidths at room temperature were determined using previously derived isothermal compressibility values [1] with $\overline{N}=6$ [12].

The correlation between the SC predicted absolute inhomogeneous broadening linewidths and the measured inhomogeneous broadening linewidths (FWHM) are shown in Figure 1. The GAH predicted inhomogeneous broadening linewidths, normalized to the SC absolute predictions using methyl sulfide, are also given. Notice that, although both predictions display the correct trend, the predictions do not span the full range of measured inhomogeneous linewidths.

The SC correlation improves upon the GAH correlation for the small molecules. This suggests that $\langle\Omega_A\rangle$ contributes to inhomogeneous broadening. For the larger, less spherical molecules, the correlation is not improved. This is perhaps because the SC model does not account for the shape of the molecule.

There is a close correspondence between the SC and GAH correlations. The inclusion of $\langle\Omega_A\rangle$ causes the points to shift, but most points shift only a small fraction of the entire range observed.

TABLE 1. Parameters used to calculate the SC absolute inhomogeneous broadening linewidths.

FIG. 1. Correlation between the predicted inhomogeneous broadening linewidths and the measured inhomogeneous broadening linewidths (FWHM).

TABLE 1

Molecule	$\overline{\Delta r}(10^{-2}$Å)	$\langle\overline{F_R}\rangle$(cm^{-1}/Å)	$\langle\overline{\Omega_R}\rangle$(cm^{-1})	$\langle\Omega\rangle_{exp}$(cm^{-1})	Exp.data from Ref	$\langle\Omega_A\rangle$(cm^{-1})	SC Absolute Inhomogeneous Linewidth(cm^{-1})
1. Trichloroethane	2.19	565.6	+12.4	-13	[15]	-25.4	3.58
2. Methyl Iodide	2.28	719.3	+16.4	-14	[16-19]	-30.4	4.78
3. Acetonitrile	2.32	874.5	+20.3	-11	[20-22]	-31.3	4.94
4. Methyl Sulfide	2.32	582.5	+13.5	-16	[23]	-29.5	5.50
5. Dimethylsulfoxide	2.29	798.0	+18.3	-19	[23]	-37.3	4.73
6. Acetic Anhydride	2.20	556.0	+12.2	-22	[24]	-34.2	6.82
7. Acetone	2.29	582.5	+13.4	-13	[25]	-26.4	5.26
8. Methyl Formate	2.23	645.2	+14.4	-15	[26]	-29.4	5.95
9. Pentane	2.30	367.9	+ 8.5	-15	[1,27]	-23.5	5.52

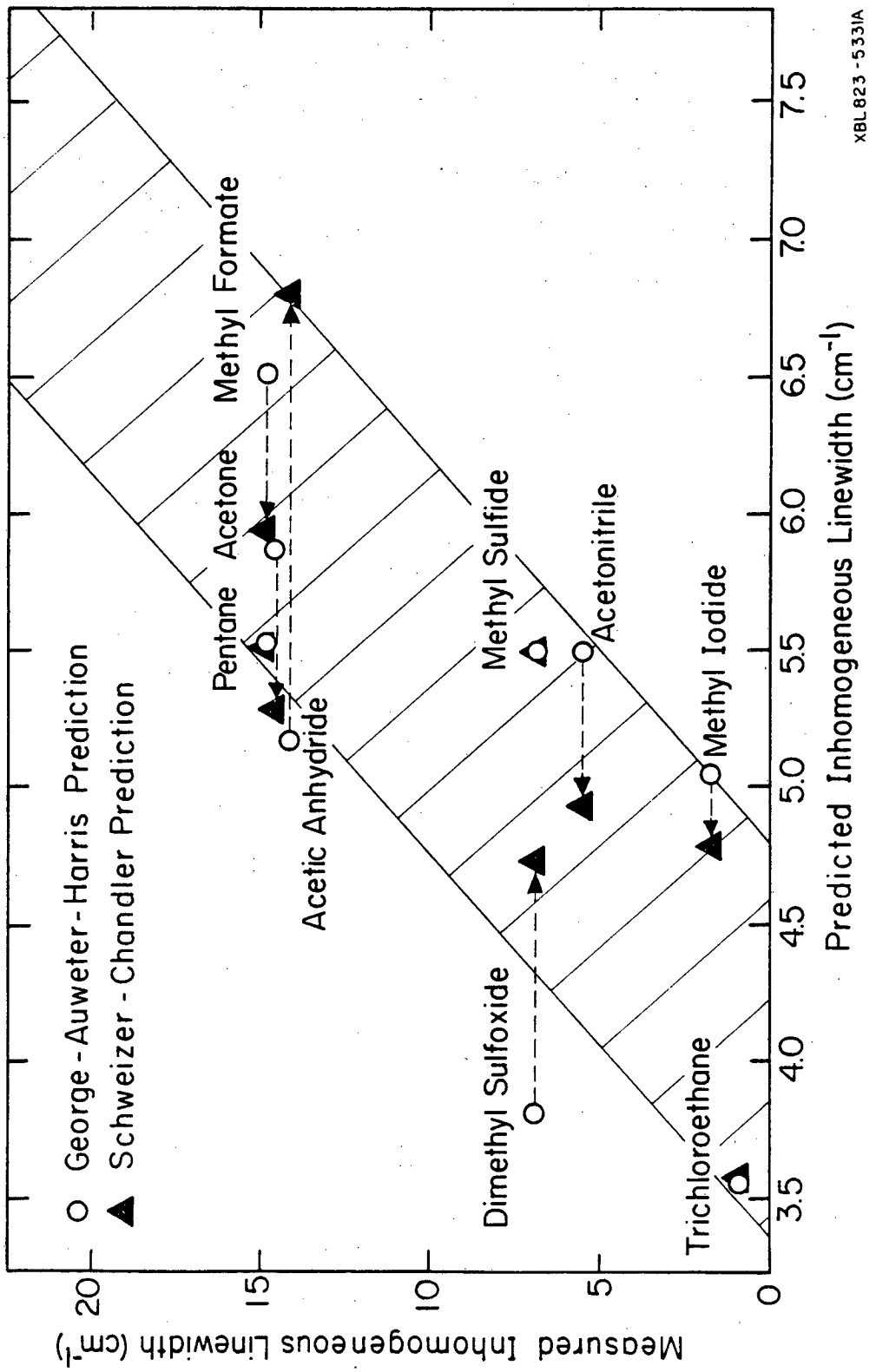
O George-Auweter-Harris Prediction
▲ Schweizer-Chandler Prediction
Pentane
Acetone
Methyl Formate
Acetic Anhydride
Methyl Sulfide
Acetonitrile
Methyl Iodide
Dimethyl Sulfoxide
Trichloroethane
Measured Inhomogeneous Linewidth (cm⁻¹)
Predicted Inhomogeneous Linewidth (cm⁻¹)
0
5
10
15
20
3.5
4.0
4.5
5.0
5.5
6.0
6.5
7.0
7.5
XBL823-533IA

Figure 1

This demonstrates that σ_ρ is more important than $\langle\Omega_A\rangle$ in determining the relative inhomogeneous broadening magnitude for these symmetric CH_3-stretching vibrations.

The similarity between the correlations also indicates that the $\langle\Omega_A\rangle$ values for the symmetric CH_3-stretching vibration in various liquids are somewhat constant (see Table 1). Because of varying intermolecular interactions and vibrational mode characteristics, however, other types of vibrations may have different $\langle\Omega_A\rangle$ values [12]. Therefore, although σ_ρ largely determines the relative inhomogeneous broadening magnitudes for symmetric CH_3-stretching vibrations in various liquids, $\langle\Omega_A\rangle$ may determine the relative inhomogeneous broadening magnitudes for different types of vibrations.

References

1. S.M. George, H. Auweter and C.B. Harris, J. Chem. Phys. 73, 5573(1980).
2. W. Schindler and J. Jonas, J. Chem. Phys. 72,5019(1980); J. Chem. Phys. 73, 3547(1980).
3. A.M. Benson, Jr. and H.G. Drickamer, J. Chem. Phys. 27, 1164(1957); R.R. Wiederkehr and H.G. Drickamer, J. Chem. Phys. 28, 311(1958).
4. J. Yarwood, R. Ackroyd, K.E. Arnold, G. Doge and R. Arndt, Chem. Phys. Lett. 77, 239(1981).
5. D.W. Oxtoby, J. Chem. Phys. 70, 2605(1979).
6. S.F. Fischer and A. Laubereau, Chem. Phys. Lett. 35, 6(1975).
7. B.P. Hills and P.A. Madden, Mol. Phys. 35, 807(1978); Mol. Phys. 37, 937(1979).
8. S. Bratos and E. Marechal, Phys. Rev. A 4, 1078(1971).
9. D.W. Oxtoby, Adv. Chem. Phys. 40, 1(1979).
10. L.R. Pratt, C.S. Hsu and D. Chandler, J. Chem. Phys., 68, 4202(1978).
11. L.R. Pratt and D. Chandler, J. Chem. Phys. 72, 4045(1980).
12. K.S. Schweizer and D. Chandler, J. Chem. Phys. 76, 2296(1982).
13. S.M. George, A.L. Harris, M. Berg and C.B. Harris, (submitted to J. Chem. Phys.).
14. J. Overend and K. Machida, Spectrochim. Acta 26A, 1225(1970).
15. D.C. McKean and E.W. Laurie, J. Mol. Struct. 27, 317(1975).
16. D.C. McKean, Spectrochim. Acta 29A, 1559(1973).
17. A.D. Dickson, I.M. Mills and B. Crawford, Jr., J. Chem. Phys. 27, 445(1957).

18. H.S. Goldberg and P.S. Pershan, J. Chem. Phys. 58, 3816(1973).

19. W.K. Glass and A.D.E. Pullin, Trans. Faraday Soc. 59, 25(1963).

20. C. Breuillard-Alliot and J. Soussen-Jacob, Mol. Phys. 28, 905(1974).

21. D.C. McKean, Spectrochem. Acta 30A, 1169(1974).

22. J. Schroeder, V.H. Schiemann, P.T. Sharko and J. Jonas, J. Chem. Phys. 66, 3215(1977).

23. G. Geiseler and G. Hanschmann, J. Mol. Struct. 11, 283(1972).

24. P. Mirone, B. Fortunato and P. Canziani, J. Mol. Struct. 5, 283(1970).

25. G. Dellepiane and J. Overend, Spectrochim. Acta 22, 593(1966).

26. J.K. Wilmshurst, J. Mol. Struct. 1, 201(1957).

27. L.M. Sverdlov, M.A. Kovner and E.P. Krainov, Vibrational Spectra of Polyatomic Molecules (John Wiley and Sons, New York, 1974).

Chapter 5: Picosecond Studies of the Temperature Dependence of Homogeneous and Inhomogeneous Vibrational Linewidth Broadening in Liquid Acetonitrile

I. Introduction

Vibrational linewidths in liquids are broadened by many different mechanisms and experimental separation of the various mechanisms has been extremely difficult. Recently, selective picosecond vibrational dephasing experiments [1-5] have attempted to separate the broadening processes which act on rapidly and slowly varying timescales. The rapidly varying liquid processes are associated with homogeneous broadening, whereas the slowly varying processes are associated with inhomogeneous broadening. Recent theoretical work has placed this separation of timescales on firm theoretical foundations and has linked the slowly varying processes to attractive interactions in the liquid [6]. Previous work has already established a connection between rapidly varying liquid processes and repulsive interactions [7,8].

The vibrational linewidth broadening of the symmetric CH_3- stretching vibrational mode (ν_1) of acetonitrile has been studied extensively by isotropic Raman investigations [9-12]. Despite these investigations, the exact mechanism of vibrational linewidth broadening has remained elusive. Some studies have revealed that short range repulsive, collisional mechanisms may be dominant [9,10]. Other studies have emphasized the importance of the long range attractive dipole-dipole or dispersion broadening mechanisms [11,12]. Unfortunately,

because isotropic Raman lineshapes can be both homogeneously and inhomogeneously broadened, isotropic Raman investigations can not separate the homogeneous and inhomogeneous vibrational linewidth broadening contributions. At the present date, only picosecond vibrational dephasing experiments combined with isotropic Raman investigations can separate these contributions.

In order to test the various homogeneous and inhomogeneous linewidth broadening mechanisms, we measured the temperature dependence of the picosecond dephasing times and isotropic Raman linewidths of the symmetric CH_3-stretching vibration in liquid acetonitrile over its entire liquid range from -40° to 70° C at P=1 Atm. [13]. The excite-and-probe vibrational dephasing experiments were conducted using a selective technique based on transient stimulated Raman scattering in high laser depletion [14]. This is the first picosecond examination of the temperature dependence of the homogeneous and inhomogeneous vibrational linewidth broadening in a liquid. The results demonstrate that both rapidly and slowly varying processes contribute to vibrational linewidth broadening.

II. Selectivity in Vibrational Dephasing Experiments

Vibrational dephasing experiments are performed with excitation pulses and time-delayed probe pulses [1]. Selectivity is the ability of the probing process to select out a single, distinct vibrational subgroup from a vibrational lineshape which is composed of a slowly varying frequency distribution of vibrational subgroups, i.e. inhomogeneously broadened. The higher the selectivity, the more

accurately the decay of the probe scattering is related to the homogeneous dephasing time T_2 of a single vibrational subgroup.

We have recently developed a general theory for excite-and-probe vibrational dephasing experiments conducted using transient stimulated Raman scattering in low and high depletion of the excitation laser pulse [14]. The theory reveals that selectivity in the probing process of the vibrational dephasing experiment is very different in high and low laser depletion. Selectivity is low in low laser depletion. In marked contrast, high laser depletion produces a distinctive new behavior which leads to greatly enhanced selectivity. The results indicate that high laser depletion is necessary to measure the homogeneous vibrational dephasing time T_2 to a high level of accuracy in an inhomogeneously broadened vibrational linewidth [14].

Zinth et al. [15] have recently presented results from vibrational dephasing experiments conducted in low depletion of the excitation laser pulse. In agreement with theoretical interpretations [14,15], the measurements indicated that the excite-and-probe vibrational dephasing experiments conducted in low laser depletion were <u>not</u> selective. On the other hand, many previous excite-and-probe vibrational dephasing experiments by Kaiser and coworkers [1,2,16,17] and Harris and coworkers [3-5] have given results which have displayed significant selectivity. These experiments were believed to have been conducted in low laser depletion. Consequently, these selective results [1-5,16,17] are in disagreement with the theoretical interpretation for vibrational dephasing experiments conducted in low laser depletion [14,15].

The previous experimental results [1-5,16,17] which have displayed selectivity are consistent with the high laser depletion results of the

general theory [14]. Thus the discrepancies between these vibrational dephasing experiments and their theoretical interpretations can be explained if these excite-and-probe vibrational dephasing experiments were actually conducted in high laser depletion. This explanantion is highly probable because of the likelihood of high laser depletion in transient stimulated Raman scattering [14,18]. We note that our previous vibrational dephasing experiments [3-5] which have displayed significant selectivity are now known to have been undertaken in high laser depletion [18].

III. Experimental

Homogeneous linewidths were extracted from the symmetric CH_3-stretching vibrational linewidth in liquid acetonitrile using the selective excite-and-probe vibrational dephasing experiment based on high laser depletion of the excitation laser pulse and collinear coherent Stokes probe scattering [14]. The fundamentals of excite-and-probe vibrational dephasing experiments have been previously discussed [1,3,14]. Because of the discrepancies in recent picosecond vibrational dephasing studies [1-5,15-17], however, there is a great need to present explicit and thorough experimental details. Therefore, this section will discuss the many details and procedures which are important for accurate, reproducible experimental results.

A. Picosecond Pulse Generation

A schematic of the picosecond pulse generating system is shown in

Fig. 1. The selective excite-and-probe vibrational dephasing experiments were performed with single picosecond pulses selected from the rising edge of pulse trains emitted by a TEM_{00} selective, passively mode-locked Nd:glass laser oscillator. The design, operation and performance of this laser have been given in thorough detail [19]. A Pockels cell driven by a low jitter electronic circuit [20] consistently selected the 4th-8th intense pulse from the rising edge of pulse trains of 30-45 pulses. A fast photodiode and a Tektronix 7834 fast storage oscilloscope monitered the pulse trains. Shots which displayed multiple pulse trains were excluded from the data. The selected pulse was amplified by two Nd:glass amplifiers. The pulse energy after amplification was determined to be approximately 1 mJ using a Korad/Hadron Model 100 thermopile. Throughout this experiment, the pulse energy was kept essentially constant.

B. Pulse Characterization

In order to determine the width of the 1.06 μ pulse, the pulse autocorrelation widths were measured using two photon fluorescence (TPF). Unfortunately, the approximately 1 mJ 1.06 μ pulses used in this experiment were not intense enough for sufficient TPF signals. Higher pulse energies of approximately 20 mJ obtained using three Nd:glass amplifiers were required. Burn spots from these pulses on developed but unexposed Polaroid film taken before the TPF apparatus had diameters of 5-6 mm and showed no substructure.

The entire unfocused 1.06 μ pulse was sent into a standard TPF apparatus [21-23] shown in Fig. 1. The TPF signal was obtained from a

FIG. 1. Schematic of the picosecond pulse generating system.

FIG. 2. Experimental setup for stimulated Stokes excitation and collinear Stokes probe scattering in a 10 cm Raman cell. Excitation Stokes and probe Stokes signals are separated because of their different polarizations and simultaneously detected using a two-dimensional OMA.

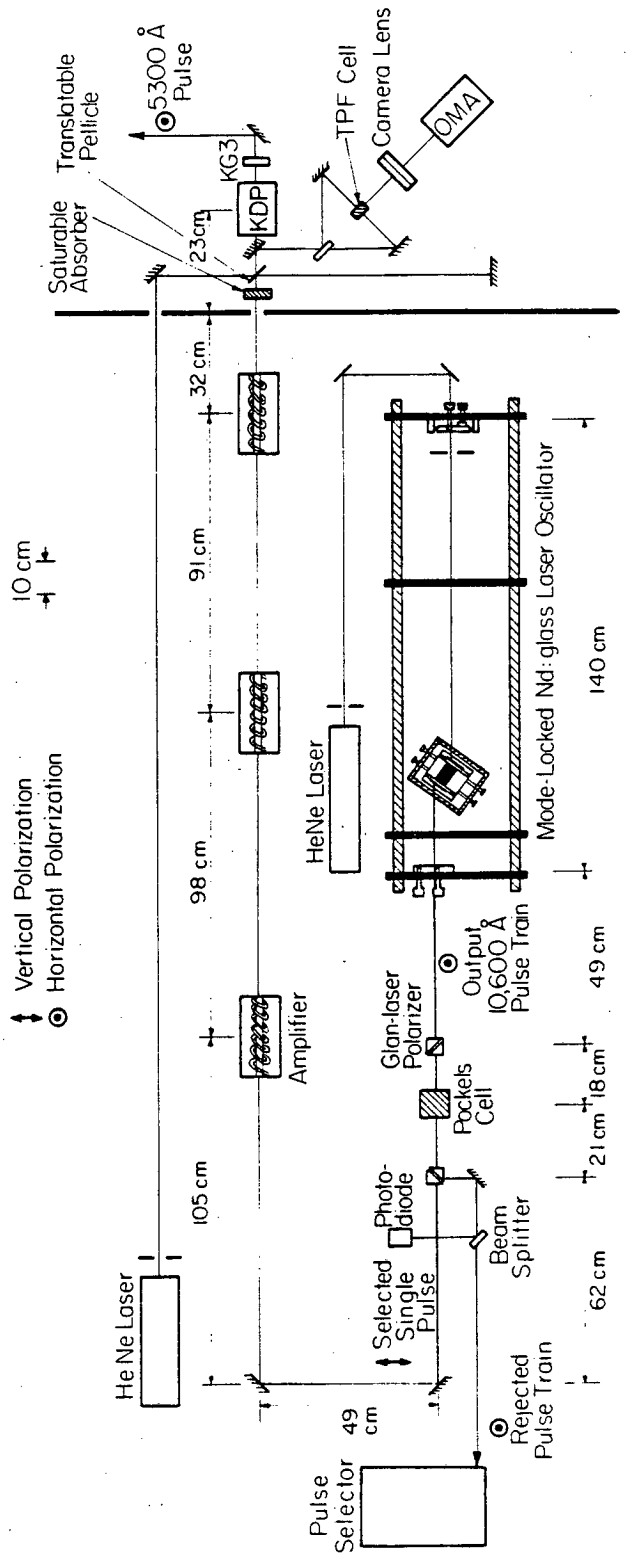
Translatable Pellicle
5300 Å Pulse
Saturable Absorber
23cm
KG3
KDP
TPF Cell
Camera Lens
OMA
32 cm
91 cm
98 cm
10 cm
Vertical Polarization
Horizontal Polarization
HeNe Laser
Mode-Locked Nd:glass Laser Oscillator
140 cm
Output 10,600 Å Pulse Train
49 cm
Glan-laser Polarizer
Pockels Cell
18 cm
21 cm
Photo-diode
Beam Splitter
Amplifier
105 cm
He Ne Laser
Selected Single Pulse
62 cm
Rejected Pulse Train
49 cm
Pulse Selector
XBL 824-5627

Figure 1

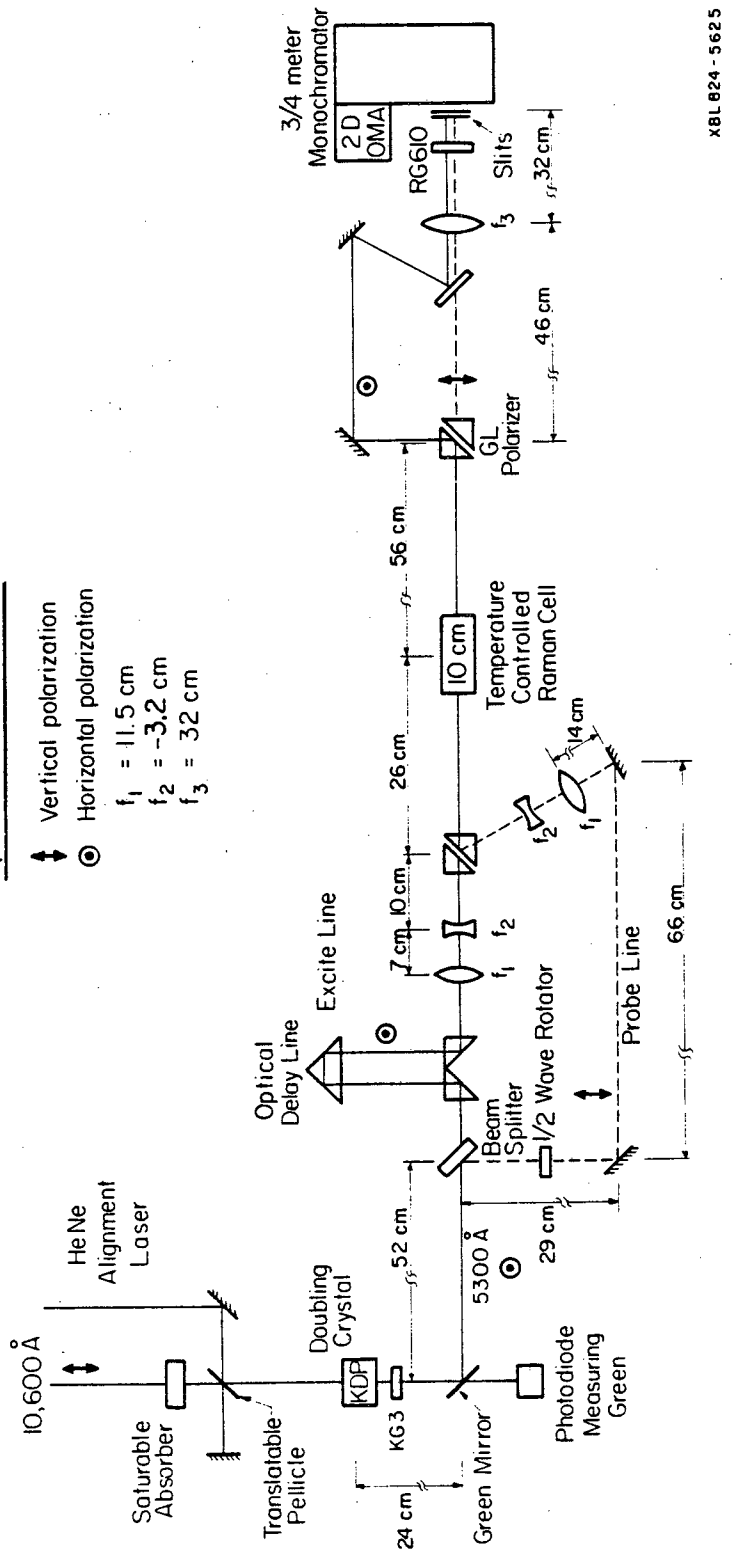
Optics Table Schematic
Vertical polarization
Horizontal polarization
f1 = 11.5 cm
f2 = -3.2 cm
f3 = 32 cm
10,600 Å
He Ne Alignment Laser
Saturable Absorber
Translatable Pellicle
Doubling Crystal
KDP
KG3
Green Mirror
Photodiode Measuring Green
Optical Delay Line
Excite Line
Beam Splitter
1/2 Wave Rotator
Probe Line
Temperature Controlled Raman Cell
10 cm
GL Polarizer
RG610
Slits
2D OMA
3/4 meter Monochromator
5300 Å
24 cm
52 cm
29 cm
7 cm
10 cm
26 cm
56 cm
46 cm
32 cm
14 cm
66 cm
XBL 824-5625

Figure 2

1×10^{-3} M methanol solution of rhodamine 6G in a 1 cm cell. An 85 mm camera lens imaged the TPF trace with a magnification of approximately 1.0 on a Princeton Applied Research (PAR) Model 1254 optical multichannel analyzer (OMA) ISIT detector. High f-numbers of f/22 to f/8 were used to maximize the depth of field. The OMA was interfaced to a minicomputer which displayed the TPF intensity plot on a CRT screen [24]. Calibration, focus and resolution of the lens-OMA system were determined using a calibrated copper mesh at the TPF cell position.

TPF peak-to-background ratios were in the range 2.8-3.0 to 1.0 on all shots. This indicates excellent pulse coherence. Autocorrelation widths of 1.69 ±0.20 mm were obtained for pulses early in the rising edge of the pulse trains. This indicates that the pulses display small shot-to-shot pulse width fluctuations. Assuming pulse shapes intermediate between Gaussian and Lorentzian, the autocorrelation width corresponds to pulse widths of ≈9 psec [25]. Given the ≈400 micron mode-locking dye cell length in our Nd:glass laser oscillator [19], this measurement is in excellent agreement with previous studies of the 1.06 μ pulsewidth as a function of mode-locking dye cell length [26,27].

C. Pulse Compression and Frequency Doubling

Before frequency doubling, the 1.06 μ pulses were compressed using a saturable absorber [28]. The saturable absorber, Eastman Kodak dye #9860, was dissolved in 1,2-dichloroethane in a 1 cm cell until an optical density of 1.0 was measured at 1.06 μ. The cell was placed after the final ampliflier as shown in Fig. 1. The dye absorbs the

rising edge of the 1.06 μ pulse, then bleaches, allowing the main portion of the pulse to pass. Using this saturable absorber, our excite-and-probe vibrational dephasing experiments have measured coherent Stokes signal decays as rapid as $T_2/2$=0.5-0.7 psec in dimethylsulfoxide in agreement with previous measurements [3]. This indicates that the rising edge of the pulse is ≤0.5-0.7 psec. This rapid rising edge is important for adequate time resolution in this experiment.

The effect of the saturable absorber on the 1.06 μ pulse width was also investigated using the TPF apparatus. The effect of the saturable absorber on pulses of approximately 20 mJ was studied. The average measured pulse shortening ratios were 0.89 and 0.80 at optical densities of 1.0 and 2.0, respectively [29]. These pulse shortening ratios are based on the average of 20-30 individual shots at each optical density. Smaller ratios are expected for the ≈1 mJ pulses used in the experiment. In addition, the saturable absorber did not significantly broaden the pulse's spectral bandwidth. Spectral examinations of the frequency doubled 5306 Å pulse revealed that the compressed pulse spectrum was broadened by <10 % relative to an uncompressed pulse.

The compressed pulses were centered into a KDP angle-tuned doubling crystal and the crystal was adjusted for maximum doubling effeciency by monitoring both the incident 1.06 μ pulse and the transmitted 5306 Å pulse. The spatial profile of the transmitted 5306 Å pulse was very sensitive to the crystal angle. When the crystal was set at the maximum doubling efficiency, the spatial profile was round and clean with no substructure. Before each experimental run, the doubling crystal was adjusted for optimum efficiency and the quality of the spatial profiles

was monitored. We observed that stimulated Raman excitation occured at much lower energy thresholds when the pulse had high quality spatial profiles.

Spectral examinations of these 5306 Å pulses using the PAR Model 1254 OMA ISIT detector displayed spectral bandwidths (FWHM) of 5.0 ± 1.2 cm^{-1}. Assuming pulse shortening in the saturable absorber and in the KDP crystal, pulsewidths of approximately 6-8 psec were estimated for the 5306 Å pulses. The resultant bandwidth product of ≈ 0.9 indicates that the pulses were essentially bandwidth limited.

D. Optics Alignment and Experimental Adjustments

The selective, picosecond Stokes scattering technique is dependent upon collinear overlap of the excite and probe pulses to assure selectivity [14]. In order to easily align the optics for proper overlap, a Helium-neon laser beam was aligned collinear to the Helium-neon laser beam which was used to align the Nd:glass laser oscillator. This was accomplished using a translatable pellicle shown in Figs. 1 and 2. Using this brighter second beam, the optics could be easily aligned.

The excitation and probe telescopes were both adjusted for focal lengths at the center of the 10 cm acetonitrile [30] Raman cell shown in Fig. 2. The beams were collinearly overlapped by xy adjustments of the convex lens on the excite and probe line telescopes and by xy adjustments of the two mirrors in the probe line. Before each experimental run, the overlap was carefully checked at the first Glan-laser polarizer, at the 10 cm acetonitrile cell and at the second Glan-

laser polarizer with both the Helium-neon alignment beam and the 5306 Å pulses.

The minimum divergence, α, of the excitation Stokes pulse with respect to the axis of the excitation laser pulse is important for reproducible results and minimum depolarization in the second Glan-laser polarizer. Before each experimental run, the stimulated Stokes divergence was monitored and the intensity of the excitation laser pulse was adjusted for the minimum Stokes divergence which occurs for a narrow range of laser pulse energies just above the stimulated Raman threshold. Assuming a point source at the center of the Raman cell shown in Fig. 2, cones of stimulated Stokes light with α=3-10 mrad were observed at the second Glan-laser polarizer for laser excitation pulses within this narrow energy range of acceptable data shots. Shots of greater energy could generate cones of stimulated Stokes with $\alpha \geq 15$ mrad.

E. Optical Detection and Data Selection

The stimulated Stokes excitation pulse and the coherent Stokes probe pulse are collinear and their separation relies upon their perpendicular polarizations. Because the excitation Stokes pulse is much larger than the probe Stokes pulse, depolarization of the excitation Stokes pulse in the crossed Glan-laser polarizers or in the 10 cm Raman cell can completely overwhelm the coherent probe Stokes signal. For this reason, high quality, polarizers with extinctions of approximately 1×10^{-6} were used [31]. The temperature-controlled Raman cell is discussed in Sec. IV.

As shown in Fig. 2, the excitation Stokes pulse and the coherently scattered probe Stokes pulse were separated by the second Glan-laser polarizer because of their different polarizations. They were spatially separated on the slits of a Spex 3/4 m monochromator and were simultaneously detected, but spatially resolved, on the target of a two-dimensional optical multichannel analyzer. This analyzer is interfaced to a minicomputer which displayed and integrated the spectral line shapes of the excite and probe Stokes pulses [24].

The stimulated Stokes spectrum (FWHM) determined from laser shots within the acceptable range was 16±7 cm^{-1}. Laser shots of greater energy generated much broader, very random excitation Stokes spectra. We spectrally observed each shot and discarded any shot which displayed significant frequency modulation. The transmitted excitation laser pulse spectrum (FWHM) determined from laser shots within the acceptable range was 8.3±2.8 cm^{-1}, broadened considerably from the incident excitation laser pulse spectrum (FWHM) of 5.0 ±1.2 cm^{-1}. This broadening of the transmitted excitation laser pulse spectrum is consistent with the shortening of the excitation laser pulse in high laser depletion [14].

Before signals were calculated, the coherent probe Stokes signal was corrected for excitation Stokes signal depolarization. Probe Stokes signals were measured as a function of excitation Stokes energy with the laser probe pulse blocked. Within a certain range of excitation laser pulse energies and excitation Stokes pulse energies, this depolarization was very linear. At higher excitation energies, the deplorization became large and unpredictable. This point was approximately where the Stokes divergence became large and where the Stokes spectrum began to

modulate. Shots above this level were excluded from the data.

Shots which showed very low Stokes conversion from lower energy laser excitation pulses also displayed significant scatter in the probe signal. This scatter may reflect the selectivity differences in high and low laser depletion [14]. These low Stokes conversion shots were also excluded from the data. Only shots within the restricted range shown in Fig. 3 were accepted. Shots within this narrow window displayed some scatter, but the scatter did not correlate with the excitation pulse energy.

F. Excitation Laser Pulse Depletion

In order to characterize the laser pulse depletion in this experiment, we measured the excitation laser pulse depletion in the 10 cm acetonitrile Raman cell. Figure 3 shows the transmitted laser pulse energy versus the incident laser pulse energy at 5306 Å with and without the 10 cm Raman cell. The approximate range of laser pulse energies used in the experiment is also given.

Figure 3 shows that immediately after the stimulated Raman scattering threshold is reached, the laser can be depleted $\geq$10% and depletion approaches $\approx$50% as the incident laser energy increases. In other studies [18], we measured both transmitted laser and Stokes pulse energies after the Raman cell as a function of incident laser pulse energy. Coincident sharp thresholds for stimulated Stokes scattering and subsequent laser depletion versus incident laser pulse energy were observed. There was a nearly one-to-one relationship between photons removed from the transmitted laser pulse and photons added to the

transmitted Stokes pulse. Consequently, we are confident that this vibrational dephasing experiment was performed with excitation pulses in the high laser depletion regime.

IV. Temperature-Controlled Cell

In order to minimize depolarization in the 10 cm Raman cell, the temperature-controlled cell shown in Fig. 4 was designed. Birefringence in the windows of the cell was the major difficulty and low birefringence glass windows were required. Schott glass SF-57 was selected because of its extremely low birefringence. Unfortunately, SF-57 is a soft, high density lead glass and is difficult to polish. Using the proper polishing techniques, the 2 mm thick SF-57 glass flats used in this experiment were polished optically flat ($\simeq\lambda/2$) with nearly parallel surfaces. After polishing and between experimental runs, the windows were stored in a dessicator. This precaution was taken because the SF-57 glass surface is sensitive to water and other chemicals.

The birefringence problem was complicated by the different thermal expansion coefficients of the various materials in the cell. A strain relieving copper window mount identical to the design presented by Mollenauer et al. [32] was used to eliminate the thermally-induced strain birefringence. We had difficulties with their epoxy recipe because the curing cycle at 150° C caused the SF-57 glass to be chemically etched. We resorted to a 50-50 mixture of Shell Epon Resin 828 and Versamid 140 polyamide resin [33]. This epoxy mixture cures at room temperature in approximately 48 hours and gives a flexible, leak-tight and temperature resistent seal. The window mounts were attached

FIG. 3. Excitation laser pulse depletion examined by monitering the transmitted laser pulse energy with and without a 10 cm acetonitrile Raman cell. The approximate range of laser pulse energies used in the vibrational dephasing experiment is also shown.

FIG. 4. Vertical cross section of the temperature-controlled Raman cell equipped with the "gas window" design.

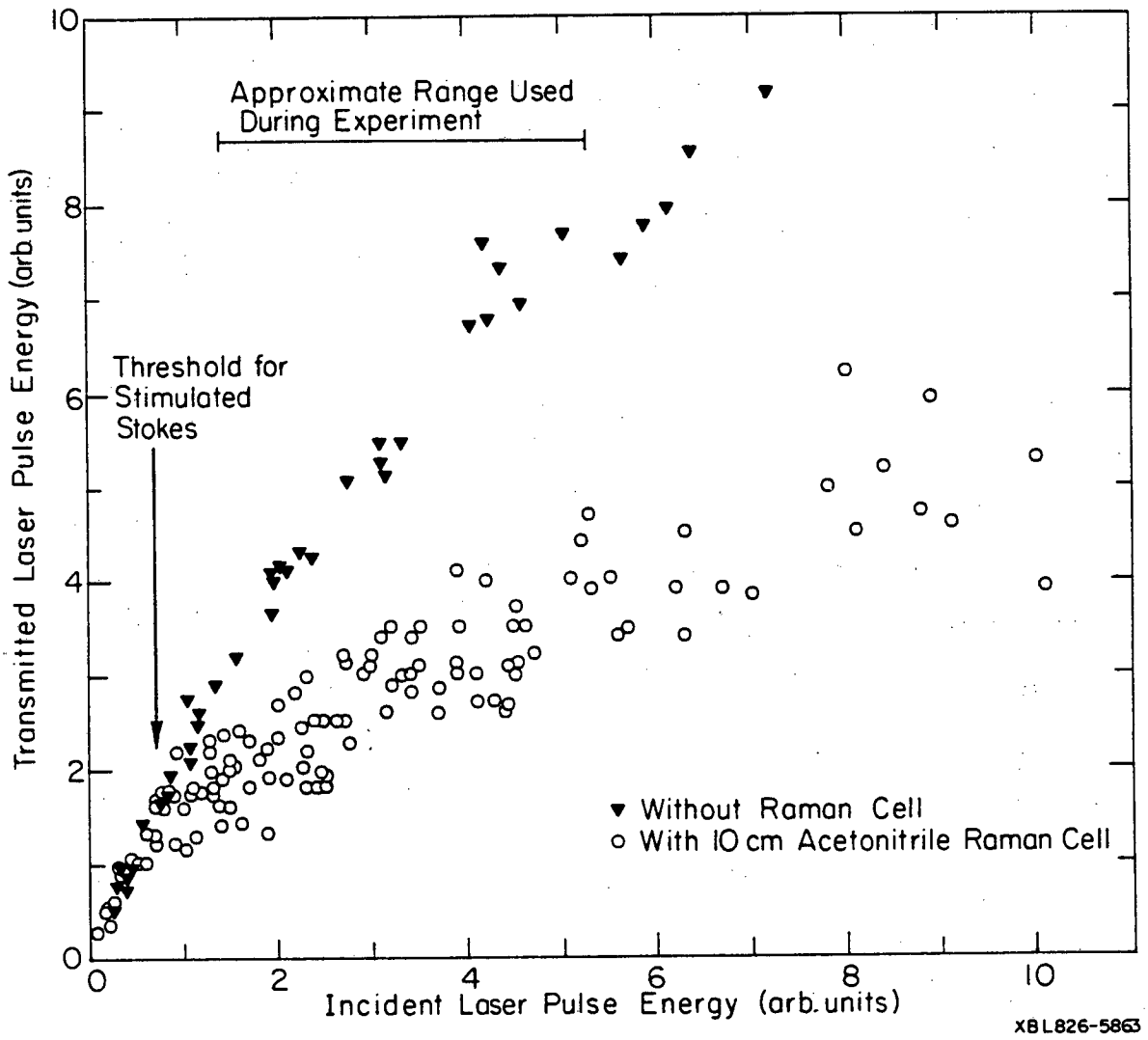
Approximate Range Used
During Experiment
Threshold for
Stimulated
Stokes
Transmitted Laser Pulse Energy (arb. units)
Incident Laser Pulse Energy (arb. units)
▼ Without Raman Cell
○ With 10 cm Acetonitrile Raman Cell
0
2
4
6
8
10
XBL826-5863

Figure 3

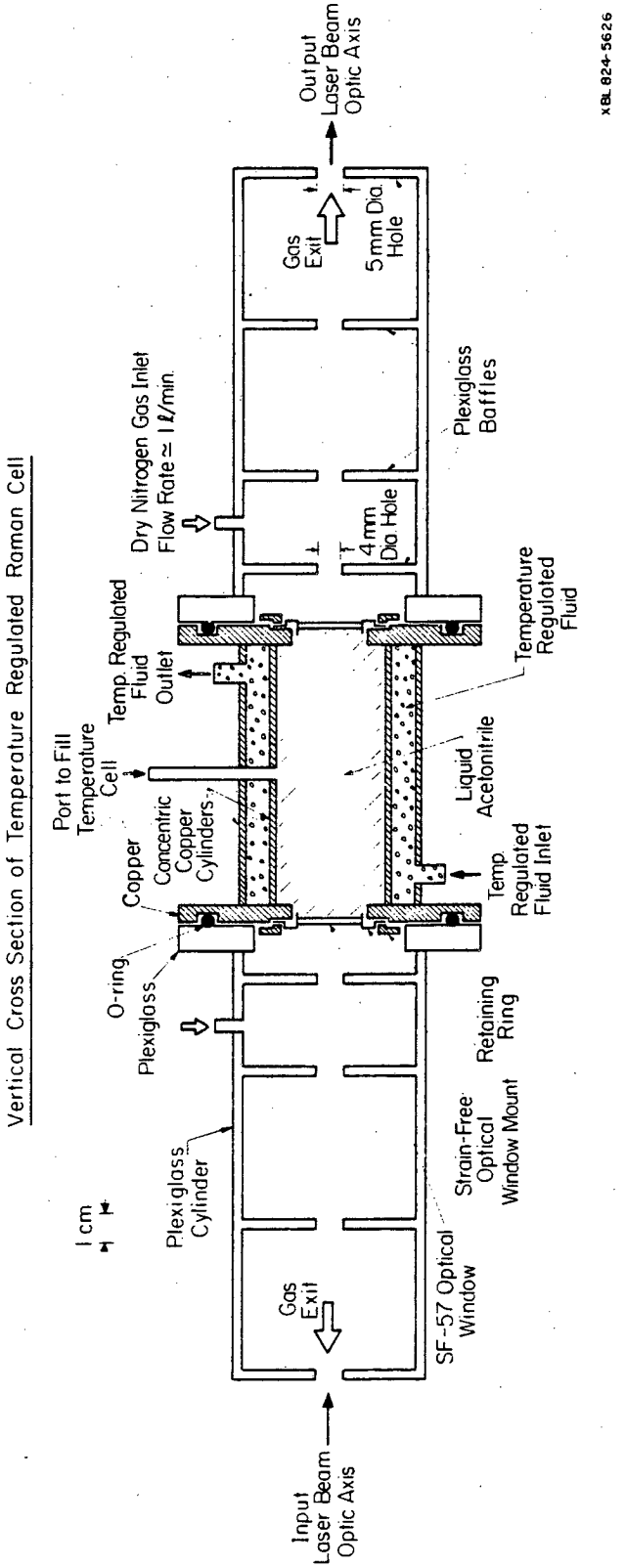
Vertical Cross Section of Temperature Regulated Raman Cell
1 cm
Input Laser Beam Optic Axis
Output Laser Beam Optic Axis
Gas Exit
Gas Exit
Plexiglass Cylinder
Plexiglass
O-ring
Copper
Concentric Copper Cylinders
Port to Fill Temperature Cell
Temp. Regulated Fluid Outlet
Dry Nitrogen Gas Inlet Flow Rate ≃ 1 ℓ/min.
5 mm Dia. Hole
4 mm Dia Hole
Plexiglass Baffles
Temperature Regulated Fluid
Liquid Acetonitrile
Temp. Regulated Fluid Inlet
Retaining Ring
Strain-Free Optical Window Mount
SF-57 Optical Window
XBL 824-5626

Figure 4

to the copper low temperature cell using a retaining ring which was screwed down around the copper window mount and allowed the windows to be taken on and off easily. A flat teflon ring formed the seal between the window mount and the copper low temperature cell.

An additional special design was employed for the -40° C and -10° C temperature points. This design involved flowing nitrogen gas through a series of baffles [34]. A vertical cross section of the temperature regulating cell utilyzing this design is shown in Fig. 4. Using the "gas windows", the temperature gradient between the windows of the 10 cm cell and room temperature was accepted by the outwardly flowing dry nitrogen gas and the flowing gas prevented water vapor from condensing on the windows. As a result, the "gas window" design avoided the necessitity of using two additional outside windows and a vacuum jacket. During experimental runs, nitrogen gas flow rates of approximately 1 liter per minute were used for each window. More vigorous flow rates are were used to flush out the system prior to cooling the low temperature cell.

When controlling the cell at -40°, -10°, 45° and 70° C, the temperature cell was insulated with styrofoam. The temperature of the cell was regulated at 70°, 45° and -10° C using a Lauda K-2/R circulator. The temperature was controlled at -40° C using a dry ice/o-xylene/m-xylene slush bath [35] to control the circulating coolant temperature. The cell temperature was monitered using a copper/constantan thermocouple mounted on the copper block of the cell.

V. Results

Some representative normalized coherent Stokes signals versus delay time at the various temperatures are shown in Figs. 5(a) and 5(c) and Figs. 6(a) and 6(c). Each point in the slope region of these vibrational dephasing curves is an arithmetic average of approximately 10-25 individual shots. The error bars represent the standard deviation of the individual coherent Stokes signals. If the standard deviation of the mean was used, the calculated error bars were less because of the large number of individual shots. The error bars associated with the standard deviation of the mean led to an accuracy of ±0.2 psec in the slope measurement.

The central point average [36] indicated by the open triangles is also shown in the slope region of Figs. 5(a) and 5(c) and Figs. 6(a) and 6(c). Close agreement of the arithmetic average and the central point average illustrates that the pulse durations are not fluctuating significantly. This is in agreement with the TPF investigations in Sec. III.B.

The experimental dephasing times from individual measurements are shown in Fig. 7. The measurements are numbered according to the sequence in which they were performed. Figure 7 illustrates that the decay times from individual measurements at the various temperatures are consistently different and reproducible. The experimental error of ±0.2 psec on the individual $T_2/2$ measurements is well within the differences between various temperatures.

Recent theoretical studies have indicated that non-selective behavior is expected in low laser depletion [14,15]. On the other hand,

FIG. 5. Experimental data for the symmetric CH_3-stretching vibration in acetonitrile versus temperature. Coherently scattered Stokes signal as a function of probe delay at (a) -40° C and (c) -10° C. Isotropic Raman line shapes and homogeneous Lorentzian line shapes calculated from measured dephasing times at (b) -40° C and (d) -10° C.

FIG. 6. Experimental data for the symmetric CH_3-stretching vibration in acetonitrile versus temperature. Coherently scattered Stokes signal as a function of probe delay at (a) 18° C and (c) 70° C. Isotropic Raman line shapes and homogeneous Lorentzian line shapes calculated from measured dephasing times at (b) 18° C and (d) 70° C.

FIG. 7. Experimental dephasing times from individual measurements versus temperature. The measurements are numbered according to the sequence in which they were performed.

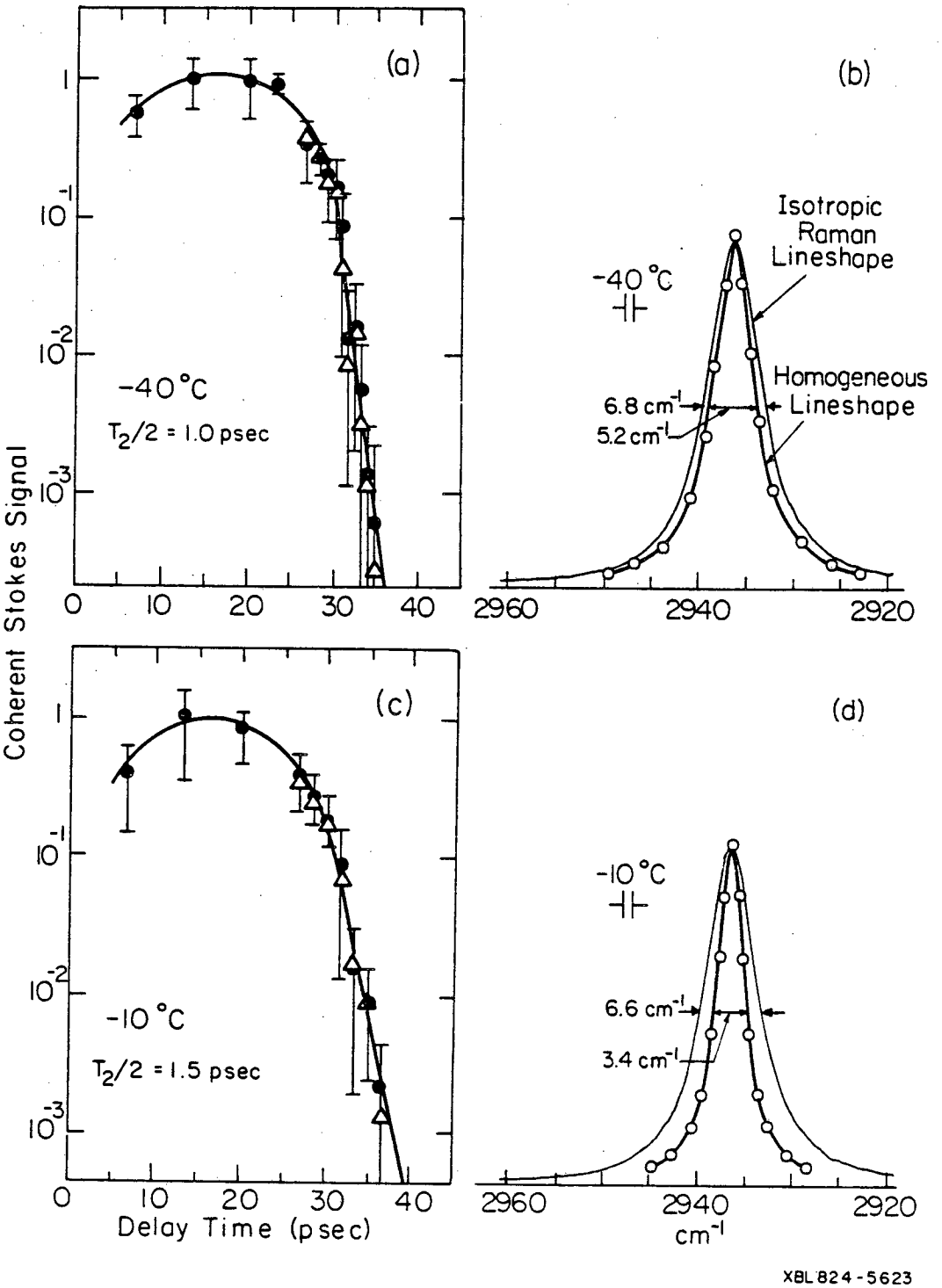
(a)
(b)
(c)
(d)
Coherent Stokes Signal
-40 °C
$T_2/2$ = 1.0 psec
-10 °C
$T_2/2$ = 1.5 psec
Delay Time (psec)
Isotropic Raman Lineshape
Homogeneous Lineshape
6.8 cm^{-1}
5.2 cm^{-1}
6.6 cm^{-1}
3.4 cm^{-1}
cm^{-1}
XBL824-5623

Figure 5

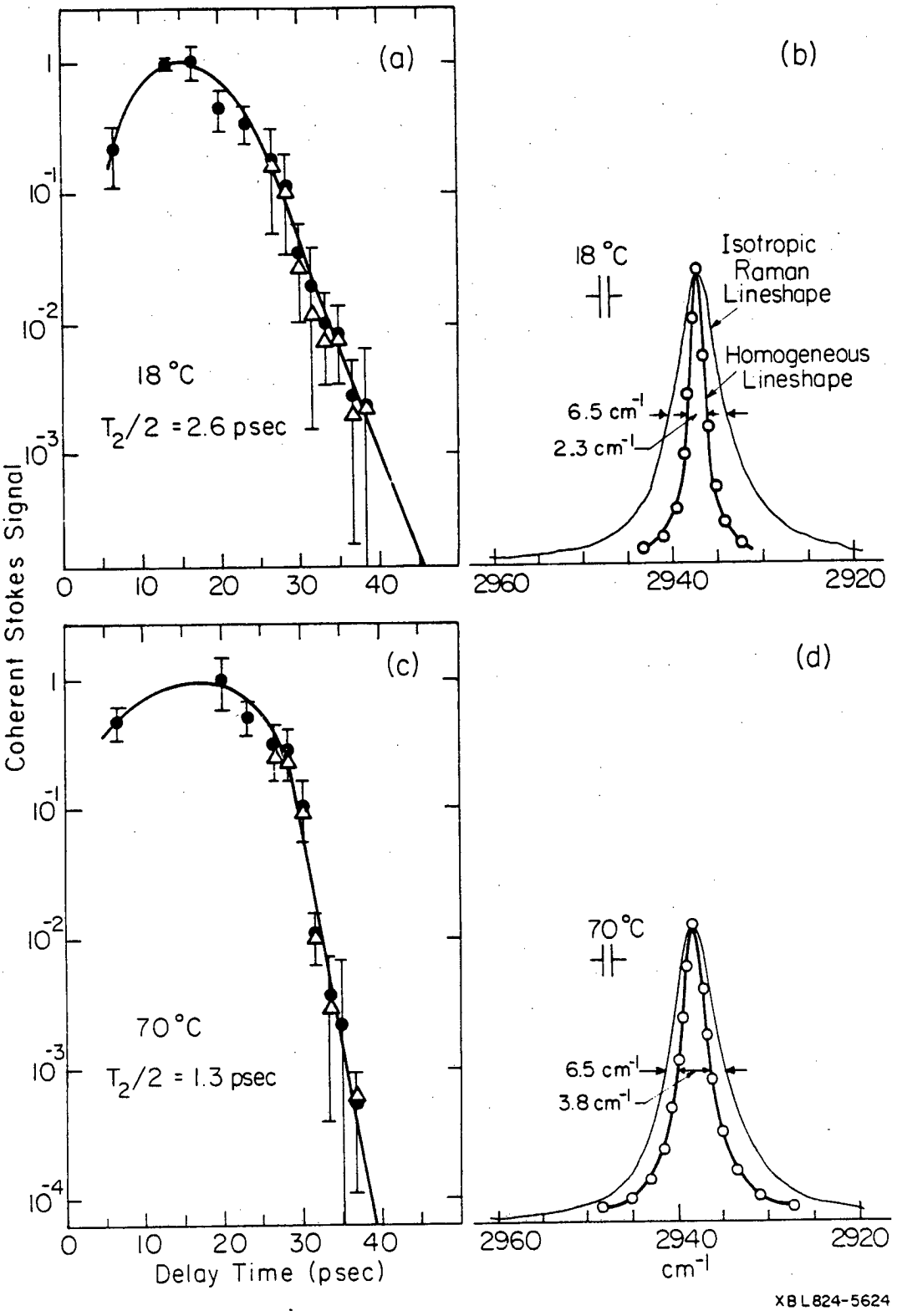
(a)
(b)
(c)
(d)
18 °C
$T_2/2$ = 2.6 psec
70 °C
$T_2/2$ = 1.3 psec
Coherent Stokes Signal
Delay Time (psec)
Isotropic Raman Lineshape
Homogeneous Lineshape
6.5 cm^{-1}
2.3 cm^{-1}
3.8 cm^{-1}
cm^{-1}
XBL824-5624

Figure 6

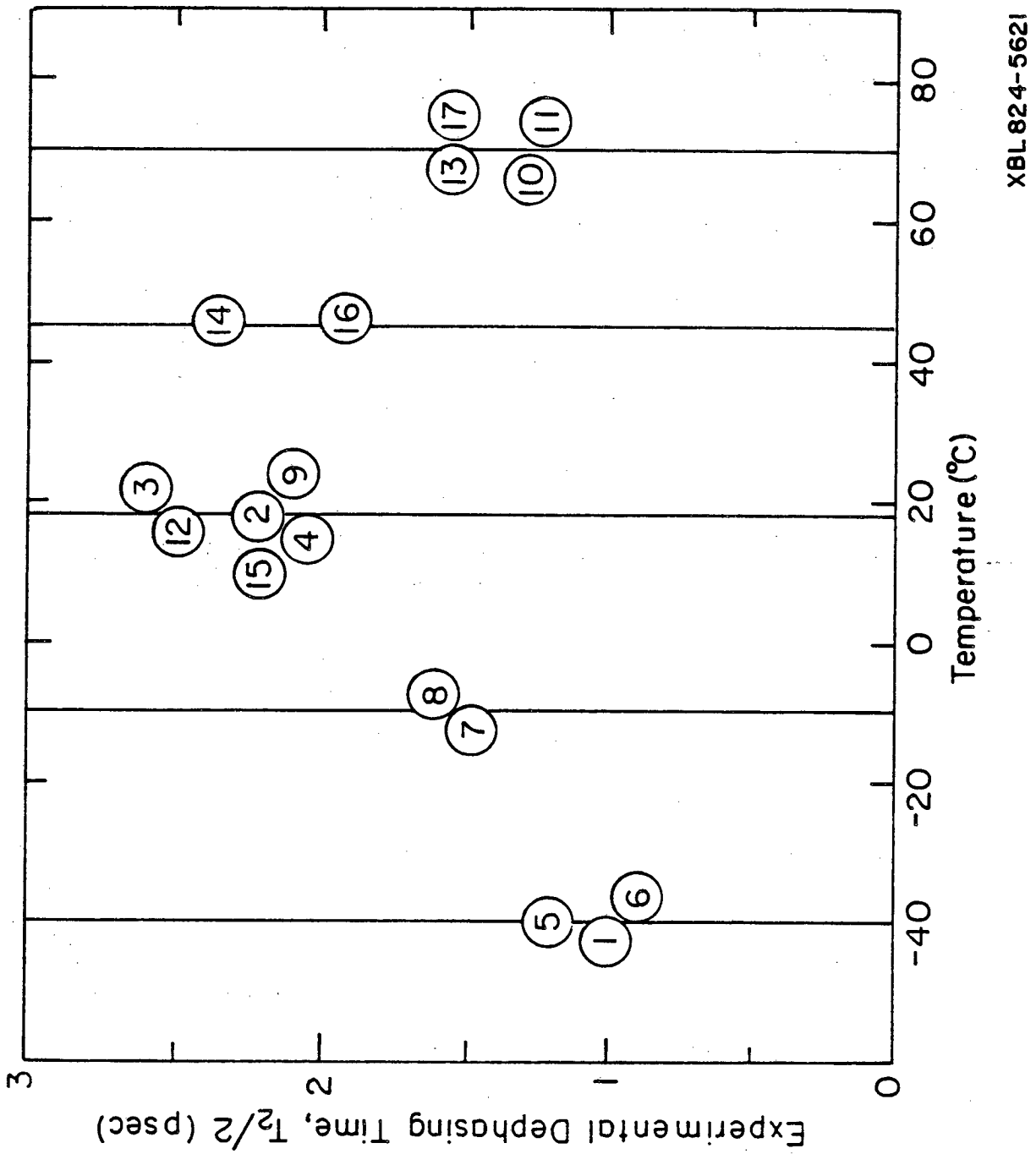
Experimental Dephasing Time, $T_2/2$ (psec)
0
1
2
3
-40
-20
0
20
40
60
80
Temperature (°C)
1
2
3
4
5
6
7
8
9
10
11
12
13
14
15
16
17
XBL824-5621

Figure 7

our general theory has revealed that high laser depletion leads to enhanced selectivity which enables homogeneous dephasing time T_2 to be measured to a high level of accuracy in inhomogeneously broadened vibrational linewidths [14]. We note that if this high laser depletion experiment was not selective, the probing process should have yielded nearly identical rapid coherent Stokes signal decay curves at each temperature [14,15]. This predicted non-selective behavior corresponds to the nearly invariant temperature-dependent isotropic Raman linewidth of the symmetric CH_3-stretching vibration in liquid acetonitrile [11]. Figure 7 demonstrates that this behavior was not observed. Thus the different, reproducible vibrational dephasing times measured using high laser depletion support the results of our general theory [14].

The level of accuracy of the T_2 measurement in high laser depletion has been previously discussed [14]. In this experiment, we estimate that the measured decay time is approximately >80-90% of the actual $T_2/2$ homogeneous decay time. Because of this high level of accuracy, we assumed that the experimentally measured decay is equivalent to $T_2/2$ in the following analysis.

The isotropic spontaneous Raman lineshapes at the various temperatures are shown in Figs. 5(b) and 5(d) and Figs. 6(b) and 6(d). The homogeneous linewidths $\Delta\omega_H$ (FWHM) of the Lorentzian lineshapes corresponding to the average measured homogeneous dephasing times, $T_2/2$, were calculated using:

$$\Delta\omega_H(cm^{-1}) = 1/c\pi T_2 \qquad (1)$$

The homogeneous Lorentzian lineshapes are drawn in Figs. 5(b) and 5(d)

and Figs. 6(b) and 6(d). From these superimposed lineshapes, the inhomogeneous broadening can easily be visualized.

The inhomogeneous broadened linewidths were calculated by deconvoluting the homogeneous lineshapes from the spontaneous Raman lineshapes. The deconvolution method assumed a Lorentzian homogeneous lineshape and a Gaussian inhomogeneous lineshape and has been previously discussed [3]. The average experimental $T_2/2$ times, the calculated homogeneous linewidths(FWHM), the measured isotropic Raman spontaneous linewidths(FWHM) and the calculated Gaussian inhomogeneous linewidths(FWHM) are given in Table 1.

VI. Temperature Dependent Vibrational Linewidth Broadening

A. Homogeneous Broadening

Many homogeneous linewidth broadening mechanisms have been proposed [8]. The binary collision [7], the hydrodynamic [37], and the Lynden-Bell [38] models assume that pure dephasing mechanisms predominate and are frequently employed because their predictions are made in terms of measurable physical parameters. For example, predicted homogeneous linewidths are proportional to: $\eta T/\rho$ for the binary collision model; ηT for the hydrodynamic model; and $\rho\eta/T$ for the Lynden-Bell model where ρ is the liquid number density, η is the viscosity and T is the temperature.

Figure 8(a) shows the temperature dependence of the correlation between the homogeneous linewidths calculated from the measured dephasing times using Eq. (1) and the predicted homogeneous

TABLE 1. Experimental dephasing times, calculated homogeneous linewidths, isotropic Raman linewidths and inhomogeneous broadening linewidths for the symmetric CH_3-stretching vibration in acetonitrile versus temperature.

TABLE 1

Temperature (°C)	Average Experimental $T_2/2$ (ps)	Calculated Homogeneous $\Delta\omega$ (cm^{-1})	Isotropic Raman $\Delta\omega$ (cm^{-1})	Gaussian Inhomogeneous Δ (cm^{-1})
70	1.4	3.8	6.5	4.1
45	2.1	2.5	6.5	5.1
18	2.3	2.3	6.5	5.2
-10	1.6	3.4	6.6	4.5
-45	1.0	5.2	6.8	3.3

linewidths. The predicted theoretical values were calculated using measured density [39-43] and viscosity [40,41,43,44] values. The predicted homogeneous linewidths were normalized to give the experimentally determined homogeneous linewidth at 18° C.

The homogeneous broadening models correctly predict broader homogeneous linewidths at lower temperatures. The broader predicted linewidths are largely due to higher viscosity at lower temperatures. Assuming a collisional mechanism in which a collision perturbs the frequency of the vibration, the higher viscosity indicates a higher repulsive collision rate which increases the homogeneous linewidth. The data at lower temperatures do not support one theory more than the others. None of these theories can account for the increased homogeneous linewidth above 45° C. This deviation at higher temperatures will be discussed in Sec. VII.

B. Inhomogeneous Broadening

Using picosecond excite-and-probe vibrational dephasing experiments which are now known to have been conducted using transient stimulated Raman scattering in high laser depletion, George, Auweter and Harris [3] measured dephasing times for symmetric CH_3-stretching vibrations in a variety of liquids. In conjunction with isotropic Raman studies, they showed that the vibrational linewidths for symmetric CH_3-stretching vibrations in nonhydrogen-bonded liquids at room temperature were inhomogeneously broadened to various degrees. A correlation was observed between the inhomogeneous broadening and the width of the number density distribution in the liquid [3]. The correlation

suggested that a distribution of different, slowly varying, local number densities in a liquid creates a distribution of distinct vibrational frequencies.

Schweizer and Chandler (SC) have recently proposed a comprehensive vibrational dephasing theory. Their theory places the correlation between inhomogeneous broadening and the width of the local number density distribution in a liquid on firm theoretical grounds. Furthermore, their theory shows that long range attractive forces provide the coupling between the slowly varying local number density and the vibration [6].

When the attractive force correlation time, $T_A=\infty$, the SC theory leads to the prediction that $\Delta\omega_{INH}$, the absolute inhomogeneous broadening linewidth (FWHM) is given by:

$$\Delta\omega_{INH} = 2(2\ln 2)^{1/2}/(\bar{N})^{1/2} \times \langle\Omega_A\rangle(\rho\, k_B T\, \kappa_T)^{1/2} \qquad (2)$$

where ρ is the number density, k_BT is the thermal energy, κ_T is the isothermal compressibility, $\bar{N}$ is the estimated average number of nearest neighbors and $\langle\Omega_A\rangle$ is the attractive force contribution to the gas-to-liquid frequency shift. Using this expression, SC [6] found that their predictions were in agreement with isothermal density dependent isotropic Raman linewidths in isobutylene [45]. In addition, the correlation between the predicted and measured inhomogeneous broadening linewidths observed by George, Auweter and Harris [3] was recently shown to be improved by the inclusion of the attractive forces in the SC theory [46].

The SC absolute inhomogeneous broadening linewidth is dependent on

FIG. 8. Temeperature dependent vibrational linewidth broadening in acetonitrile. (a) Correlation of experimentally determined homogeneous linewidths and predicted homogeneous linewidths normalized at 18° C. (b) Correlation of experimentally determined inhomogeneous linewidths and absolute inhomogeneous linewidths predicted by the Schweizer-Chandler theory using three representative $\bar{N}$ values.

FIG. 9. Isothermal compressibility versus temperature in acetonitrile. The filled-in circles are experimental values from A. Wurflinger (Refs. 47,48). The line shows the fit of a hard sphere model (Ref. 49) to the experimental values.

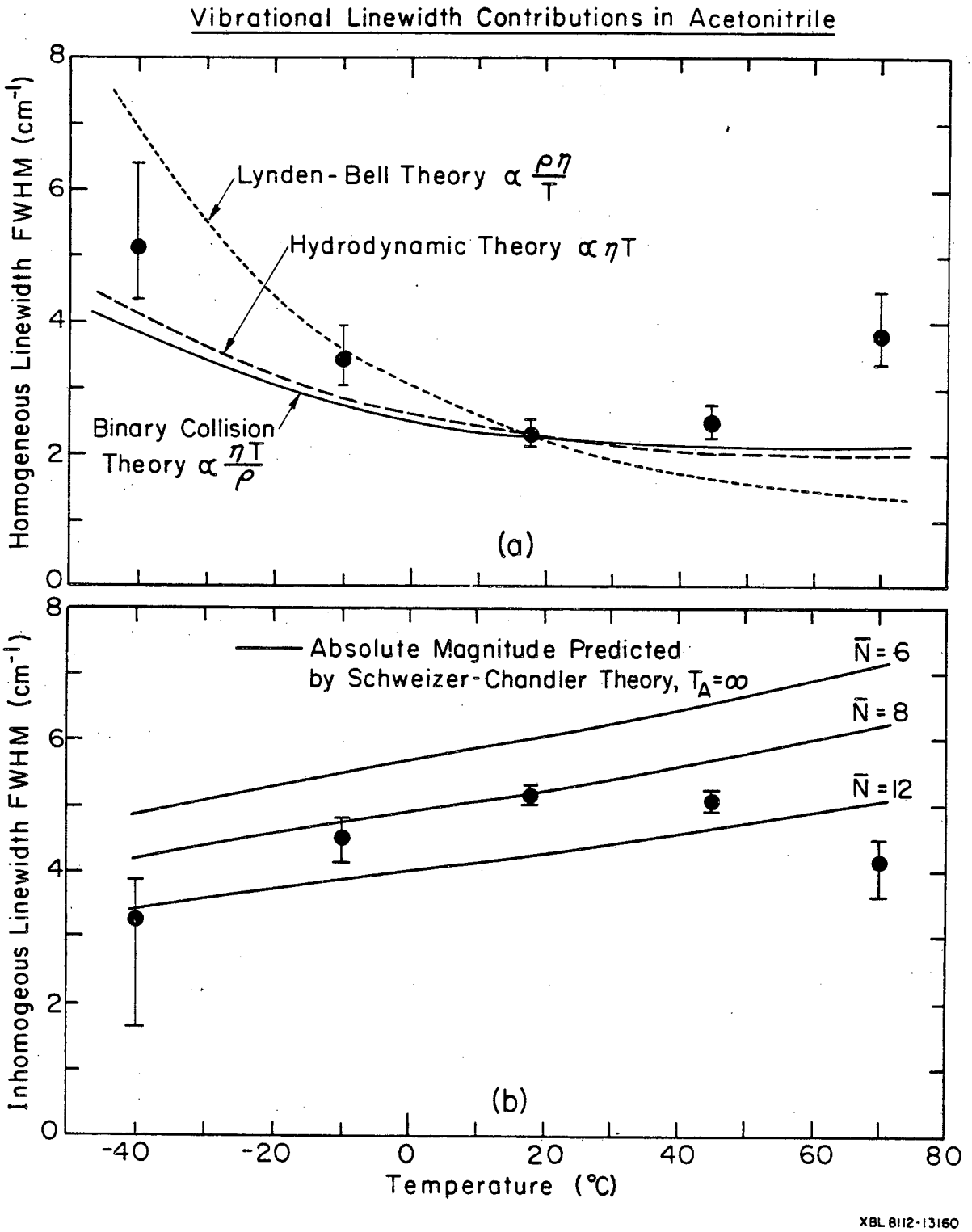
Vibrational Linewidth Contributions in Acetonitrile
Homogeneous Linewidth FWHM (cm⁻¹)
Lynden-Bell Theory α ρη/T
Hydrodynamic Theory α ηT
Binary Collision Theory α ηT/ρ
(a)
Inhomogeneous Linewidth FWHM (cm⁻¹)
Absolute Magnitude Predicted by Schweizer-Chandler Theory, T_A=∞
N̄=6
N̄=8
N̄=12
(b)
Temperature (°C)
XBL 8112-13160

Figure 8

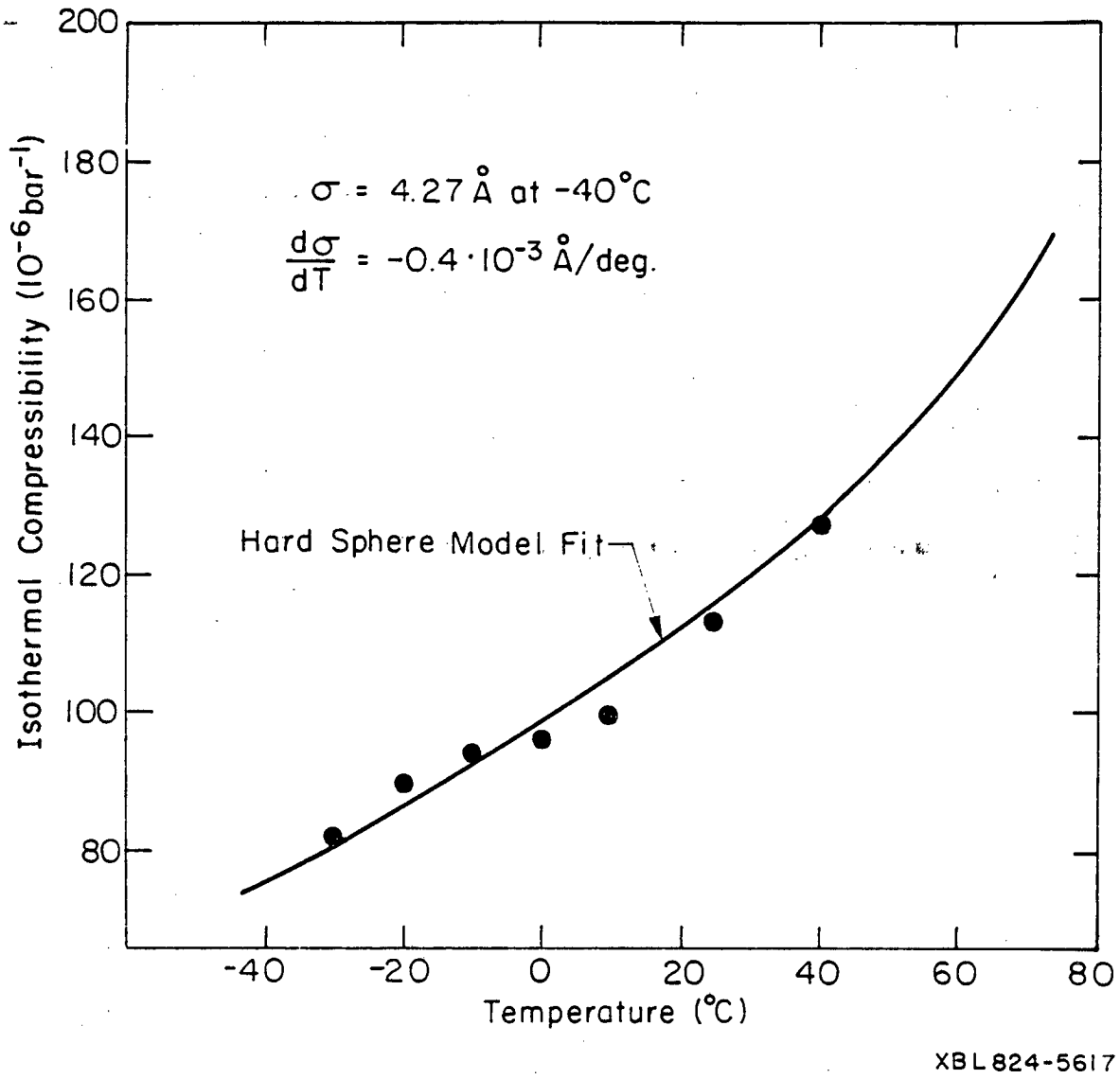
200
180
160
140
120
100
80
Isothermal Compressibility (10^{-6}bar^{-1})
σ = 4.27 Å at -40°C
$\frac{d\sigma}{dT}$ = -0.4·10^{-3} Å/deg.
Hard Sphere Model Fit
-40
-20
0
20
40
60
80
Temperature (°C)
XBL824-5617

Figure 9

κ_T, the isothermal compressibility. Temperature-dependent isothermal compressibility values for acetonitrile were calculated from experimental PVT data [47] using the Tait equation [48]. In order to obtain κ_T values for temperatures outside of the measured range, a hard sphere isothermal compressibility model [49] was fit to the experimental values using σ= 4.27 Å at -40° C and $d\sigma/dT = -0.4\ \Omega\ 10^{-3}$/deg where σ is the hard sphere diameter. These parameters are close to the values derived by Jonas et al. [9]. The temperature dependent heat of vaporization values used in the hard sphere model were calculated from heat capacity data [50]. The hard sphere model's fit to the experimental values is shown in Fig. 9.

The SC absolute inhomogeneous linewidth is also dependent on $\langle\Omega_A\rangle$, the attractive force contribution to the gas-to-liquid shift. Temperature-dependent $\langle\Omega_A\rangle$ values for the symmetric CH_3-stretching vibration in acetonitrile were calculated according to the SC theory as previously described [46]. For consistency with the hard sphere model of isothermal compressibility, σ=4.27 Å at -40°C and $d\sigma/dT$=-0.4 X 10^{-3}Å/deg were used to evaluate the temperature-dependent cavity distribution function [6]. In addition, the small observed temperature-dependent vibrational frequency shift of ≈1.3 X 10^{-2}cm^{-1}/deg was used to evaluate the experimental gas-to-liquid vibrational frequency shift [6]. Resultant $\langle\Omega_A\rangle$ values were -29.3, -28.6, -27.6, -26.8 and -25.8 cm^{-1} at -40°, -10°, 18°, 45° and 70° C.

Figure 8(b) shows the SC absolute inhomogeneous linewidths, $\Delta\omega_{INH}$, calculated according to Eq. (2) for three different representative $\bar{N}$ values [6]. These absolute predictions, based on T_A=∞, are remarkably close to the experimentally determined inhomogeneous linewidths. Below

45° C, the SC theory correctly predicts broader inhomogeneous linewidths at higher temperatures. The temperature dependence of the inhomogeneous linewidth is determined largely by $(\kappa_T)^{1/2}$. Consequently, the higher liquid compressibility at higher temperatures increases the predicted absolute inhomogeneous linewidths. Above 45° C, the measured inhomogeneous linewidths are narrowed in comparison to the theoretical predictions. This deviation at higher temperatures will be discussed in Sec. VII.

C. Conclusions

These results demonstrate that homogeneous and inhomogeneous broadening contributions change significantly with temperature. Figures 8(a) and 8(b) reveal that the variations in the homogeneous and inhomogeneous linewidth broadening with temperature have opposing effects. Below 45° C, the homogeneous linewidth decreases and the inhomogeneous linewidth increases with increasing temperature. In the case of acetonitrile, these counterbalancing homogeneous and inhomogeneous temperature dependences lead to little observed change in the isotropic Raman linewidth [11]. We note that these opposing temperature trends are predicted by the Schweizer-Chandler vibrational dephasing theory [6].

The agreement between experiment and theory supports the association of homogeneous broadening with rapidly varying short range processes. These rapidly varying processes, e.g., collisions, probably affect the vibration through repulsive forces. Likewise, the results support the association of inhomogeneous broadening with a distribution

of slowly varying local number density sites. These local density sites are thought to interact with the vibration through the long range attractive forces in the liquid.

VII. Deviation from Theory at High Temperatures

Experimental [3] and theoretical [6] results suggest that a distribution of local density sites creates an inhomogeneous distribution of distinct vibrational frequencies through attractive force interactions. The lifetime of these local density sites determines the degree of separation between homogeneous and inhomogeneous broadening processes. When the lifetime is long, e.g., >10 psec, there is a clear separation. As the lifetime becomes shorter, the separation becomes less distinct and the inhomogeneous processes become homogeneous processes as previously discussed [3].

The local density sites are expected to persist for a lifetime approximately equal to the time necessary for a molecule to travel the range of the local density perturbation. Consequently, the lifetime of the local density sites is expected to be proportional to 1/D where D is the translational diffusion constant. The temperature-dependent translational self-diffusion constants in acetonitrile are obtained from NMR spin-echo measurements [51,52] and are shown in Fig. 10.

In the Schweizer-Chandler theory, the correlation time of the attractive force interactions, T_A, characterizes the lifetime of the various local density sites which give rise to inhomogeneous broadening through attractive force interactions. As expected, T_A is proportional

to 1/D. Actual values of T_A are calculated in the Schweizer-Chandler theory by:

$$T_A > \sigma^2/(\pi^2 D) \tag{3}$$

where σ is the hard core diameter [6]. When the temperature is low and the translational diffusion constant is small, Eqn. (3) predicts that T_A or the lifetime of the local density sites is long. Consequently, the selective excite-and-probe vibrational dephasing experiment can measure the homogeneous linewidth of a single, distinct vibrational isochromat corresponding to a single local density site. Likewise, when the temperature is high and the translational diffusion constant is large, Eqn. (3) predicts that the lifetime of the local density sites is shorter.

Because the various local density sites form a closed set, a short lifetime for a local density site is equivalent to a rapid rate of interconversion or exchange between the various sites. The faster rate of site exchange at higher temperatures would have two effects: First, the inhomogeneous distribution of local density sites would be reduced by motional narrowing. Second, the homogeneous linewidth would be broadened by dephasing resulting from exchange between sites with different frequencies. Motional narrowing could account for the narrowing of measured inhomogeneous linewidths in comparison to theoretical predictions at higher temperatures shown on Fig. 8(b). Likewise, site exchange dephasing could account for the broadening of measured homogeneous linewidths in comparison to theoretical predictions at higher temperatures shown on Fig. 8(a).

FIG. 10. Translational self-diffusion constant versus temperature in acetonitrile. The filled-in circles are experimental values from M.D. Zeidler (Ref. 51). The open triangles are experimental values from A. Kratochwill (Ref. 52).

FIG. 11. Correlation between experimentally measured dephasing times, $T_2/2$, and the predicted $T_2/2$ times calculated using Eqn. (4) which includes diffusional site exchange. The predicted $T_2/2$ dephasing times were fit to the data using τ=4 psec at 70° C. The pure dephasing times, $T_2^*/2$, from the hydrodynamic dephasing theory are also shown.

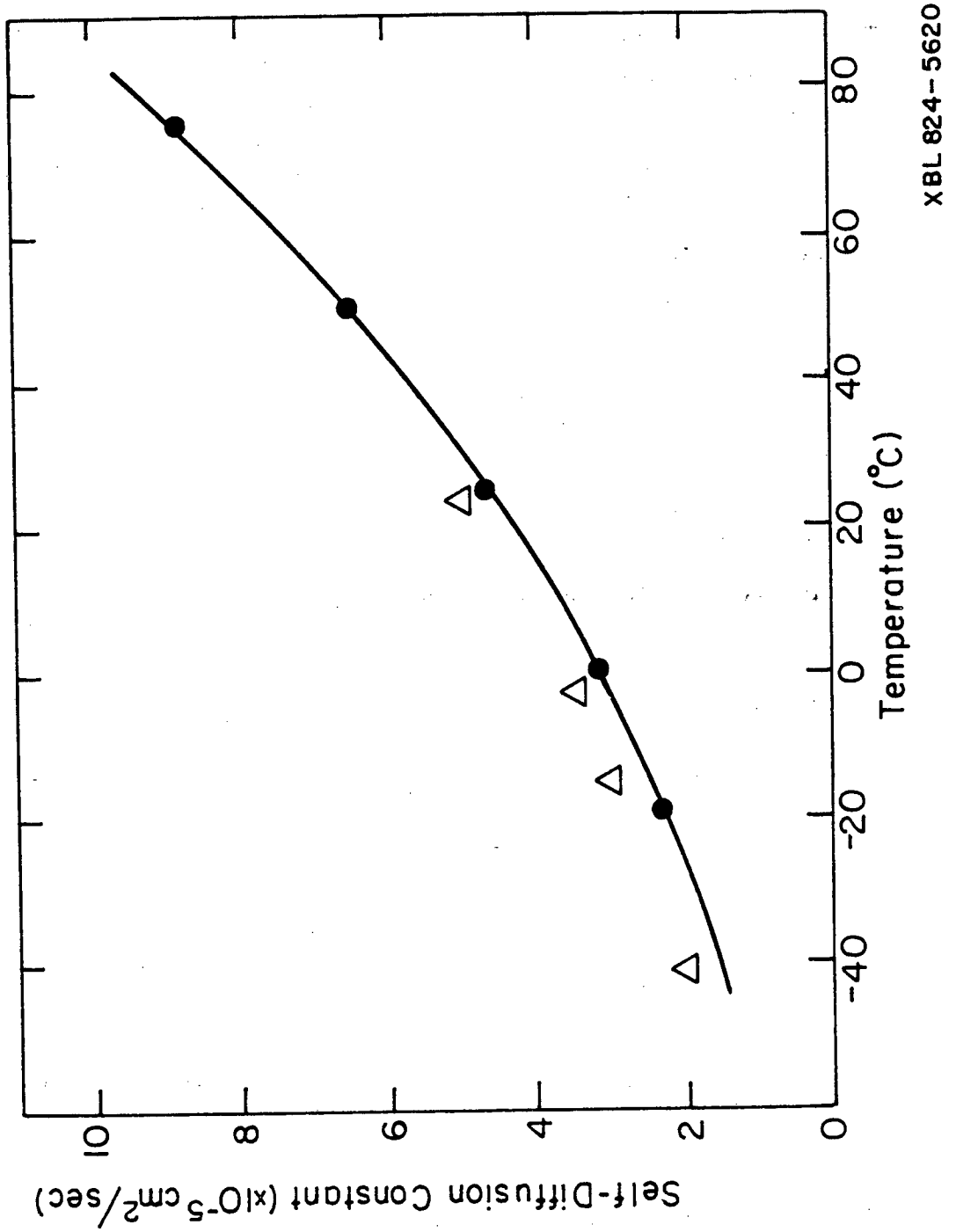
Self-Diffusion Constant ($\times 10^{-5}$ cm^2/sec)
0
2
4
6
8
10
-40
-20
0
20
40
60
80
Temperature (°C)
XBL 824-5620

Figure 10

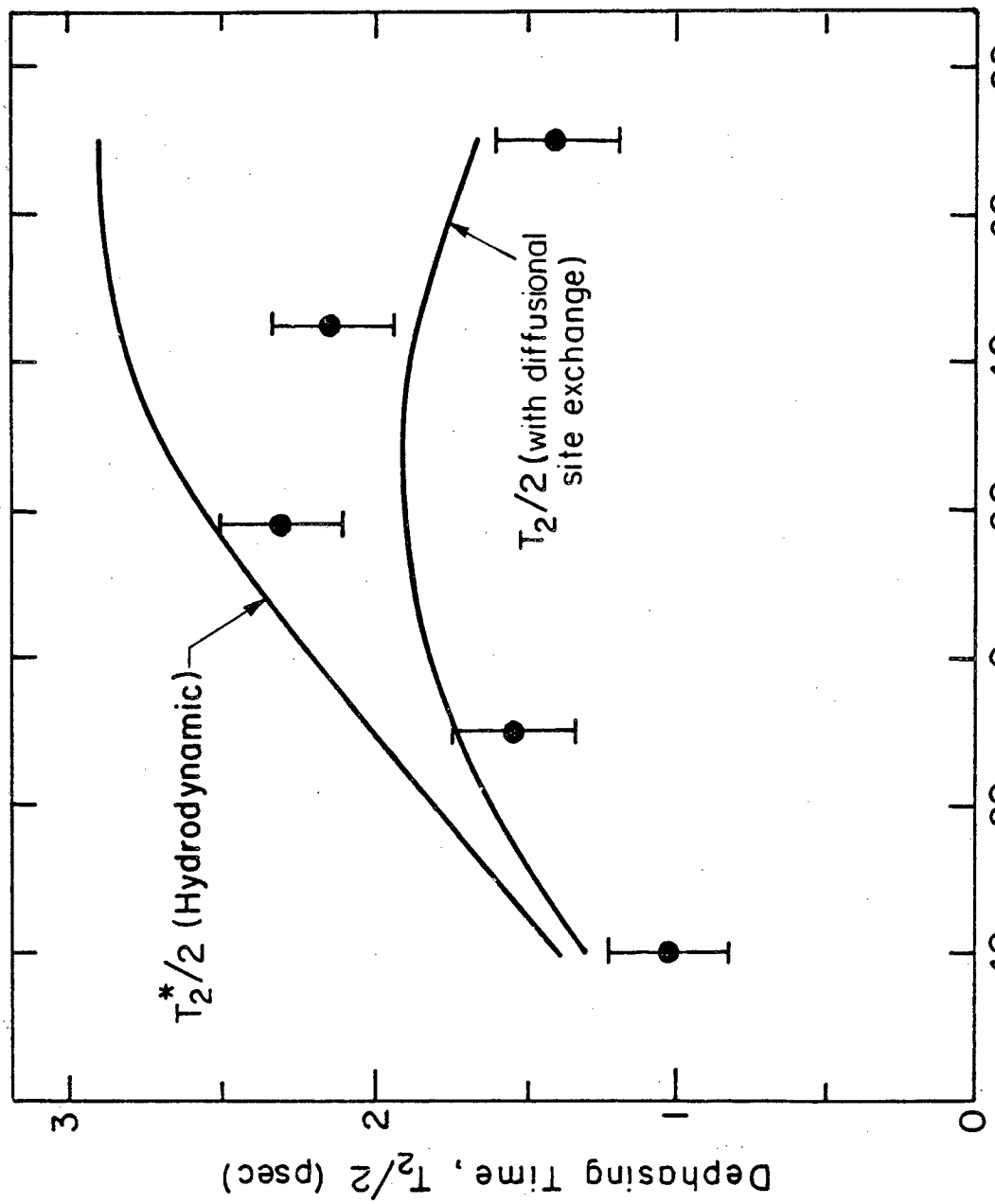
Dephasing Time, $T_2/2$ (psec)
3
2
1
0
-40
-20
0
20
40
60
80
Temperature (°C)
$T_2^*/2$ (Hydrodynamic)
$T_2/2$ (with diffusional site exchange)
XBL824-5619

Figure 11

The homogeneous linewidth broadening from site exchange would depend on the exact nature of the site exchange. Assuming two separate isochromats undergoing exchange in the Markov limit, the individual linewidths would broaden as $1/\tau$ where τ is the exchange time [53]. Consequently, as a simple extension of two-site exchange, the effect of diffusional site exchange on the homogeneous dephasing time T_2 was modeled according to:

$$2/T_2 = 2/T_2^* + 1/\tau \qquad (4)$$

where T_2^* is the pure dephasing time and τ is proportional to $1/D$. Notice that the effect of τ on T_2 is similar to the effect of T_1, the population lifetime, on T_2 [7].

A fit to the data when τ = 4 psec at 70° C and T_2^* is based on the hydrodynamic dephasing model [37] is shown in Fig. 11. Figure 11 shows that the predicted $T_2/2$ times including diffusional site exchange display the correct qualitative behavior. We note that a τ= 4 psec at 70° C is in approximate agreement with the calculated $T_A \geq 2.3$ psec calculated from the Schweizer-Chandler theory using Eq. (3) with σ = 4.3 Å and D = 8.3 x 10^{-5} cm^2/sec. We believe that these results are consistent with the first observation of the interconversion of local density sites or "spectral diffusion" in a liquid.

VIII. Alternative Broadening Mechanisms

A. Other Possible Homogeneous Broadening Mechanisms

Many diverse mechanisms may influence the T_2 homogeneous dephasing time [8]. Ignoring the dephasing contribution from site exchange discussed in Sec. VII, the major T_2 dephasing contributions in liquids are generally believed to be: the pure dephasing time, T_2^*; the resonant energy transfer time, T_r; and the population relaxation time, T_1. In certain limits, the T_2 dephasing time can be expressed as [8]:

$$2/T_2 = 2/T_2^* + 2/T_r + 1/T_1 \qquad (5)$$

Isotope dilution studies indicate little contribution to T_2 from resonant vibrational energy transfer [9,11]. In addition, the population lifetime is generally assumed to be much longer that T_2^*. If this assumption is valid, Eqn. (5) indicates that $T_2 \simeq T_2^*$. This assumption was utilized in Sec. VI.A. On the other hand, recent experimental measurements have revealed that T_1 for the symmetric CH_3-stretching vibration in liquids can be extremely rapid [54,55]. Consequently, T_1 effects can make a significant contribution to T_2 and an analysis of the vibrational dephasing mechanisms must include possible population relaxation effects.

The rapid T_1 population relaxation times for the symmetric CH_3-stretching vibration are believed to be determined by the Fermi resonance between the symmetric CH_3-stretching vibration and overtones

of the CH_3-bend [54-56]. Although T_1 has not been measured for acetonitrile, there are several indications which suggest that acetonitrile may have a Fermi resonance. Using the intensity method of determining Fermi resonance [57], a Fermi resonance would be predicted in acetonitrile between the symmetric CH_3-stretching vibration and the overtone of the symmetic CH_3-bending mode [58]. In addition, comparison of CH-stretching frequencies in CH_3CN and CHD_2CN provides a means to assess the Fermi resonance frequency shift [57]. Using this method, a positive Fermi resonance shift is determined [59].

The above evidence suggests that T_1 effects may make a contribution to the observed T_2 dephasing times. We note that, although our analysis of T_2 was performed assuming that $T_2^* \approx T_2$, a T_2 dominated by T_1 should have approximately the same temperature dependence. For example, in the binary collision model [7], T_1 depends directly on the collision rate and shows roughly the same dependence on macroscopic liquid parameters as T_2^*.

B. Other Possible Inhomogeneous Broadening Mechanisms

In addition to the inhomogeneous broadening mechanism based on slowly varying local density fluctuations, other slowly varying attractive or repulsive mechanisms may also establish various local sites in liquid acetonitrile and lead to inhomogeneous broadening. For example, the large electric dipole moment of acetonitrile can lead to dipole-dipole associativity. Thermodynamic investigations have emphasized the importance of dipole-dipole associativity [60-62]. Spectroscopic studies also have indicated the formation of dipole pairs

or dipole-dipole complexes [63-67]. On the other hand, theoretical investigations have shown that hard core repulsive forces create clusters of orientational correlation in liquid acetonitrile [68]. Whatever the exact mechanism, X-ray and neutron scattering investivations have revealed the existence of correlation clusters in liquid acetonitrile with a diameter ≈11Å [69,70].

The existence of dipole-dipole associativity and correlation clusters in liquid acetonitrile suggests that a distribution of various slowly-varying dipole-dipole complexes or correlation clusters could create an inhomogeneous distribution of distinct vibrational frequencies. The distribution width of the various correlation clusters may be determined by the distribution width of the local number densities. Consequently, the temperature dependence of this inhomogeneous broadening would be expected to be similar to the predicted inhomogeneous broadening discussed in Sec. VI.B. In a similar manner to the local density sites discussed in Sec. VII, the lifetime of the correlation clusters would also be expected to be proportional to 1/D, where D is the translational diffusion constant. As a result, the deviation of the measured homogeneous and inhomogeneous linewidths from the theoretical predictions at high temperatures could also be explained using this inhomogeneous broadening mechanism.

IX. Summary

The temperature dependence of homogeneous and inhomogeneous vibrational linewidth broadening is presented for the symmetric CH_3-stretching vibration in liquid acetonitrile from -40° to 70° C at P=1 Atm. The separation of homogenoeus and inhomogeneous broadening is accomplished using the combined results of isotropic spontaneous Raman studies and selective excite-and-probe vibrational dephasing experiments. The results show that homogeneous and inhomogeneous vibrational linewidth broadening contributions change in opposing directions with temperature.

At lower temperatures, the homogeneous linewidth decreases and the inhomogeneous linewidth increases with increasing temperature. The qualitative agreement between the measured homogeneous linewidths and the pure dephasing models supports previous suggestions that homogeneous broadening is caused by rapidly varying repulsive forces. The nearly quantitative agreement between the measured inhomogeneous linewidths and the absolute inhomogeneous linewidths predicted by the Schweizer-Chandler theory supports the suggestion that inhomogeneous broadening is caused by slowly varying attractive forces.

Inhomogeneous broadening contributes a substantial fraction to the symmetric CH_3-stretching linewidth in liquid acetonitrile. The temperature-dependent inhomogeneous broadening results supports the idea that a distribution of local number densities in the liquid creates an inhomogeneous distribution of distinct vibrational frequencies. At higher temperatures, the lifetime of the local number density sites affects the separation of homogeneous and inhomogeneous broadening

processes. The results are consistent with the first observation of the interconversion of local density sites or "spectral diffusion" in a liquid.

Different, reproducible vibrational dephasing times are measured at various temperatures using a technique based on transient stimulated Raman scattering in high laser depletion. This work supports the conclusions of a recent theory for selective vibrational dephasing experiments in high laser depletion [14]. The results indicate that, contrary to the work in low laser depletion [15], selective excite-and-probe experiments are possible in high laser depletion. Previous vibrational dephasing experiments [1-5,16,17] which are in conflict with the low laser depletion theory [14,15] can be explained if they were conducted in high laser depletion.

References

1. A. Laubereau and W. Kaiser, Rev. Mod. Phys. 50, 607(1978).
2. A. Laubereau, G. Wochner and W. Kaiser, Chem. Phys. 28, 363(1978).
3. S.M. George, H. Auweter and C.B. Harris, J. Chem. Phys. 73, 5573(1980).
4. C.B. Harris, H. Auweter and S.M George, Phy. Rev. Lett. 44, 737(1980).
5. C.B. Harris, H. Auweter and S.M. George, in Picosecond Phenomena II, ed. by R.M. Hochstrasser, W. Kaiser and C.V. Shank, Springer Ser. Chem. Phys. 14 (Springer-Verlag, Berlin, Heidelberg, New York, 1980) p. 151.
6. K.S. Schweizer and D. Chandler, J. Chem. Phys. 76, 2296(1982).
7. S.F. Fischer and A. Laubereau, Chem. Phys. Lett. 35, 6(1975).
8. D.W. Oxtoby, Adv. Chem. Phys. 40, 1(1979).
9. J. Schroeder, V.H. Schiemann, P.T. Sharko and J. Jonas J. Chem. Phys. 66, 3215(1977).
10. K. Tanabe, Chem. Phys. 38, 125(1979).
11. J. Yarwood, R. Arndt and G. Doge, Chem. Phys. 25, 387(1977).
12. J. Yarwood, R. Ackroyd, K.E. Arnold, G. Doge and R. Arndt, Chem. Phys. Lett. 77, 239(1981).
13. S.M. George, A.L. Harris, M. Berg and C.B. Harris, in Picosecond Phenomena III, ed. by K.B. Eisenthal, R.M. Hochstrasser, W. Kaiser and A. Laubereau, Springer Ser. Chem. Phys. 23 (Springer-Verlag, Berlin, Heidelberg, New York, 1982) p. 196.
14. S.M. George and C.B. Harris, (submitted to Physical Review A).

15. W. Zinth, H.J. Polland, A. Laubereau and W. Kaiser
Appl. Phys. B26, 77(1981).

16. A. Laubereau, G. Wochner and W. Kaiser
Phy. Rev. 13A, 2212(1976); Opt. Commun. 17, 91(1976).

17. W. Zinth, A. Laubereau and W. Kaiser, Opt. Commun. 26, 457(1978).

18. D. Ben-Amotz, S.M. George and C.B. Harris,
(submitted to Chem. Phys. Lett.).

19. S.M. George and C.B. Harris, Rev. Sci. Instrum. 52, 852(1981).

20. S.J. Davis, J.E. Murray, D.C. Downs and W.H Lowdermilk
Appl. Opt. 17, 3184(1978).

21. D.J. Bradley and G.H.C. New, Proc. IEEE 62, 313(1974).

22. D. von der Linde, O. Bernecker and W. Kaiser,
Opt. Commun. 2, 149(1970).

23. J.A. Giordmaine, P.M. Rentzepis, S.L. Shapiro and K.W. Wecht
Appl. Phys. Lett. 11, 216(1967).

24. J.L. Chao., Appl. Spect. 35, 281(1981).

25. The pulse widths Δt were determined using the expression $\Delta t=\beta\Delta\tau$ where $\Delta\tau=2n\Delta z/c$ is the time width of the TPF autocorrelation width and β is the ratio of Δt and $\Delta\tau$ (Ref. 71). For Gaussian pulses, $\beta=1/(2)^{1/2}$ and for Lorentzian pulses $\beta=1/2$ (Ref. 71). Measured methanol refractive indices in the visible were extrapolated to give $n=1.3235$ at 1.06 μ.

26. D.J. Bradley, G.H.C. New and S.J. Caughey,
Opt. Commun. 2, 41(1970).

27. D.J. Bradley and W. Sibbett, Opt. Commun. 9, 17(1973).

28. A. Penzkofer, Opto-Electron. 20, 87(1972).

29. The effect of Dye #5 as a saturable absorber was also studied. Under the same conditions, pulse shortening ratios of 0.84, 0.74 and 0.71 were observed for Dye #5 at optical densities of 1.0, 2.0 and 3.0, respectively. These smaller pulse shortening ratios were obtained at the cost of significant reduction of the pulse peak intensity.

30. Fresh spectrophotometric grade (99+%) acetonitrile was used from the bottle without further purification for each experimental run.

31. The Glan-laser double escape Q-switch polarizers were obtained from the Karl Lambrecht Corporation, 4204 N. Lincoln Avenue, Chicago, Illinois, 60618.

32. L.F. Mollenauer, C.D. Grandt, W.B. Grant and H. Panepucci, Rev. Sci. Instrum. 39, 1958(1968).

33. Shell Epon Resin 828 is made by the Shell Chemical Company. Versamid 140 polyamide resin is made by General Mills Chemicals, Inc.

34. The design for the low temperature cell was suggested by G. Williams, Univ. College of Wales, Aberystwyth, United Kingdom, and M.S. Beevers, Univ. of Aston, Birmingham, United Kingdom.

35. A.M. Phipps and D.N. Hume, J. Chem. Educ. 45, 664(1968). We used a mixture of approximately 0.6 volume fraction of o-xylene and 0.4 volume fraction of m-xylene.

36. W. Zinth, Appl. Phys. B26, 213(1981).

37. D.W. Oxtoby, J. Chem. Phys. 70, 2605(1979).

38. R.M. Lynden-Bell, Mol. Phys. 33, 907(1977).

39. J. Timmermans, Physico-Chemical Constants of Pure Organic Compounds (Elsecier, New York, 1950). p. 528.

40. A. Diamond, A. Fanelli and S. Petrucci, Inorg. Chem. 12, 611(1973).

41. Handbook of Chemistry and Physics,
(Chemical Rubber Company, Cleveland).

42. A.Z. Francesconi, E.U. Franck and H. Lentz,
Ber. Bunsenges. Phys. Chem. 79, 897(1975). Interpolated from liquid-vapor coexistence data at P=1 atmosphere.

43. K.A. Akhmetkarimov, I.I. Mai and Z.M. Muldakhmetov
J. Gen. Chem. USSR 43, 460(1973).

44. F. Mato and J.L. Hernandez, Anal. Quim. 65, 9(1969).

45. W. Schindler and J. Jonas, J. Chem. Phys. 72, 5019(1980);
J. Chem. Phys. 73, 3547(1980).

46. S.M. George and C.B. Harris, J. Chem. Phys. 77, 4781(1982).

47. R. Landau and A. Wurflinger, Ber. Bunsenges.
Phys. Chem. 84, 895(1980).

48. Calculated isothermal compressibility values were obtained from A. Wurflinger, Dept. of Chemistry, Univ. of Bochum, 4630 Bochum 1, Federal Republic of Germany.

49. K. Arakawa and K. Kojima, Bull. Chem. Soc Jpn. 48, 26(1975).

50. Lange's Handbook of Chemistry, 12th Edition, ed. by J.A. Dean (McGraw-Hill, New York, 1979).

51. M.D. Zeidler, Ber. Bunsenges. Phys. Chem. 75, 769(1971).

52. A. Kratochwill, Ber. Bunsenges. Phys. Chem. 82, 783(1978).

53. A. Abragam, Principles of Nuclear Magnetism (Oxford Univ. Press, London, 1961) Chap.X. Sec.IV.

54. A. Fendt, S.F. Fischer and W. Kaiser, Chem. Phys. 57, 55(1981).

55. A. Laubereau, S.F. Fischer, K. Spanner and W. Kaiser,
Chem. Phys. 31, 335(1978).

56. R. Zygan-Maus and S.F. Fischer, Chem. Phys. 41, 319(1979).

57. D.C. McKean, Spectrochim. Acta 29A, 1559(1973).

58. G. Herzberg, Molecular Spectra and Molecular Structure, Vol. II, (Van Nostrand Reinhold, New York, 1945) p. 332.

59. D.C. McKean, Spectrochim. Acta 30A, 1169(1974).

60. A.M. Saum, J. Polymer Science 42, 57(1960).

61. J.S. Rowlinson, Trans. Faraday Soc. 45, 974(1949).

62. J.D. Lambert, G.A.H. Roberts, J.S. Rowlinson and V.J. Wilkinson, Proc. Roy. Soc. (London) A196, 113(1949).

63. A. Loewenschuss and N. Yellin, Spectrochim. Acta 31A, 207(1975).

64. T.B. Freedman and E.R. Nixon, Spectrochim. Acta 28A, 1375(1972).

65. R.J. Jakobsen and J.W. Brasch, J. Am. Chem. Soc. 86, 3571(1964).

66. B.J. Bulkin, Helv. Chem. Acta 52, 1348(1969).

67. H. Saito, Y. Tanaka, S. Nagata and K. Nukada, Can. J. Chem. 51, 2118(1973).

68. C.S. Hsu and D. Chandler, Mol. Phys. 31, 215(1978).

69. A. Kratochwill, J.U. Weidner and H. Zimmerman, Ber. Bunsen. Gesellschaft 77, 408(1973).

70. H. Bertagnolli and M.D. Zeidler, Mol. Phys. 35, 177(1978).

71. E.P. Ippen and C.V. Shank in Ultrashort Light Pulses, Topics in Applied Physics, Vol 18, ed. by S.L. Shapiro (Springer-Verlag, Berlin, 1977).

Chapter 6: A Passively Mode-Locked Nd:glass Laser Oscillator Optimized for TEM_{00} Selectivity and Long Term Stability and Reliability

I. Introduction

Passively mode-locked Nd:glass laser oscillators are used extensively as a source of high power picosecond light pulses [1]. Limiting this laser oscillator to the TEM_{00} transverse mode is desirable because the TEM_{00} transverse mode produces a uniform and uniphase radial intensity profile, the smallest beam divergence, and the highest power density [2]. Unfortunately, passively mode-locked Nd:glass lasers restricted exclusively to the TEM_{00} operation are notoriously unstable, unreliable and difficult to align.

Although the generation and applications of passively mode-locked picosecond light pulses has been reviewed [3,4] and passively mode-locked Nd:glass picosecond pulses have been studied [5,6], an optimized, detailed design for a stable, reliable and TEM_{00} selective passively mode-locked Nd:glass laser oscillator has never been presented. This is particularly unfortunate, because minute details can make extraordinary differences in the laser's performance [7,8,9]. Therefore, knowledge of a detailed design is extremely important to the user of TEM_{00} selective, passively mode-locked Nd:glass lasers.

In this paper, we report on the design, operation, and performance of a passively mode-locked Nd:glass laser oscillator which produces essentially bandwidth-limited ≈9 picosecond pulses and has been

optimized for TEM_{00} selectivity and long term stability and reliability. We discuss the important aspects of the design in detail, with special emphasis on the reasons for the design. Because many of the design criteria are not limited to the passively mode-locked Nd:glass laser, the paper should also be useful to designers of other laser systems. In addition, we include a detailed alignment procedure because proper alignment is critical for stable, reliable and TEM_{00} selective laser operation.

The optimized laser will run stably and reliably in the TEM_{00} transverse mode for >12 hours after initial alignment. This optimized laser oscillator has made possible recent excite-and-probe experiments [10-12] which have demanded spatially coherent, bandwidth-limited ≈9 picosecond pulses for >12 hours because of long alignment and data accumulation times. These experiments, which were previously intractable, are now successfully accomplished.

II. Design Criteria

Ever since the original work of DeMaria et al. [13], many problems have plagued the user of passively mode-locked Nd:glass lasers. These problems have included: irreproducible pulse train envelopes [14]; unreliable mode-locking [7,8]; multiple pulse train mode-locking [14,15]; and unstable and extremely sensitive alignment [8]. Although many experiments have been performed with picosecond pulses from passively mode-locked Nd:glass lasers [1], these difficulties have limited the laser's utility. This has been especially true for passively mode-locked Nd:glass lasers restricted exclusively to TEM_{00}

operation.

The problems listed above involve many aspects of the passively mode-locked Nd:glass laser oscillator. These factors include: thermal and mechanical cavity instabilities; thermal distortions in the laser rod; non-linear optical effects in the laser rod; poor flashlamp pumping of the laser rod; poorly constructed laser heads [8]; internal reflections in the oscillator cavity; irreproducible power supply charging voltages; the stochastic nature of the mode-locking process [16-18]; inadequate laser head alignment facilities; imprecise and unstable mirror micrometers and mirror mounts; unstable mode-locking dyes; and poor TEM_{00} discrimination.

In order to surmount these difficulties, we carefully considered each aspect of the passively mode-locked Nd:glass laser. Our design criteria were optimum stability, reliability, and TEM_{00} selectivity, as well as minimum pulse duration.

III. Laser Cavity

Calculations have demonstrated that TEM_{00} transverse mode selectivity is strongly dependent on resonator geometry. TEM_{00} selectivity, using either diffraction or aperature loss mechanisms, is greatest for a confocal or half-confocal resonator and smallest for a plane-parallel resonator [19]. Although confocal and half-confocal resonators are on the edge of stability [20]. near confocal or near half-confocal resonators are stable resonators and have also displayed more reliable mode-locking than plane-parallel resonators [7]. Therefore, the optimized laser oscillator cavity is a near half-confocal

optical resonator. The front output mirror has a 3 meter radius of curvature and a 60% reflectivity at 1.06 micron [21]. The cavity length is 140 centimeters. The front mirror's relatively high 60% reflectivity reduces the lasing gain threshold and lowers the energy stored in the Nd:glass laser rod which minimizes the peak power and many possible detrimental non-linear effects which can spectrally and temporally broaden the mode-locked bandwidth-limited light pulse [22].

IV. Laser Head

Efficient optical pumping is essential for minimal thermal distortions in the laser rod. In addition, uniform illumination of the laser rod is important for TEM_{00} operation. Therefore, the laser head (see Fig. 1) is a cloverleaf design machined from brass and electroplated with nickel and then gold to provide high reflectivity over almost all the Nd:glass pumping bands [23]. Four linear xenon flashlamps are mounted slightly off the center of each cylindrical leaf in a close-coupled reflector design that provides uniform illumination of the rod. The four flashlamps are mounted in cylindrical pyrex jackets which block the flashlamp's UV output. The UV output does not effectively pump Nd:glass, whereas the UV output does contribute to deleterious thermal distortions in the laser rod which can lead to unreliable oscillator performance. The jackets allow the flashlamps to be air-cooled, whereas the rod is water-cooled for more efficient heat transfer. The water is circulated and temperature regulated at approximately 12 degrees Centigrade by a Laude K-2/R circulator [24].

The Nd:glass laser rod has a diameter of 1/4 inch and a length of

6 1/8 inches [25]. The 1/4 inch diameter rod had significantly fewer thermal distortion problems than a previously used 3/8 inch diameter rod. The rod has a rough acid barrel finish and is Brewster-angled at both ends. The Brewster angle configuration introduces a beam displacement of approximately 64 millimeters in the horizontal plane. The front end of the laser rod is positioned approximately 24 centimeters from the curved output mirror because the beam diameter is greatest at the curved mirror. This allows a larger active volume of the laser rod to be utilized.

Accurate alignment is crucial for stable and reliable TEM_{00} operation. For precise and easy alignment, the laser head sits in a stainless steel carriage which is attached to an adjustable stainless steel housing (see Figs. 2 and 3). The carriage allows the laser head to be rotated to align the rod's Brewster angle. The housing can move angularly by pivoting on a central point. The angular alignment is secured by tightening a machine screw which is positioned in a slotted arc connected to the housing. The housing lifts the laser vertically by means of four adjustment screws which move through four tapped holes in the carriage base plate. The housing translates the laser head laterally by means of four adjustment screws which secure a lateral position inside two sideboard runners. This adjustable housing design facilitates accurate and rapid alignment of the laser head.

FIG. 1. Cross sectional view of the close-coupled cloverleaf laser head.

FIG. 2. Side view of the adjustable laser head housing.

FIG. 3. Top view of the adjustable laser head housing.

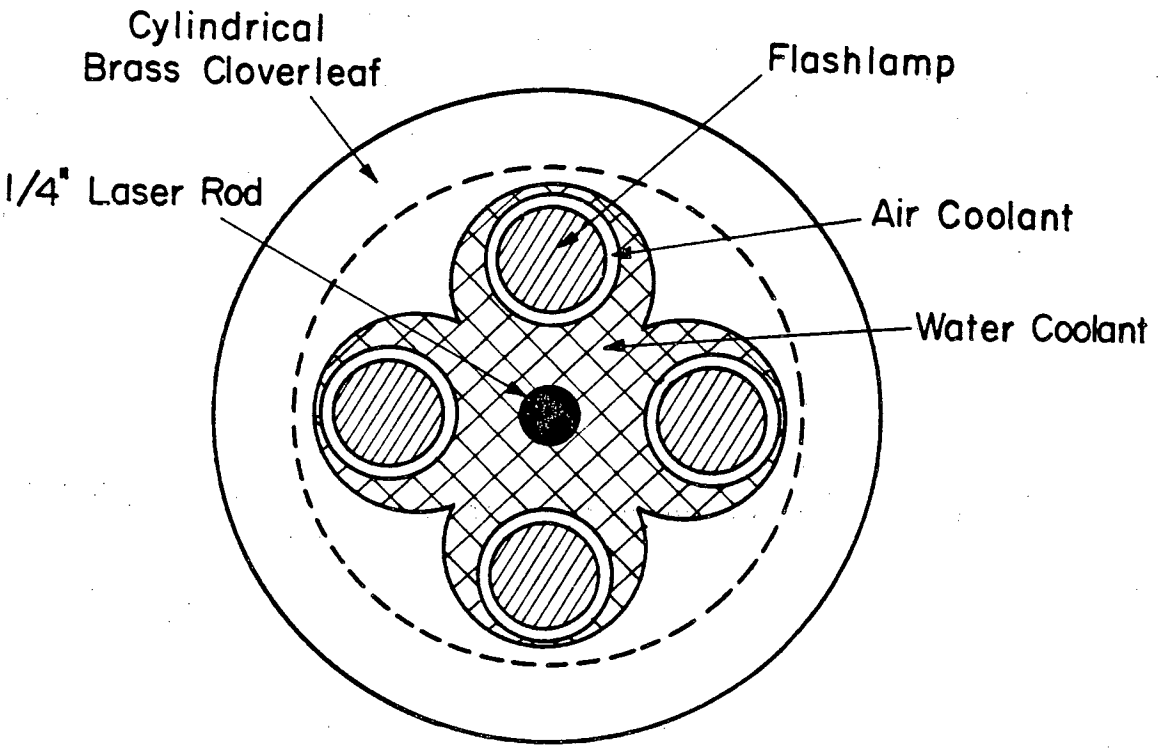
Cylindrical
Brass Cloverleaf
Flashlamp
1/4" Laser Rod
Air Coolant
Water Coolant
XBL 8012-13343

Figure 1

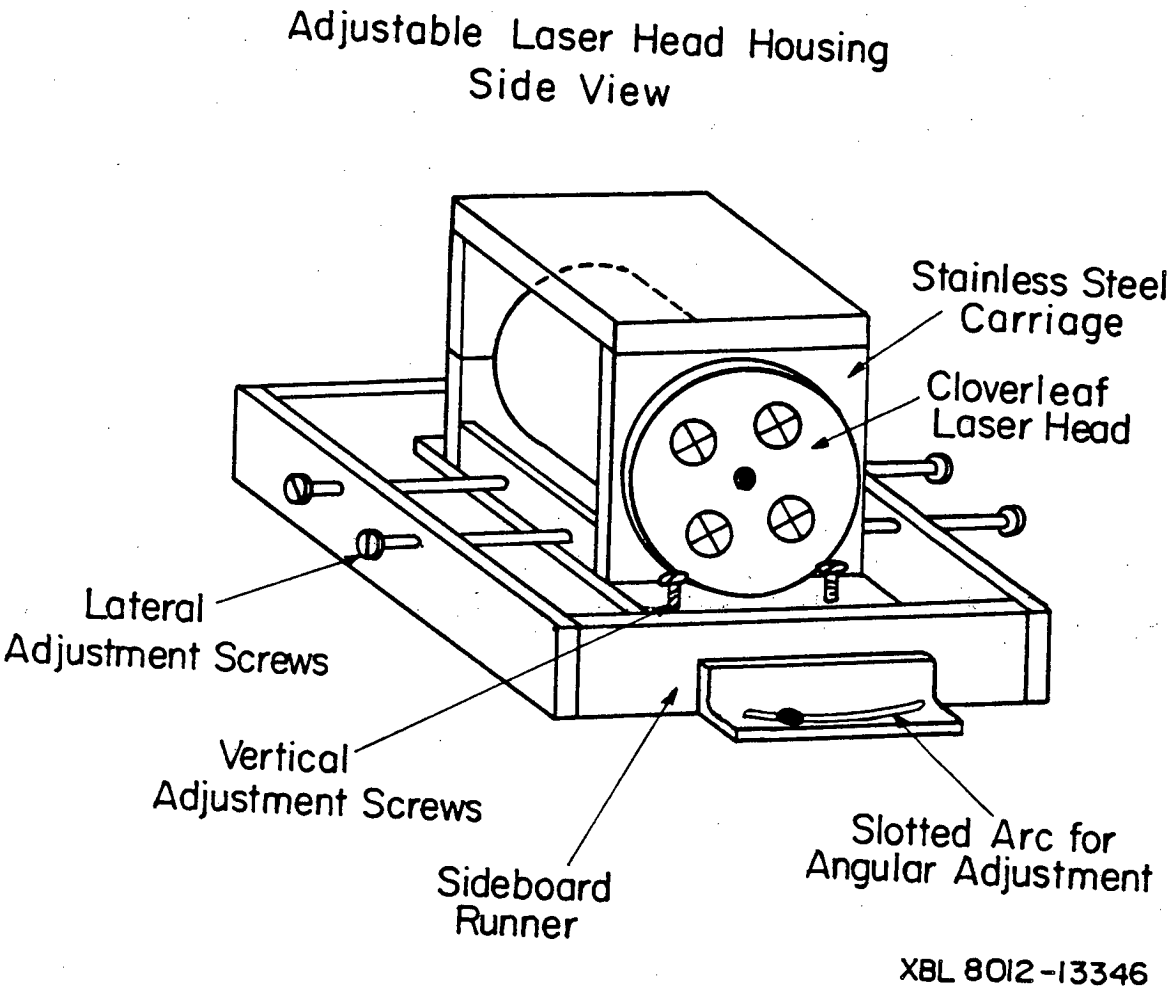
Adjustable Laser Head Housing
Side View
Stainless Steel
Carriage
Cloverleaf
Laser Head
Lateral
Adjustment Screws
Vertical
Adjustment Screws
Sideboard
Runner
Slotted Arc for
Angular Adjustment
XBL 8012-13346

Figure 2

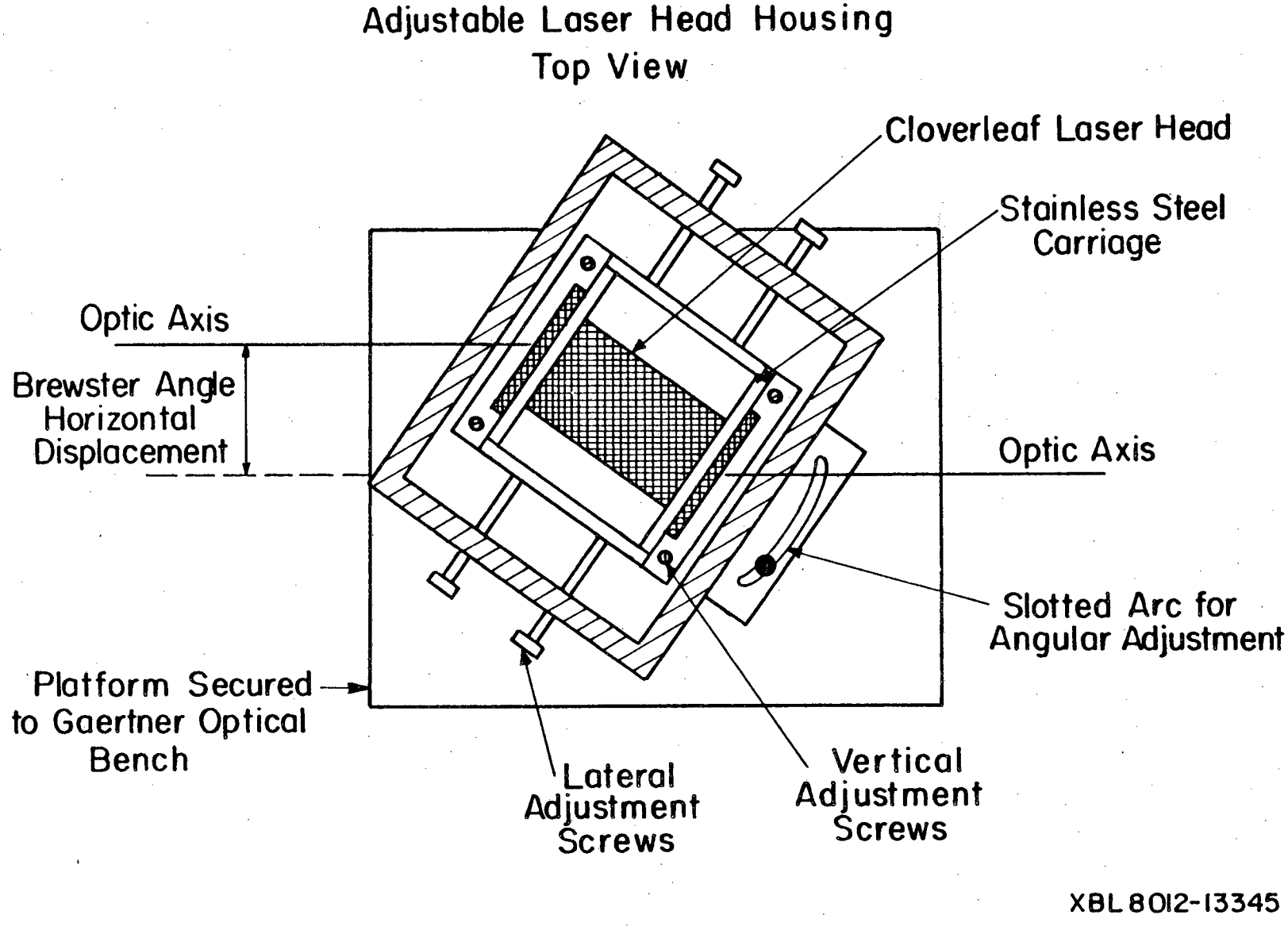
Adjustable Laser Head Housing
Top View
Cloverleaf Laser Head
Stainless Steel Carriage
Optic Axis
Brewster Angle Horizontal Displacement
Optic Axis
Slotted Arc for Angular Adjustment
Platform Secured to Gaertner Optical Bench
Lateral Adjustment Screws
Vertical Adjustment Screws
XBL8012-13345

Figure 3

V. Flashlamp Driving Circuit

Efficient flashlamp pumping is necessary to minimize thermal distortions in the laser rod which can lead to unstable and unreliable oscillator performance. The most efficient flashlamp driving circuit is determined by: the type of flashlamp; the discharge energy; the discharge pulsewidth; and the circuit damping parameter [26].

For EG&G FX 47C-5 linear xenon flashlamps in series are used to optically pump the Nd:glass laser rod. Flashlamp configurations are characterized by K_0, a flashlamp parameter with units of ohm-amps$^{1/2}$ [26]. For xenon flashlamps, K_0 1.275 X arclength/boresize [27]. The four flashlamps in series have a K_0 50. Given this K_0 value, a capacitance C=240 microfarads, a desired discharge energy of approximately 800 Joules, a desired pulsewidth of approximately 650 microseconds [28], and a desired circuit damping parameter, α, approximately equal to 0.75 for critical damping, the discharge circuit inductance, L=330 microhenries, was determined using the procedure of Markiewicz and Emmett [26].

The capacitor is charged by a regulated power supply capable of giving reproducible charging voltages to approximately one part in a thousand. This accuracy in the charging voltage is necessary to consistently operate the oscillator at just above the lasing threshold voltage. Experience has shown that optimum mode-locking performance occurs just above the lasing threshold voltage [8].

VI. Mode-locking Dye Solution and Dye Cell

Several studies have shown that satellite pulses are avoided [5,29] and mode-locking is more reliable [5,8,29] when the dye cell is in contact with one of the resonator's mirrors. In addition, several investigations have determined the relationship between dye cell length and pulse duration [6,29]. These studies have revealed that short dye cell lengths produce the shortest mode-locked pulses. Therefore, the mode-locking dye sits in contact with the back mirror. The dye cell is defined by the back mirror, two narrow teflon shims with a thickness of ≈400 microns, and a wedged optical flat with anti-reflection coating for 1.06 micron on the surface in contact with the dye. The actual dye cell length is probably ≤400 microns since the two teflon shims are pressed very tightly between the two glass plates. An illustration of the dye cell assembly is shown in Fig. 4. The mode-locking dye cell assembly is constructed entirely of stainless steel in order to minimize thermal instabilities.

The recovery times of saturable absorber dyes commonly used to mode-lock λ=1.06 micron have been determined [30]. Eastman Kodak Q-switch dye #9860 has one of the fastest recovery times, τ=7±1 picosecond [30]. Because pulse duration is a function of the absorber recovery time, Q-switch dye #9860 in Eastman Kodak Q-switch 1,2-dichloroethane was used as the mode-locking dye solution. Experience has shown that the Q-switch dye is more stable and reliable if the 1,2-dichloroethane is purified by passage through a column of basic aluminum oxide and then filtered through a 0.45 micron pore size Millipore filter to remove the residual aluminum oxide particulates [31].

The most reliable operation from mode-locking dye solutions occurs when the dye is circulated through the dye cell from a large reservoir [32]. This arrangement provides fresh dye for each laser pulse, assures uniform mixing and constant concentration of the dye, and minimizes thermal effects in the dye cell [33]. The 1,2-dichloroethane is added to a resevoir which is connected to the dye cell and a variable speed magnetic drive gear pump [34]. The total volume of the dye cell, tubing, pump and reservoir is approximately 70 milliliters. Inert, baffled, 1/4 inch tubing [35] is used to connect the reservoir, pump and dye cell, and also to quench vibrations from the pump which can couple into the cavity and lead to mechanical instabilities. In addition, the pump is turned off approximately five seconds before the laser fires to minimize the disturbance from the flowing dye.

Studies have shown that mode-locked pulse durations are shortest when T, the saturable absorber's low light level transmittance, is as high as possible [8]. We have also determined that the most reliable and reproducible pulse trains occur when the dye solution has an optical density of 1.05 ±0.05 at a 1.06 micron wavelength in a 0.5 centimeter spectrophotometric cell. This corresponds to the relatively high transmittance of >75%(double pass) in the <400 micron dye cell. Thus after filling the dye solution system with 1,2-dichloroethane, Kodak #9860 dye is slowly added to the 1,2-dichloroethane until the solution has an optical density of 1.05 ±0.05 at a 1.06 micron wavelength in a 0.5 centimeter cell. For reproducible, reliable operation, this dye solution should be changed every day.

VII. Oscillator Frame Construction

Mechanical and thermal stability are crucial for long term oscillator reliability and stability. Therefore, the optimized laser oscillator is stabilized by four 1-1/8 inch diameter invar rods [36]. These rods are connected to two 1/2 inch thick stainless steel endplates and two 3/8 inch thick stainless steel support plates. The invar rods feed through 1-1/8 inch holes in the stainless steel plates. There is minimal clearance through these holes and initial assemply is difficult because the plates bind unless they remain perpendicular to all the invar rods. After assembly, however, the frame is very rigid. Stainless steel set screws provide additional stability. All parts of the laser oscillator are constructed of stainless steel whenever possible to minimize thermal instability. The invar stabilized oscillator frame is illustrated in Fig. 5.

VIII. Oscillator Frame Connection to the Optics Table

The oscillator frame rests on four stainless steel ball bearings. These ball bearings help to decouple the oscillator from the optics table and also allow the oscillator frame to move freely to relieve possible strain which could lead to oscillator instabilities [37]. One ball bearing sits securely in a hole. Two ball bearings sit in channels which allow for either x-axial or y-lateral movement. The fourth ball bearing sits on a plane which allows both x and y freedom. This design is illustrated in Fig. 6.

The ball bearings sit on plates which are mounted to a

FIG. 4. Cross sectional view of the mode-locking dye cell.

FIG. 5. Side view of the invar stabilized oscillator cavity.

FIG. 6 Illustration of the decoupling and strain relieving ball bearing design which connects the oscillator frame to the Gaertner optical bench.

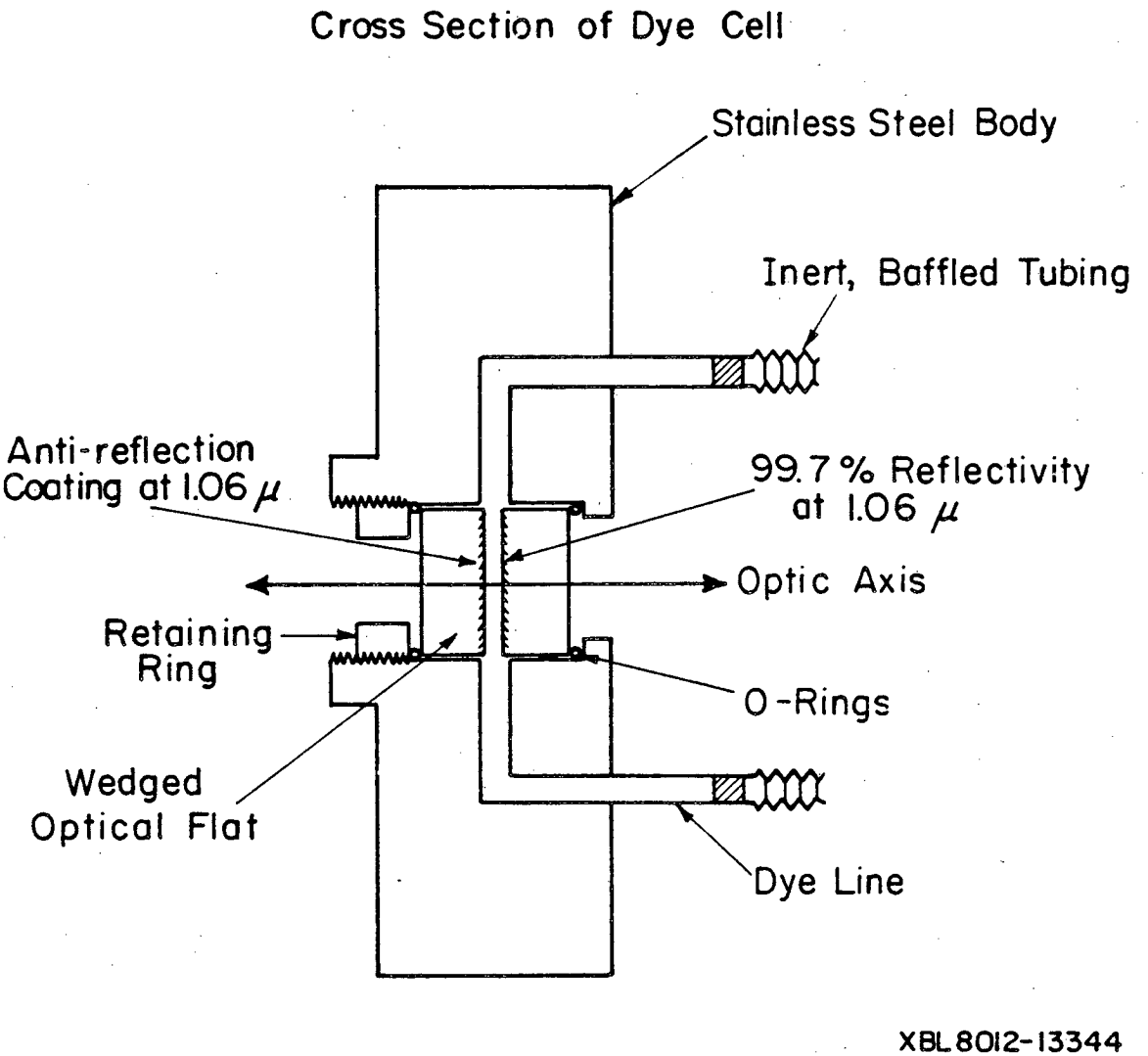
Cross Section of Dye Cell
Stainless Steel Body
Inert, Baffled Tubing
Anti-reflection Coating at 1.06 μ
99.7 % Reflectivity at 1.06 μ
Optic Axis
Retaining Ring
O-Rings
Wedged Optical Flat
Dye Line
XBL8012-13344

Figure 4

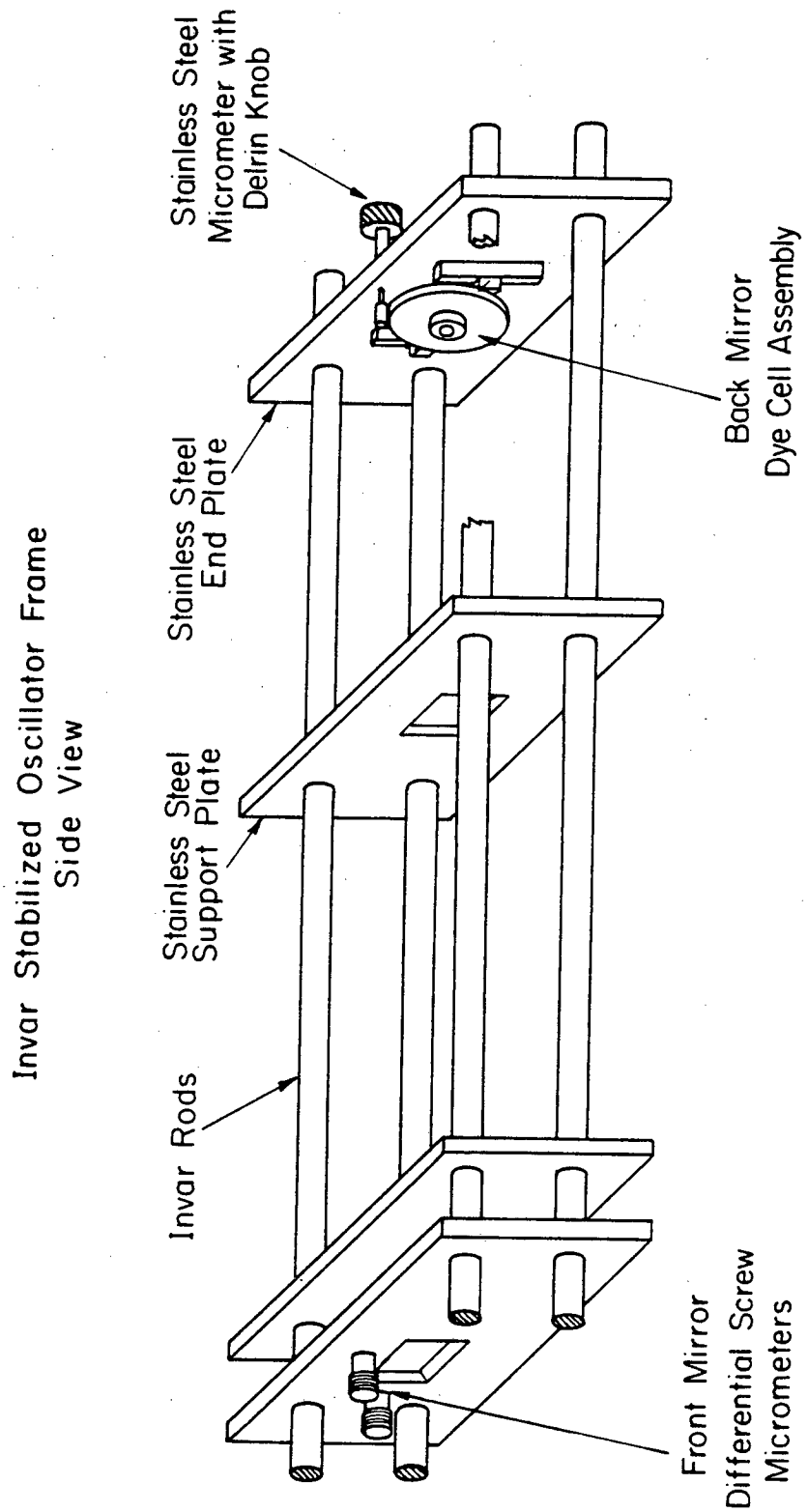
Invar Stabilized Oscillator Frame
Side View
Stainless Steel
Micrometer with
Delrin Knob
Stainless Steel
End Plate
Stainless Steel
Support Plate
Invar Rods
Back Mirror
Dye Cell Assembly
Front Mirror
Differential Screw
Micrometers
XBL 8012-13348

Figure 5

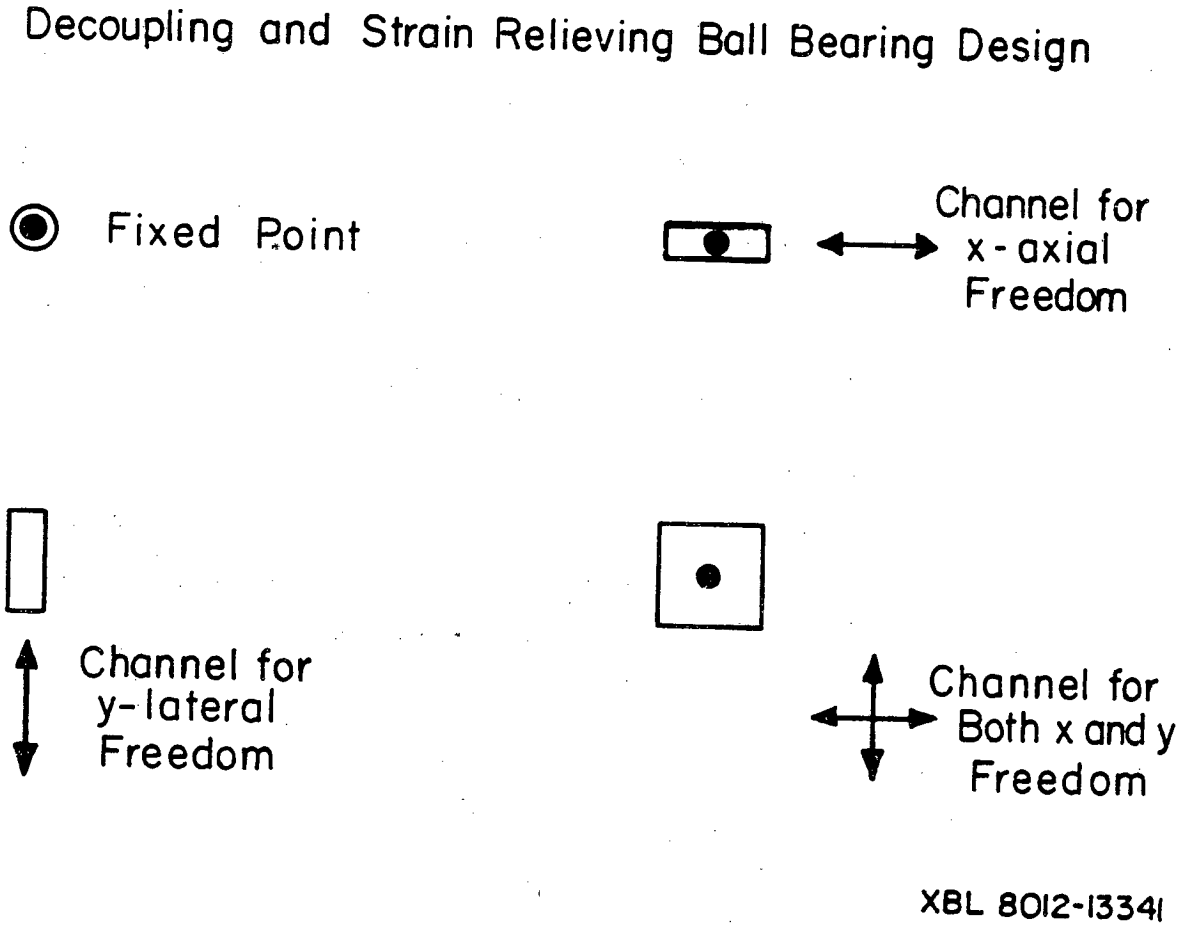
Decoupling and Strain Relieving Ball Bearing Design
Fixed Point
Channel for x-axial Freedom
Channel for y-lateral Freedom
Channel for Both x and y Freedom
XBL 8012-13341

Figure 6

160 centimeter Gaertner Corporation precision lathe bed optical bench [38]. The inside housing of the Gaertner lathe bed optical bench is lined with lead bricks to provide enhanced stability.

IX. Micrometers and Mirror Mounts

Extraordinary stability and adjustment precision are necessary for TEM_{00} passively mode-locked Nd:glass laser alignment. These requirements are met by a Burleigh Star-Gimbal stainless steel mirror mount [39] with Lansing differential screw micrometers [40] on the front mirror, and Starret precision stainless steel micrometers with Delrin knobs [41] on the back mirror stainless steel dye cell assembly. The differential screw micrometers can make translations as small as a millionth of an inch. Experience has shown that, using the Star-Gimbal mirror mount, alignment for TEM_{00} operation must be accurate to within $\approx$40 millionths of an inch on the front horizontal Lansing differential screw micrometer, i.e., $\approx$0.4 seconds of arc, for stable, reproducible behavior at the minimum lasing threshold.

X. Alignment Procedure and Aperature Placement

A proper alignment procedure can lead to rapid and reliable operation of a TEM_{00} passively mode-locked Nd:glass laser oscillator. The following alignment procedure has evolved over the last several years and has been very effective. Refer to Fig. 7 during the following discussion.

A 5.0 milliwatt Helium-Neon laser is aperatured to remove off-axis

light. The side of the aperature away from the Helium-Neon laser is colored white. The Helium-Neon light beam is brought into the oscillator by a 50% beam splitter located behind the back mirror. The Helium-Neon beam is positioned parallel to the optics cavity. An iris diaphram on an xy micrometer stage mounted on a platform which can slide on the Gaertner optical bench is very convenient for this purpose.

Next the laser head housing is positioned so the Helium-Neon beam is centered on the front and back faces of the laser rod. Positioning the iris diaphram close to the laser head and closing down the diaphram on the Helium-Neon beam greatly facilitates this process. For correct alignment of the Brewster angle, the Helium-Neon beam should reflect off the face of the laser rod and remain in the same plane, at the same height, as the incoming Helium-Neon beam.

After the laser rod is properly aligned, the front mirror is adjusted so the beam reflected from the front mirror is centered on the white-colored aperature positioned in front of the Helium-Neon laser. Part of the beam reflected from the front mirror passes through the 50% beam splitter. A white screen is placed behind the beam splitter to view the reflection from the front mirror. Then the back mirror is adjusted so the reflection from the cavity-defining surface of the dye cell is coincident with the reflection from the front mirror. Sharp, concentric interference fringes should appear when the cavity is properly aligned.

Next the intracavity aperature for TEM_{00} selectivity is placed in the oscillator, on an xy micrometer stage mounted on a platform which can slide on the Gaertner optical bench. The intracavity aperature is positioned approximately 8 centimeters from the dye cell, centered with

FIG. 7. Top view of the laser assembly.

FIG. 8. (a) Oscillogram of an ordinary pulse train. (b) Oscillogram of a multiple pulse train. Both output pulse trains are taken with a PIN photodiode and a Tektronix 519 oscilloscope at 50 nsec/div.

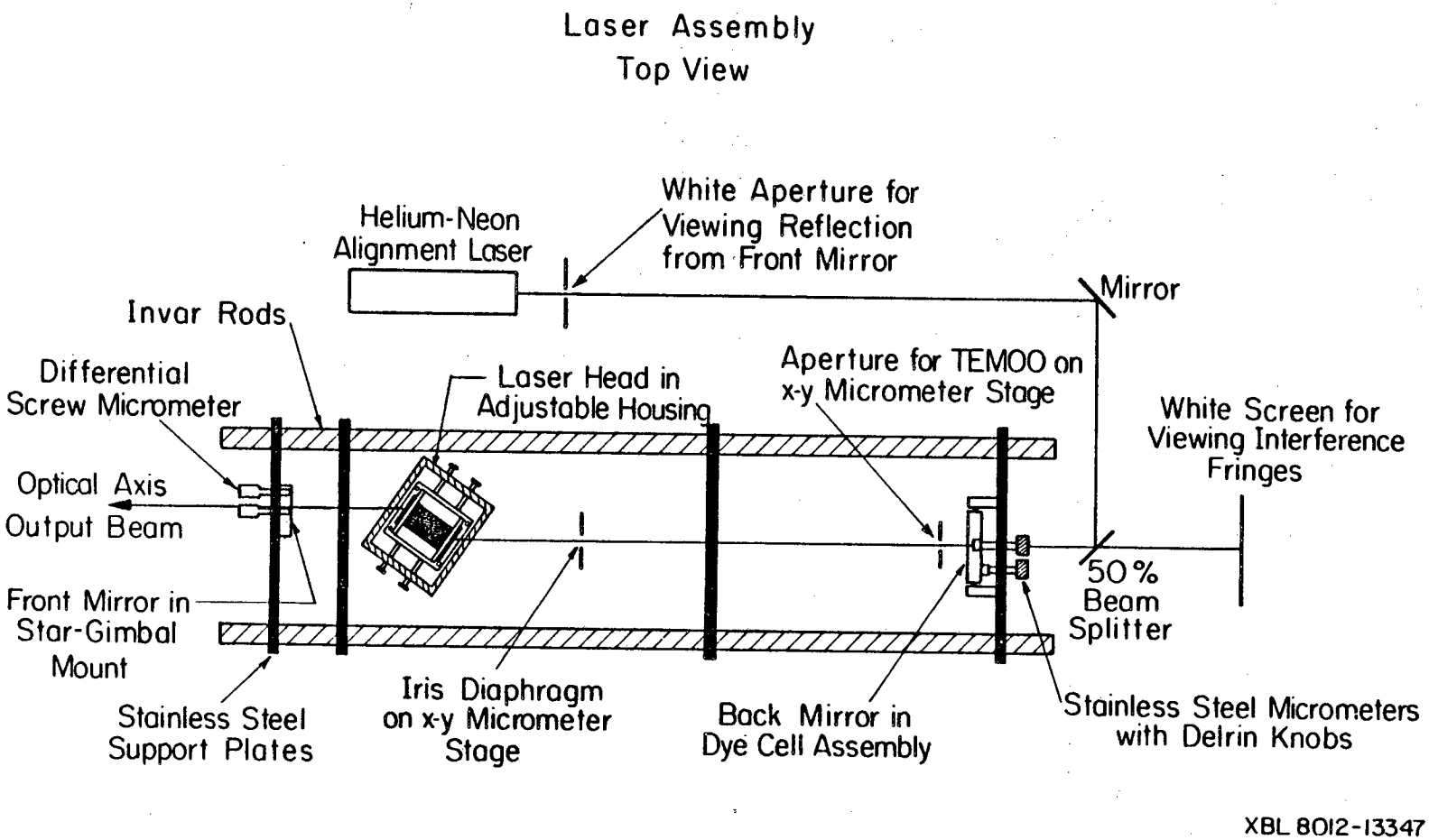
Laser Assembly
Top View
Helium-Neon
Alignment Laser
White Aperture for
Viewing Reflection
from Front Mirror
Mirror
Invar Rods
Differential
Screw Micrometer
Laser Head in
Adjustable Housing
Aperture for TEMOO on
x-y Micrometer Stage
White Screen for
Viewing Interference
Fringes
Optical Axis
Output Beam
Front Mirror in
Star-Gimbal
Mount
50%
Beam
Splitter
Stainless Steel
Support Plates
Iris Diaphragm
on x-y Micrometer
Stage
Back Mirror in
Dye Cell Assembly
Stainless Steel Micrometers
with Delrin Knobs
XBL 8012-13347

Figure 7

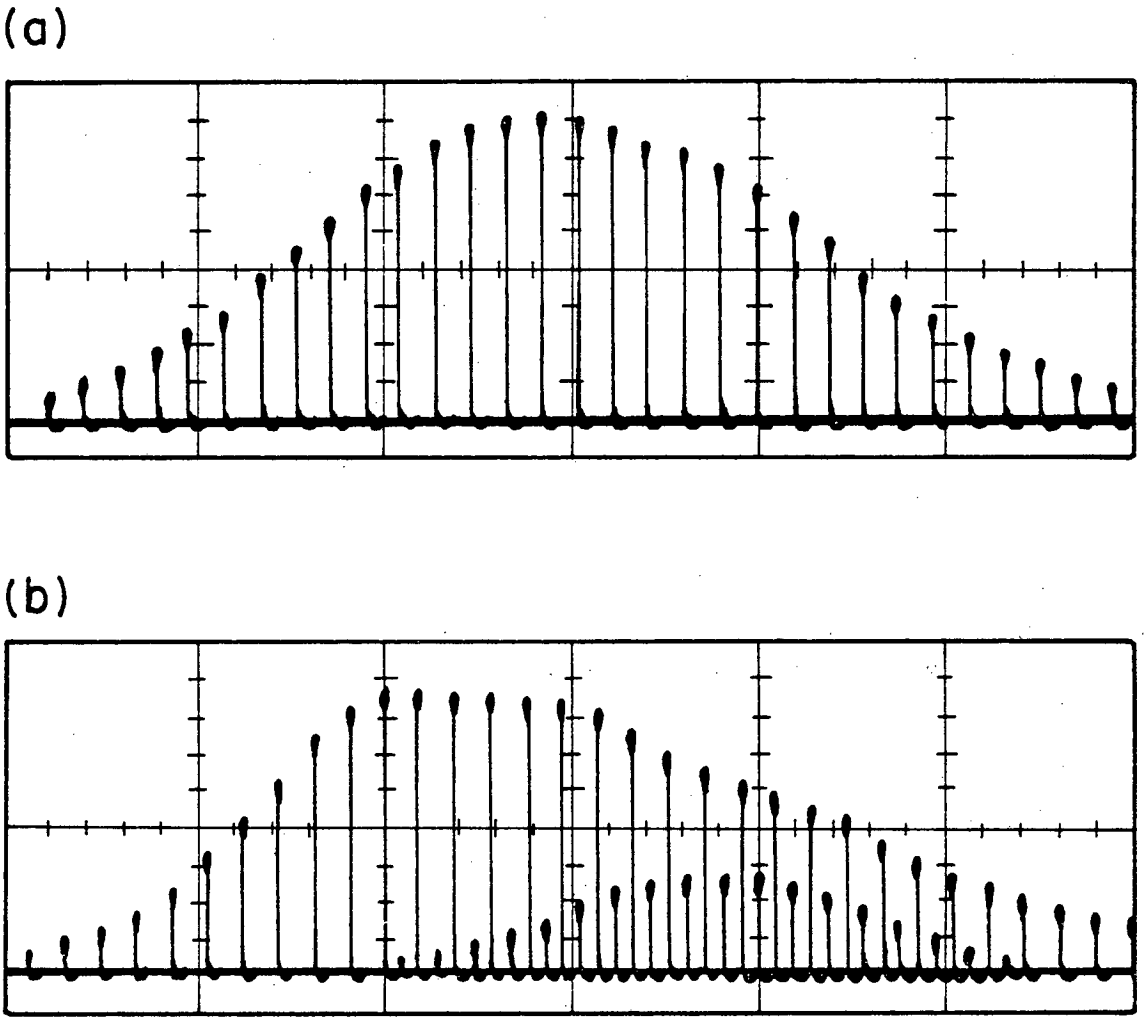

Figure 8

respect to the Helium-Neon beam [2,19]. The aperature can be accurately centered by closing the diaphram down on the beam to make a small spot and then centering on this small spot. The aperature has a diameter of 2.18 mm. For the position close to the dye cell, aperature diameters smaller than 2.18 mm, e.g., 2.08 mm, introduce too much light loss and diameters larger than 2.18 mm, e.g., 2.26 mm, allow the TEM_{01} mode and higher order modes to occur. For aperature positions further from the dye cell, the laser's performance was less reliable.

XI. Adjustment for Optimum Lasing Action

Once the laser is aligned, the flashlamps can be fired and the alignment can be adjusted for optimum lasing action. The lasing action can be observed by placing developed but unexposed Polaroid film near the front mirror and watching for laser burn spots. The power supply voltage should be increased until a burn spot is observed. If a burn spot is not observed the front horizontal differential screw micrometer can be adjusted. If the differential screw micrometer has to be moved more than 250 millionths of an inch, either the voltage is still too low or the initial alignment is faulty. With proper alignment, lasing should occur within ±200 millionths of an inch, i.e., ±1.8 seconds of arc, from the initial setting. The voltage threshold is minimized by adjusting the front horizontal differential screw micrometer and observing if the lasing threshold is lowered. The laser oscillator must be operated at its minimum voltage for the most reliable and reproducible laser performance. The front horizontal differential screw adjustment is the only adjustment which should be necessary after inital

alignment.

XII. Dependability

The optimized, TEM_{00} selective, passively mode-locked Nd:glass laser oscillator described above is capable of running at a repetition rate of one shot every 20 seconds for >12 hours with only minor adjustments. The repetition rate is limited by the power supply charge time. If the voltage threshold increases significantly, the threshold can generally be brought back down by adjustment of ≈30 millionths of an inch on the front horizontal differential screw micrometer, i.e., ≈0.3 seconds or arc. We suspect that the need for minor adjustments is related to the fluctuations in the room temperature [8].

If multiple trains occur, the voltage should be turned down. Examples of ordinary and multiple pulse trains observed using a Hewlett-Packard PIN photodiode [42] and a Tektronix 519 oscilloscope are shown in Fig. 8. Optimum pulse trains with fairly reproducible pulse train envelopes occur approximately 80-90% of the time when the voltage is just above the lasing threshold voltage.

References

1. Ultrashort Light Pulses, ed. by S.L. Shapiro (Springer-Verlag, New York, 1977).

2. W. Koechner, Solid State Laser Engineering (Springer-Verlag, New York, 1976).

3. A.J. DeMaria, W.H. Glenn, Jr., M.J. Brienza and M.E. Mack Proc. IEEE 57, 2(1969).

4. A. Laubereau and W. Kaiser, Opto-Electronics 6, 1(1974).

5. D. von der Linde, IEEE J. Quantum Electronics 8, 328(1972).

6. D.J. Bradley and W. Sibbett, Optics Comm. 9, 17(1973).

7. P.N. Everett, Rev. Sci. Inst. 41, 1495(1970).

8. H. Weichel, J. Appl. Phys. 44, 3635(1973).

9. W. Koechner, op.cit., p. 467 ff.

10. C.B. Harris, H. Auweter and S.M. George, Phys. Rev. Lett. 44, 737(1980).

11. S.M. George, H. Auweter and C.B. Harris, J. Chem. Phys. 73, 5573(1980).

12. C.B. Harris, H. Auweter and S.M. George, in Picosecond Phenomena II, ed. by R. Hochstrasser, W. Kaiser and C.V. Shank (Springer-Verlag, New York, 1980).

13. A.J. DeMaria, D.A. Stetser and H. Heynau, Appl. Phys. Lett. 8, 174(1966).

14. R. Harrach and G. Kachen, J. Appl. Phys. 39, 2482(1968).

15. W. Koechner, op. cit., pp. 467-8.

16. V.S. Letokhov, Sov. Phys. JETP 27, 746(1968); Sov. Phys. JETP 28, 562(1969); Sov. Phys. JETP 28, 1026(1969).

17. W. Koechner, op. cit., p. 461 ff.

18. W.H. Lowdermilk, "Technology of Bandwidth-Limited Pulse Generation", in Laser Handbook, Vol. 3, ed. by M.L. Stitch (North-Holland Publishing Company, New York, 1979).

19. T. Li, Bell Sys. Tech. Journal 44, 917(1965).

20. A.E. Siegman, An Introduction to Lasers and Masers, (McGraw-Hill, New York, 1971) p. 293 ff.

21. Both mirrors have 1.0 inch diameters and were obtained from CVI Laser Corporation, Albequerque, New Mexico, 87192.

22. Private communciation from Robert L. Carman, Los Alamos Scientific Laboratory, Univ. of California, Los Alamos, New Mexico, 87545.

23. This laser head design is an adaptation of a prototype from the Lawrence Livermore Laboratory, Univ. of California, Livermore, California, 94550.

24. Lauda Instruments Division, Brinkmann Instruments, Inc., Westbury New York, 11590.

25. The Nd:glass laser rod was Owens-Illinois ED-2 glass with standard doping for 1/4 inch diameter rods obtained from Owens-Illinois, Toledo, Ohio, 43666.

26. J.P. Markiewicz and J.L. Emmett, IEEE J. Quantum Electronics 2, 707(1966).

27. EG&G technical information, EG&G Inc., Electro-Optics Division, Salem, Mass. 01970.

28. Optimum efficiency for pumping ED-2 Nd:glass occurs when the flashlamp pulsewidth is between 400-750 microseconds. Private communication from John Trenholme, Lawrence Livermore Laboratory, Univ. of California, Livermore, California, 94550, and from Robert C. Turner, ILC Technology, Sunnyvale, California, 94086.

29. D.J. Bradley, G.H.C. New and S.J. Caughey, Optics Comm. 2, 41(1970).

30. D. von der Linde and K.F. Rogers, IEEE J. Quantum Electronics 9, 960(1973).

31. Private communication from G. Wilse Robinson, Dept. of Chemistry, Texas Tech Univ., Lubbock, Texas, 79409.

32. W. Koechner, op.cit., p. 470.

33. A.R. Clobes and M.J. Brienza, IEEE J. Quantum Electronics 6, 651(1970).

34. The variable speed magnetic drive gear pump was obtained from Micropump Corporation, Concord, California, 94524.

35. The inert, baffled 1/4 inch tubing was obtained from Penntube Plastics Comp., Clifton Heights, Pennsylvania.

36. The invar was Carpenter Invar 36 available from Carpenter Steel, Redding, Pennsylvania.

37. This design was suggested by Dirk J. Kuizenga, Lawrence Livermore Laboratory, Univ. of California, Livermore, California, 94550.

38. Gaertner Scientific Corporation, 1201 Wrightwood Avenue, Chicago, Illinois, 60614.

39. The Burleigh Star-Gimbal Stainless Steel Mirror Mounts Model Number SG-201 were obtained from Burleigh Instruments, Inc., Fishers, New York, 14453.

40. The Lansing differential screw micrometers, Model Number 22.501, were obtained from Lansing Research Corporation, Ithaca, New York, 14850.

41. The L.S. Starrett Co. stainless steel micrometers Model Number 1263 were obtained from Burleigh Instruments, Fishers, New York, 14453. The Burleigh designation for the Starrett micrometer is Model Number MC-79.

42. The Hewlett-Packard PIN photodiode, Type 5082-4203, was obtained from Hewlett-Packard, 1501 Page Mill Road, Palo Alto, California, 94304.

Chapter 7: Picosecond Pulse Characterization

I. Introduction

A wide range of picosecond pulse temporal and spectral widths have been reported from passively mode-locked Nd glass lasers. For example, pulse temporal widths between 2-15 picoseconds and pulse spectral widths between 3-200 cm^{-1} have been documented [1-15]. These strikingly broad ranges are determined by many experimental parameters. These parameters include the type of mode-locking dye; the mode-locking dye cell thickness, the position of the extracted pulse in the pulse train; and non-linear effects in the laser rod.

In this chapter, we report our efforts to characterize the pulses from our passively mode-locked Nd:glass laser. This laser has been previously described in Chap. 6. We observed the temporal width of the fundamental 1.06 μ pulse using the two photon fluorescence (TPF) technique as discussed in Chaps. 5 and 8. We observed the spectral width of the frequency-doubled 5306 Å pulse using a standard 3/4 meter spectrometer in second order as discussed in Chap. 5.

II. Temporal Width of 1.06 μ Pulses versus Position in Pulse Train

Figure 1 shows the observed autocorrelation width for the 1.06 μ pulse versus position in a typical pulse train emitted from our passively mode-locked Nd:glass laser. Single 1.06 μ pulses were extracted selectively from the pulse train using the electronic pulse

selector referenced in Chap. 5. These 1.06 μ pulses were amplified to approximately 20 mJ and were not compressed using a saturable absorber. The effect of saturable absorbers on the pulse width is discussed in Chap. 8.

The autocorrelation widths were determined from TPF measurements. Actual pulse temporal widths calculated from these autocorrelation widths assuming Gaussian pulse shapes are also given. This is a pessimistic estimate for the pulse widths because the actual pulse shapes are probably somewhat intermediate between Gaussian and Lorentzian.

Figure 2 displays a histogram of the data summarized in Fig. 1. Figure 2 demonstrates that the shot-to-shot pulse width fluctuations increase dramatically if the pulse is selected later in the pulse train at locations C or D. Consequently, the vibrational dephasing experiments discribed in this thesis were performed with pulses from locations A or B.

III. Spectral Width of 5306 Å Pulses versus Position in Pulse Train

Figure 3 shows the observed spectral widths for the frequency-doubled 5306 Å pulses versus the position in a typical pulse train. These 5306 Å pulses were derived from 1.06 μ pulses that had been amplified to approximately 1-2 mJ. The effect of the saturable absorber dye #9860 with an optical density of 1.0 is also given.

Figure 4 displays a histogram of the data summarized in Fig. 3. In a similar manner to the temporal widths, large shot-to-shot fluctuations in the spectral width are dramatically apparent for pulses selected

FIG. 1. Autocorrelation width of the 1.06 μ pulse versus position in a typical pulse train emitted from our passively mode-locked Nd:glass laser. Temporal widths assuming Gaussian pulse shapes are also given.

FIG. 2. Histogram of the data summarized in Fig. 1.

FIG. 3. Spectral widths of the frequency-doubled 5306 Å pulses versus position in a typical pulse train. The effect of the saturable absorber dye #9860 is also given.

FIG. 4. Histogram of the data summarized in Fig. 3.

Pulsewidth vs. Position in Pulse Train

400 μ dye cell, ML dye #9860

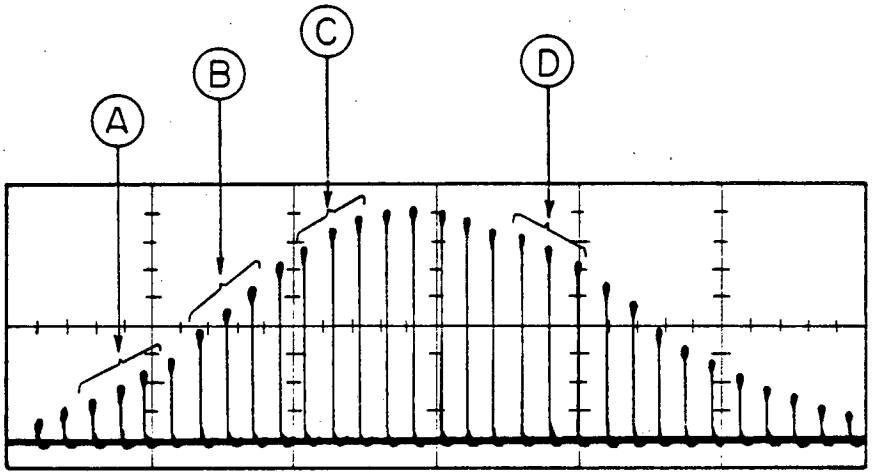

Location	Pulse	Autocorrelation Width, mm	Gaussian Pulse Width, psec
(A)	3rd-5th	1.69 ± 0.20	10.5 ± 1.2
(B)	7th-9th	1.78 ± 0.19	11.1 ± 1.2
(C)	11th-13th	1.79 ± 0.33	11.2 ± 2.1
(D)	19th-21st	2.27 ± 0.33	14.2 ± 2.1

XBL814-5555

Figure 1

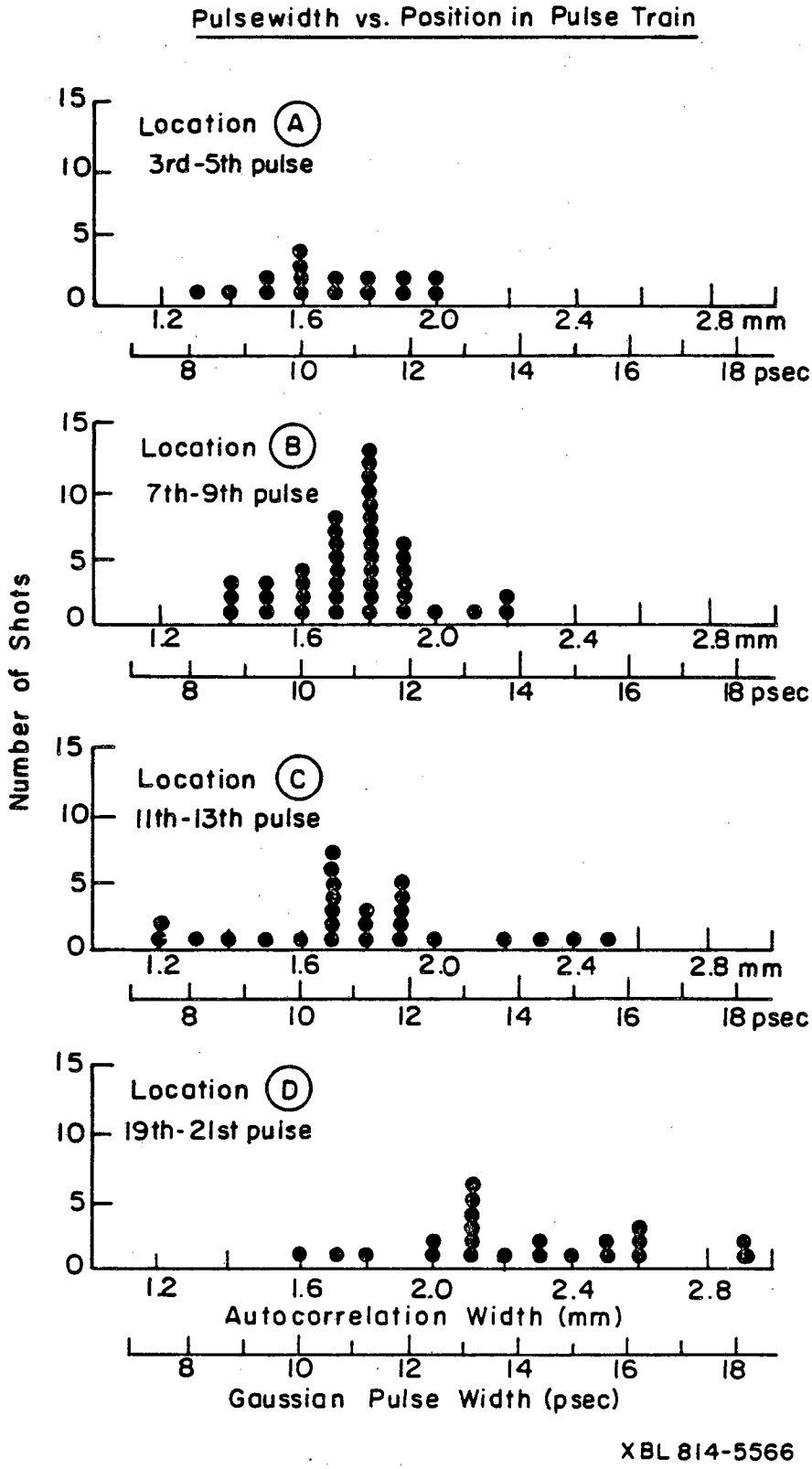
Pulsewidth vs. Position in Pulse Train
Location A
3rd-5th pulse
Location B
7th-9th pulse
Location C
11th-13th pulse
Location D
19th-21st pulse
Number of Shots
15
10
5
0
1.2
1.6
2.0
2.4
2.8 mm
8
10
12
14
16
18 psec
Autocorrelation Width (mm)
Gaussian Pulse Width (psec)
XBL 814-5566

Figure 2

Spectral Width vs. Position in Pulse Train

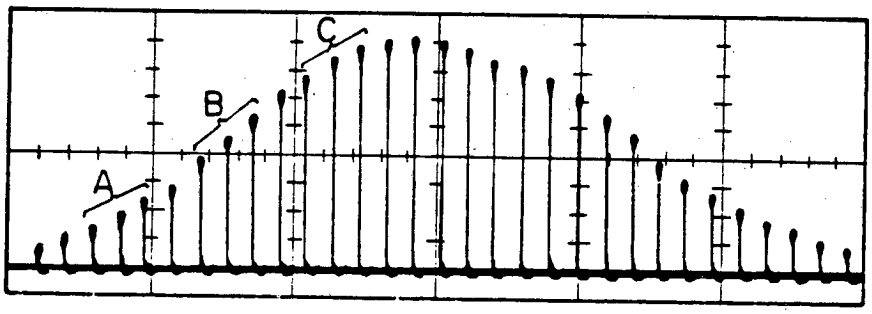

Location	Pulse	Spectral Width FWHM (cm^{-1})	Shots	Condition
A	3rd - 5th	4.6 ± 1.0	6	Without saturable absorber
		4.6 ± 0.8	7	With saturable absorber OD=1
		4.6 ± 0.8	13	All shots
B	7th - 9th	7.2 ± 2.6	30	Without saturable absorber
		8.8 ± 3.2	28	With saturable absorber OD=1
		7.8 ± 3.0	58	All shots
C	11th - 13th	11.6 ± 3.6	7	With saturable absorber OD=1

XBL818-6225

Figure 3

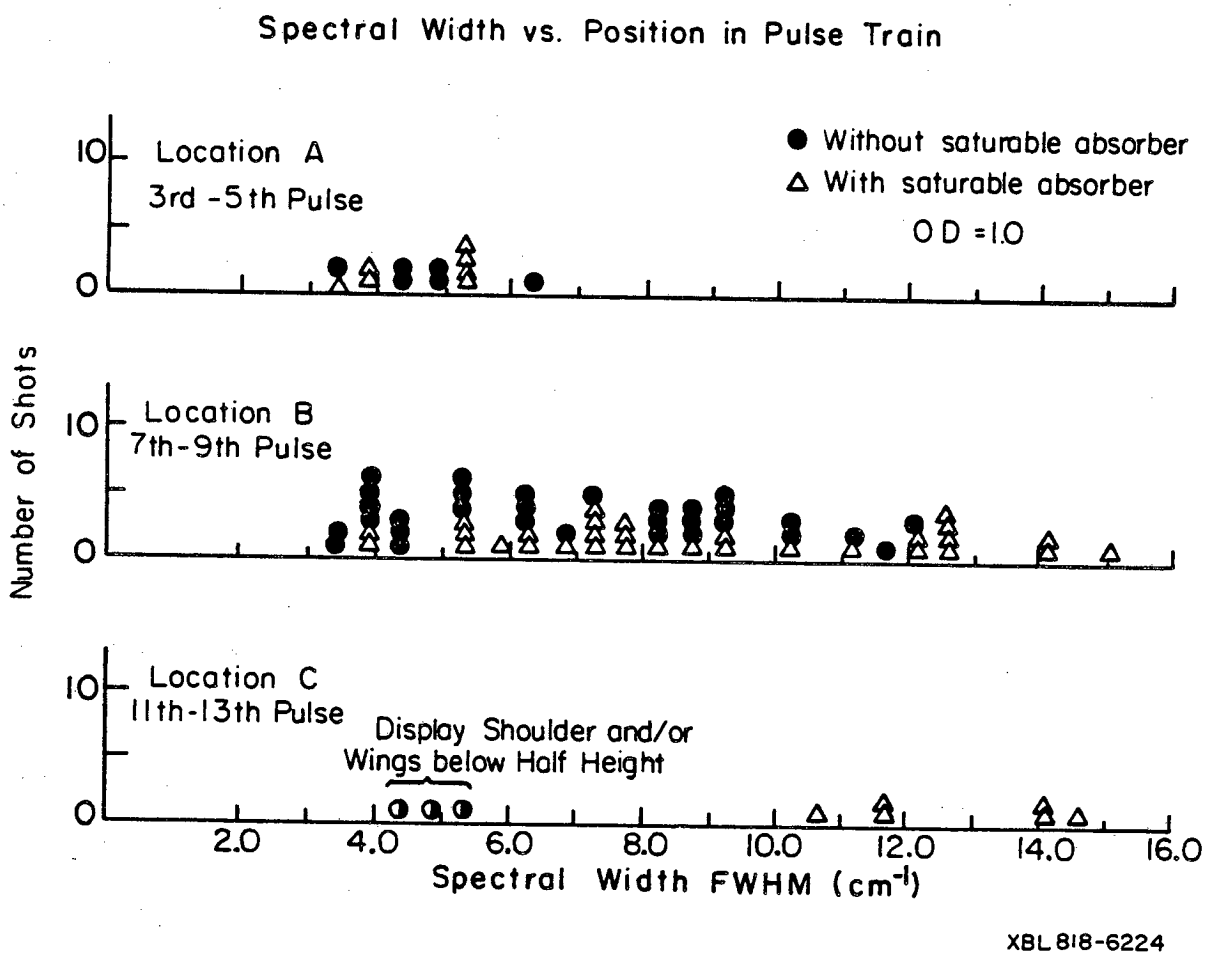
Spectral Width vs. Position in Pulse Train
Location A
3rd -5th Pulse
Without saturable absorber
With saturable absorber
O D =1.0
Location B
7th-9th Pulse
Location C
11th-13th Pulse
Display Shoulder and/or
Wings below Half Height
Number of Shots
10
0
2.0
4.0
6.0
8.0
10.0
12.0
14.0
16.0
Spectral Width FWHM (cm⁻¹)
XBL 818-6224

Figure 4

later in the pulse trains.

IV. Spectra of Individual Shots

Figure 5 shows spectra from individual pulses that were picked from locations between the 4th and 7th pulse in pulse trains of 30-40 pulses. In contrast, Figures 6 and 7 demonstrate the multiplet structure of pulse spectra that can be observed. On "good" days, most of the spectra from pulses picked from locations between the 4th-8th pulse are either singlets similar to Figs. 5(a)-5(d) or quasi-doublets similar to Figs. 6(a) and 6(b). On "bad" days, however, most of the spectra from the same pulse train positions can be higher order multiplets similar to Figs. 6(c) and 6(d) and Figs. 7(a)-7(d). In addition, Fig. 8 shows spectra from individual shots that were picked later in the pulse trains. On "bad" days, these spectra can also occur in the rising edge to the pulse trains.

Luckily for the vibrational dephasing experiments, "good" days occured much more frequently than "bad" days. We are not sure of the cause for the multiplet and messy spectra. These spectra are not significantly affected by amplification voltage. Thus non-linear effects in the amplifier rods or the doubling crystal do not give rise to these spectra. In fact, on "bad" days these spectra were observed even with the amplifiers turned off. Consequently, these spectra seem to be generated in the laser oscillator.

Because of the infrequent occurence of the "bad" spectra, these interesting spectra did not interfer with the vibrational dephasing experiments. Consequently, the relationship between the experimental

parameters and these "bad" spectra was not exhaustively studied. We did notice that when the mode-locking dye cell was rotated and the laser realigned after one "bad" day. the spectra were consistently clean singlets or partial doublets. Thus a burned or partially burned mode-locking dye cell may cause the "bad" spectra.

The multiplet structure of the pulse spectrum is partially consistent with phase modulation of the pulse in the laser oscillator discussed by Zinth et al. [1] and Eckardt et al. [2]. But the non-linear effects occuring in phase modulation should shift the spectral intensity to the red and the blue, depleting the spectral intensity at the central frequency in a very characteristic way [2]. This was not observed. The multiplet-structured spectra are almost always peaked at the central frequency of 5306 Å. On the other hand. an interaction between the gain bandwidth and the phase modulation may be occuring which preferentially amplifies the spectral intensity at the central frequency. The relationship between this process and a burned dye cell is not known.

V. Evaluation of Laser Variables

The effect of the dye cell transmittance on the autocorrelation widths of the 1.06 μ pulses was examined using the TPF apparatus. Figure 9 demonstrates that the dye cell transmittance had no significant effect on the autocorrelation widths on the day that the tranmittance was intentionally varied. Mode-locking could not be acheived outside of the displayed range. The laser was normally operated using a transmittance of ≈75% (double pass) in the mode-locking dye cell.

FIG. 5. (a)-(d) Representative spectra from individual pulses that were picked from locations between the 4th and 8th pulse in a typical pulse train.

FIG. 6. (a)-(d) Representative spectra from individual pulses that display the multiplet structure that can be observed later in the pulse train or early in the pulse train on "bad" days.

FIG. 7. (a)-(d) Representative spectra from individual pulses that display the multiplet structure that can be observed later in the pulse train or early in the pulse train on "bad" days.

FIG. 8. Representative spectra from individual pulses that are generally observed later in the pulse train.

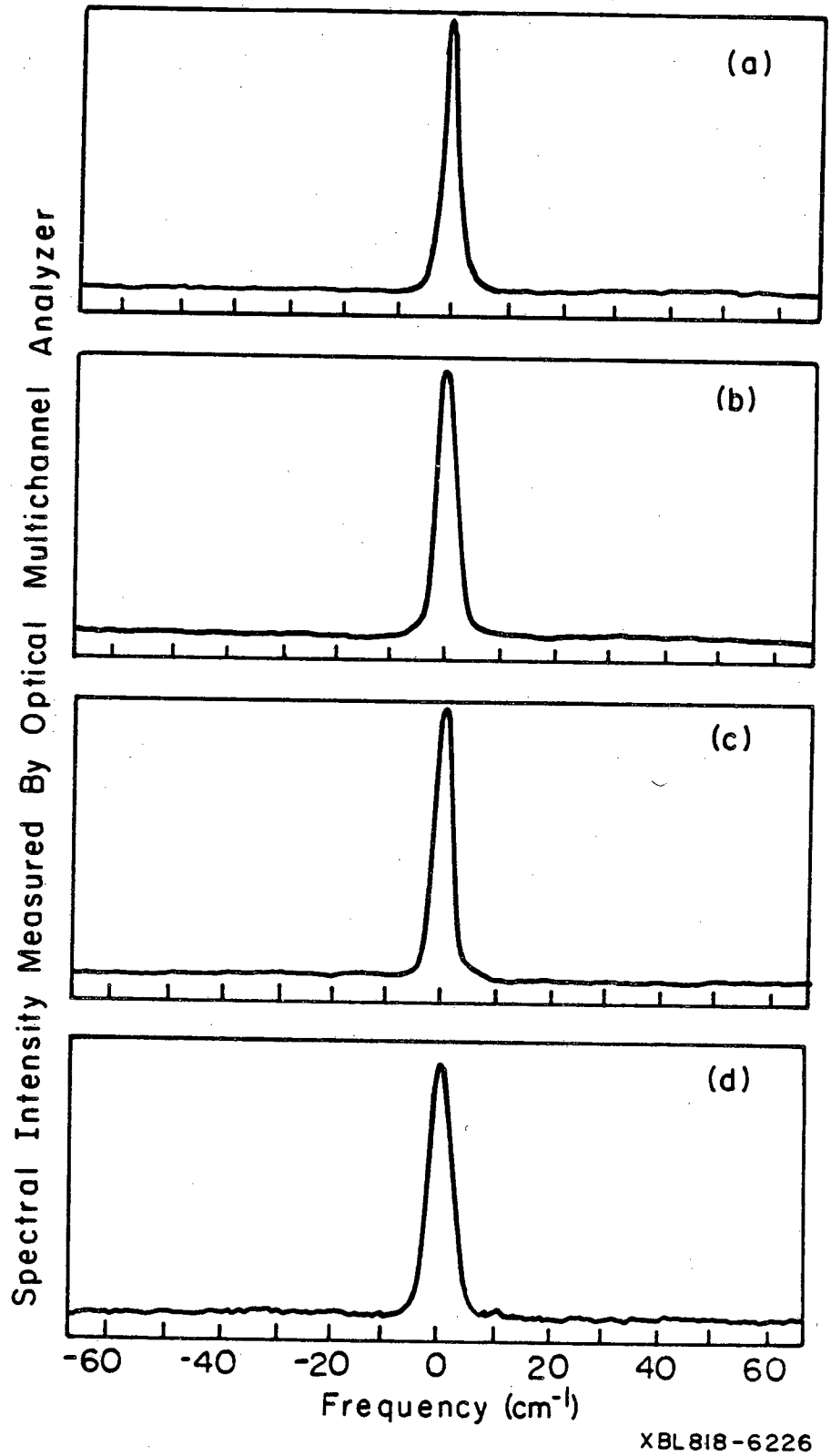
(a)
(b)
(c)
(d)
Spectral Intensity Measured By Optical Multichannel Analyzer
-60
-40
-20
0
20
40
60
Frequency (cm⁻¹)
XBL818-6226

Figure 5

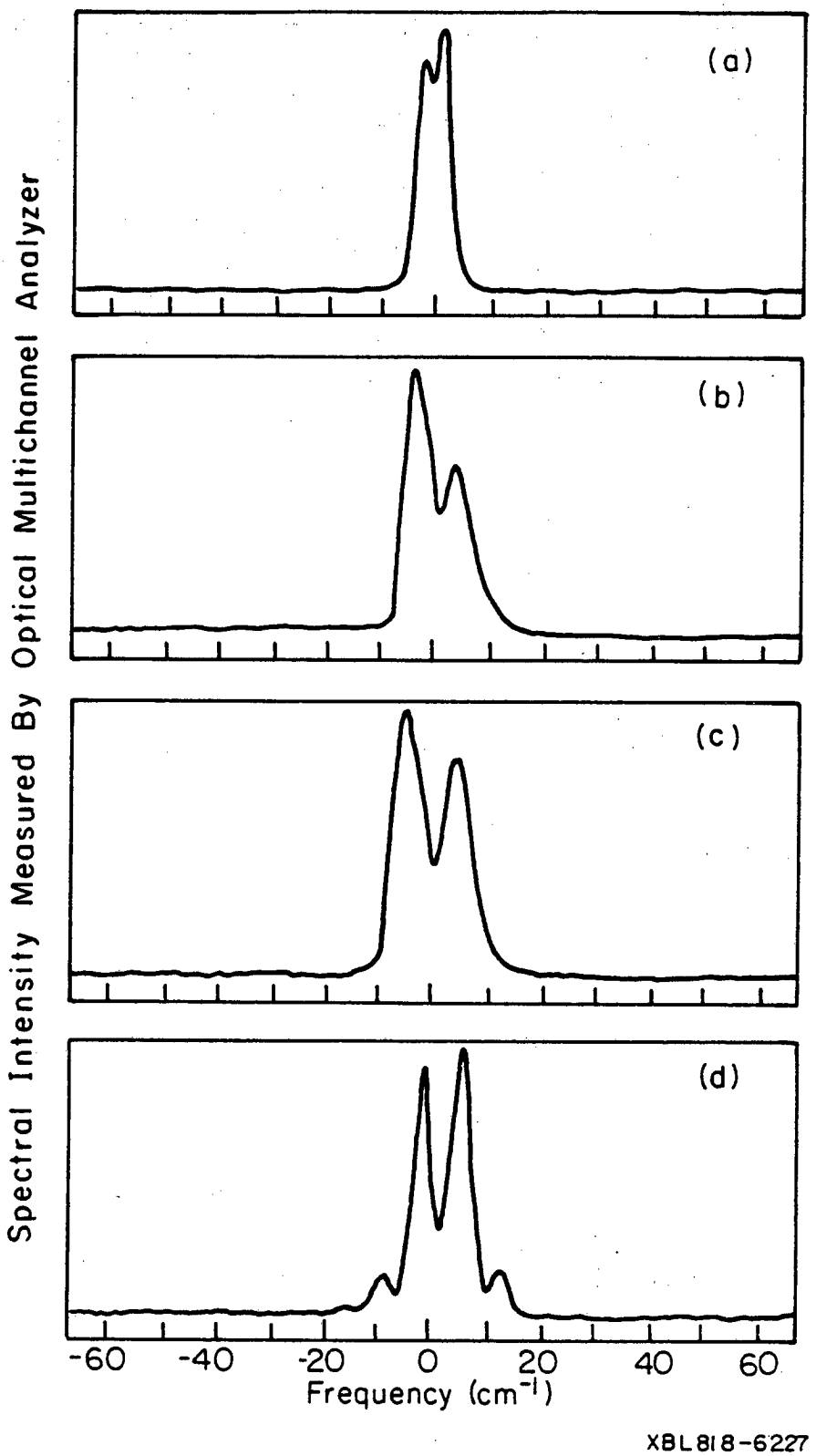
(a)
(b)
(c)
(d)
Spectral Intensity Measured By Optical Multichannel Analyzer
-60
-40
-20
0
20
40
60
Frequency (cm^{-1})
XBL818-6227

Figure 6

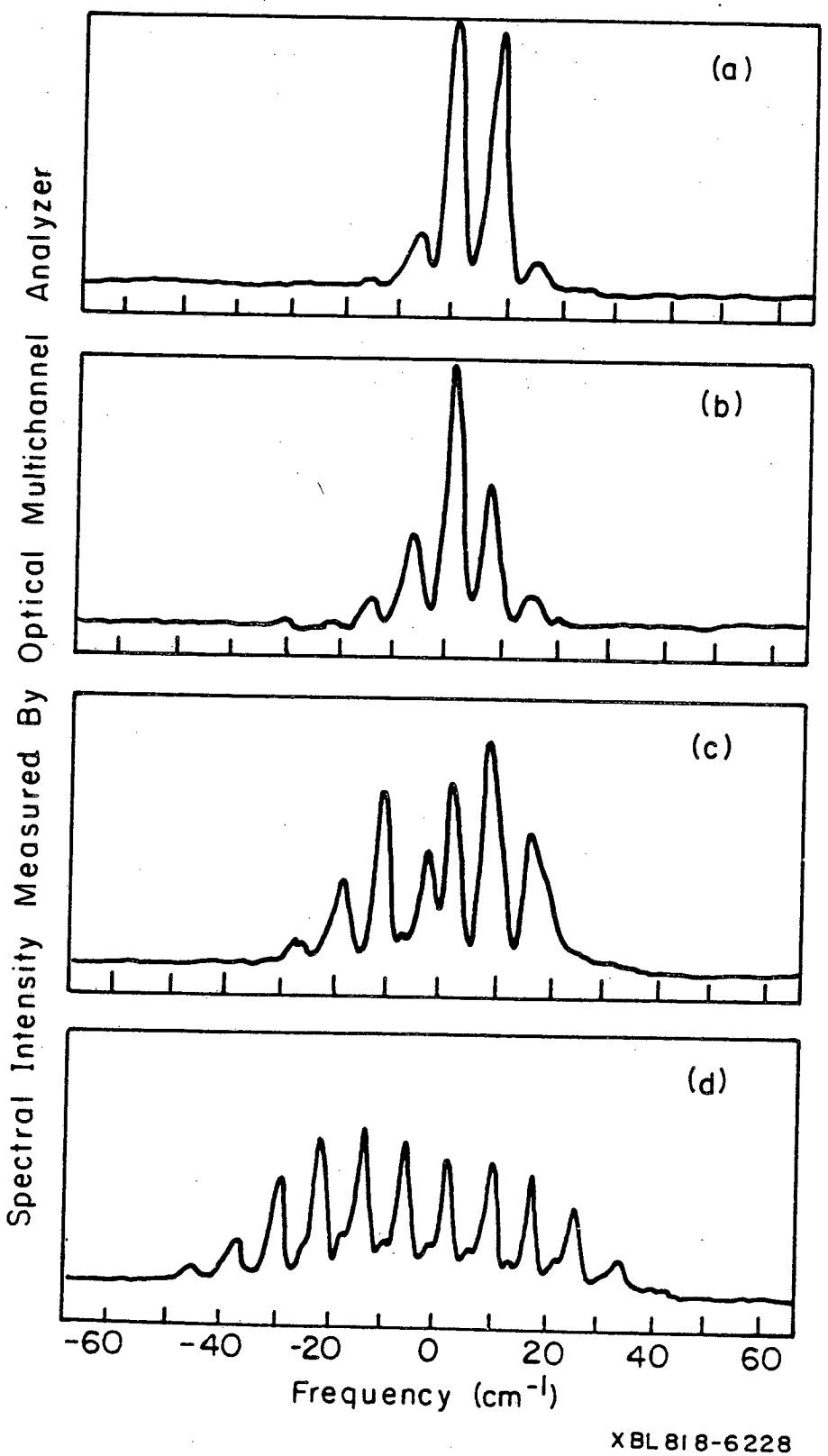
(a)
(b)
(c)
(d)
Spectral Intensity Measured By Optical Multichannel Analyzer
-60
-40
-20
0
20
40
60
Frequency (cm⁻¹)
XBL 818-6228

Figure 7

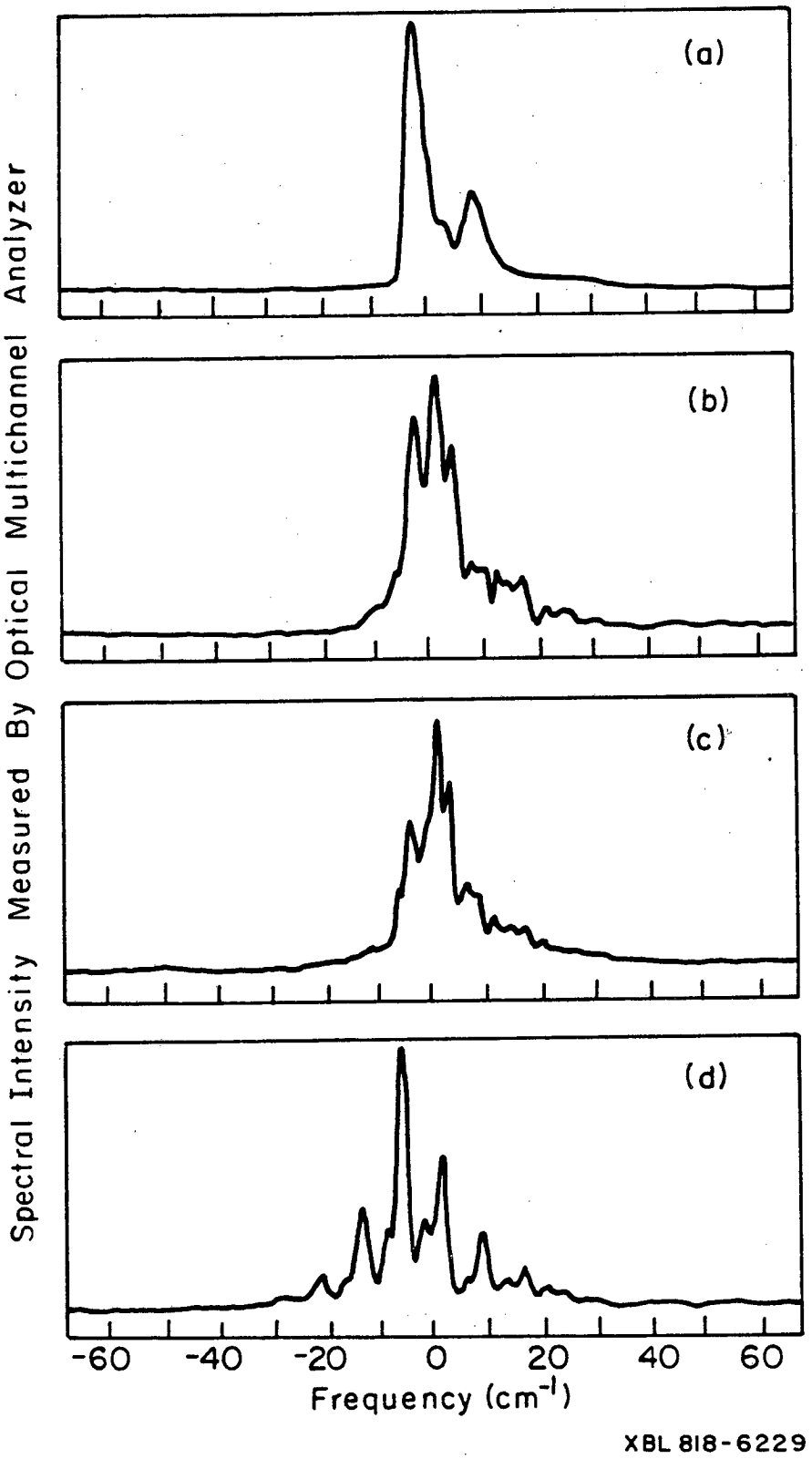
(a)
(b)
(c)
(d)
Spectral Intensity Measured By Optical Multichannel Analyzer
-60
-40
-20
0
20
40
60
Frequency (cm^{-1})
XBL 818-6229

Figure 8

The effect of day-to-day realignment on the autocorrelation widths of the 1.06 μ pulses was also evaluated by comparing the pulse widths determined from the previous TPF studies discussed in this chapter and in Chap. 8. Figure 10 shows that the day-to-day fluctuations were minor. The fluctuations that were observed may have resulted from slight variations in the position of the selected 1.06 μ pulse in the pulse train.

The average 1.06 μ pulse energy obtained after amplification in three Nd:glass laser amplifiers is shown in Fig. 11. The vibrational dephasing experiments described in Chap. 5 were conducted using amplifier voltages of approximately 14, 14 and 0 kV. Lastly, the appearance of the pulse trains in relation to the timing diagram for the picosecond pulse generating system is shown in Fig. 12.

FIG. 9. The effect of dye cell transmittance on the autocorrelation width of the 1.06 μ pulse.

FIG. 10. The effect of day-to-day realignment on the autocorrelation width of the 1.06 μ pulse.

FIG. 11. The average 1.06 μ pulse energy obtained after amplification in our three Nd:glass laser amplifiers.

FIG. 12. The position of the pulse trains emitted by the passively mode-locked Nd:glass laser oscillator in relation to the timing diagram for the picosecond pulse generating system.

Same Day Comparison of Pulsewidth vs.
Mode-Locking Dye Cell Light Transmittance

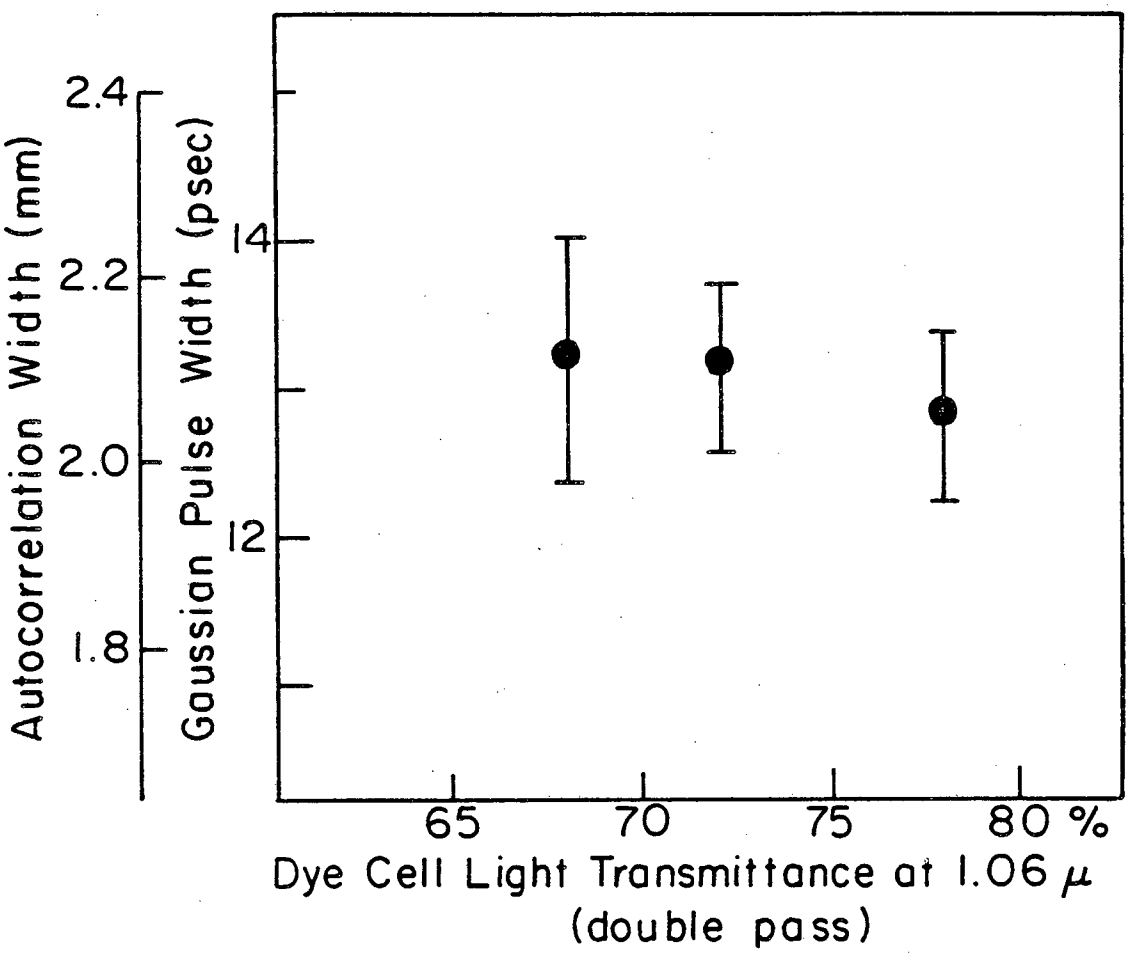

XBL 814-5558

Figure 9

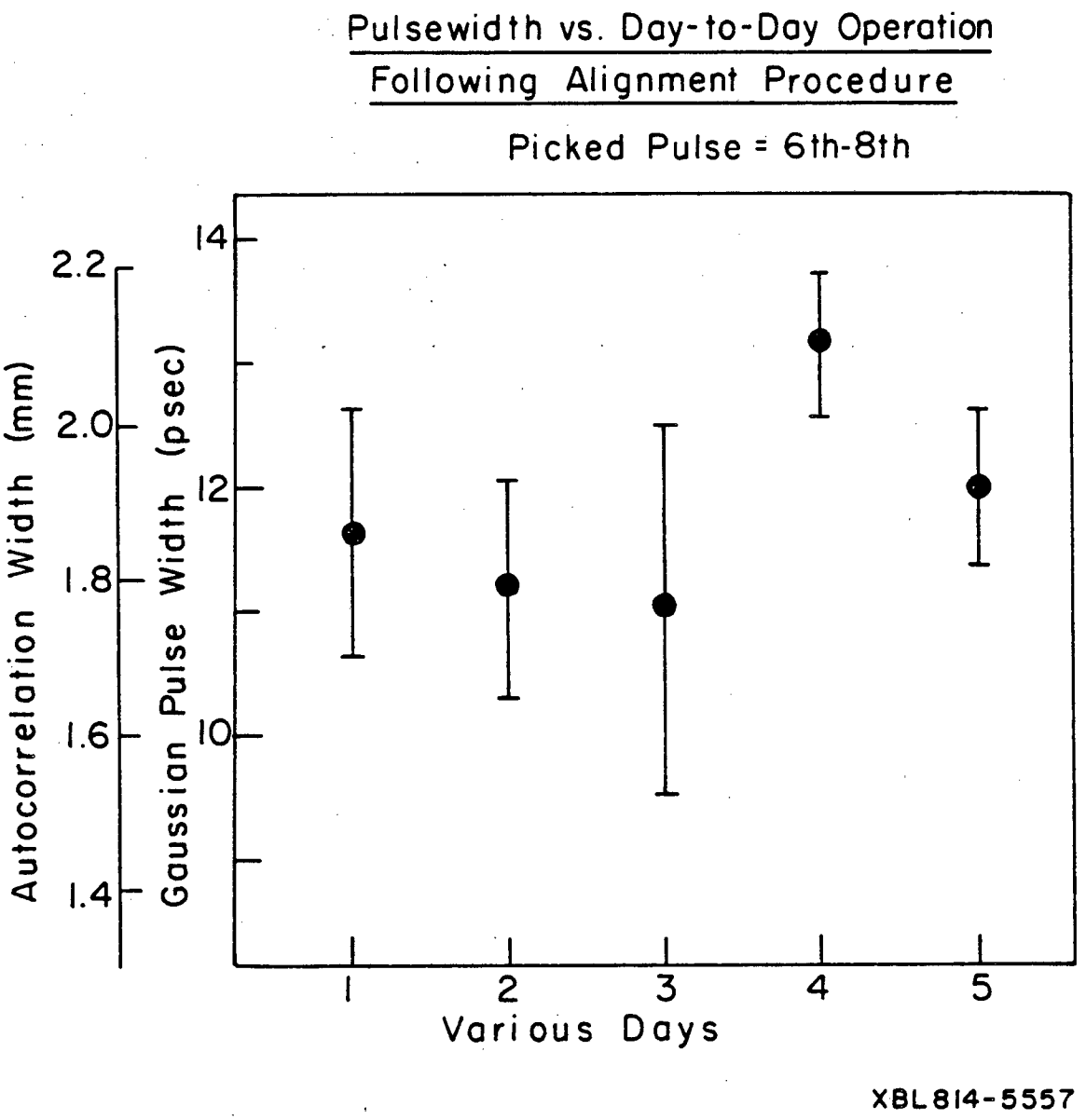
Pulsewidth vs. Day-to-Day Operation
Following Alignment Procedure
Picked Pulse = 6th-8th
Autocorrelation Width (mm)
Gaussian Pulse Width (psec)
2.2
2.0
1.8
1.6
1.4
14
12
10
1
2
3
4
5
Various Days
XBL814-5557

Figure 10

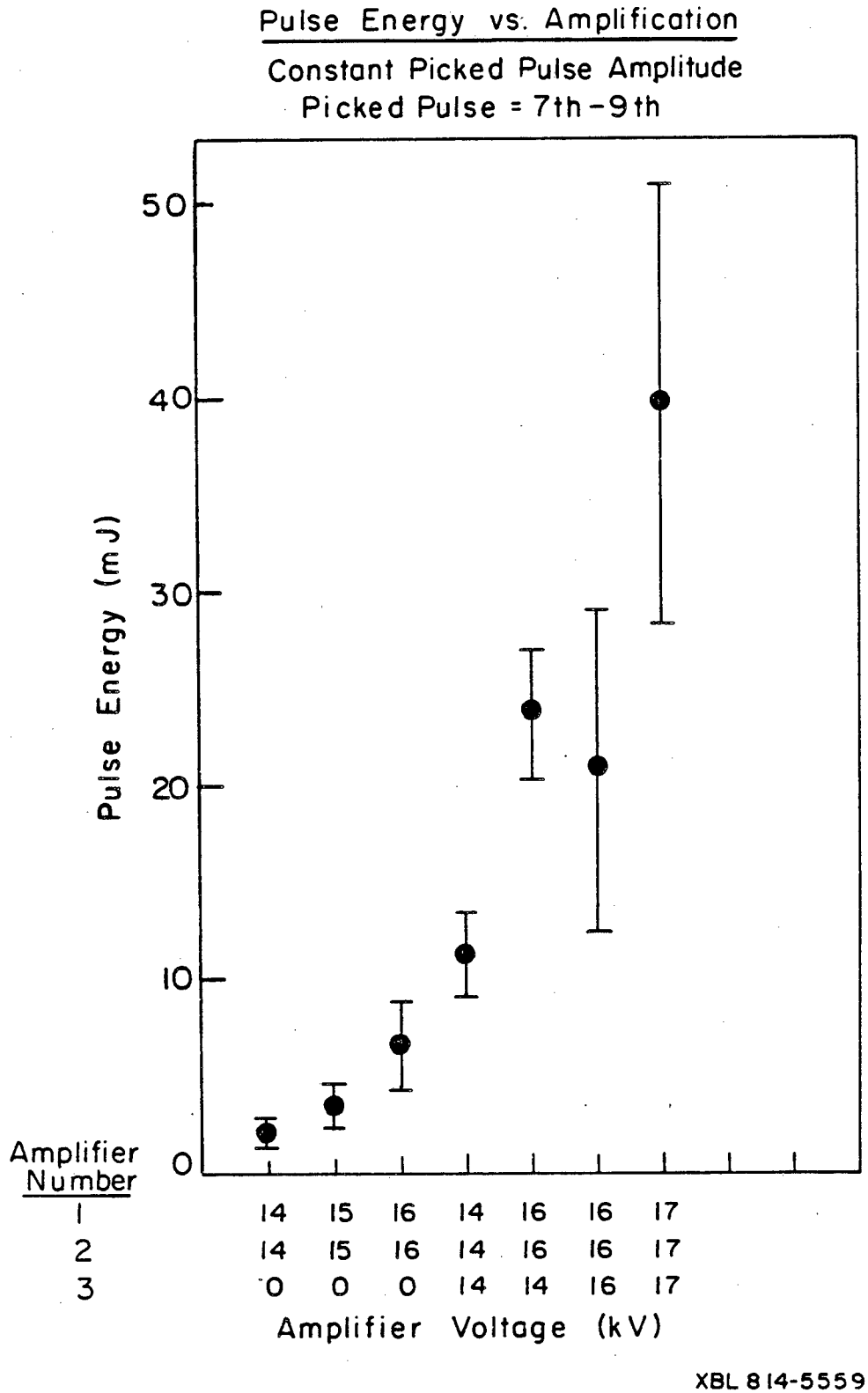
Pulse Energy vs. Amplification
Constant Picked Pulse Amplitude
Picked Pulse = 7th-9th
Pulse Energy (mJ)
50
40
30
20
10
0
Amplifier Number
1
2
3
14 15 16 14 16 16 17
14 15 16 14 16 16 17
0 0 0 14 14 16 17
Amplifier Voltage (kV)
XBL 814-5559

Figure 11

Oscillator Amplifier Flashlamp Synchronization

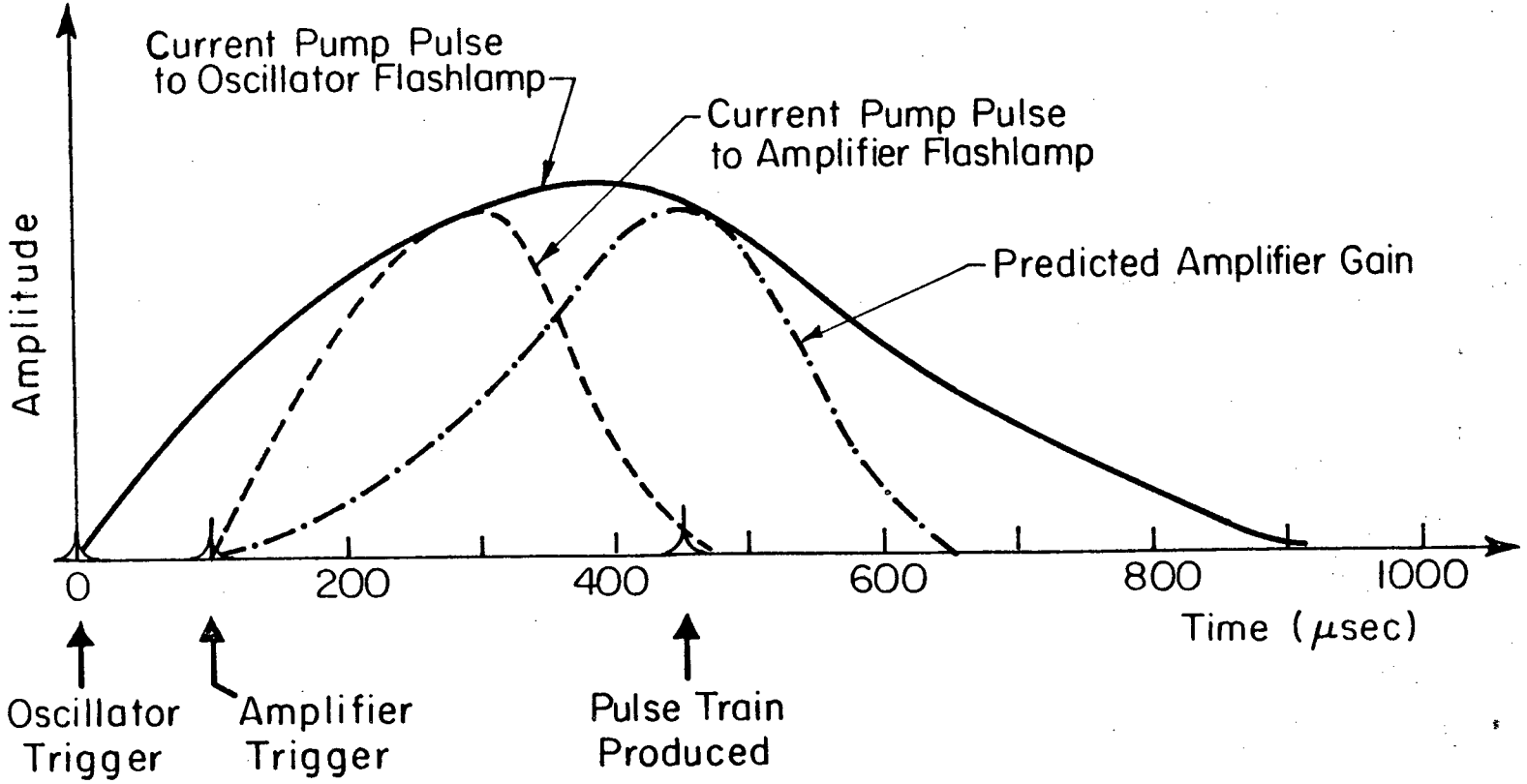

Figure 12

References

1. W. Zinth, A. Laubereau and W. Kaiser, Optics Comm. 22, 161(1977).

2. R.C. Eckardt, C.H. Lee and J.N. Bradford, Opto-Elect. 6, 67(1974).

3. R.C. Eckardt, IEEE J. Quantum Elect. 10, 48(1974).

4. D. von der Linde, O. Bernecker and W. Kaiser, Optics Comm. 2, 149(1970).

5. D. von der Linde, IEEE J. Quantum Elect. 8, 328(1972).

6. D.J. Bradley and W. Sibbett, Optics Comm. 9, 17(1973).

7. M.C. Richardson, IEEE J. Quantum Elect. 9, 768(1973).

8. J.R. Klander, M.A. Duguay, J.A. Giordmaine and S.L. Shapiro, Appl. Phys. Lett. 13, 174(1968).

9. G. Kachen, L. Steinmetz and J. Kysilka, Appl. Phys. Lett. 13, 229(1968).

10. C. Kolmeder and W. Zinth, Appl. Phys. 24, 341(1981).

11. J.A. Giordmaine, P.M. Rentzepis, S.L. Shapiro and K.W. Wecht, Appl. Phys. Lett. 11, 216(1967).

12. A. Laubereau and W. Kaiser, Opto-Elect. 6, 1(1974).

13. D.J. Bradley, B. Liddy and W.E. Sleat, Optics Comm. 2, 391(1971).

14. J.R. Taylor, W. Sibbett and A.J. Cormier, Appl. Phys. Lett. 31, 184(1977).

15. G.R. Fleming, I.R. Harrowfield, A.E.W. Knight, J.M. Morris, R.J. Robbins and G.W. Robinson, Optics Comm. 20, 36(1977).

Chapter 8: Picosecond Pulse Shortening using Dye #5 or Dye #9860 as a Saturable Absorber

I. Introduction

The shortest possible light pulses are desired for optimum time resolution in picosecond studies. One method used to shorten a light pulse is to pass the pulse through a saturable absorber external to the laser cavity [1,2]. Although some theory for the effect of a saturable absorber on a picosecond light pulse has been presented [2], there has been little experimental work on the pulse shortening or intensity reducing effects of external saturable absorbers.

Recently, Reynolds and Drexhage [3], reported on a new infrared absorbing dye, Kodak heptamethine pyrylium dye #5, which has a very fast absorption recovery time of 2.7 psec compared to 6.5 psec for Kodak dye #9860 [4]. Others have reported [4,5] that dye #5 used as a mode-locking dye in Nd:glass laser oscillators gave pulses substantially shorter than those obtained using dye #9860. Kopainsky et al. [4] have also suggested the use of dye #5 as an external saturable absorber.

In this chapter, we report on the effect of dye #5 and dye #9860 used as external saturable absorbers on the width and intensity of single, high power pulses from our Nd:glass oscillator/ampliflier system. The experimental results are compared to the results of a theoretical model. In addition, the saturable absorber effects of dye #5 and dye #9860 are compared on the same day at optical density O.D.=2.0.

II. Experimental

A single picoseond pulse was selected from the rising edge of pulse trains emitted by a TEM_{00} selective, passively mode-locked Nd:glass laser oscillator [6]. A Pockels cell driven by a low jitter electronic circuit [7] consistently selected the 6^{th}-8^{th} intense pulse from pulse trains of 30-45 pulses. A fast photodiode and a Tektronix 7834 fast storage oscilloscope monitored the pulse trains. Shots which displayed multiple pulse trains were excluded from the data.

The selected pulse was amplified in a three stage Nd:glass amplifier. The pulse energy after amplification was determined to be approximately 20 mJ using a Korad/Hadron Model 100 thermopile. Throughout this study, the pulse energy was kept essentially constant.

Dye #5 and dye #9860 were obtained from Eastman Kodak. The dyes were dissolved in 1,2-dichloroethane and the optical densities were measured at 1.06 μ in a 1 cm cell. The dye solution was placed in a 1 cm cell after the final amplifier as shown in Figs. 1 and 2 in Chap. 5. The laser pulse burn spots on developed but unexposed Polaroid film positioned in front of the dye cell had a diameter of 4-5 mm and showed no substructure.

To measure pulse widths, the entire unfocused pulse was sent into a standard two photon fluorescence (TPF) apparatus [8]. The TPF signal was obtained from a 1 X 10^{-3} M methanol solution of rhodamine 6G in a 1 cm cell. An 85 mm camera lens imaged the TPF trace with a magnification of approximately 1.0 on a Princeton Applied Research Model 1254 optical multichannel analyzer (OMA) ISIT detector. High f-numbers of f/22 to f/8 were used to maximize the depth of field. The OMA was interfaced to

a minicomputer which displayed the TPF intensity plot on a CRT screen. Calibration, focus and resolution of the lens-OMA system were determined using a calibrated fine copper mesh at the TPF cell position.

III. Results

Several TPF screen displays are shown in Fig. 1. The display is linear with respect to TPF intensity. TPF peak-to-background ratios were in the range of 2.8-3.0 to 1 on all shots. TPF intensity traces taken without a saturable absorber are shown in Figs. 1(a) and 1(b). Figures 1(c) and 1(d) show TPF intensity traces taken using O.D.=2.0 for saturable absorber dye #9860 and dye #5, respectively.

Pulse widths were determined by measuring the full width at half maximum of the TPF intensity traces. In all figures, each point is an average of 20-30 measurements, and the bars show the standard deviation of the data for each point. Figure 2 displays the TPF autocorrelation widths measured with no saturable absorber and with dye #5 at O.D.=1.0, 2.0 and 3.0. Figure 3 displays a histogram of the data summarized in Fig. 2. All data were taken on the same day under identical amplification and pulse selection conditions.

Assuming Gaussian pulses, the pulse widths, t_p, were calculated using the formula $t_p=(2\ \Delta z\ n)/(2^{1/2} c)$, where Δz is the measured TPF autocorrelation width, n is the refractive index at 1.06 μ in the TPF cell, and c is the speed of light [9,10]. Measured methanol refractive indices in the visible were extrapolated to give n≈1.3235 at 1.06 μ. The measured pulse shortening ratios using dye #5 were 0.84, 0.74 and 0.71 at optical densities 1.0, 2.0 and 3.0, respectively.

FIG. 1 CRT screen traces of TPF intensity profiles measured by an OMA for constant energy light pulses using: (a)-(b) no saturable absorber; (c) saturable absorber dye #9860 at O.D.=2.0 and (d) saturable absorber dye #5 at O.D.=2.0.

FIG. 2. The dependence of the pulse autocorrelation width on the optical density of saturable absorber dye #5 using constant energy light pulses.

FIG. 3. Histogram of the data summarized in Fig. 2.

FIG. 4. The dependence of the pulse autocorrelation width on the optical density of saturable absorber dye #9860 using nearly constant energy light pulses.

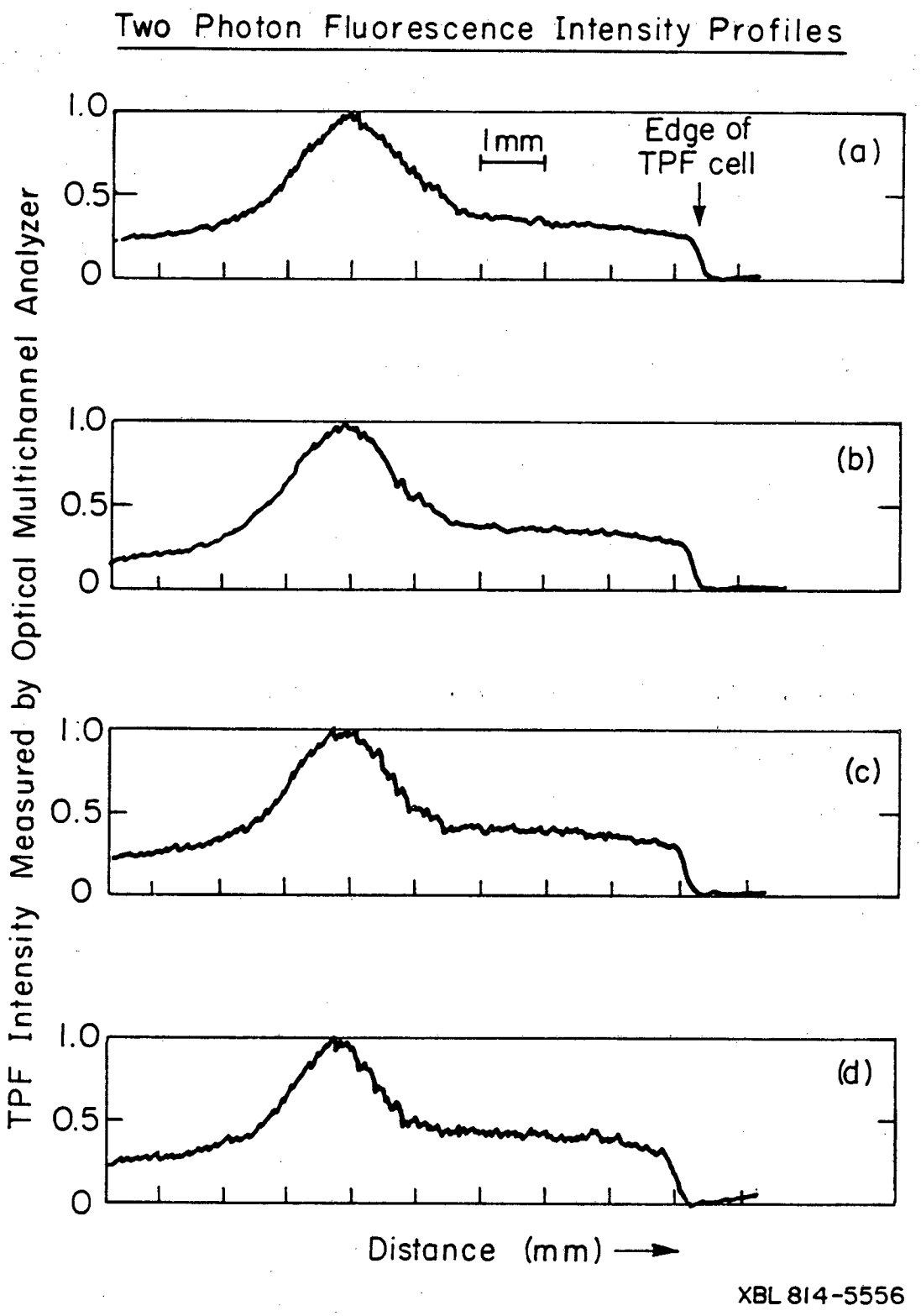
Two Photon Fluorescence Intensity Profiles
TPF Intensity Measured by Optical Multichannel Analyzer
1.0
0.5
0
1mm
Edge of TPF cell
(a)
(b)
(c)
(d)
Distance (mm)
XBL 814-5556

Figure 1

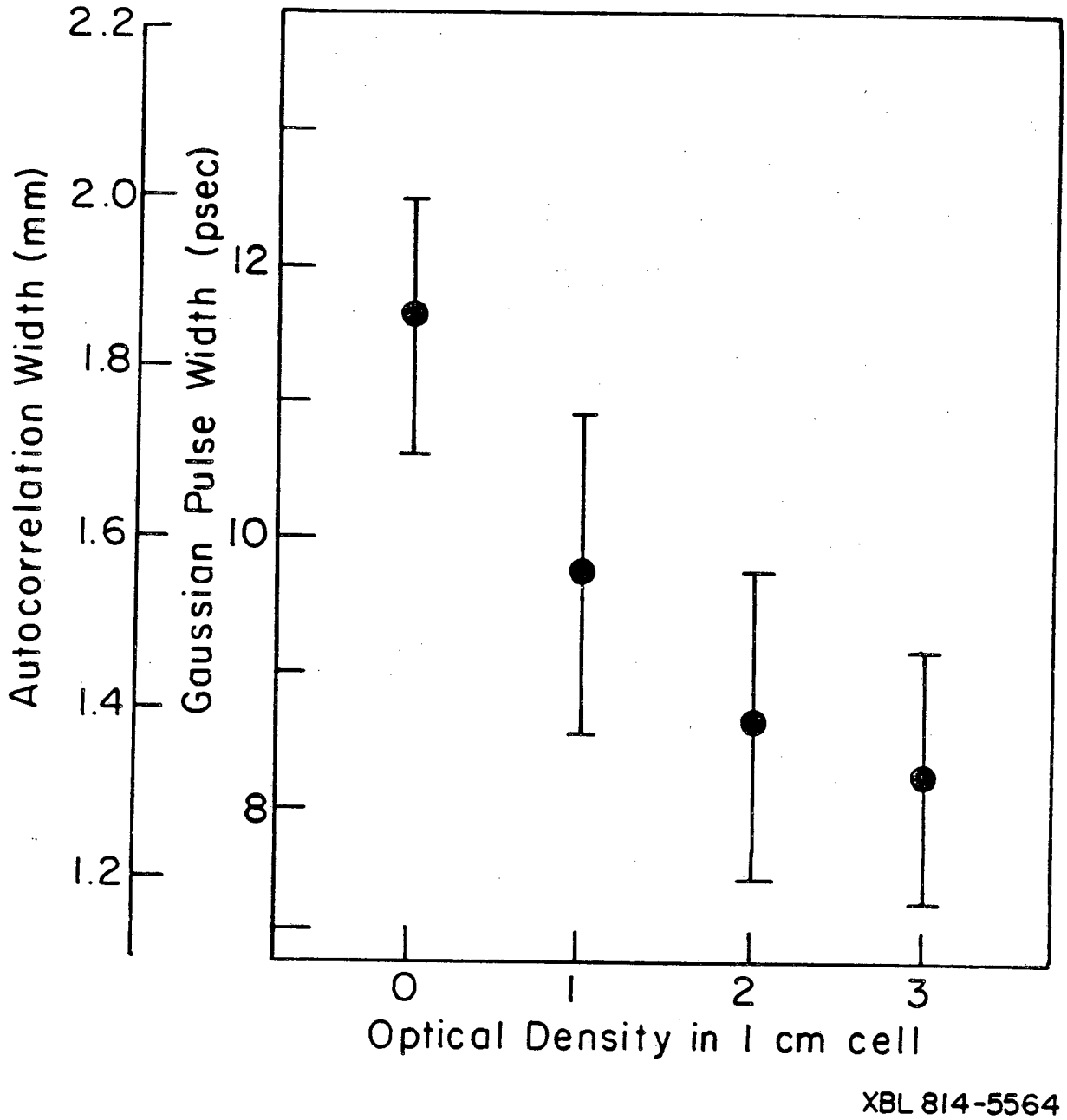
Autocorrelation Width (mm)
2.2
2.0
1.8
1.6
1.4
1.2
Gaussian Pulse Width (psec)
12
10
8
0
1
2
3
Optical Density in 1 cm cell
XBL 814-5564

Figure 2

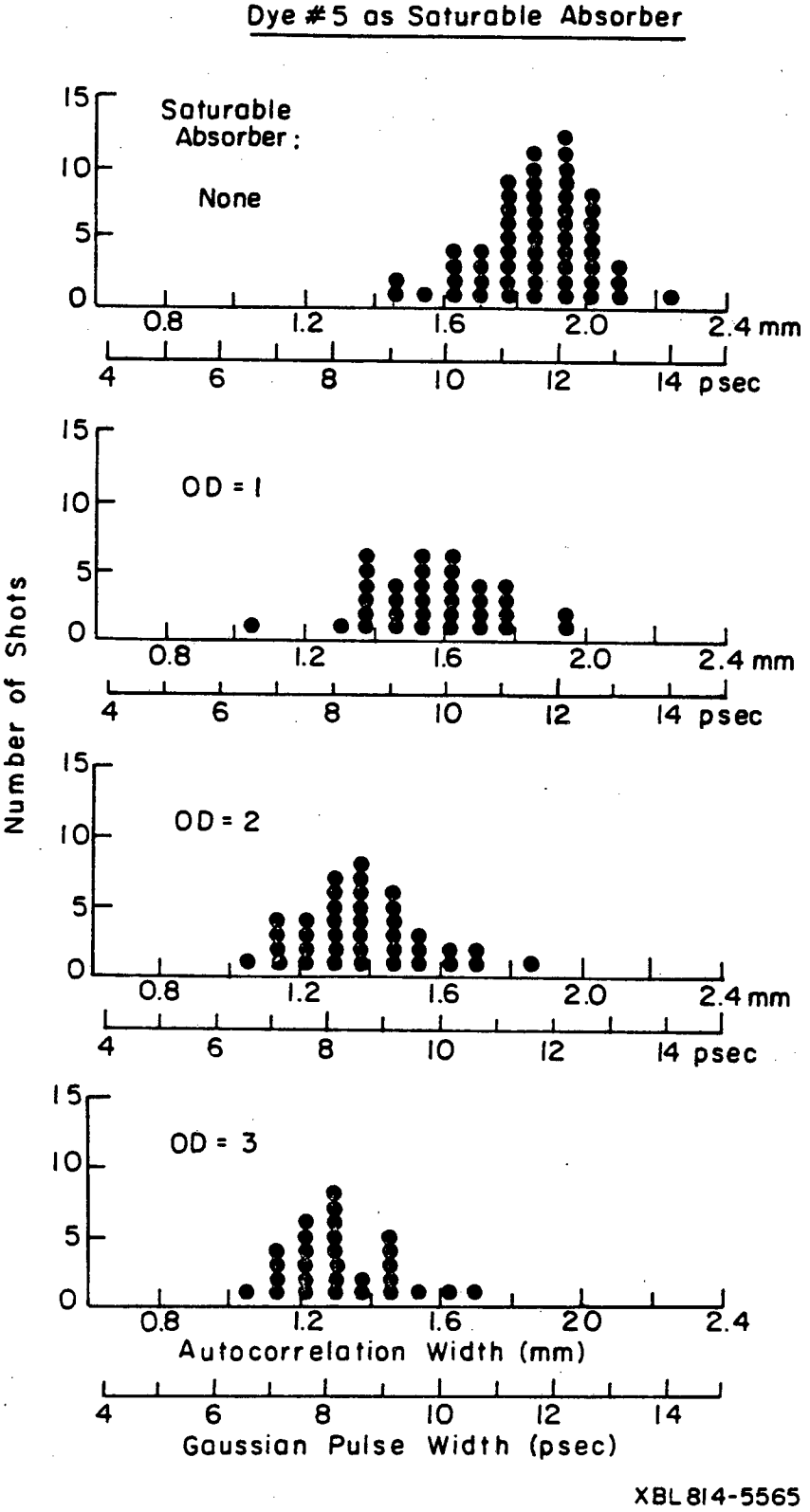
Dye #5 as Saturable Absorber
Saturable Absorber :
None
OD = 1
OD = 2
OD = 3
Number of Shots
0.8
1.2
1.6
2.0
2.4 mm
4
6
8
10
12
14 psec
Autocorrelation Width (mm)
Gaussian Pulse Width (psec)
XBL814-5565

Figure 3

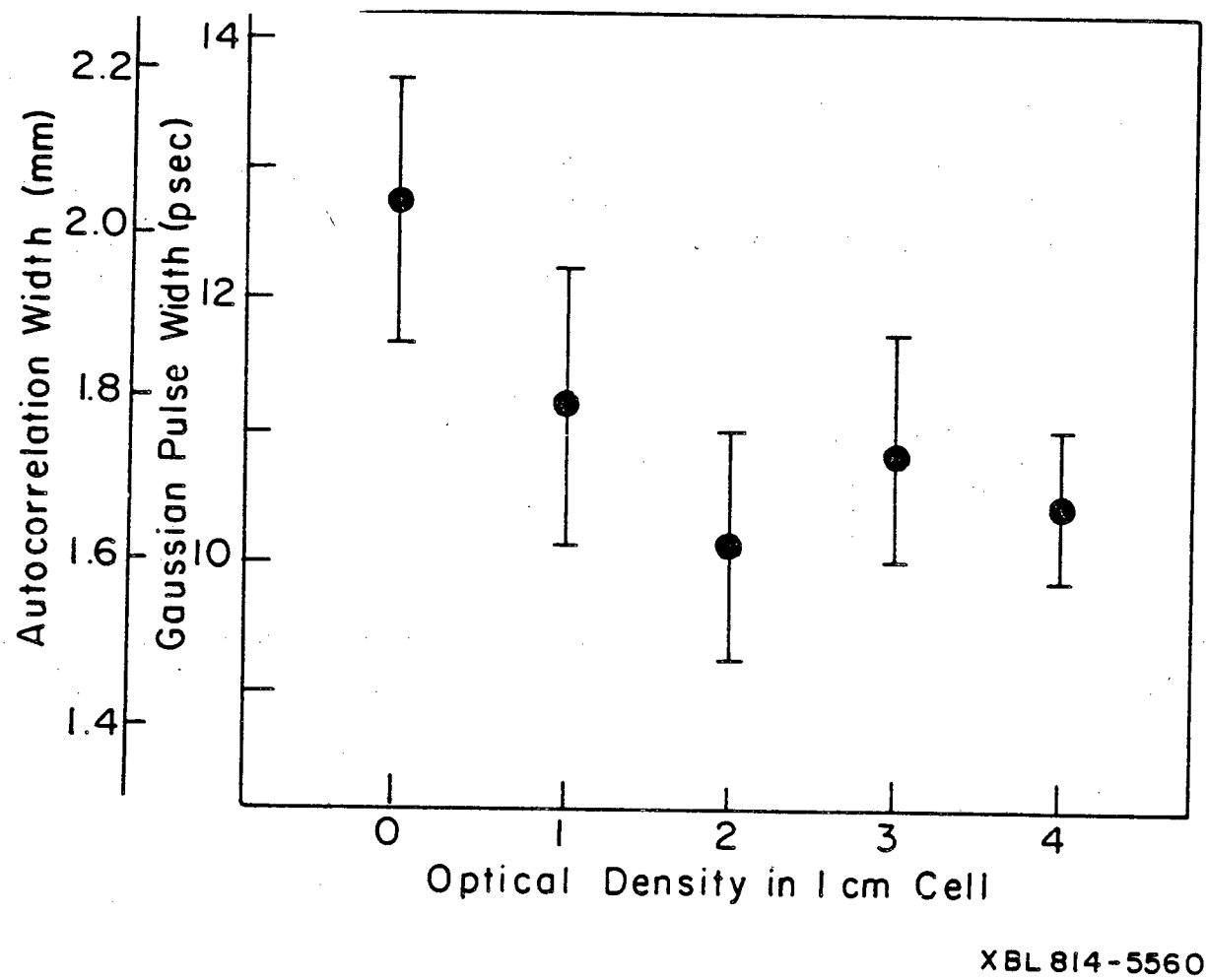
Autocorrelation Width (mm)
2.2
2.0
1.8
1.6
1.4
Gaussian Pulse Width (psec)
14
12
10
0
1
2
3
4
Optical Density in 1 cm Cell
XBL 814-5560

Figure 4

Figure 4 displays the TPF autocorrelation widths measured with no saturable absorber and with dye #9860 at O.D.= 1.0, 2.0, 3.0 and 4.0. All data were taken on the same day. The pulse widths on Fig. 4 are somewhat longer than those on Fig. 2. This difference occured because the position of the selected 1.06 pulse in the pulse train was somewhat later. In addition, the pulse widths at O.D.= 3.0 and 4.0 are not as reliable because the pulse energy was fluctuating more than usual on this day.

The mean squared intensity of the light pulse after passing through the saturable absorber was determined from the peak TPF intensity [8]. Changes in the mean squared intensity emphasize intensity changes near the peak of the pulse. Figure 5 shows the relative TPF peak intensities measured with no saturable absorber and with dye #5 at O.D.=1.0, 2.0 and 3.0.

Dye #5 and dye #9860 were compared by measuring TPF autocorrelation widths and TPF peak intensities with both dyes at O.D.=2.0. Measurements were made on the same day at constant amplification and selected pulse energy. The results are shown in Figs. 6 and 7. Dye #5 gives a shorter TPF autocorrelation width and a greater reduction in pulse intensity than dye #9860 at the same optical density.

FIG. 5. TPF peak intensity dependence on optical density of saturable absorber dye #5 using constant energy light pulses.

FIG. 6. Same day comparison of pulse autocorrelation width dependence on saturable absorber dye #9860 and dye #5 at O.D.=2.0 using constant energy light pulses.

FIG. 7. Same day comparison of TPF peak intensity dependence on saturable absorber dye #9860 and dye #5 at O.D.=2.0 using constant energy light pulses.

FIG. 8. Coherent Stokes signal decay curves in dimethylsulfoxide with and without the saturable absorber dye #9860 at an optical density of 1.0. Assuming $T_2 \simeq 0$, the coherent Stokes signal decay curve is equivalent to the temporal shape of the 5306 Å pulse.

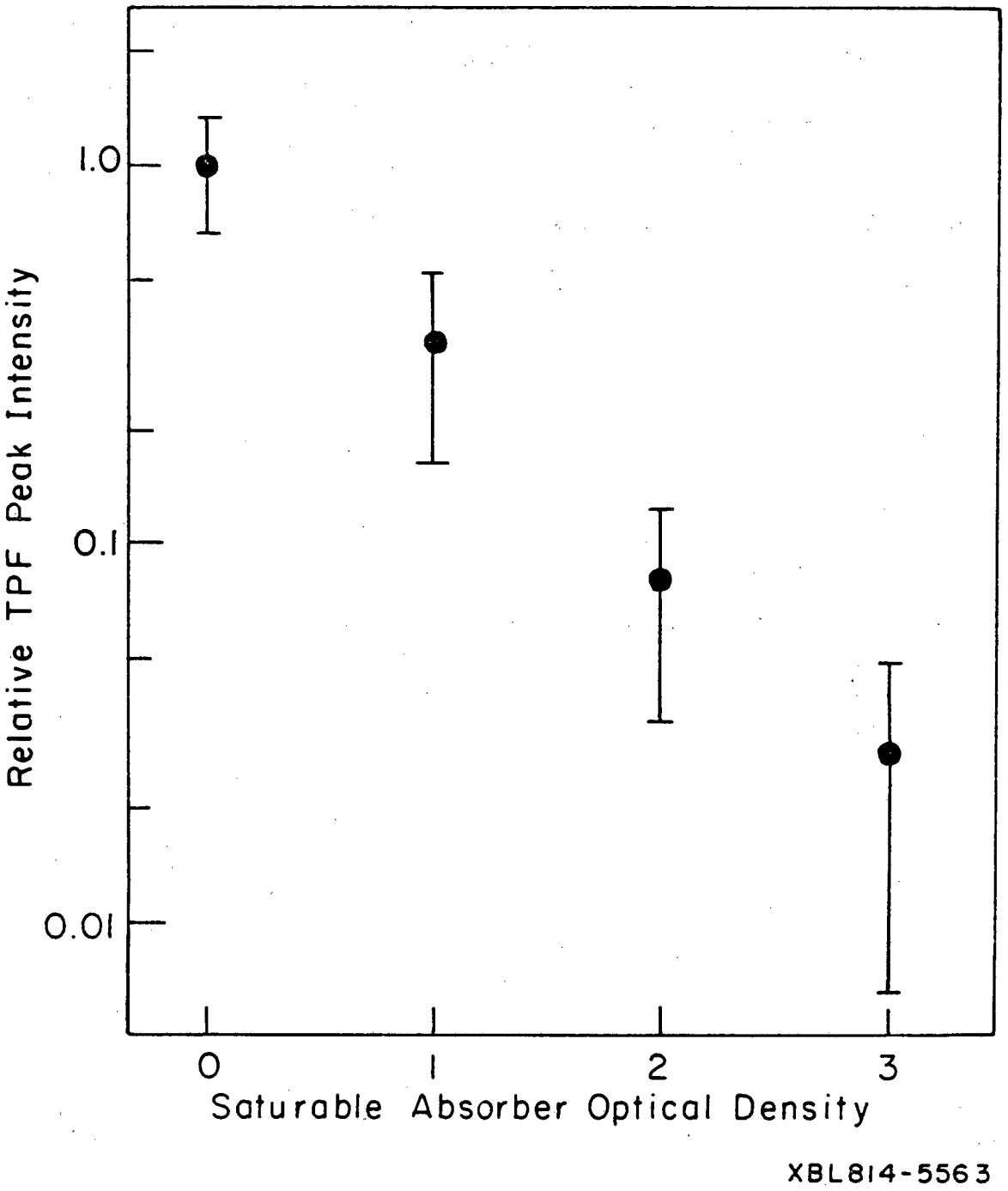
1.0
0.1
0.01
Relative TPF Peak Intensity
0
1
2
3
Saturable Absorber Optical Density
XBL814-5563

Figure 5

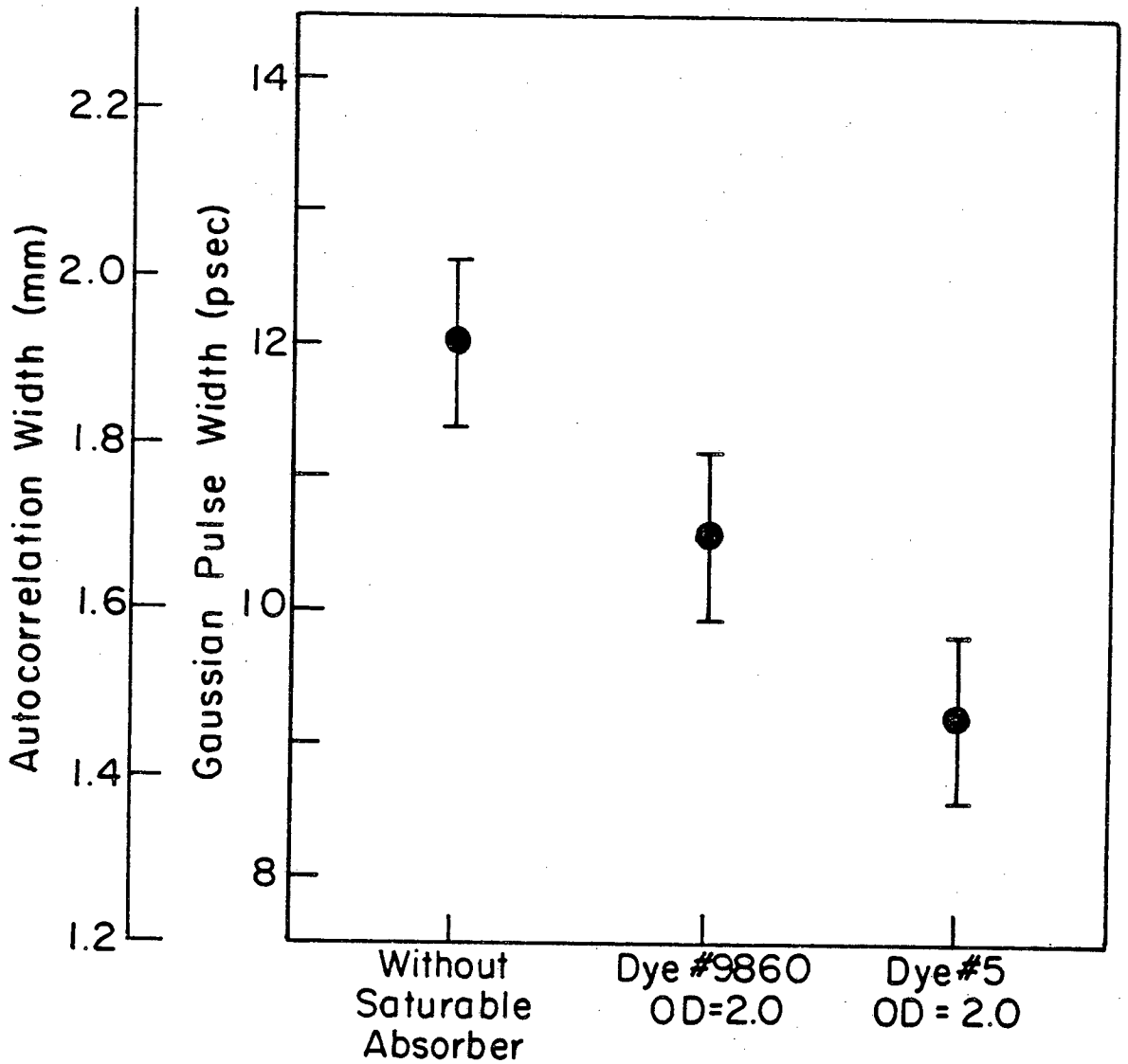
Autocorrelation Width (mm)
2.2
2.0
1.8
1.6
1.4
1.2
Gaussian Pulse Width (psec)
14
12
10
8
Without Saturable Absorber
Dye #9860 OD=2.0
Dye #5 OD = 2.0
XBL 814-5561

Figure 6

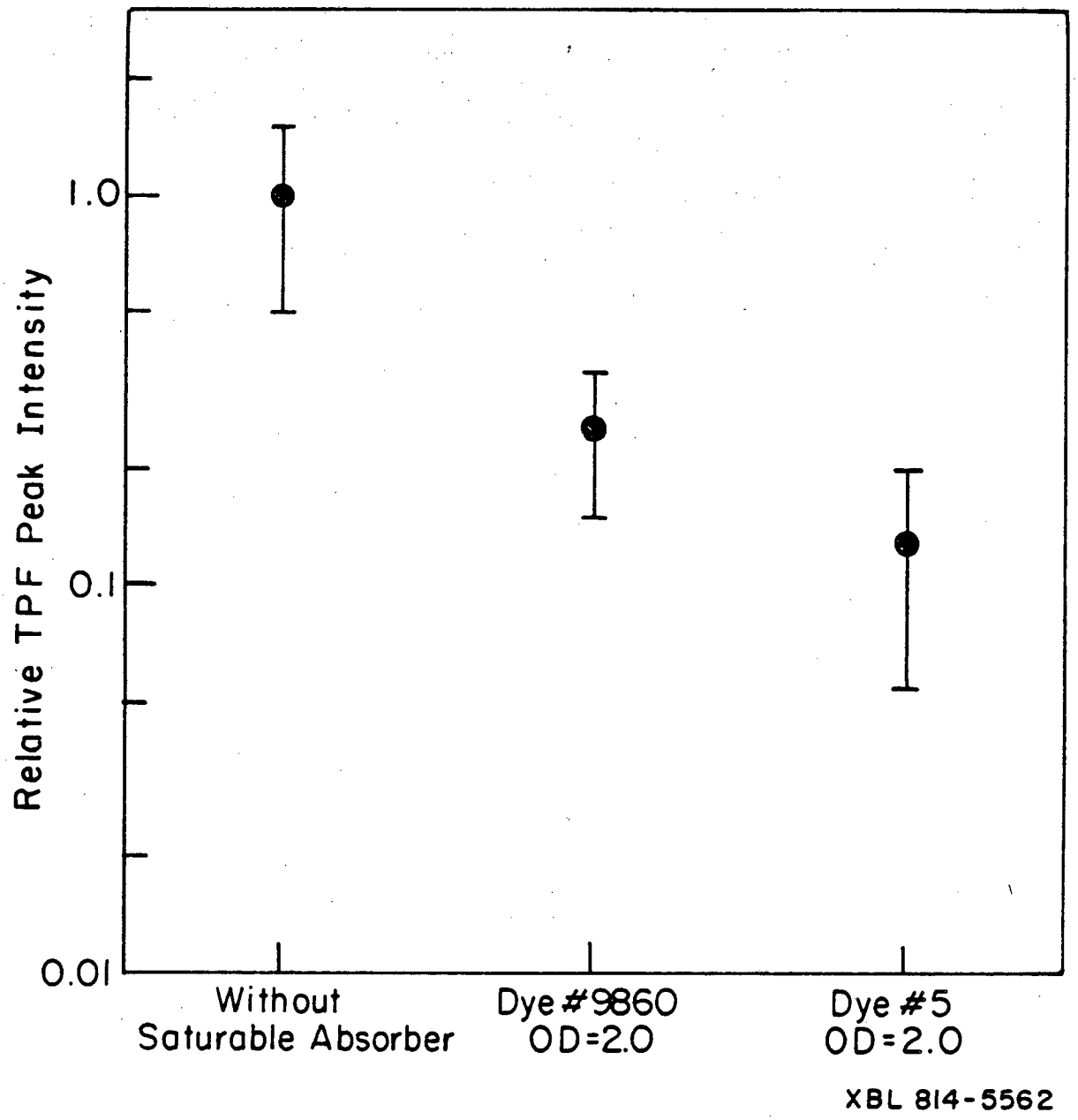
Relative TPF Peak Intensity
1.0
0.1
0.01
Without
Saturable Absorber
Dye #9860
OD=2.0
Dye #5
OD=2.0
XBL 814-5562

Figure 7

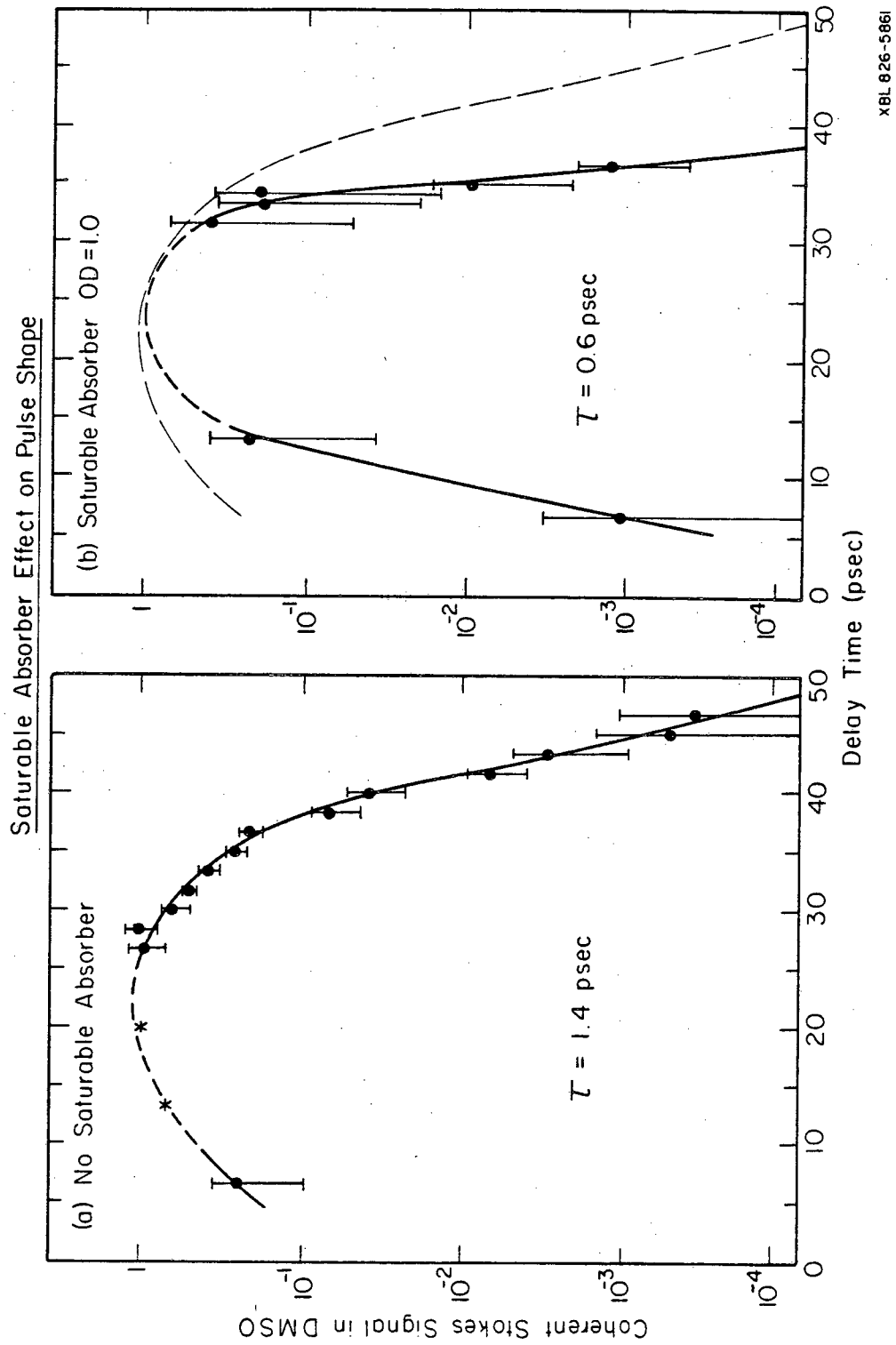
Saturable Absorber Effect on Pulse Shape
(a) No Saturable Absorber
τ = 1.4 psec
(b) Saturable Absorber OD=1.0
τ = 0.6 psec
Coherent Stokes Signal in DMSO
Delay Time (psec)
XBL 826-5861

Figure 8

IV. Discussion

A. Qualitative Agreement with a Numerical Model

Penzkofer [2] has numerically investigated light pulse shortening and intensity reduction effects using saturable absorber parameters modeled for dye #9860. His calculations suggest that dyes having a smaller ratio of relaxation time to pulse width should show qualitatively similar behavior (see Fig. 5 of Ref. 2).

Penzkofer presented a graphical summary of the numerical results for the pulse shortening ratio (Fig. 4 of Ref. 2) and for the peak intensity transmission (Fig. 8 of Ref. 2) as a function of input peak intensity and saturable absorber optical density. Both the pulse shortening ratio and the peak intensity transmission show qualitatively different behavior at low input peak intensities of 1-6 X 10^8 W cm^{-2} compared to the behavior with input peak intensities above 6 X 10^8 W cm^{-2}.

At low input peak intensities, the calculated pulse shortening ratios decrease with increasing optical density, then level off, with ratios remaining in the range 0.9-0.5 for optical densities greater than O.D.=1-5. In the same low intensity region, the peak intensity transmissions show a steady decrease with increasing optical density.

With input peak intensities above 6 X 10^8 W cm^{-2}, the pulse shortening ratios do not level off until much higher optical densities of 7-40, at which point very small pulse shortening ratios of 0.5-0.2 are obtained. With these high intensity pulses, the peak intensity transmissions do not decrease significantly at low optical densities,

but show a sudden reduction above a particular transition optical density in the range O.D.=5-40.

Our experimental pulse shortening ratios for dye #5 decrease with increasing optical density and begin to level off at a value of 0.7 for O.D.=3.0. Likewise, the measured mean squared intensity transmissions show a steady decrease with increasing optical density. These results are qualitatively consistent with Penzkofer's numerical results for low input peak intensities. A quantitative comparison with Penzkofer's results was not attempted.

B. Experimental Considerations and Pulse Shapes

The short relaxation time of τ=2.7 psec for dye #5 enables this saturable absorber to quickly recover after being bleached by the pulse's rising edge. This short relaxation time enables dye #5 to be more effective in pulse shortening than dye #9860 at the same optical density. However, the rapid recovery of dye #5 significantly reduces the peak intensity of the pulse.

For our 1.06 μ pulses with $t_p \simeq 9$ psec, we believe dye #9860 with a relaxation time of τ=6.5 psec is better suited for use as a saturable absorber. Dye #9860 absorbs the rising edge of our 1.06 μ pulses, then bleaches, allowing the peak and the main portion of the pulse to be transmitted with little attenuation. More generally, if pulses with sharp rising edges but with little peak intensity reduction are required, the relaxation time of the saturable absorber should roughly match the pulse temporal width.

Using the dye #9860 at O.D.=1.0 as a saturable absorber, our

excite-and-probe vibrational dephasing experiments have measured coherent Stokes signal decays as rapid as $T_2/2$=0.5-0.7 psec in dimethylsulfoxide. This indicates that the rising edge of the frequency-doubled 5306 Å pulse is <0.5-0.7 psec. Assuming impact excitation and $T_2 \simeq 0$, the measured coherent Stokes signal decay curves are equivalent to the temporal shape of the 5306 Å pulse.

Pulse shapes obtained with and without the dye #9860 are illustrated in Fig. 8. Because of the short T_2 in DMSO, higher pulse intensities were required to reach the threshold for stimulated Raman scattering. Consequently, the probe Stokes signals corresponding to points at the top of these curves where the excite and probe pulses directly overlap were usually severely frequency broadened. The Stokes probe signals displayed a "continuum-like" appearance with spectral widths typically $\geq$100 cm^{-1}. This was also a problem at the top of the decay curves for the other methyl liquids on larger shots.

References

1. A. Penzkofer, D. von der Linde, A. Laubereau and W. Kaiser, Appl. Phys. Lett. 20, 351(1972).

2. A. Penzkofer, Opto-Electron. 20, 87(1972).

3. G.A. Reynolds and K.H. Drexhage, J. Organ. Chem. 42, 885(1977).

4. B. Kopainsky, W. Kaiser and K.H. Drexhage, Opt. Commun. 32, 451(1980).

5. R.R. Alfano, N.H. Schiller and G.A. Reynolds, IEEE J. Quantum Electron. QE-17, 290(1981).

6. S.M. George and C.B. Harris, Rev. Sci. Instrum. 52, 852(1981).

7. S.J. Davis, J.E. Murray, D.C. Downs and W.H. Lowdermilk, Appl. Opt. 17, 3184(1978).

8. D.J. Bradley and G.H.C. New, Proc. IEEE 62, 313(1974).

9. D. von der Linde, O. Bernecker and W. Kaiser, Opt. Commun. 2, 149(1970).

10. J.A. Giordmaine, P.M. Rentzepis, S.L. Shapiro and K.W. Wecht, Appl. Phys. Lett. 11, 216(1967).

Chapter 9: Summary

What is the mechanism of vibrational linewidth broadening in liquids? What is the relationship between vibrational linewidth broadening and the dynamics and structure of liquids? Focusing on symmetric CH_3-stretching vibrational linewidths in liquids, this thesis has provided some answers to these questions.

The work presented in this thesis is consistent with the picture that vibrational linewidths are broadened by short and long range interactions between the vibration and the surrounding liquid solvent. Assuming a Lennard-Jones 6-12 intermolecular potential between the vibration and the neighboring molecules, the short range 1/12 Lennard-Jones repulsive potential gives rise to rapidly varying interactions associated with "billard ball" type hard core collisional dynamics. These rapidly varying interactions lead to homogeneous broadening.

On the other hand, the long range 1/6 Lennard-Jones attractive potential gives rise to slowly varying interactions associated with multipole or dispersion forces. Quite distinct from the short range hard core collisions, these multipole interactions average over several coordination spheres of surrounding molecules. Thus the vibration interacts with the surrounding liquid dielectric structure which can be characterized by a local number density. Consequently, a distribution of local number densities in a liquid gives rise to a distribution of multipole interaction energies. If the lifetime of the local number density sites is long, this distribution leads to inhomogeneous broadening.

The work presented in this thesis, along with the general Schweizer-Chandler vibrational dephasing theory [1] and the Schindler-Jonas analysis of the isothermal density dependent isotropic Raman linewidths in isobutylene [2] provide a firm foundation for an understanding of vibrational linewidth broadening in liquids. In comparison to the understanding ten years ago, the most novel aspect of this present day foundation is the recognition of the importance of slowly varying, attractive forces which give rise to inhomogeneous broadening. We now recognize that vibrational linewidths in liquids are broadened by both rapidly varying liquid dynamics and slowly varying liquid structure.

Future investigations of T_2 homogeneous dephasing times and vibrational linewidth broadening will proceed along many various avenues. As long as inhomogeneous broadening is not ignored, isotropic spontaneous Raman studies will continue to have an important utility in mapping out the general trends in vibrational linewidth broadening [3,4]. Selective excite-and-probe vibrational dephasing experiments will also continue to be employed, especially as high power picosecond technology advances.

In addition, several new techniques will probably improve the ability to measure the T_2 dephasing time in liquids. For example, as tunable infrared pulsed lasers continue to be developed, excite-and-probe infrared hole-burning experiments [5-7] will have a wide applicability for a wide variety of vibrations in liquids. These infrared hole-buring experiments certainly have the potential to acheive what electronic hole-burning experiments [8] have already accomplished.

Picosecond coherent Stokes [9] or Anti-Stokes [10] Raman experiments using two overlapped light pulses tuned so that their difference frequency is equal to the vibrational frequency also have a great potential. However, the main issue to be resolved in these experiments is their selectivity. Are they measuring T_2 homogeneous dephasing times or simply the Fourier transform of the vibrational bandwidth that they coherently excite?

In addition, the characteristics of transient stimulated Raman scattering in high laser depletion are dependent upon the T_2 homogeneous dephasing time. Consequently, streak camera studies of the width of the Stokes pulse with respect to the incident laser pulse and the position of the Stokes pulse peak with respect to the laser pulse peak would reveal information about the T_2 dephasing time. Streak camera investigations of this kind have never been conducted using picosecond pulses in liquids.

Lastly, given that the T_2 homogeneous dephasing time has been measured, an important question still remains: What are the contributions of T_2^*, the pure dephasing relaxation time, and T_1, the population relaxation time, to T_2? Only a few T_1 population relaxation times have been measured for a handful of C-H vibrations in liquids at room temperature. As tunable infrared lasers continue to be developed, however, this situation may change considerably. Ultimately, a more thorough and complete understanding of vibrational linewidth broadening in liquids will emerge when accurate measurements of T_2 and T_1 can be routinely made for a wide variety of vibrations.

References

1. K.S. Schweizer and D. Chandler, J. Chem. Phys. 76, 2296(1982).

2. W. Schindler and J. Jonas, J. Chem. Phys. 72, 5019(1980); J. Chem. Phys. 73, 3547(1980).

3. K.A. Wood and H.L Strauss, J. Chem. Phys. 74, 6027(1981).

4. K. Tanabe, Chem. Phys. 63, 135(1981).

5. P. Felder and Hs.H. Gunthard, Chem. Phys. Lett. 88, 473(1982).

6. M. Dubs, L. Ermanni and Hs.H. Gunthard, J. Mol. Spec. 91, 458(1982).

7. M. Harig, R. Charneau and H. Dubost, Phys. Rev. Lett. 49, 715(1982).

8. For example, S. Volker, R.M. MacFarlane, A.Z. Genack, H.P. Trommsdorff and J.H. van der Waals, J. Chem. Phys. 67, 1759(1977).

9. J.P. Heritage, Appl. Phys. Lett. 34, 470(1979).

10. W.H. Hesselink, B.H. Hesp and D.A. Wiersma, in Picosecond Phenomena II, ed. by R.M. Hochstrasser, W. Kaiser and C.V. Shank, (Springer-Verlag, New York, 1980), p. 138.

ACKNOWLEDGEMENTS

The work presented in this thesis would not have been possible without the help and support from many people. I especially thank my research advisor, Prof. Charles B. Harris, for setting the direction of this work and for providing constant encouragement and support. His unique scientific insights and goals have always been instructional and inspirational.

I am deeply grateful to Helmut Auweter who came to Berkeley as a post-doc during the beginning of this work. We worked side-by-side for month after month until the vibrational dephasing experiments were finally on a productive course.

After Helmut left, I was extremely lucky to have Alexander Harris and Mark Berg as coworkers. Together we overcame the many technical challenges which ultimately enabled us to do the temperature-dependent vibrational dephasing experiments.

I am also grateful to Dor Ben-Amotz for helping to characterize transient stimulated Raman scattering in high depletion. In addition, I thank James Chao and Paul Cornelius for interfacing and programing the optical multichannel analyzer used in this work.

I am thankful to the past and present members of the C.B. Harris research group for their help and fellowship. The environment that they have provided has been a very important part of my education and life. I am also grateful to Vijaya Narasimham for her efforts to keep the group running smoothly.

I would also like to thank the many support personnel who made this

work possible. In particular, Fred Wolff, Andy Anderson and others in the Chemistry machine shop helped design and construct the custom equipment used in these experiments. Don Wilkinson in the Chemistry electronics shop was always willing to help with the many electronics projects and difficulties encountered during this work. Gloria Pelatowski drew and labelled all the figures in this thesis.

Lastly, I would like to thank my wife, Maggie, who has put up with me during this work.

This work was supported in part by the National Science Foundation and the Director, Office of Energy Research, Office of Basic Energy Sciences, Chemical Sciences Division of the U.S. Department of Energy under Contract Number DE-AC03-76SF00098.

.....At that subtle moment when man glances backward over his life, Sisyphus returning toward his rock, in that slight pivoting he contemplates that series of unrelated actions which becomes his fate, created by him, combined under his memory's eye and soon sealed by his death. Thus, convinced of the wholly human origin of all that is human, a blind man eager to see who knows that the night has no end, he is still on the go. The rock is still rolling.

I leave Sisyphus at the foot of the mountain! One always finds one's burden again. But Sisyphus teaches the higher fidelity that negates the gods and raises rocks. He too concludes that all is well. This universe henceforth without a master seems to him neither sterile nor futile. Each atom of that stone, each mineral flake of that night-filled mountain, in itself forms a world. The struggle itself toward the heights is enough to fill a man's heart. One must imagine Sisyphus happy.

-Albert Camus

"The Myth of Sisyphus"

APPENDIX: Computer Programs for Transient Stimulated Raman Scattering in High Laser Depletion

The following programs were run on the 7600 computer at the computer center at Lawrence Berkeley Laboratory (LBL). The listings include representative control cards.

I. STOKES

The program STOKES is the main program used to solve the transient stimulated Raman equations in high laser depletion. The following STOKES program is for a 5-component vibrational linewidth. The program is documented extensively by comment cards in the running text of the program.

This program relies on the subroutine SGEFCS to solve the set of simultaneous equations determined by the implicit Crank-Nicolson method. SGEFCS is available from the CORE library at LBL (see the CORE library writeup). SGEFCS is an LBL adaption form the LINPACK library of mathematical subroutines. SGEFCS is employed in the program STOKES shortly after line number 166.

The input and output of STOKES can come from or go to punched cards or a PSS file. PSS is the user storage system (see PSS writeup). The LIBCOPY and LIBRITE control cards copy from or write to the SMGLIB library on PSS.

II. SPLOT

The program SPLOT plots the output data from the program STOKES. SPLOT utilizes the IDDS graphics package (see the IDDS writeup). This program can be used to plot the time-dependent amplitude or intensity of the laser pulse, the Stokes pulse or the vibrational amplitude.

III. CURVE

The program CURVE takes the selectivity data calculated from the program STOKES and generates Stokes probe signals versus delay time. In addition, the program uses the subroutine VCONVO to convolute the pure vibrational amplitude decay with the shape of the probe pulse. VCONVO is a subroutine in the IMSL library of mathematical subroutines at LBL (see the IMSL library writeup).

```
C       CONTROL CARDS
C
TSRMV,7,400,400521, SM GEORGE
$ID=CBHARRIS
*USERPF
MATHLIB,
LIBCOPY,SMGLIB,TAPE5/RR,FSEC9,
FTN4,LCM=1,OPT=2,
LINK,X,PP=[TAPE5],
LIBRITE,SMGLIB,TAPE20/RR,FSEC9,486,W=[GEORGE,S],
EXIT,
DUMP,0,
C
C
C
C
        PROGRAM STOKES(INPUT,OUTPUT,TAPE 5=INPUT,TAPE 20)
C
C       ************************DEFINITIONS*************************
C       PL= POSITION OF LASER PULSE PEAK
C       RL= 1/ FWHM OF LASER PULSE IN T UNITS
C       DT= TIME INCREMENT
C       DZ= SPACE INCREMENT
C       T2= DEPHASING TIME IN PSEC
C       GAMMA= 1/T2  (UNIT OF PSEC-1)
C       GAIN= STEADY STATE GAIN  (UNITS OF M/TW)
C       GAIN IS G IN LITERATURE DIVIDED BY 2
C       NOTICE THAT G IS FOR STOKES INTENSITY,  G/2 FOR STOKES FIELD
C       CMR= MANLEY-ROWE CONSTANT
C       CMR= LASER FREQ / STOKES FREQ  (DIMENSIONLESS)
C       EL= LASER FIELD AMPLITUDE  (UNITS OF SQUARE ROOT OF INTENSITY)
C       INTENSITY IS APPROX 1 GW/CM**2  OR 10 TW/M**2
C       ES= STOKES FIELD AMPLITUDE  (UNITS OF SQUARE ROOT OF INTENSITY)
C       Q= VIBRATIONAL AMPLITUDE  (UNITS OF INTENSITY)
C       INTENSITY UNITS = TW/M**2
C       ELMAX= MAXIMUM AMPLITUDE OF LASER FIELD
C       ELMAX IN UNITS OF SQUARE ROOT OF TERAWATT PER SQUARE METER
C       ESHHA= STOKES PULSE HALF-HEIGHT AMPLITUDE
C       PEHH= TIME POSITION ON STOKES PULSE RISING EDGE WHEN STOKES PULSE
C       AMPLITUDE EQUALS ESHHA
C       FEHH= TIME POSITION ON STOKES PULSE FALLING EDGE WHEN STOKES
C       PULSE AMPLITUDE EQUALS ESHHA
C       SGAIN= LOG OF MAXIMUM STOKES AMPLITUDE AT Z DIVIDED BY
C       MAXIMUM STOKES AT Z=0
C       PLMAX= TIME POSITION OF LASER PULSE MAXIMUM AT GIVEN Z
C       PSMAX = TIME POSITION OF STOKES PULSE MAXIMUM AT GIVEN Z
C       SWIDTH= WIDTH OF STOKES PULSE IN TIME UNITS AT GIVEN Z
C       TDELAY= TIME DELAY BETWEEN LASER AND STOKES PULSE PEAKS AT
C       GIVEN Z
C       TTIME= TOTAL TIME IN PICOSECONDS
C       ZCELL= TOTAL CELL LENGTH IN METERS
C
C
C
C       ************************DIMENSION STATEMENTS*************************
C
C       THE FOLLOWING ARE ARRAYS IN Z SPACE
C
        REAL A(7,400), B(400)
        REAL DUMMY(400)
        INTEGER IPVT(400)
```

```
C
      REAL ELOLD(200),ESOLD(200)
      REAL ELNEW(200), ESNEW(200)
      REAL ELSAVE(200), ESSAVE(200)
C
      REAL QOLD(200),QNEW(200),Q2NEW(200)
      REAL QOLD1(200),QOLD2(200)
      REAL QOLD3(200), QOLD4(200)
      REAL QNEW1(200),QNEW2(200)
      REAL QNEW3(200), QNEW4(200)
C
      REAL QSAVE(200), QSAV1(200)
      REAL QSAV3(200)
C
      REAL FQ(200),FQ1(200),FQ2(200)
      REAL FQ3(200),FQ4(200)
      REAL SUMQ(200)
C
      REAL Q2NW1(200),Q2NW2(200)
      REAL Q2NW3(200), Q2NW4(200)
C
      INTEGER PQMAX(200),PQ1MX(200),PQ3MX(200)
C
      REAL POLD1(200),POLD2(200)
      REAL PNEW1(200),PNEW2(200)
      REAL P2NW1(200),P2NW2(200)
      REAL POLD3(200), POLD4(200)
      REAL PNEW3(200),PNEW4(200)
      REAL P2NW3(200), P2NW4(200)
C
      REAL CCS1(200),CCS2(200)
      REAL XCOS1(200),XCOS2(200)
      REAL COS3(200),COS4(200)
      REAL XCOS3(200),XCOS4(200)
C
      REAL SIN1(200),SIN2(200)
      REAL XSIN1(200),XSIN2(200)
      REAL SIN3(200), SIN4(200)
      REAL XSIN3(200), XSIN4(200)
C
      REAL QICOS(200),SIGQ(200),SIGQ1(200)
      REAL Q3COS(200), SIGQ3(200)
C
      REAL SLINT(40),XCONV(40)
C
      INTEGER PLMAX(200),PSMAX(200)
      REAL SGAIN(200), ESHA(200)
      INTEGER TDELAY(200)
C
      INTEGER SWITCH(50)
      INTEGER REHH(50), FEHH(50)
C
C     THE FOLLOWING ARE ARRAYS IN T TIME
C
      REAL ELZERO(400),ESZERO(400)
      REAL QZ1(400),EL1(400),ES1(400)
      REAL QZ1V1(400),QZ1V2(400)
      REAL ESZ(400,10),ELZ(400,10)
C
      REAL ELBC(400), ESBC(400), QBC(400)
      REAL QBC1(400),QBC2(400)
      REAL QBC3(400), QBC4(400)
```

```
C
      REAL DPV1(400),DPV2(400)
      REAL DPV3(400), DPV4(400)
C
      REAL FOFF1(400),FOFF2(400)
      REAL FOFF3(400), FOFF4(400)
C
      REAL XELSC(400),ZLSC(400)
C
      INTEGER T,Z,TMAX,ZMAX,PL
      INTEGER TSP
      INTEGER ZBC
C
      REAL PZERC
      REAL PZR03
C
      REAL EL,ES,C
      REAL C1,C2,PV1,PV2
      REAL C3, C4, PV3, PV4
C
      LEVEL 2, EL,ES,C,C1,C2,PV1,PV2,C3,C4,PV3,PV4
      COMMON /LCM/ EL(400,40),ES(400,40), C(400,40),
     1 C1(400,40),C2(400,40),PV1(400,40),PV2(400,40)
C
      COMMON /LCM1/ C3(400,40),C4(400,40),PV3(400,40),PV4(400,40)
C
C
C
C     ******************DEFINE PRIMARY CONSTANTS******************
C
      ZMAX=200
      TMAX=400
      PL=TMAX/2
      EL=5./FLOAT(TMAX)
C     FWHM OF THE PULSE IS 1/5 OF THE TOTAL TIME OF 35.0 PSEC
C     I.E., THE PULSE WIDTH IS 7.0 PSEC
      CMR=1.19432
      GAIN=25.0
      LDA=7
      INFO=1
      ML=2
      MU=2
      EMAX=6.33
      GAUSS= 4*ALOG(2.0)
      TTIME=35.0
      ZCELL=0.0125
      T2=7.0
C
C     INDEX DETERMINES WHICH BOUNDARY CONDITIONS ARE USED
C
C     INDEX=0 INDICATES THE BEGINNING OF THE CELL
C     INDEX=1 INDICATES USING PUNCHED CARDS CONTAINING PREVIOUS
C     SOLUTIONS AS BOUNDARY CONDITIONS
C     INDEX=2 INDICATES USING PREVIOUS SOLUTIONS IN MEMORY AS
C     BOUNDARY CONDITIONS
C
      INDEX=1
C
C
C
C     DEL IS THE OFF RESONANT DELTA OMEGA
C     IN THIS CALCULATION, DEL=1.5 CM-1
```

```
C       DEL1 AND DEL2 ARE IN UNITS OF RADIANS/TIME POINT
C       8.75E-2= PSEC/TIME POINT T
C       8.75E-14= SEC/TIME POINT T
C       2*PI(RADIANS)*C(CM/SEC)*DEL(CM-1)=2.8274E11(RADIANS/SEC)
C       2.8274E11(RADIANS/SEC)*8.75E-14(SEC/TIME POINT)=2.474E-2(RADIANS
C       PER TIME POINT)
C       THEREFORE 1.5 CM-1=2.474E-2 RADIANS/TIME POINT IN THIS PROGRAM
C
C
C       THIS IS TRUE FOR CALCULATION A
C
C       **********FOR CALCULATION B, DEL = 3.00 CM-1 ***********
C       3.00 CM-1 = 4.9480084E-2 RADIANS/TIME POINT
C
C       ***********FOR CALCULATION C, DEL=4.50 CM-1***************
C       4.50 CM-1 = 7.4220126E-2 RADIANS/TIME POINT
C
C
C       ***********FOR CALCULATION D, DEL= 3.00 CM-1 ************
C       $$$$$$$$$$ IN CALCULATION D, T2= 3.5 PSEC $$$$$$$$$$$$$$
C
C
C       *******IN CALCULATIONS A,B, AND C, T2= 7.0 PSEC***********
C
C       *******FOR CALCULATION E, DEL = 3.0 CM-1************
C       $$$$$$$$$$IN CALCULATION E, T2 = 14.0 PSEC$$$$$$$$$$$$$$$
C
        DEL1=-2.4740042E-2
        DEL2= 2.4740042E-2
        DEL3=-4.9480084E-2
        DEL4= 4.9480084E-2
C
C
C       XXCM CONVERTS RADIANS PER TIME POINT INTO WAVENUMBERS CM-1
C
        XXCM=60.630456
C
C
C       PZERO IS THE CONSTANT SPATIAL PHASE THAT DEVELOPES FOR THE
C       OFF RESONANT VIBRATIONAL AMPLITUDE PRIOR TO SATURATION
C       THIS MUST BE FIRST DETERMINED BY RUNNING THE EARLY SECTORS
C       THESE SECTORS MUST THEN BE RERUN TO CALCULATE THE SIGNAL
C
        PZERO=5.73
        PZRO3=11.45
C
C       XLSUM IS THE AREA UNDER THE INITIAL LASER INTENSITY
C       PROFILE AT Z=ZERO
C       XLSUM IS CALCULATED WHEN INDEX=0
C       XLSUM IS INPUT AS A CONSTANT FOR SUBSEQUENT SECTORS
C
        XLSUM=0.21111674066E+03
C
C
C       ********DEFINE OTHER CONSTANTS IN TERMS OF PRIMARY CONSTANTS*******
        DT=TTIME/FLOAT(TMAX)
        DZ=ZCELL/FLOAT(ZMAX)
        N=ZMAX*2
        BETA1=2.0*DZ*GAIN*CMR
        BETA2=2.0*DZ*GAIN
        PHI1=BETA1/2.0
        PHI2=BETA2/2.0
```

```
      GAMMA=1.0/T2
      NN=(N/2)-1
      NN2=N-2
      LMAX=ZMAX/5
      ZBC=ZMAX-3
C
C
C
C
C     **********INITIALIZATION SECTION**********
C
C     INITIALIZE ELSAVE AND ESSAVE FOR USE IN DETERMINING THE
C     TIME POSITIONS OF THE LASER AND STOKES PEAKS AT VARIOUS Z
C     ALSO INITIALIZE QSAVE,QSAV1, AND QSAV2
C
      DO 60 Z=1,ZMAX
      QSAVE(Z)=0.0
      QSAV1(Z)=0.0
      QSAV3(Z)=0.0
      ELSAVE(Z)=0.0
 60   ESSAVE(Z)=0.0
C
C     INITIALIZE REFF AND FEHH FOR USE IN DETERMINING
C     THE WIDTH OF THE STOKES PULSE
C
      DO 61 Z=1,ZMAX
      REFH(Z)=0
      FEHH(Z)=0
 61   CONTINUE
C
C
C     DEFINE BOUNDARY CONDITIONS FOR ALL TIME AT Z=0  **********
C
C     FOR THE STARTING CELL SECTOR THESE BOUNDARY CONDITIONS ARE
C     DEFINED BY A GAUSSIAN FUNCTION
C     FOR SUBSEQUENT CELL SECTORS, THE BOUNDARY CONDITIONS ARE THE
C     COMPUTER GENERATED SOLUTION NEAR THE END OF THE PREVIOUS
C     CELL SECTOR
C
      IF(INDEX.EQ.0) GOTO 64
      IF(INDEX.EQ.1) GOTO 70
      IF(INDEX.EQ.2) GOTO 75
C
C     FOR THE STARTING SECTOR, THE BOUNDARY CONDITIONS ARE GIVEN
C     BY A GAUSSIAN LASER PULSE AND GAUSSIAN STOKES NOISE PULSE
C     STOKES NOISE = BASE E ** -13
C     BASE E ** -13 = 2.2603E-6
C
C
 64   DO 65 T=1,TMAX
      ELZERO(T)=EMAX*EXP(-GAUSS*((FLOAT(T-PL)*RL)**2))
      ESZERO(T)=ELZERO(T)*2.2603E-6
 65   CONTINUE
C
C     USE SIMPSONS RULE TO CALCULATE THE AREA UNDER THE INTIAL LASER
C     INTENSITY PROFILE AT Z=ZERO
C     THE TOTAL AREA, XLSUM, WILL BE USED TO CALCULATE THE
C     AMOUNT OF LASER CONVERSION
C
      XLSUM=0.0
      AREA=0.0
C
```

```
      DO 66 T=1,TMAX
 66   XELSQ(T)=ELZERC(T)*ELZERC(T)
C
      DO 67 T=1,397,2
      AREA=(DT/3.)*(XELSQ(T)+4.*XELSQ(T+1)+XELSQ(T+2))
      XLSUM=XLSUM+AREA
 67   CONTINUE
C
      PRINT 68,XLSUM
 68   FORMAT(/1X,*XLSUM=*,E18.11)
C
      IF(INDEX.EQ.0) GOTO 84
C
C     READ DATA FROM PUNCHED CARDS
C
C     ALTERNATIVELY, READ DATA FROM PSS FILE
C
C     WHETHER DATA IS READ FROM PUNCHED CARDS OR PSS FILE
C     IS DETERMINED BY THE CONTROL CARDS
C
 70   READ(5,2) (ELBC(I),I=1,TMAX)
      READ(5,2) (ESBC(I),I=1,TMAX)
 2    FORMAT(4(E18.11,1X))
      DO 71 T=1,TMAX
      ELZERC(T)=ELBC(T)
 71   ESZERC(T)=ESBC(T)
      IF(INDEX.EQ.1) GOTO 84
C
C     READ BACK DATA FROM MEMORY FROM PREVIOUS SOLUTION
C
 75   DO 76 T=1,TMAX
      ELZERC(T)=ELBC(T)
 76   ESZERO(T)=ESBC(T)
C
C
C     PRINT OUT BOUNDARY CONDITIONS
C
 84   PRINT 85
 85   FORMAT(/1X,*BOUNDARY CONDITIONS FOR ALL TIME AT Z=0*)
      PRINT 86
 86   FORMAT(/1X,*T=*,10X,*ELZERC=*,15X,*ESZERC=*)
C
      DO 100 T=4,TMAX,4
      PRINT 90,T,ELZERC(T),ESZERC(T)
 90       FORMAT(I4,5X,E13.05,8X,E13.05)
 100  CONTINUE
C
C
C     DEFINE INITIAL CONDITIONS FOR ALL SPACE AT T=0  **********************
C
C     PRINT OUT INITIAL CONDITIONS
      PRINT 102
 102  FORMAT(/1X,*INITIAL CONDITIONS FOR ALL SPACE AT T=0*)
C
C
         ELINT=EMAX*EXP(-GAUSS*((FLOAT(-PL)*RL)**2))
      ESINT=ELINT*2.2633E-6
C
C
      DO 110 Z=1,ZMAX
      ELOLD(Z)=ELINT
      ESOLD(Z)=ESINT
```

```
      QOLD(Z)=0.0
      QOLD1(Z)=0.0
      QOLD2(Z)=0.0
      QOLD3(Z)=0.0
      QOLD4(Z)=0.0
C
      POLD1(Z)=0.0
      POLD2(Z)=0.0
      POLD3(Z)=0.0
      POLD4(Z)=0.0
C
  110 CONTINUE
C
      PRINT 111,ELINT,ESINT
  111 FORMAT(/1X,*INITIAL ELOLD=*,E13.05,5X,*INITIAL ESOLD=*,E13.05)
C
      PRINT 112,QOLD(1),QOLD1(1),QOLD2(1)
  112 FORMAT(/1X,*INITIAL QOLD=*,E13.05,5X,*INITIAL QOLD1=*,E13.05,
     1 5X,*INITIAL QOLD2=*,E13.05)
C
C     NOW BEGIN PREDICTOR-CORRECTOR METHOD  ************************
C     FIRST USE EULER TIME STEP.
C     THIS IS THE PREDICTOR STEP.  PROJECT ONE STEP IN TIME
C
C
      DO 255 T=1,TMAX
      K=0
C
C
C     DEFINITIONS FOR PREDICTOR STEP
C     PREDICTOR FOR VIBRATIONS AND PHASE
C
C
      DO 115 Z=1,ZMAX
C
      COS1(Z)=COS(DEL1*FLOAT(T)+POLD1(Z))
      COS2(Z)=COS(DEL2*FLOAT(T)+POLD2(Z))
      COS3(Z)=COS(DEL3*FLOAT(T)+POLD3(Z))
      COS4(Z)=COS(DEL4*FLOAT(T)+POLD4(Z))
C
      SIN1(Z)=SIN(DEL1*FLOAT(T)+POLD1(Z))
      SIN2(Z)=SIN(DEL2*FLOAT(T)+POLD2(Z))
      SIN3(Z)=SIN(DEL3*FLOAT(T)+POLD3(Z))
      SIN4(Z)=SIN(DEL4*FLOAT(T)+POLD4(Z))
C
  115 CONTINUE
C
      DO 120 Z=1,ZMAX
C
      QNEW(Z)=(DT*GAMMA*(ELOLD(Z)*ESOLD(Z)-QOLD(Z)))+QOLD(Z)
C
      QNEW1(Z)=(DT*GAMMA*(ELOLD(Z)*ESOLD(Z)*COS1(Z)-QOLD1(Z)))+QOLD1(Z)
C
      QNEW2(Z)=(DT*GAMMA*(ELOLD(Z)*ESOLD(Z)*COS2(Z)-QOLD2(Z)))+QOLD2(Z)
C
      QNEW3(Z)=(DT*GAMMA*(ELOLD(Z)*ESOLD(Z)*COS3(Z)-QOLD3(Z)))+QOLD3(Z)
C
      QNEW4(Z)=(DT*GAMMA*(ELOLD(Z)*ESOLD(Z)*COS4(Z)-QOLD4(Z)))+QOLD4(Z)
C
      IF(T-1)116,116,117
C
  116 PNEW1(Z)=0.0
```

```
      PNEW2(Z)=0.0
      PNEW3(Z)=0.0
      PNEW4(Z)=0.0
C
      GOTO 120
C
  117 PNEW1(Z)=POLD1(Z)-(DT*GAMMA*((ELOLD(Z)*ESOLD(Z))/COLD1(Z))
     1 *SIN1(Z))
C
      PNEW2(Z)=POLD2(Z)-(DT*GAMMA*((ELOLD(Z)*ESOLD(Z))/COLD2(Z))
     1 *SIN2(Z))
C
      PNEW3(Z)=POLD3(Z)-(DT*GAMMA*((ELOLD(Z)*ESOLD(Z))/COLD3(Z))
     1 *SIN3(Z))
C
      PNEW4(Z)=POLD4(Z)-(DT*GAMMA*((ELOLD(Z)*ESOLD(Z))/COLD4(Z))
     1 *SIN4(Z))
C
  120 CONTINUE
C
C     PRINT OUT QNEW FOR FIRST FEW TIME STEPS
C     ALSO PRINT OUT QNEW1,QNEW2,PNEW1,PNEW2
C
      IF(T.LE.2) GOTO 121
      IF(T.GT.2) GOTO 136
  121 PRINT 122,T
  122 FORMAT(/1X,*QNEW AFTER EULER TIME STEP,  T=*,I4)
C
      PRINT 124
  124 FORMAT(/1X,*Z=*,10X,*QNEW=*,15X,*QNEW1=*,15X,*QNEW2=*,15X,
     1 *PNEW1=*,15X,*PNEW2=*)
C
      DO 135 Z=10,200,10
      PRINT 125,Z,QNEW(Z),QNEW1(Z),QNEW2(Z),PNEW1(Z),PNEW2(Z)
  125 FORMAT(I4,5X,E13.05,8X,E13.05,8X,E13.05,8X,E13.05,8X,E13.05)
C
  135 CONTINUE
  136 CONTINUE
C
C
  140 DO 141 Z=1,ZMAX
C
C     PREPARE FOR SUBROUTINE.  CORRECT COSINE TERMS FOR PHASE
C     CORRECT SINE TERMS FOR UPCOMING CORRECTOR STEP
C
      XCOS1(Z)=COS(DEL1*FLOAT(T)+PNEW1(Z))
      XCOS2(Z)=COS(DEL2*FLOAT(T)+PNEW2(Z))
      XCOS3(Z)=COS(DEL3*FLOAT(T)+PNEW3(Z))
      XCOS4(Z)=COS(DEL4*FLOAT(T)+PNEW4(Z))
C
      XSIN1(Z)=SIN(DEL1*FLOAT(T)+PNEW1(Z))
      XSIN2(Z)=SIN(DEL2*FLOAT(T)+PNEW2(Z))
      XSIN3(Z)=SIN(DEL3*FLOAT(T)+PNEW3(Z))
      XSIN4(Z)=SIN(DEL4*FLOAT(T)+PNEW4(Z))
C
C     SET UP SUMMATION FOR TOTAL VIBRATIONAL AMPLITUDE
C
      FQ(Z)=0.4*QNEW(Z)
      FQ1(Z)=0.2*QNEW1(Z)*XCOS1(Z)
      FQ2(Z)=0.2*QNEW2(Z)*XCOS2(Z)
      FQ3(Z)=0.1*QNEW3(Z)*XCOS3(Z)
      FQ4(Z)=0.1*QNEW4(Z)*XCOS4(Z)
```

```
      SUMQ(Z)=FC(Z)+FC1(Z)+FC2(Z)+FC3(Z)+FC4(Z)
C
 141  CONTINUE
C
C     DEFINE ELEMENTS OF B(J) FOR SUBROUTINE SGBFCS    ****************
      B(1)=EL ZERO(T)
      B(2)=ES ZERO(T)
      DO 142 J=3,N
 142  B(J)=0.0
C
C
C     FIRST REZERO A(I,J)
      DO 144 I=1,7
      DO 144 J=1,N
 144  A(I,J)=0.0
C
C
C     DEFINE THE NONCHANGING ELEMENTS OF A(I,J) FOR SUBROUTINE SGBFCS
C     THIRD ROW ELEMENTS*************************************************
C
      DO 146 J=3,N
 146  A(3,J)=1.0
C
C     FIFTH ROW ELEMENTS*************************************************
C
      DO 148 J=1,NN2
 148  A(5,J)=0.0
      A(5,N-1)=1.0
      A(5,N)=1.0
C
C     SEVENTH ROW ELEMENTS***********************************************
C     NN2 EQUALS N-2
      DO 150 J=1,NN2
 150  A(7,J)=-1.0
C
C
C
C     DEFINE THE ELEMENTS OF A(I,J) WHICH CHANGE DEPENDING ON Q
C
C     FOURTH ROW ELEMENTS  **********************************
C     N/2= ZMAX       /
C     NN EQUALS N/2-1
C
C
      DO 165 J=1,NN
 165  A(4,2*J)=BETA1*SUMQ(J)
      A(4,N)=PHI1*SUMQ(N/2)
C
C     SIXTH ROW ELEMENTS  ***********************************
C
      DO 166 J=1,NN
 166  A(6,2*J-1)=-BETA2*SUMQ(J)
      A(6,N-1)=-PHI2*SUMQ(N/2)
C
C
C     CALL SUBROUTINE SGBFCS IN MATHLIB  ********************
      CALL SGBFCS(A,LDA,N,ML,MU,B,INFC,RCOND,IPVT,DUMMY)
C
C
C     PRINTING INFORMATION FOR FIRST TIME THROUGH ONLY
      IF(T.GT.2) GOTO 180
      PRINT 177,INFO
```

```
      PRINT 179,RCCND
  177   FORMAT(/1X,*INFC=*,I3)
  179   FORMAT(/1X,*RCCND=*,E13.05)
C
C       SOLUTIONS X(I) ARE OUTPUT IN B(I).
C       THUS THE ORIGINAL CONSTANTS ARE REPLACED BY THE SOLUTIONS.
C       RELATE OUTPUT B(I) TO EL AND ES.
C
C
C
C
  180   DO 182 Z=1,ZMAX
        ELNEW(Z)=B(2*Z-1)
  182   ESNEW(Z)=B(2*Z)
C
C
C       PRINT OUT ELNEW AND ESNEW FOR FIRST FEW TIME STEPS
C
        IF(T.LE.2) GOTO 194
        IF(T.GT.2) GOTO 190
C
  184   PRINT 185,T
  185   FORMAT(/1X,*ELNEW AND ESNEW AFTER SUBROUTINE,  T=*,I4)
        PRINT 186
  186   FORMAT(/1X,*Z=*,10X,*ELNEW=*,15X,*ESNEW=*)
        DO 188 Z=10,200,10
        PRINT 187,Z,ELNEW(Z),ESNEW(Z)
  187     FORMAT(I4,5X,E13.05,8X,E13.05)
  188   CONTINUE
  190   CONTINUE
C
C
      K=K+1
C       IF K=2, END OF SECOND TIME THROUGH.  END OF CYCLE.
        IF(K.EQ.2) GOTO 205
C
C
C NOW HAVE A TENTATIVE ELNEW(Z) AND ESNEW(Z).**************************
C NOW CALCULATE A CORRECTOR FOR GNEW,CORRECTED GNEW IS Q2NEW.***********
C       CALCULATE THE CORRECTOR FOR THE VIBRATIONS AND PHASE
C
C
      DO 195 Z=1,ZMAX
C
        Q2NEW(Z)=((DT/2.)*GAMMA*(-GOLD(Z)-GNEW(Z)+
     1((ELOLD(Z)*ESOLD(Z))+(ELNEW(Z)*ESNEW(Z))))+QOLD(Z)
C
        Q2NW1(Z)=((DT/2.)*GAMMA*((ELOLD(Z)*ESOLD(Z)*COS1(Z))-GOLD1(Z)
     1 +(ELNEW(Z)*ESNEW(Z)*XCOS1(Z))-QNEW1(Z)))+QOLD1(Z)
C
        Q2NW2(Z)=((DT/2.)*GAMMA*((ELOLD(Z)*ESOLD(Z)*COS2(Z))-GOLD2(Z)
     1 +(ELNEW(Z)*ESNEW(Z)*XCOS2(Z))-QNEW2(Z)))+QOLD2(Z)
C
        Q2NW3(Z)=((DT/2.)*GAMMA*((ELOLD(Z)*ESOLD(Z)*COS3(Z))-GOLD3(Z)
     1 +(ELNEW(Z)*ESNEW(Z)*XCOS3(Z))-QNEW3(Z)))+QOLD3(Z)
C
        Q2NW4(Z)=((DT/2.)*GAMMA*((ELOLD(Z)*ESOLD(Z)*COS4(Z))-GOLD4(Z)
     1 +(ELNEW(Z)*ESNEW(Z)*XCOS4(Z))-QNEW4(Z)))+QOLD4(Z)
C
        IF(T-1)192,192,193
  192   P2NW1(Z)=0.0
        P2NW2(Z)=0.0
```

```
      P2NW3(Z)=0.0
      P2NW4(Z)=0.0
      GOTO 195
C
 193  P2NW1(Z)=POLD1(Z)-(DT/2.)*GAMMA*(((ELOLD(Z)*ESOLD(Z))/QOLD1(Z))
     1 *SIN1(Z)+((ELNEW(Z)*ESNEW(Z))/QNEW1(Z))*XSIN1(Z))
C
      P2NW2(Z)=POLD2(Z)-(DT/2.)*GAMMA*(((ELOLD(Z)*ESOLD(Z))/QOLD2(Z))
     1 *SIN2(Z)+((ELNEW(Z)*ESNEW(Z))/QNEW2(Z))*XSIN2(Z))
C
      P2NW3(Z)=POLD3(Z)-(DT/2.)*GAMMA*(((ELOLD(Z)*ESOLD(Z))/QOLD3(Z))
     1 *SIN3(Z)+((ELNEW(Z)*ESNEW(Z))/QNEW3(Z))*XSIN3(Z))
C
      P2NW4(Z)=POLD4(Z)-(DT/2.)*GAMMA*(((ELOLD(Z)*ESOLD(Z))/QOLD4(Z))
     1 *SIN4(Z)+((ELNEW(Z)*ESNEW(Z))/QNEW4(Z))*XSIN4(Z))
C
 195  CONTINUE
C
C
C     PRINT Q2NEW FOR THE FIRST FEW TIME STEPS
C     ALSO PRINT OUT Q2NW1,Q2NW2,P2NW1,P2NW2
C
      IF(T.LE.2) GOTO 196
      IF(T.GT.2) GOTO 201
C
 196  PRINT 197,T
 197  FORMAT(/1X,*Q2NEW AFTER CORRECTOR,  T=*,I4)
      PRINT 198
 198  FORMAT(/1X,*Z=*,10X,*Q2NEW=*,15X,*Q2NW1=*,15X,*Q2NW2=*,15X,
     1 *P2NW1=*,15X,*P2NW2=*)
C
      DO 200 Z=10,200,10
      PRINT 199,Z,Q2NEW(Z),Q2NW1(Z),Q2NW2(Z),P2NW1(Z),P2NW2(Z)
 199  FORMAT(I4,5X,E13.05,8X,E13.05,8X,E13.05,8X,E13.05,8X,E13.05)
 200   CONTINUE
 201  CONTINUE
C
C
C REDEFINE QNEW FOR THE CORRECTOR CYCLE.THESE QNEW WILL BE ***********
C INTRODUCED INTO C*X*8 SYSTEM OF COUPLED EQUATIONS ******************
C Q(T,Z) IS THE Q DATA ARRAY *************************************
C     THE REDEFINITION OF QOLD WILL BE USED IN THE NEXT TIME STEP
C
C
      DO 203 Z=1,ZMAX
C
          QNEW(Z)=Q2NEW(Z)
          QOLD(Z)=Q2NEW(Z)
      QNEW1(Z)=Q2NW1(Z)
      QOLD1(Z)=Q2NW1(Z)
      QNEW2(Z)=Q2NW2(Z)
      QOLD2(Z)=Q2NW2(Z)
      QNEW3(Z)=Q2NW3(Z)
      QOLD3(Z)=Q2NW3(Z)
      QNEW4(Z)=Q2NW4(Z)
      QOLD4(Z)=Q2NW4(Z)
C
      PNEW1(Z)=P2NW1(Z)
      POLD1(Z)=P2NW1(Z)
      PNEW2(Z)=P2NW2(Z)
      POLD2(Z)=P2NW2(Z)
      PNEW3(Z)=P2NW3(Z)
```

```
      POLD3(Z)=P2NW3(Z)
      PNEW4(Z)=P2NW4(Z)
      POLD4(Z)=P2NW4(Z)
C
 203  CONTINUE
C
C     SAVE Q FOR Z=1
C
      QZ1(T)=Q2NEW(1)
      QZ1V1(T)=Q2NW1(1)
      QZ1V2(T)=Q2NW2(1)
C
C     SAVE Q FOR EVERY FIFTH Z STEP VALUE
C     SAVE PHASE FOR EVERY FIFTH Z STEP VALUE
C
      DO 204 L=1,LMAX
C
      PV1(T,L)=P2NW1(5*L)
      PV2(T,L)=P2NW2(5*L)
      PV3(T,L)=P2NW3(5*L)
      PV4(T,L)=P2NW4(5*L)
C
      Q(T,L)=Q2NEW(5*L)
      Q1(T,L)=Q2NW1(5*L)
      Q2(T,L)=Q2NW2(5*L)
      Q3(T,L)=Q2NW3(5*L)
      Q4(T,L)=Q2NW4(5*L)
 204  CONTINUE
C
C
C     SAVE Q FOR ZBC=ZMAX-3 ZSTEP
C
      QBC(T)=Q2NEW(ZBC)
      QBC1(T)=Q2NW1(ZBC)
      QBC2(T)=Q2NW2(ZBC)
      QBC3(T)=Q2NW3(ZBC)
      QBC4(T)=Q2NW4(ZBC)
C
C
C
C     NOW SET INFO =2 AND RETURN TO REDEFINE A(I,J) AND B(J)
C     THIS IS IMPORTANT BECAUSE BOTH A(I,J) AND B(J) CHANGE ON RETURN
C     FROM THE SUBROUTINE
C     THEN SOLVE THE SYSTEM OF LINEAR EQUATIONS AGAIN
C     RETURN TO LINE 140
C
      INFO=2
      GO TO 140
C
C
C AFTER COMPLETE SECOND CYCLE, REDEFINE ELOLD AND ESOLD FOR NEXT ******
C TIME STEP ************************************************************
C EL(T,Z) AND ES(T,Z) ARE THE LASER AND STOKES FIELDS DATA ARRAYS*******
C
C
 205  DO 206 Z=1,ZMAX
          ELOLD(Z)=ELNEW(Z)
 206      ESOLD(Z)=ESNEW(Z)
C
C     SAVE EL AND ES FOR Z=1
C
      EL1(T)=ELNEW(1)
```

```
      ES1(T)=ESNEW(1)
C
C     SAVE FIRST TEN Z STEP VALUES
C
      DO 207 Z=2,10
      ELZ(T,Z)=ELNEW(Z)
 207  ESZ(T,Z)=ESNEW(Z)
C
C     SAVE EVERY FIFTH Z STEP VALUE
C
C
      DO 208 L=1,LMAX
      EL(T,L)=ELNEW(5*L)
 208  ES(T,L)=ESNEW(5*L)
C
C     SAVE THE LASER AND STOKES FOR ZBC=ZMAX-3 ZSTEP
C     THESE WILL BE NEW BOUNDARY CONDITIONS
C
      ELBC(T)=ELNEW(ZBC)
      ESBC(T)=ESNEW(ZBC)
C
C
C
C     SET INFO=2 FOR NEXT CALL OF SUBROUTINE
C
      INFO=2
C
C***************THIS COMPLETES CYCLE FOR ONE T **********************
C INCREMENT TIME AND REPEAT ENTIRE CYCLE FOR NEXT T OF DO LOOP ********
C
C
C
C     FIRST KEEP TRACK OF THE TIME POSITION OF THE LASER AND STOKES
C    PULSE PEAK FOR VARIOUS Z LOCATIONS
C     ALSO KEEP TRACK OF THE TIME POSITION OF THE VARIOUS VIBRATIONAL
C     AMPLITUDE PEAKS
C
      DO 250 Z=1,ZMAX
C
      IF(ELNEW(Z)-ELSAVE(Z))220,220,216
 216  PLMAX(Z)=T
      ELSAVE(Z)=ELNEW(Z)
C
 220  IF(ESNEW(Z)-ESSAVE(Z))240,240,230
 230      PSMAX(Z)=T
      ESSAVE(Z)=ESNEW(Z)
C
 240  IF(Q2NEW(Z)-QSAVE(Z))242,242,241
 241  PQMAX(Z)=T
      QSAVE(Z)=Q2NEW(Z)
C
 242  IF(Q2NW1(Z)-QSAV1(Z))244,244,243
 243  PQ1MX(Z)=T
      QSAV1(Z)=Q2NW1(Z)
C
 244  IF(Q2NW3(Z)-QSAV3(Z))250,250,245
 245  PQ3MX(Z)=T
      QSAV3(Z)=Q2NW3(Z)
C
 250   CONTINUE
C
C
```

```
 255   CONTINUE
C
C      ****************************************************************
C      ****************************************************************
C
C      AFTER T DO LOOP IS COMPLETED
C      CALCULATE STOKES PULSE WIDTH AND STOKES PULSE GAIN
C      AT VARIOUS Z LOCATIONS
C
C      ESZO IS THE MAXIMUM STOKES VALUE AT Z=0
C      THIS OCCURS AT Z=0 WHEN T=FL
C      ESZO=EMAX*2.2603E-6
C
C      ESZO=6.33*2.2603E-6
C
       ESZO=1.43076953E-5
C
C
      DO 260 Z=1,ZMAX
C
      SGAIN(Z)=ALOG(ESSAVE(Z)/ESZO)
C
C CALC. TIME DELAY BETWEEN LASER PULSE PEAK AND STOKES PULSE PEAK*******
C
      TDELAY(Z)=PSMAX(Z)-PLMAX(Z)
C
C
C      CALCULATE ESHHA FOR USE IN DETERMINING STOKES PULSE WIDTHS
C
 260  ESHHA(Z)=ESSAVE(Z)*.5
C
C      ****************************************************************
C
C CALCULATE STOKES PULSE WIDTHS AT VARIOUS Z ***************************
C
       DO 420 L=1,LMAX
C
       TSP=PSMAX(L*5)
C
       DO 300 T=1,TSP
       IF(ES(T,L)-ESHHA(L*5))298,298,300
 298   FEHH(L)=T
 300   CONTINUE
C
       DO 320 T=TSP,TMAX
       IF(ES(T,L)-ESHHA(L*5))320,318,318
 318   FEHH(L)=T
 320   CONTINUE
C
       SWIDTH(L)=FEHH(L)-REHH(L)
C
C
 420  CONTINUE
C
C      CALCULATE THE LASER CONVERSION AT EACH L SPATIAL POINT
C      SLINT IS THE TOTAL AREA UNDER THE LASER INTENSITY
C      XCONV IS THE FRACTIONAL CONVERSION
C
       DO 438 L=1,LMAX
C
       ZLSUM=0.0
       ZAREA=0.0
```

```
C
      DO 422 T=1,TMAX
 422  ZLSQ(T)=EL(T,L)*EL(T,L)
C
      DO 424 T=1,397,2
      ZAREA=(DT/3.)*(ZLSQ(T)+4.*ZLSQ(T+1)+ZLSQ(T+2))
      ZLSUM=ZLSUM+ZAREA
 424  CONTINUE
C
      SLINT(L)=ZLSUM
      XCONV(L)=ZLSUM/XLSUM
 438  CONTINUE
C
C
C     PRINT OUT INFORMATION ABOUT PARAMETERS USED IN THIS CALCULATION
C
C
     PRINT 440,TMAX,ZMAX
 440  FORMAT(/1X,*IN THIS CALCULATION TMAX=*,I4,5X,*ZMAX=*,I4)
     PRINT 441,GAIN,EMAX
 441  FORMAT(/1X,*GAIN=*,E13.05,5X,*EMAX=*,E13.05)
     PRINT 445,TTIME
 445  FORMAT(/1X,*TOTAL TIME=*,E11.03,3X,*PICOSEC*)
     PRINT 446,DT
 446  FORMAT(/1X,*DT=*,E13.05,3X,*PICOSEC*)
     PRINT 447,ZCELL,DZ
 447  FORMAT(/1X,*ZCELL LENGTH=*,E11.03,3X,*METERS*,3X,*DZ=*,E13.05,
    13X,*METERS*)
C
C
      PRINT 448,BETA1,BETA2
 448  FORMAT(/1X,*BETA1=*,E13.05,10X,*BETA2=*,E13.05)
C
      PRINT 449,PHI1,PHI2
 449  FORMAT(/1X,*PHI1=*,E13.05,10X,*PHI2=*,E13.05)
C
      PRINT 450,GAMMA,N
 450  FORMAT(/1X,*GAMMA=*,E13.05,10X,*N=*,I4)
C
      PRINT 451,ESZO
 451  FORMAT(/1X,*ESZO=*,E13.05)
C
C
C     PRINT OUT INFORMATION FOR TIME POSITION OF STOKES AND
C     LASER PEAKS, TIME DELAY BETWEEN PEAKS, STOKES GAIN, AND
C     STOKES PULSE WIDTH
C
C
     PRINT 455
 455  FORMAT(/1X,*FOR Z=*,5X,*PLMAX=*,5X,*PSMAX=*,5X,*TDELAY=*,
    110X,*SGAIN=*,12X,*ESSAVE=*)
C
      DO 461 Z=1,ZMAX
     PRINT 460,Z,PLMAX(Z),PSMAX(Z),TDELAY(Z),SGAIN(Z),
    1ESSAVE(Z)
 460      FORMAT(I4,8X,I4,7X,I4,7X,I4,8X,E13.05,6X,E13.05)
 461  CONTINUE
C
C     PRINT OUT INFORMATION FOR TIME POSITION AND VALUE OF VIBRATIONAL
C     PEAK VERSUS Z
C
      PRINT 462
```

```
 462   FORMAT(/1X,*FOR Z=*,5X,*PCMAX=*,5X,*PC1MX=*,5X,*PC3MX=*,10X,
     1 *QSAVE=*,12X,*QSAV1=*,12X,*QSAV3=*)
C
       DO 465 Z=1,ZMAX
       PRINT 464,Z,PCMAX(Z),PC1MX(Z),PC3MX(Z),QSAVE(Z),QSAV1(Z),QSAV3(Z)
 464   FORMAT(I4,9X,I4,7X,I4,7X,I4,8X,E13.05,6X,E13.05,6X,E13.05)
 465   CONTINUE
C
C
C PRINT OUT TIME PROFILE OF LASER AND STOKES PULSES AND **************
C Q AMPLITUDES AT VARIOUS Z LOCATIONS ********************************
C
C
       PRINT 466
 466   FORMAT(/1X,*Z=1*)
       PRINT 467
 467       FORMAT(/1X,*TIME=*,10X,*LASER=*,10X,*STOKES=*,
     1 15X,*Q=*,15X,*Q1=*,15X,*Q2=*)
C
       DO 468 T=4,TMAX,4
 468   PRINT 469,T,EL1(T),ES1(T),QZ1(T),QZ1V1(T),QZ1V2(T)
 469      FORMAT(I4,9X,E13.05,5X,E13.05,5X,E13.05,5X,E13.05,5X,E13.05)
C
C
       DO 522 Z=2,10
      PRINT 470,Z
 470       FORMAT(/1X,*Z=*,I4)
      PRINT 480
 480       FORMAT(/1X,*TIME=*,10X,*LASER=*,10X,*STOKES=*)
C
       DO 515 T=20,TMAX,20
 515       PRINT 520,T,ELZ(T,Z),ESZ(T,Z)
 520      FORMAT(I4,9X,E13.05,5X,E13.05)
C
 522   CONTINUE
C
       PRINT 524
 524   FORMAT(/1X,*L=Z STEP NUMBER/5*)
C
C
C      CALCULATE THE INSTANTANEOUS FREQUENCY SHIFT CAUSED BY THE
C      PHASE CHANGING WITH TIME
C      THIS IS REPRESENTED BY DPV1 AND DPV2
C      UNITS OF RADIANS PER TIME POINT
C      THIS IS PHASE-PULLING OR FORCED OSCILLATOR BEHAVIOR
C
C      ALSO CALCULATE THE AMOUNT OF OFF-RESONANCE IN WAVENUMBERS CM-1
C      THIS IS REPRESENTED BY FOFF1 AND FOFF2
C
C
       DO 535 L=4,LMAX,4
C
       DPV1(1)=0.0
       DPV2(1)=0.0
       DPV3(1)=0.0
       DPV4(1)=0.0
C
       FOFF1(1)=0.0
       FOFF2(1)=0.0
       FOFF3(1)=0.0
       FOFF4(1)=0.0
C
```

```
      DO 525 T=2,TMAX
C
      DPV1(T)=PV1(T,L)-PV1(T-1,L)
      DPV2(T)=PV2(T,L)-PV2(T-1,L)
      DPV3(T)=PV3(T,L)-PV3(T-1,L)
      DPV4(T)=PV4(T,L)-PV4(T-1,L)
C
      FOFF1(T)=XXCM*(CEL1+DPV1(T))
      FOFF2(T)=XXCM*(CEL2+DPV2(T))
      FOFF3(T)=XXCM*(CEL3+DPV3(T))
      FOFF4(T)=XXCM*(CEL4+DPV4(T))
C
  525 CONTINUE
C
      PRINT 526, L
  526 FORMAT(/1X,*L=*,I4)
C
      PRINT 527
C
  527 FORMAT(/1X,*TIME=*,5X,*LASER=*,8X,*STOKES=*,
     1 13X,*Q=*,13X,*C1=*,13X,*C2=*,13X,*C3=*,13X,*C4=*)
C
      DO 528 T=4,TMAX,4
  528   PRINT 529,T,EL(T,L),ES(T,L),C(T,L),Q1(T,L),Q2(T,L),
     1 Q3(T,L),C4(T,L)
  529 FORMAT(I4,4X,E13.05,3X,E13.05,3X,E13.05,3X,
     1 E13.05,3X,E13.05,3X,E13.05,3X,E13.05)
C
C
      PRINT 532
  532 FORMAT(/1X,*TIME=*,5X,*PV1=*,13X,*PV2=*,12X,*PV3=*,12X,
     1 *PV4=*,12X,*FOFF1=*,10X,*FOFF2=*,10X,*FOFF3=*,10X,*FOFF4=*)
C
      DO 533 T=4,TMAX,4
  533 PRINT 534,T,PV1(T,L),PV2(T,L),PV3(T,L),PV4(T,L),
     1 FOFF1(T),FOFF2(T),FOFF3(T),FOFF4(T)
  534 FORMAT(I4,2X,E13.05,3X,E13.05,3X,E13.05,3X,E13.05,3X,E13.05,
     1 3X,E13.05,2X,E13.05,2X,E13.05)
C
  535 CONTINUE
C
C
      PRINT 537
  537 FORMAT(/1X,*L=*,10X,*SWIDTH=*,14X,*SLINT=*,14X,*XCONV=*)
      DO 540 L=1,LMAX
  540 PRINT 542,L,SWIDTH(L),SLINT(L),XCONV(L)
  542 FORMAT(I4,9X,I4,9X,E13.05,5X,E13.05)
C
      PRINT 545
  545 FORMAT(1X,*Z=ZERO*)
      PRINT 546
  546 FORMAT(/1X,*TIME=*,5X,*LASER=*,7X,*STOKES=*,
     1 13X,*Q=*,13X,*C1=*,13X,*Q2=*,13X,*Q3=*,13X,*Q4=*)
C
      DO 548 T=4,TMAX,4
  548 PRINT 549,T,ELBC(T),ESBC(T),QBC(T),CBC1(T),QBC2(T),
     1 QBC3(T),CBC4(T)
  549 FORMAT(I4,4X,E13.05,3X,E13.05,3X,E13.05,3X,E13.05,3X,
     1 E13.05,3X,E13.05,3X,E13.05)
C
C
C     PZERO IS THE CONSTANT SPATIAL PHASE THAT DEVELOPES FOR THE
```

```
C       OFF RESONANT VIBRATIONAL AMPLITUDE PRIOR TO SATURATION
C       THIS IS REDEFINED AS PHI=0 FOR THE COHERENT PROBE PROCESS
C       PROBE STOKES SEES PHASE CHANGES REFERENCED TO ZERO
C
C       Q1COS IS THE REAL AMPLITUDE OF /Q1/*EXP(IPHI) WHICH
C       GIVES RISE TO PROBE STOKES SIGNAL
C
C       SIGQ IS THE RUNNING SUM OF VIBRATIONAL AMPLITUDE
C       THIS IS PROPORTIONAL TO THE PROBE STOKES AMPLITUDE
C
C       THE TOTAL PROBE STOKES SIGNAL IS THE SUMMATION OF
C       EL(PROBE)*Q OVER ALL Z
C
        SIG=0.0
        SIG1=0.0
        SIG3=0.0
C
        DO 550 Z=1,ZMAX
C
        Q1COS(Z)=Q2NW1(Z)*COS(PZERO-P2NW1(Z))
        Q3COS(Z)=Q2NW3(Z)*COS(PZRO3-P2NW3(Z))
C
        SIGQ(Z)=SIG+Q2NEW(Z)
        SIG=SIGQ(Z)
C
        SIGQ1(Z)=SIG1+Q1COS(Z)
        SIG1=SIGQ1(Z)
C
        SIGQ3(Z)=SIG3+Q3COS(Z)
        SIG3=SIGQ3(Z)
C
  550   CONTINUE
C
C
C       PUNCH OUT ON CARDS THE LASER AND STOKES SOLUTIONS AT Z=ZBC
C       ALSO PUNCH ON CARDS THE VIBRATIONAL AMPLITUDE SOLUTION AT Z=ZBC
C
C       ALTERNATIVELY, STORE DATA ON PSS FILE
C
C       WHETHER DATA IS PUNCHED ON CARDS OR STORED ON PSS FILE
C       IS DETERMINED BY THE CONTROL CARDS
C
        WRITE(20,1) (ELBC(I),I=1,TMAX)
        WRITE(20,1) (ESBC(I),I=1,TMAX)
        WRITE(20,1) (QBC(I),I=1,TMAX)
        WRITE(20,1) (QBC1(I),I=1,TMAX)
        WRITE(20,1) (QBC3(I),I=1,TMAX)
    1   FORMAT(4(E18.11,1X))
C
C
        PRINT 555
  555   FORMAT(/1X,*VIBRATIONAL PHASE AND VIBRATIONAL AMPLITUDE
       1 LEFT BEHIND AT T=400*)
        PRINT 560
  560   FORMAT(/1X,*Z=*,10X,*Q=*,13X,*Q1=*,13X,*PV1=*,
       1 13X,*Q3=*,13X,*PV3=*,13X,*Q1COS=*,13X,*Q3COS=*)
C
        DO 565 Z=1,ZMAX
  565   PRINT 570,Z,Q2NEW(Z),Q2NW1(Z),P2NW1(Z),Q2NW3(Z),
       1 P2NW3(Z),Q1COS(Z),Q3COS(Z)
  570   FORMAT(I4,4X,E13.05,3X,E13.05,3X,E13.05,
       1 3X,E13.05,3X,E13.05,3X,E13.05,3X,E13.05)
```

```
C
      PRINT 575
 575  FORMAT(/1X,*Z=*,15X,*SIGC=*,15X,*SIGC1=*,15X,*SIGC3=*)
      DO 580 Z=1,ZMAX
 580  PRINT 585,Z,SIGC(Z),SIGC1(Z),SIGC3(Z)
 585  FORMAT(I4,9X,E13.05,5X,E13.05,5X,E13.05)
C
C
C
C
      STOP
      END
```

```
C       CONTROL CARDS
C
SPLOT.400521, SM GEORGE
$ID=CBHARRIS
*USERPR
FTN4,R=3.
FETCHPS,IDDS,ULIB,ULIBX.
FETCHPS,GPACBN7,GP,CCBN.
LIBCOPY,SMGLIB,TAPE5/FF,BSEC10.
LINK,X,F=LGO,F=GP,P=ULIB.
DISPOSE,FILM=PL.
EXIT.
DUMP,0.
FETCHPS,IDDS,SYMTAB,SYMTABX.
GRUMP,P,P=SYMTAB.
FIN.
C
C
C
C
      PROGRAM SPLOT(INPUT,OUTPUT,TAPE5,TAPE6=OUTPUT,FILM)
      COMMON /IGSZZZ/ Z(200)
      REAL EL(400), ES(400)
      REAL C(400)
      REAL C1(400)
      REAL SQEL(400), SQES(400)
      REAL SQC(400)
      REAL SQC1(400)
      INTEGER T
      DIMENSION X(400),ITLF(2)
C
      DATA ITLF/*TSRMV***,*Z=ZBC*/
      READ (5,100) (EL(I),I=1,400)
      READ (5,100) (ES(I),I=1,400)
      READ (5,100) (C(I),I=1,400)
      READ(5,100) (C1(I),I=1,400)
  100 FORMAT(4(E18.11,1X))
C
      DO 105 T=1,400
      SQEL(T)=EL(T)*EL(T)
      SQES(T)=ES(T)*ES(T)
      SQQ(T)=4.*(C(T)*C(T))
      SQQ1(T)=4.*(Q1(T)*Q1(T))
  105 X(T)=FLOAT(T)
      CALL MODESG(Z,6,ITLF)
      CALL OBJCTG(Z,15.,15.,85.,85.)
      CALL SUBJEG(Z,0.,0.,400.,44.)
      CALL GRIDG(Z,C.,C.,C.,C.)
      CALL SETSMG(Z,102,2.)
      CALL SETSMG(Z,103,2.)
      CALL LABELG(Z,0,40.,C,3)
      CALL LABELG(Z,1,4.,0,5.1)
      CALL TITLEG(Z,4,4HTIME,9,9HINTENSITY,0,8HPLOT 001)
      CALL LINESG(Z,400,X,SQEL)
      CALL POINTG(Z,400,X,SQES)
      CALL DASHG(Z,400,X,SQQ,12528)
      CALL DASHG(Z,400,X,SQQ1,16348)
      CALL EXITG(Z)
      STOP
      END
```

```
C       CONTROL CARDS
C
CURVE,7,400.400521, SM GEORGE
$ID=CBHARRIS
*USERPR
FETCHFS,IMSL,IMSL,IMSL.
FNF4,T.
LINK,X,P=IMSL.FF.
EXIT.
GRUMP.
C
C
      PROGRAM CURVE(INPUT,OUTPUT)
C     PROGRAM TO CALCULATE STOKES PROBE SIGANAL VERSUS  DELAY TIME
C     EVERY TIME STEP = 0.1 PSEC
C     T=500 IS EQUIVCLENT TO TIME = 50 PSEC
C     F0Q0,F1Q1, ETC. VALUES FROM NUMERICAL CALCULATION
C     DEL VALUES IN RADIANS PER 0.1 PSEC
C     CHI VALUES IN RADIANS FROM NUMERICAL CALCULATION
      INTEGER LA,LB
      INTEGER IWK(11)
      REAL A(2048)
      REAL B(1024)
      INTEGER T
      REAL P1(500)
      REAL P2(500)
      REAL P3(500)
      REAL P4(500)
      REAL XEXP(500)
      REAL SUM(500)
      REAL SQA(1000)
      LA=500
      LB=399
      GAUSS=4*ALOG(2.0)
      NN=LA+LB-1
      F0Q0=99.8049
      F1Q1=7.577125
      F2Q2=7.577125
      DEL1=-0.084823
      DEL2= 0.084823
      CHI1=16.925
      CHI2=-16.925
      SNORM=F0Q0+F1Q1+F2Q2
      DO 100 T=1,500
      TT=500.-FLOAT(T)
      TTT2=(TT/70.)
      XEXP(T)=EXP(-TTT2)
100   CONTINUE
      DO 200 T=1,500
      P1(T)=F1Q1*COS(DEL1*FLOAT(T)+CHI1)
      P2(T)=F2Q2*COS(DEL2*FLOAT(T)+CHI2)
      SUM(T)=(F0Q0+P1(T)+P2(T))/SNORM
      A(T)=SUM(T)*XEXP(T)
200   CONTINUE
      DO 300 T=1,200
      GG=200.-FLOAT(T)
      GGT2=GG/70.
      SGGT2=GAUSS*(GGT2*GGT2)
      B(T)=EXP(-SGGT2)
300   CONTINUE
      DO 340 T=1,199
```

```
      B(T+200)=B(200-T)
340   CONTINUE
      CALL VCCNVO(A,B,LA,LB,IWK)
      DO 400 N=1,NN
      SQA(N)=A(N)*A(N)
400   CONTINUE
      PRINT 500
500   FORMAT(/1X,*N=*,10X,*CONVO=*,10X,*SQCONVO=*)
      DO 600 N=5,NN,5
      PRINT 550,N,A(N),SQA(N)
550   FORMAT(I4,4X,E13.05,3X,E13.05)
600   CONTINUE
      STOP
      END
```

TECHNICAL INFORMATION DEPARTMENT
LAWRENCE BERKELEY LABORATORY
UNIVERSITY OF CALIFORNIA
BERKELEY, CALIFORNIA 94720